12-2004

Synthesis and Ordering of Nanostructures Using Laser Light

Yingfeng Guan
University of Tennessee - Knoxville

To the Graduate Council:

I am submitting herewith a dissertation written by Yingfeng Guan entitled "Synthesis and Ordering of Nanostructures Using Laser Light." I have examined the final electronic copy of this dissertation for form and content and recommend that it be accepted in partial fulfillment of the requirements for the degree of Doctor of Philosophy, with a major in Materials Science and Engineering.

Anthony J. Pedraza, Major Professor

We have read this dissertation and recommend its acceptance:

Philip D. Rack, Robert N. Compton, David C. Joy, Narendra B. Dahotre, David B. Geohegan

Accepted for the Council:

Carolyn R. Hodges

Vice Provost and Dean of the Graduate School

(Original signatures are on file with official student records.)

To the Graduate Council:

I am submitting herewith a dissertation written by Yingfeng Guan entitled "Synthesis and Ordering of Nanostructures Using Laser Light." I have examined the final electronic copy of this dissertation for form and content and recommend that it be accepted in partial fulfillment of the requirements for the degree of Doctor of Philosophy, with a major in Materials Science and Engineering.

Anthony J. Pedraza
Major Professor

We have read this dissertation
and recommend its acceptance:

Philip D. Rack

Robert N. Compton

David C. Joy

Narendra B. Dahotre

David B. Geohegan

Acceptance for the Council:

Anne Mayhew
Vice Chancellor and
Dean of Graduate Studies

(Original signatures are on file with official student records.)

Synthesis and Ordering of Nanostructures Using Laser Light

A Dissertation

Presented for the

Doctor of Philosophy

Degree

The University of Tennessee, Knoxville

Yingfeng Guan

December 2004

DEDICATION

This dissertation is dedicated to my wife, Xin Zhang, my parents, Chengping Zhang and Luxiong Guan, great role models and friends, and the rest of my families.

ACKNOWLEDGEMENTS

I would like to thank all those who have helped me during my PhD study. My advisor Prof. Anthony J. Pedraza has been kindly helping me both academically and personally. Great thanks for his patience, insights, and guidance during this work. Special thanks to my group members, Jason Fowlkes, Stephen Jesse and Daryl Smith for their help.

Frank Holiway, Randy Stooksbury, Doug Fielden, Larry Smith, Sandy Maples, Carla Lawrence, Mike Neal, and Greg Jones were courteous and efficient in their assistance.

Finally, I would like to thank Dr. David Geohegan, Dr. David Joy, Dr. Philip Rack, Dr. Robert Compton, and Dr. Nerendra Dahotre for serving on my dissertation committee.

ABSTRACT

This dissertation focuses on the formation of 1-D and 2-D nanoscale structures induced by the KrF excimer UV laser irradiation of silicon (λ=248 nm). Relatively low laser energy density (E_d<=1 J/cm^2) is required to produce nanostructures. Alignment of 2-D nanoripple structures and nanoprotrusions has been realized by using Lloyd's mirror configuration.

Laser-generated silicon microcone arrays were used as templates for the growth of nanocolumns. The formation mechanism of the microstructure is reviewed, and the origin and growth of nanocolumns are discussed. The formation mechanism of nanocolumns requires highly localized melting, which explains why they fail to form on a flat surface but can grow atop the microcones.

Field emission properties from both microcones and nanocolumns have been measured. The high aspect ratio (height/tip radius) of nanocolumns makes them suitable for various field emission applications.

One- and two- dimensional (1-D and 2-D) nano-rippled structures produced in silicon by UV laser irradiation were investigated using atomic force and scanning electron microscopy. One and two beam illumination of the substrate was used to generate the nanostructures. Single beam irradiation was done using p-polarized laser light, while the two beam incidence was employed by using a Lloyd's mirror arrangement to reflect part of the beam onto the substrate. The structures were characterized by direct measurement of the ripple spacing or by measurements done on the fast Fourier transform of their AFM images. Under single beam illumination, only 1-D gratings were generated on the substrate surface. The grating lines were perpendicular

to the projection of the electric field of the incident light on the substrate surface. For the two-beam illumination, it was very difficult to obtain the Lloyd's mirror characteristic interference pattern due to the poor coherency of the laser employed. Nonetheless, the use of a Lloyd's mirror not only strongly enhanced the production of rippled structures, but also produced 2-D gratings. The gratings generated with this arrangement are many millimeters long and cover the entire laser illuminated area. In contrast with one-beam illumination, linearly polarized light was not required to promote the rippled structures. Experimental evidence strongly suggests the following:

1. The p-component of the laser light is responsible for ripple formation;
2. Ripples can propagate with increasing number of pulses;
3. The ripple structure is produced while the silicon is melted.

The occurrence of melting is further supported by a computer simulation of the thermal field during the laser pulse. An estimate done using the lubrication approximation indicates that liquid is displaced from the hotter into the cooler regions by the gradient of surface tension. At angles of incidence equal or larger than 50˚, the ripple spacing data indicate that incident laser light promotes the generation of electron plasma oscillation in the liquid silicon. These surface electromagnetic waves are responsible for the formation of ripples with lines that run parallel to the projection of the wave-vector of the incident wave on the substrate surface.

A two-dimensional array of nanoprotrusions was produced on the surface of silicon upon nanosecond UV laser irradiation using a Lloyd's mirror set up. These protrusions are 40 to 70 nm high and have a diameter of ~60 to 100 nm at their base, and in many cases display a regular rectangular lattice. Their origin and evolution were also studied

using scanning electron microscopy and atomic force microscopy. They were found to originate from a subjacent ripple structure upon continuing irradiation under the same processing conditions that originated the ripples. Their evolution is discussed in terms of fingering instabilities of melted silicon consistent with a gradient of surface tension due to a temperature gradient. This temperature gradient is produced by the same mechanism responsible for the ripple formation.

At slightly higher laser fluences, nanoparticles were observed to form using a single beam of non-polarized laser light. The nanoparticles also span a linear ordered array, with line spacing that conforms to the grating equation. Their formation mechanism has been described previously as a result of ablation and redeposition, and is thus widely different from the formation of nanoprotrusions.

The differences and similarities of nanoprotrusions and nanoparticles, and their connection with nanoripples, were studied in detail. In particular, when the ripple structure was still seen, nanoprotrusions were observed to form on ripple crests while nanoparticles were located in ripple valleys. Thermal annealing of the two nanostructures revealed a remarkable stability of the nanoprotrusions and easy displacement of the nanoparticles, with loss of their alignment.

The simple irradiation procedures used to produce these nanostructures (nanoripples and nanoprotrusions) open the possibility of using them as a template for ordering other nanostructures on a vast scale. Gold films were first sputter-deposited on the rippled surface at a grazing angle, and subsequently annealed. After heat treatment at 800 °C, long range alignment of gold nanoparticles along the nanoripples/nanoprotrusions

structures was realized. The width of gold strips can be controlled by adjusting the grazing angle of the incoming gold atom beam to the substrate.

Table of Contents

Chapter **Page**

List of Tables

Table **Page**

List of Figures

Figure **Page**

CHAPTER 1

BACKGROUND AND LITERATURE REVIEW

1.1 Introduction

One-, two- and three-dimensional (1-D, 2-D and 3-D) coherent and non-coherent nanostructures have been produced in silicon by UV laser irradiation. Nanoparticles, nanoprotrusions, nanoripples and nanocolumns are the products of laser-material interactions. The dimensions and variety of nanostructures can be controlled by laser fluence, polarization, and ambient atmospheres. Generally speaking, nanostructures are produced at energy densities lower than 1.0 J/cm^2. However, in order to obtain nanocolumns, a micro-structured template (microcones/microholes), which is produced at laser fluence ~3 J/cm^2, is required.

Melting, ablation and redeposition are the main mechanisms involved in the production of nanostructures on laser irradiated silicon.

Coherent structures are directly related to the wavelength, the angle of incidence and the polarization of the laser light. In laser-induced non-coherent structures such a direct relation is absent. For nanocolumns, the only non-coherent nanostructure developed in this research, the formation mechanism is very similar to that of microstructures, which has been studied extensively. The growth mechanism is preferential re-deposition of material at its laser-melted tip.

Three steps seem to be required to produce nanocolumns: 1) evolution of shallow surface depressions, which can reach a depth of a few micrometers and a separation distance of 20 to 30 μm; 2) upon further laser irradiation in a reactive atmosphere like

SF_6, dramatic changes occur—accelerated surface-roughening rate and formation of microhole-microcone microstructure; 3) decrease the energy density to ≤ 1 J/cm^2, the lower energy irradiation only produces melting at the very top of the microcone tip. Due to the high sticking coefficient of liquid silicon, a nanocolumn can be formed on top of each microcone.

Field emission (FE) has been measured for both microcones and nanocolumns, and an improvement of FE properties has been observed for the nanocolumns, due to their higher aspect ratio (height/diameter).

Coherent nanostructures—nanoripples, nanoparticles and nanoprotrusions have been produced on smooth silicon wafer, without microstructured template. In this research, the relationships between these three nanostructures have been compared and discussed.

The energy density used to produce nanoripples is close to the silicon melting threshold, and according to the experimental evidence, the silicon remains melted for a period of tens of nanoseconds during irradiation, and the gradient of surface tension is probably responsible for the formation of the nanoripples. The interference between incident or refracted light and scattered waves propagating parallel to the surface can modulate the energy deposited on the surface; thus, give rise to a temperature gradient, which in turn produce a gradient of surface tension. This latter gradient is the driving force of the molten silicon from the hotter region to the cooler region.

A two-beam illumination system was established through a Lloyd's mirror configuration. The Lloyd's mirror set up not only enhances the evolution of ripples but also induces the formation of 2-D structures. These 2-D structures are formed by the interaction of two orthogonal ripple systems, which break each other's lines, forming

nanoprotrusions. Two orthogonal ripple systems are interference pattern by the direct incident beam and the mirror-reflected beam, and the ripples formed under single-beam irradiation, obeying the ripple equation, respectively.

At variance with previous conclusions on nanoparticles, the author found that long-range order of nanoparticles can be obtained by non-polarized light without the microstructured template. The nanoparticles were formed at slightly higher laser fluences, and through aggregation of clusters backscattered by the gas molecules. The alignment mechanism of nanoparticles is similar to that of nanoripples and nanoprotrusions, i.e., interacting with the incoming radiation and moving into specific sites of the substrate.

The relationships between these three nanostructures have been studied. Both nanoprotrusions and nanoparticles associate with a ripple structure. However, the nanoprotrusions are detected in the crests of the ripple structure, while the nanoparticles grow in the valleys. The nanoprotrusions are more stable than nanoparticles, because samples annealing under the same conditions gave different results. Brownian motion was detected for the nanoparticles even at low temperature—423 K, while nanoprotrusions remained stable throughout the whole annealing process.

Finally, both nanoripples and nanoprotrusions have been used as templates to align other nanoscale materials by oblique deposition. In theory, it is a universal method to align any material that can be deposited on the silicon substrate.

High-resolution scanning electron microscopy (HRSEM) and atomic force microscopy (AFM) are two of the most frequently used methods in this research to characterize the nanoscale structures mentioned above.

1.2 Laser—Material Interactions

1.2.1 Material Optical Properties

The interaction of electromagnetic radiation with condensed matter can be characterized in terms of a complex frequency-dependent dielectric constant [1]:

$$\varepsilon(\omega) = \varepsilon_1(\omega) + i\varepsilon_2(\omega) \quad 1.1$$

where $\varepsilon_1(\omega)$ and $\varepsilon_2(\omega)$ are related to the real and imaginary parts of the complex refractive index, m, by the equations [1]:

$$m = n - ik \quad 1.2$$

$$\varepsilon_1 = n^2 - k^2 \quad 1.3$$

$$\varepsilon_2 = 2nk \quad 1.4$$

n and k are both frequency-dependent.

The complex dielectric function is related to the complex refractive index through the following relationship [2]:

$$m = \sqrt{\varepsilon(\omega)} \quad 1.5$$

The response of matter to light is a vast field and has been studied for centuries. Electromagnetic radiation with wavelength in the UV range only interacts with electrons, as atoms are too heavy to respond significantly to the high frequencies involved. Excimer optical wavelengths, λ, are four orders of magnitude larger than the atomic distances of an arbitrary solid material. The response of matter to light can be described by macroscopic quantities, such as the reflectivity R and the absorption coefficient α, which are related to n and k by [3]:

$$R = \frac{(n-1)^2 + k^2}{(n+1)^2 + k^2} \qquad 1.6$$

and

$$\alpha = \frac{4\pi k}{\lambda} \qquad 1.7$$

Jellison et al. found that under 248 nm KrF laser irradiation, the reflectivity of solid and liquid silicon is 0.63 and 0.70, respectively [4]. When exposed to 248 nm KrF laser radiation, the silicon absorption coefficient is 1.81×10^6 cm^{-1} [5]. Figure 1.1 shows the silicon absorption coefficient and reflectivity as a function of wavelength at room temperature.

At normal incident angle, the power density absorbed at depth z is given by

$$\Phi(z) = I(1-R)\alpha e^{-\alpha z} \qquad 1.8$$

where I is the intensity of the incident light, and both R and α vary with the light frequency. According to Equation 1.8, the maximum power absorption can be expected at the surface and decreases with an exponential decay length of α^{-1}. Thus α^{-1} is defined as the penetration depth of the radiation in the material. The above formulas indicate the mathematical relationships between various optical-related parameters. The absorption mechanisms will be reviewed in the next section.

1.2.2 Absorption Mechanisms of Semiconductors

So far five distinct mechanisms or processes for the absorption of light by semiconductors have been identified [6]:

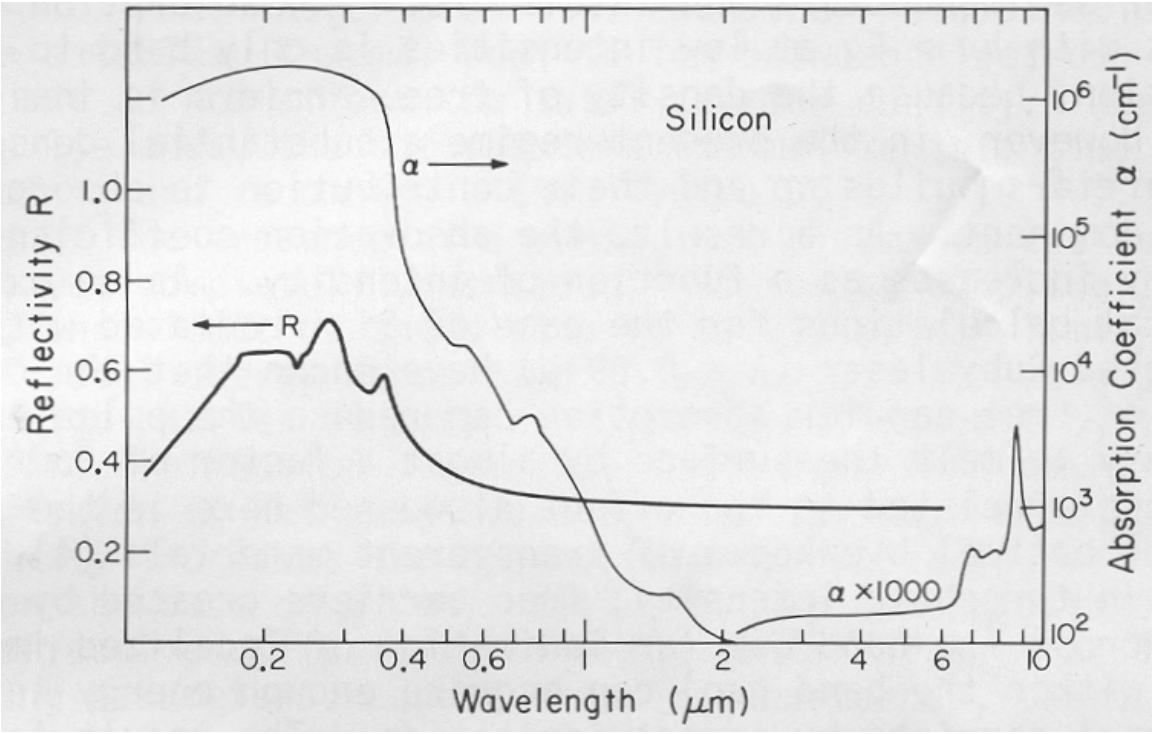

Figure 1.1 Absorption coefficient and reflectivity of Si at room temperature. [3]

Source:
[3] C. W. White and P. S. Peercy, p.6-19 in Laser and Electron Beam Processing of Materials, Academic Press, Inc.

1. Photons with energy ($h\nu$) much less than the band-gap energy (E_g) can excite lattice vibrations directly;

2. Free or nearly free carriers can be excited by absorption of light with $h\nu < E_g$; such carriers will always be present as a result of finite temperatures and/or doping. This mechanism is involved in the absorption of laser radiation of all wavelengths but is particularly important when the laser photon energies are less than E_g in heavily doped indirect band gap semiconductors such as silicon. The effects of doping may not be attributable solely to free carriers but may also involve some symmetry-breaking aspects of the presence of the dopant atoms;

3. Occurrence of metallic-like absorption due to free carriers generated by the laser radiation. The two most important parameters in this mechanism are the equilibrium density of free carriers generated by the laser radiation, and the carrier recombination rate. Due to the fast recombination rate, in the nanosecond regime of pulse durations, this mechanism is relatively unimportant compared to mechanism 4 in determining α for laser radiation well above the indirect band gap in silicon.

4. For photon energies higher than E_g, absorption will take place by direct and/or indirect (phonon-assisted) excitation of electron-hole pairs. The largest contribution to α (for nanosecond pulses) for radiation with $h\nu > E_g$ arises from this mechanism, especially in indirect band gap semiconductors, which have not been heavily damaged or made amorphous by ion implantation. The strong dependence of the absorption coefficient on temperature comes about through this mechanism and not through mechanism 2.

5. Absorption induced by broken symmetry of the crystalline lattice is possible. This mechanism is quite important in laser processing of semiconductors because ion

implantation is frequently used. In those near-surface regions where the ion implantation creates amorphous material, α may easily be increased by an order of magnitude or more over the crystalline value.

To be specific, in semiconductors, when the photon energy hν exceeds the bandgap energy electrons can be excited from the valence band to the conduction band by absorption of the photon. While electrons conduction band can increase their energy further by free carrier absorption, which is the case when many of electrons exist in the conduction band of the semiconductors. Then the energy is transferred to the lattice in 10^{-11} to 10^{-12} s by electron-phonon collisions. Before the electron-hole recombination occurs, the bandgap excitation energy remains, leaving carriers thermalized at the bottom of the conduction band. Once an electron in the conduction band recombines with a hole in the valence band, the recombination energy is given to a third carrier, which is called an Auger processes. The density of carriers decreases during the Auger process, however the total energy contained in the carrier system remains the same due to the transfer of recombination energy to carrier kinetic energy [7]. The main characteristic of an Auger process is the destruction of an electron-hole pair with the simultaneous transference of the energy involved to another electron in the conduction band. The inverse process of the Auger process is the impact ionization, in which a single electron creates an electron-hole pair. Both processes are third order in the carrier density and hence their importance increases rapidly with increasing carrier density (N_e). However, as far as energy conservation is considered, Auger processes are preferable because the minimum energy required for electron-hole recombination is just the band-gap energy, whereas an electron

in the conduction band must have an energy of at least twice E_g in order to create an additional electron-hole pair.

The bandgap of silicon is 1.1 eV, so free carrier absorption is the only possible mechanism when photon energies are less than 1.1 eV. Silicon becomes an indirect bandgap material when the photon energy is between 1.1 eV and 3.0 eV, and phonon-assisted band-to-band absorption processes become the dominant absorption processes. Once the photon energies are greater than 3.0 eV, the absorption coefficient is similar to that of a metal due to direct band-to-band transitions. Thus, the silicon absorption depth is a function of incoming beam wavelength, λ, and the absorption depth at λ=400 nm is 10 μm, while at λ=1 μm is 10 nm.

Other than the wavelength, the absorption coefficient of silicon varies with temperature and changes with the state of the materials, as shown in Figure 1.2 [7]. According to this figure, a drastic absorption depth change happens from 3 μm at room temperature to 0.2 μm at melting temperature during laser heating of crystalline silicon, due to increased free carrier absorption and bandgap narrowing as temperature increases. Molten silicon is metallic therefore when the surface melts the absorption coefficient increases to the value characteristic of the metallic state (10^6 cm^{-1}).

Yoffa [8-9] has studied the carrier-lattice interaction during pulsed laser irradiation. After the laser energy has been absorbed by the electronic system, the following processes may occur to redistribute the energy:

1. carrier collisions;

2. plasmon production;

3. electron-hole recombination by an Auger process;

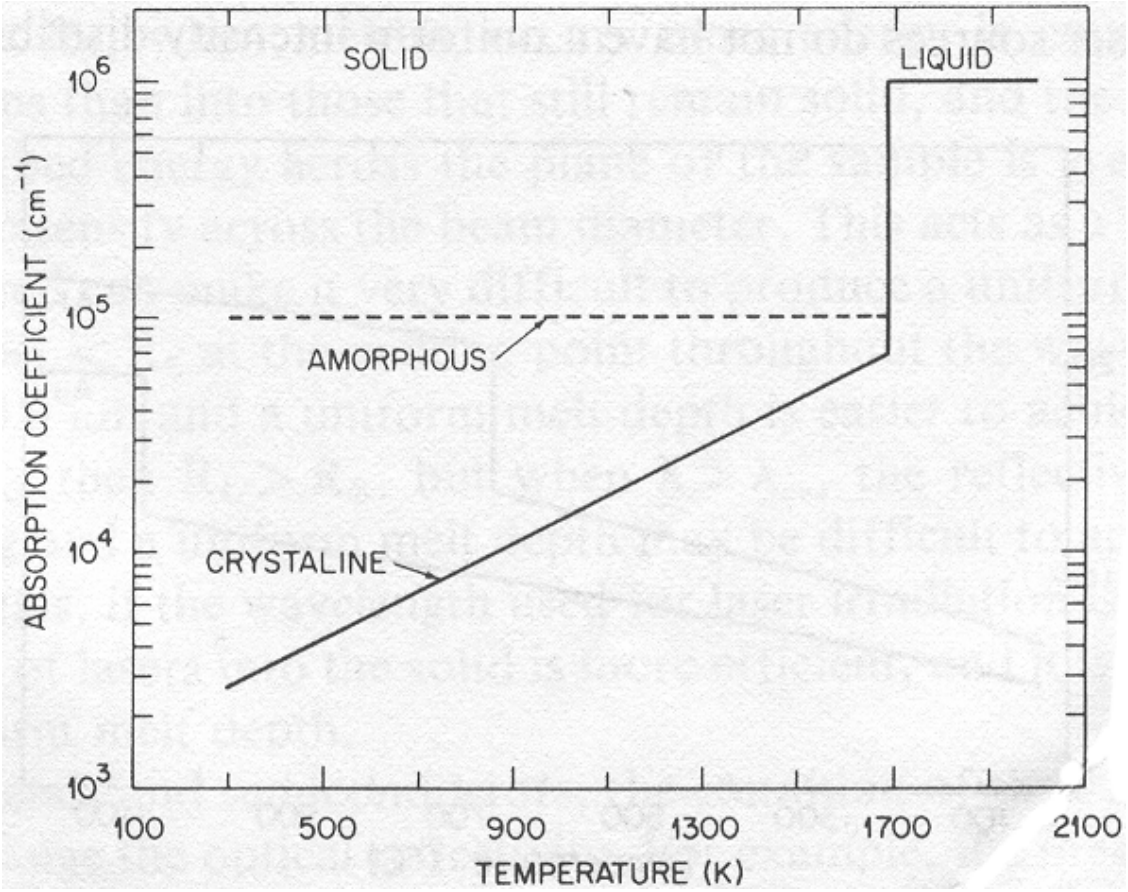

Figure 1.2 Silicon absorption coefficient as a function of temperature at λ=694 nm. [7]

Source:

[7] C. W. White and M. J. Aziz, "Energy Deposition, Heat Flow, and Rapid Solidification during Pulsed-Laser- and Electron-Beam Irradiation of Materials" p. 21 in Surface Alloying by Ion, Electron, and Laser Beams, ASM International, Metals Park, Ohio, 1987

4. electron-hole creation by impact ionization (the inverse of 3);

5. phonon emission.

The first four processes result only in the redistribution of energy among the carriers, while the last process results in transfer of energy to the lattice, thus raising its temperature.

1.2.3 Laser Melting and Ablation

1.2.3.1 General Introduction to Laser Melting

In pulsed laser processing of silicon, the laser may typically deliver to the sample surface an energy density, E_d, of 1.5 J/cm^2 in a single pulse of duration τ=15 ns (FWHM), and the corresponding power density is roughly 50 megawatts/cm^2 averaged over the pulse. The band gap in silicon at 300 K is 1.16 eV, for photon energies greater than that, as much as 70% of this power will be reflected from the surface for some wavelengths, while the rest of the light will be absorbed by electronic excitations in the sample [6].

In some of the earlier papers, the reflectivity change was attributed to the high density of photogenerated carriers, which persisted after the termination of the laser pulse. However, Blinov et al. [10] concluded that this explanation did not fit their data on the absorption of long-wavelength radiation during irradiation of Si and GaAs with pulses from a Q-switched ruby laser. They surmised instead that the reflectivity change was due to the melting of a thin surface layer.

Ready carried out calculations of heat conduction in solids subjects to intense laser in the early days of laser-related science and technology [11]. Most of these calculations

were concerned with the effects of laser radiation on metals, but some work on semiconductors was also reported. When Si, Ge, InP, and other semiconductors are irradiated with sufficiently intense laser pulses, a high-reflectivity phase is observed [10,12-13], strongly suggesting that the near-surface region melts. Simulation results based on melting model were reported by several groups [3, 14-21]. This model involved finite-difference or finite-element solutions of the heat diffusion equations and frequently took into account explicitly both the temperature dependence of the thermal properties and the possibility of melting. The applicability of the melting model concerns the lifetime of electron-hole pairs during intense laser irradiation and the transfer. Virtually all of the experimental data indicate that the transfer of energy from the carrier system to the lattice occurs in times of the order of 10^{-10} sec, or less. In fact, Svantesson et al. [22] found that in silicon the pulse width and shape of the recombination radiation in the region around 1.1 eV (indirect band gap of silicon) tracked the 30-nsec excitation pulse almost identically, exceptions are for a very low-intensity component that lasted for a few microseconds. From the decay characteristics of the radiation, the authors concluded that the fast component of the recombination was due to Auger processes.

Another simulation model is the plasma model, which assumes that at the power levels involved in pulsed laser annealing, dense electron-hole plasma is created in the sample and remains decoupled from the lattice for periods of the order of 100 ns [3, 23-26]. The model assumes that it is the plasma instead of the liquid state, which is responsible for the high-reflectivity phase observed during transient-reflectivity experiments. The disruption of the covalent bonding implied by the formation of the plasma is supposed to lead to a variety of effects normally associated with the liquid state.

1.2.3.2 Simulation of Laser Melting

In previous section, Wood's melting model was mentioned. Recently, simulation work has been carried out by Unamuno [27] and Singh [28]. Unamuno incorporated the latest values for the thermal and optical parameters of Si in the UV range, and thermal melting calculations were done for crystalline and amorphous silicon. Instead of a numerically based simulation, just based on simple energy balance considerations, Singh et al developed analytical equations for the estimation of certain thermal effects in laser-irradiated materials. The energy balance method yields results in far less time with reasonable accuracy without the necessity of computer program development.

Figure 1.3 shows Unamuno's simulation on the melt depth in crystalline silicon (c-Si) as a function of time for 50 ns laser pulse duration and 193 nm laser wavelength [27]. Figure 1.4a shows the relationship between melted depth and laser energy density for 248 nm laser wavelength calculated by Unamuno, while Figure 1.4b shows Singh's calculation [28], which is consistent with Unamuno's.

The melting threshold of c-Si as a function of the laser pulse duration was also calculated by Unamuno [27]. The simulated data fits well with the experimental data, and for a 25 ns laser pulse duration, the melting threshold value is 0.55 J/cm^2.

1.2.3.3 Laser Ablation

Both thermal and photochemical processes can yield material removal, provided large laser energy density is supplied to the target. One remarkable characteristic of the excimer laser is that the surface temperature can reach as high as 10^4 K [29]. Calculations

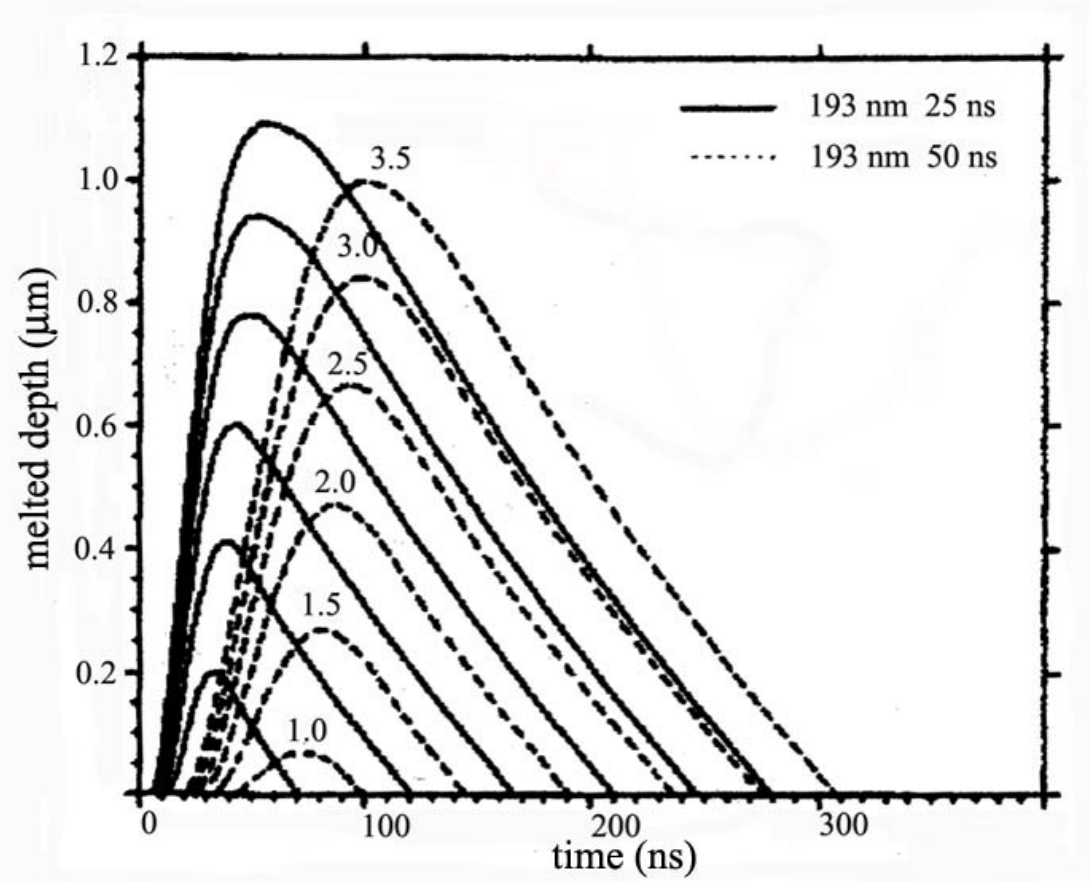

Figure 1.3 Simulation results of melted depth as a function of laser irradiation time for c-Si under 193 nm laser treatment at various laser fluences. FWHM of solid lines is 25 ns, and for dashed lines it is 50 ns. [27]

Source:

[27] S. De Unamuno and E.Fogarassy. A Thermal Description of the Melting of C- and a-Silicon Under Pulsed Excimer Lasers. *Appl. Surf. Sci.* **36**(1-4), 1-11. 1989.

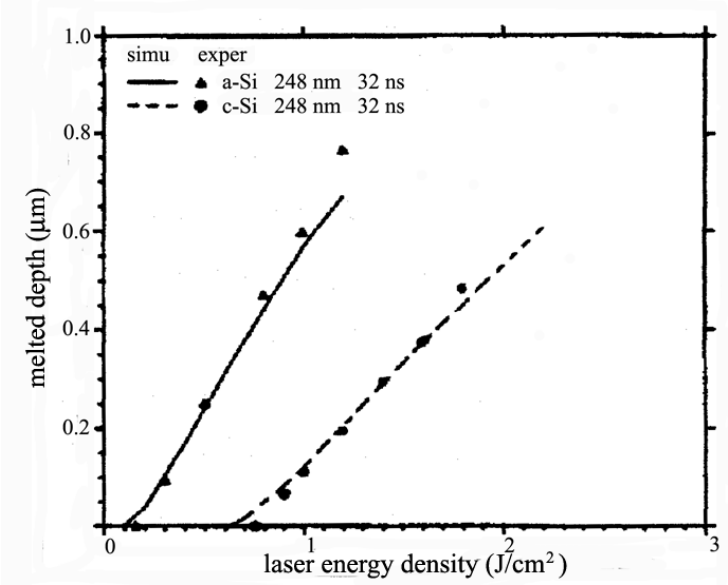

(a)

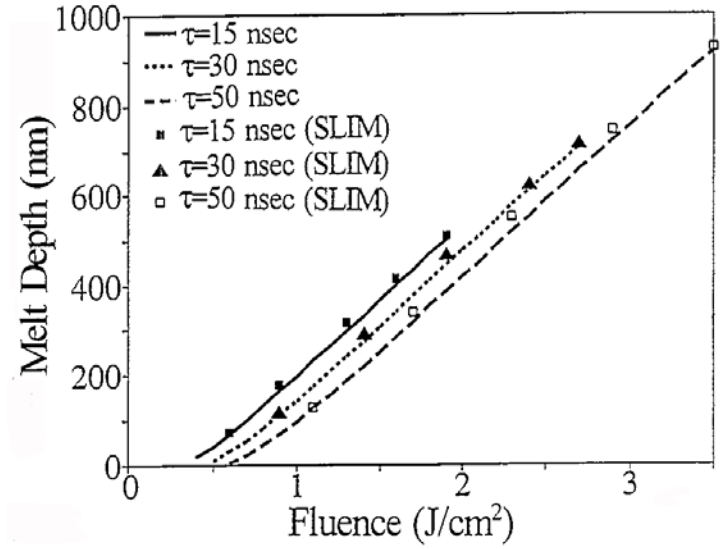

(b)

Figure 1.4 (a). Unamuno's simulation results of the melted depth of both amorphous and crystalline silicon as a function of laser energy for KrF laser. (b) Singh's simulation results based on energy balance. Melt depth values for lasers with FWHM=15, 30 and 50 ns are shown respectively. [27,28]

Source:

[27] S. De Unamuno and E.Fogarassy. A Thermal Description of the Melting of C- and a-Silicon Under Pulsed Excimer Lasers. *Appl. Surf. Sci.* **36**(1-4), 1-11. 1989.

[28] R. K. Singh, D. R. Gilbert and J. Viatella. A Novel Method to Predict Laser-Induced, Non-Linear Thermal Effects in Semiconductors. *Materials Science and Engineering B* **40**(1), 89-95. 1996.

by Shinn indicates that under 248 nm laser irradiation at a fluence of 1.3 J/cm^2, the highest temperature the target can reach is 2700 ˚C [30]. He also reported that material removal —ablation— of silicon was observed as low as 1 J/cm^2 when irradiated in 1000 Torr of He with a 14 ns ArF (λ=193 nm) laser, which is contrary to Wood's report [6]. According to Wood and other's calculations no vaporization was observed up to 5 J/cm^2 for 41 ns XeCl (λ=308 nm) laser. Even after considering a lower power density from the longer wavelength and wider FWHM of the XeCl laser, the difference between the data of two different sources is still unacceptable for the same material—silicon. Further experiments [31-34] indicate that Shinn's result is more reasonable.

Heating rates up to 10^{15} K/s have been reported over a 20-50 ns laser pulse [29]. Thermal shock, expulsion of liquid, vaporization of the target and finally modification of the microstructure and surface morphology can be expected under such high heating rates. Although the parameters related to the laser play an important role in determining the material ablation, what really matters is the target material and their thermal and optical properties under UV laser irradiation.

1.3 Laser-Induced Non Coherent Structures

1.3.1 Introduction

Structures that develop on solid or liquid surfaces by laser-material interactions can be classified into coherent structures and non-coherent structures.

Coherent structures are directly related to the wavelength, the coherence, and the polarization of the laser light. For non-coherent structures such a direct relation to these laser parameters is absent.

Possible feedback mechanisms that cause coherent or non-coherent structure formation are: changes in optical or thermal properties, local thermal expansion, surface tension effects, surface acoustic waves (SAW), capillary waves, melting, vaporization, transformation energies, and chemical reactions. [35].

When the incident laser beam interferes with scattered/excited surface waves, it can generate an oscillating radiation field on the surface of the substrate. And this field is the origin of the coherent structure, whose spatial period is therefore proportional to the laser wavelength.

The feedback mechanism is different for non-coherent structures, which are not directly related to any spatial periodicity of the energy input caused by interference phenomena. Instead, the feedback results in either spontaneous symmetry breaking or a non-trivial spatiotemporal ordering of the system [36-38].

1.3.2 Laser-Induced Surface Perturbations in Silicon

Pulsed laser irradiation can alter the topography of substrates of different materials under a variety of processing conditions. For example, it has been reported that after laser irradiation at a fluence of 1-2 J/cm^2, surface smoothening of tape-cast Al_2O_3, whose initial surface is made of micron-size particles, occurs as a result of induced melting [39]. In order to decrease the surface free energy of the system the melt spreads laterally

producing a significantly smoother surface. On the other hand, many researchers have found that a pronounced surface relief develops, when the initially smooth surface of single crystals of Si and Ge are exposed to pulsed-laser irradiation [40-45]. Even after one single laser pulse, a highly uniform and periodic surface roughness can be produced [46-48], which is the coherent LIPSS structure introduced in later sections.

In this section, the evolutions of surface perturbations (non-coherent structures) that are produced at significantly higher laser fluences are reviewed. Unlike the coherent LIPSS structure, the roughness augments continuously with the number of pulses and is not a function of the polarization of the laser beam or the angle of incidence. The initial stages of laser-induced roughening in silicon may be independent of the atmosphere used. Morphology after a few hundred laser pulses depends on the crystallographic orientation of the surface, and is related to the nature of the solidification process that follows laser melting.

The evolution of the relief on a (001) Si surface as the number of laser pulses is increased from 50 to 200 at a fluence of 3 J/cm^2 and under Ar gas is shown in a series of optical micrographs (Figure 1.5) [49]. Figure 1.6 shows the evolution of surface relief on a (111) Si surface in vacuum as the number of laser pulses is increased from 50 to 200 at a fluence of 3 J/cm^2. As the number of pulses increases, new depressions quickly develop filling the gaps between the first ones formed and start increasing in depth. A prominent feature at the upper left edge develops ahead of other perturbations. Similar results have been observed on samples irradiated in Ar gas. Figure 1.7 shows the evolution of (111) silicon surface irradiated in Ar after 40 to 600 pulses. The relief on most of the surface is very subtle after 50 pulses but becomes very marked after 200 pulses. Because the

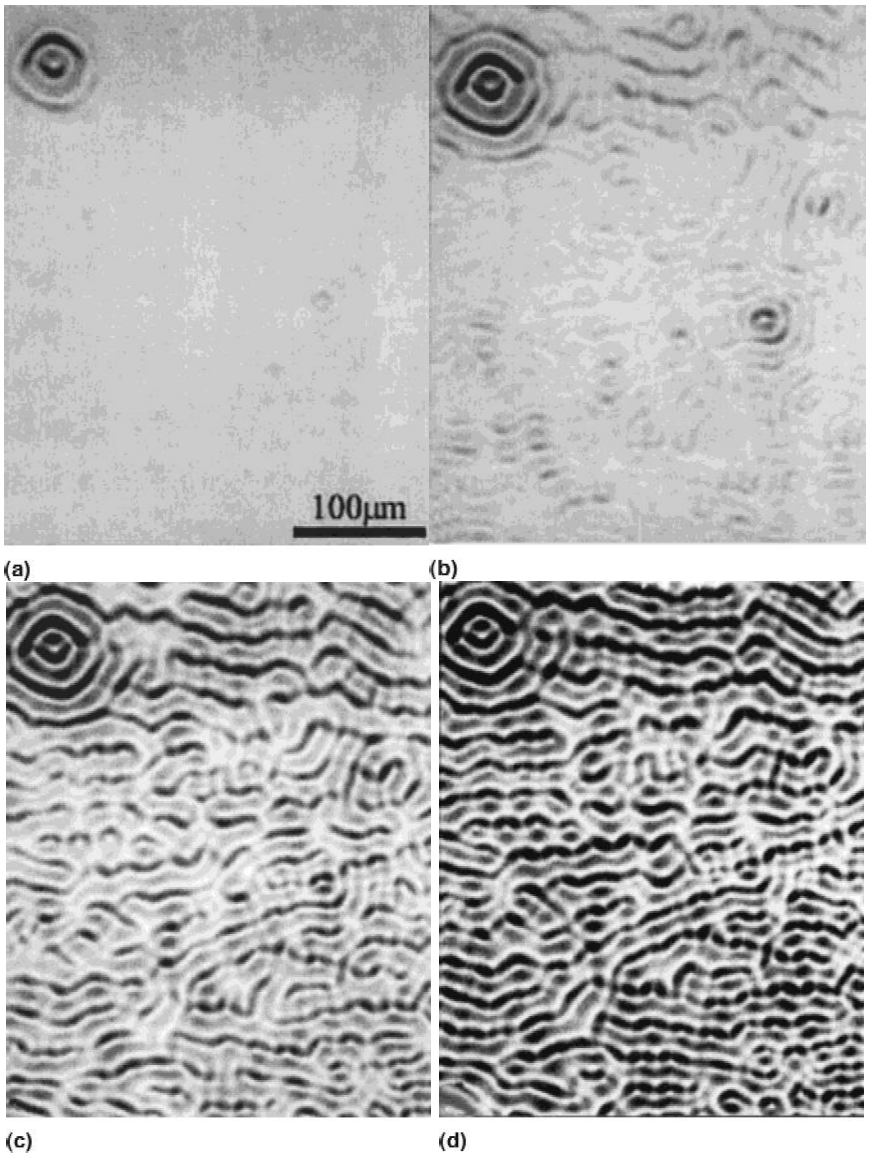

Figure 1.5 Evolution of the surface relief on (001) Si surface irradiated in 0.5-bar pressure of Ar at a fluence of 3 J/cm^2, after (a) 50 pulses, (b) 100 pulses, (c) 150 pulses, and (d) 200 pulses. [49]

[49] A. J. Pedraza, S. Jesse, Y. F. Guan, and J. D. Fowlkes, *J. Mater. Res.* **16**(12), 3599 (2001)

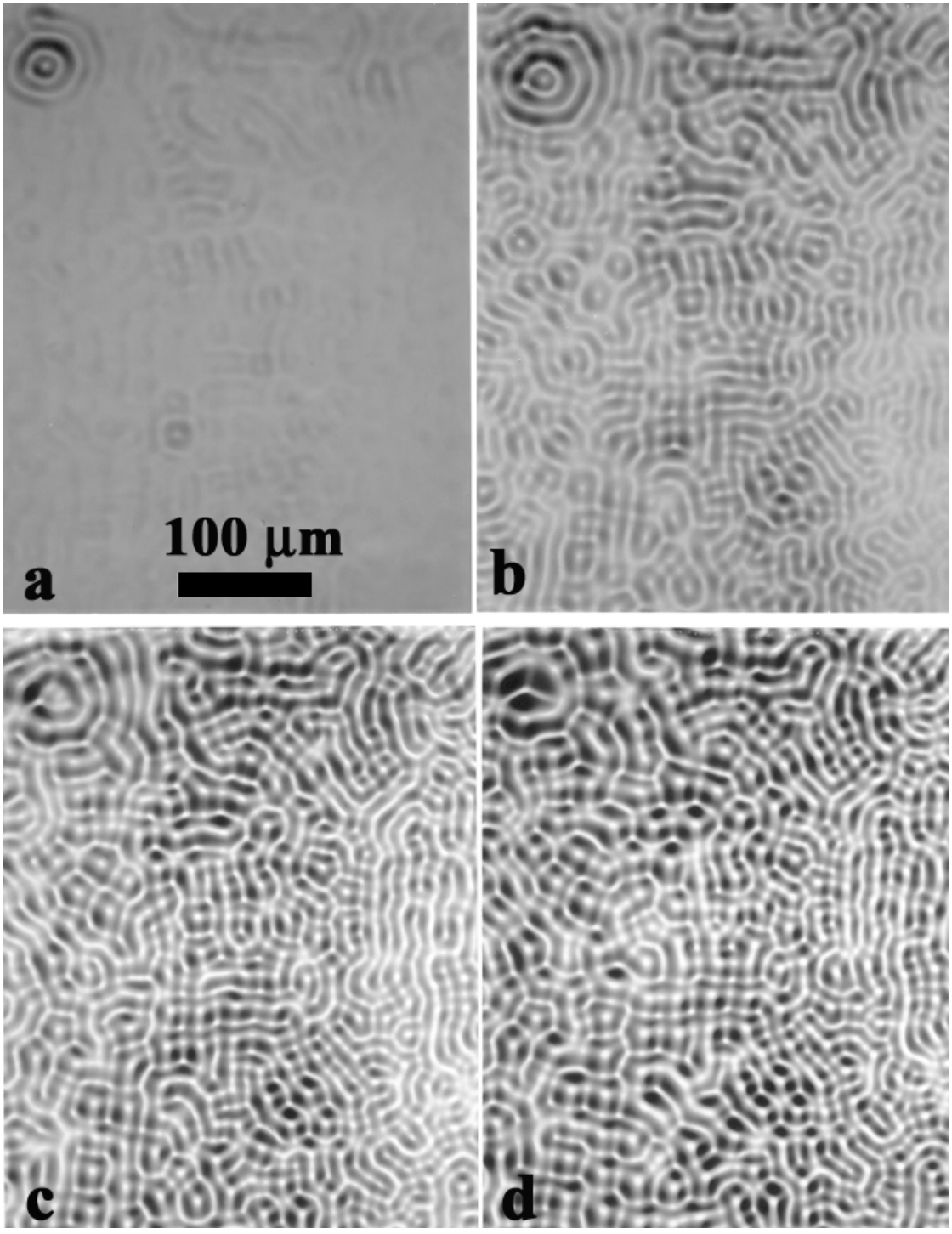

Figure 1.6 Evolution of the surface relief on (111) silicon surface irradiated in vacuum at a fluence of 3 J/cm^2, after (a) 50 pulses, (b) 100 pulses, (c) 150 pulses, and (d) 200 pulses.

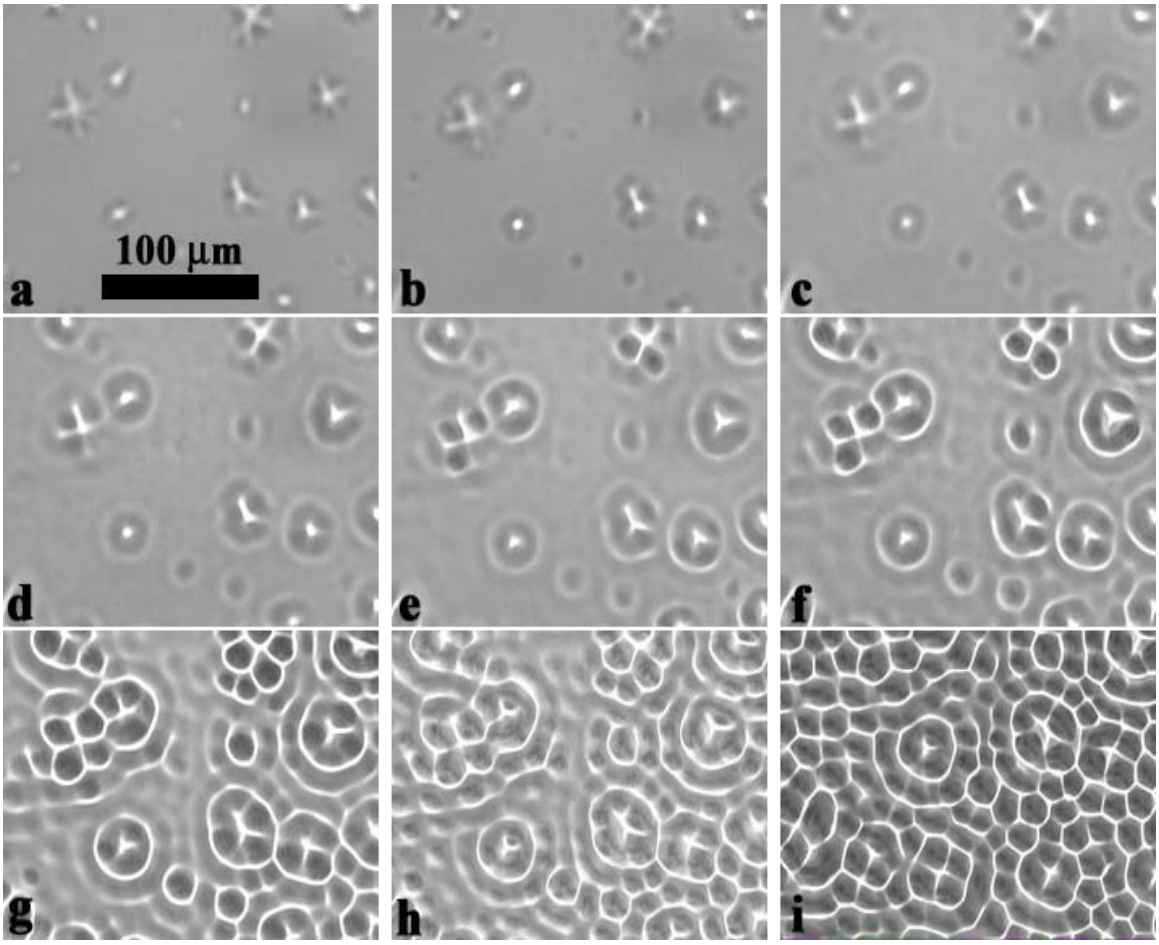

Figure 1.7 Evolution of the surface relief on (111) silicon surface irradiated in Ar at a fluence of 2.1 J/cm^2, after (a) 40 pulses, (b) 80 pulses, (c) 120 pulses, (d) 160 pulses, (e) 240 pulses, (f) 300 pulses, (g) 400 pulses, (h) 500 pulses, (i) 600 pulses.

surface relief features keep their shape and location, the microstructure is not the result of the production of capillary waves but of the deepening of shallow craters, which maintain a fairly constant diameter. The optical micrograph of Figure 1.8a reveals with remarkable clarity the (111) surface symmetry. Similar morphologies have been found in (111) silicon surfaces etched with gaseous HCl at high temperature [50]. These symmetry-related features are not present on laser-irradiated (001) surfaces (Figure 1.8c), although the morphology also appears as formed by cubes. The relief on (112) surfaces after irradiation in SF_6 at 3 J/cm^2 is composed of undulating lines along one direction (Figure 1.8b). No relief is formed on (011) surfaces even after 3000 laser pulses at a fluence of 3 J/cm^2 [49].

The comparison of Figures 1.8a, 1.8b and 1.8c shows that the surface relief produced during irradiation depends on the surface orientation.

Perturbations occurring during laser irradiation that could give rise to the observed depressions have been extensively studied in the literature [47,51-52]. Perturbations in the vapor/liquid interface were modeled assuming that they are due to vortices generated by the unstable motion of the vapor produced during irradiation [53]. This vortical motion would generate a spatial modulation of the pressure. In turn, this difference in pressure would produce motion of the liquid from the depression to the elevation increasing the amplitude of the wave in the liquid [52]. The instabilities in the liquid/vapor front departing from a planar geometry would give rise to the production of surface structures with a period between 10 and 30 μm [52]. In another model, the effect of perturbations in the solid/vapor and the liquid/vapor interfaces were studied assuming differential ablation, which produces perturbation growth [51]. Under certain conditions

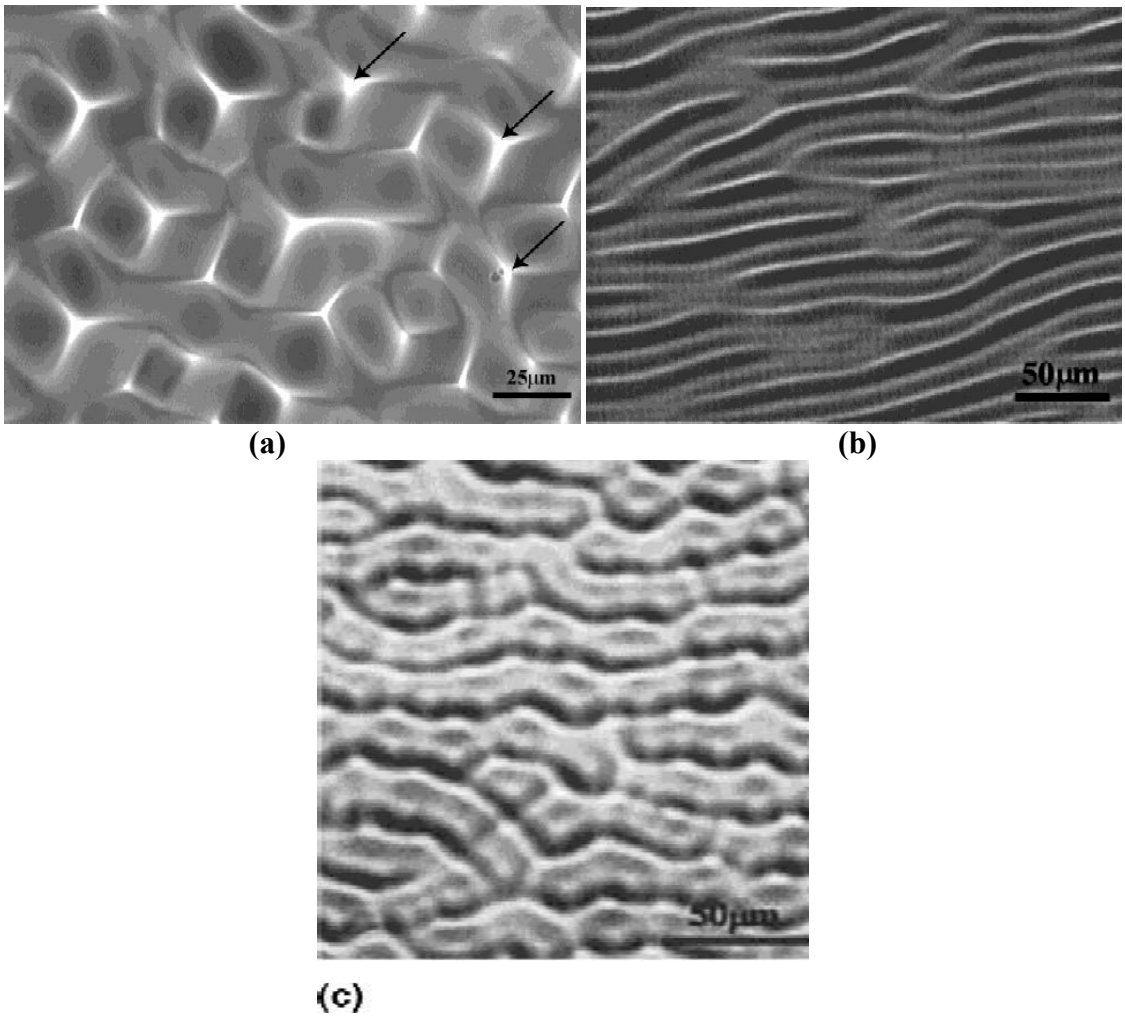

Figure 1.8 (a) Nomarski contrast image of (111) Si surface irradiated with 400 pulses at a laser fluence of 1.5 J/cm^2 in vacuum (arrows indicate apices). (b) Surface relief of (112) Si surface irradiated with 600 pulses in 0.5 bar of SF_6 at a fluence of 3 J/cm^2. (c) Surface relief of Si specimens irradiated under different atmospheres with 200 pulses at a fluence of 3 J/cm^2 on a (001) Si surface in vacuum. [49]

Source:
[49] A. J. Pedraza, S. Jesse, Y. F. Guan, and J. D. Fowlkes, *J. Mater. Res.* **16**(12), 3599 (2001)

the ablation rate of the crests is less than the ablation rate at the depressions. In this model the instabilities grow exponentially as exp (γt), where γ is growth rate. The instability grows when the parameter $\gamma > 0$. However, the calculation of this coefficient for the case of long wavelength perturbations always gave a negative value indicating that probably this mechanism is not applicable in this instance.

Jesse et al [54] found that spacing of surface features is highly dependent on the time that the substrate top layer remains liquid. Increasing the melt time can be done either by increasing the incident energy or the initial substrate temperature prior to irradiation. However, the effect of increasing incident energy is not as apparent as increasing the substrate temperature. There is a relationship between the wave spacing and the crystallographic orientation of the substrate, which can not be explained by previous models. Jesse [54] proposed a model that offers complete explanations for the evolution of laser induced surface protrusions and the relationship between different surface patterns and the surface orientations. His model constitutes an instability analysis that assumes that the surface is initially populated with perturbations of very small amplitude but having a wide range of wavelengths and that under the action of certain mechanisms, perturbations with a specific wavelength will increase in amplitude, while others will dampen. One key point of his model is to regard the spacing of surface features as a result of the changing shape of both the solid-liquid (SL) and liquid-vapor (LV) interfaces during the melt time of the substrate. The two interfaces evolve differently during the melt time, since the morphology of the SL interface is mediated by the evolving thermal field in the substrate, and morphology of the LV interface is governed by the action of capillary wave motion of the free molten surface. The feature

spacing of the surface pattern is determined by the different temporal evolution of these two interfaces.

1.3.3 Formation of Microcone-Microhole Structures by Laser Irradiation

Laser induced surface perturbations can evolve into coupled microcone/microhole structures by further laser irradiation. Drastic changes in both the roughening rate and the morphology have been reported after a large number of pulses [49]. The distance between microcones or microholes is determined by their precursor—surface perturbations.

Unlike surface perturbations, the formation of a microcone/microhole structure is very sensitive to the surrounding atmosphere. These microstructures can only be achieved in an active atmosphere, such as, SF_6 or oxygen, while in an inert ambient gas or in vacuum, the surface perturbations will not evolve into these microstructures. Figure 1.9 compares the silicon surface morphology after laser irradiation in different atmospheres, which indicates clearly the effect of surrounding atmosphere [49].

Figure 1.10 shows the relationship between the number of laser pulses and the surface roughness of specimens irradiated at 3 J/cm^2 under SF_6 and Ar atmospheres and in vacuum. It can clearly be seen that up to approximately 600 pulses the roughness is almost identical in all cases. Namely, in the first several hundred laser pulses the surface roughness is not sensitive to the surrounding atmospheres. However, after 600 pulses, the roughness of samples irradiated in SF_6 increases drastically for both (111) and (001) orientations. While for samples treated in vacuum or Ar, the roughness increase is much gentler. The dramatic change in roughening rate measured in specimens irradiated under

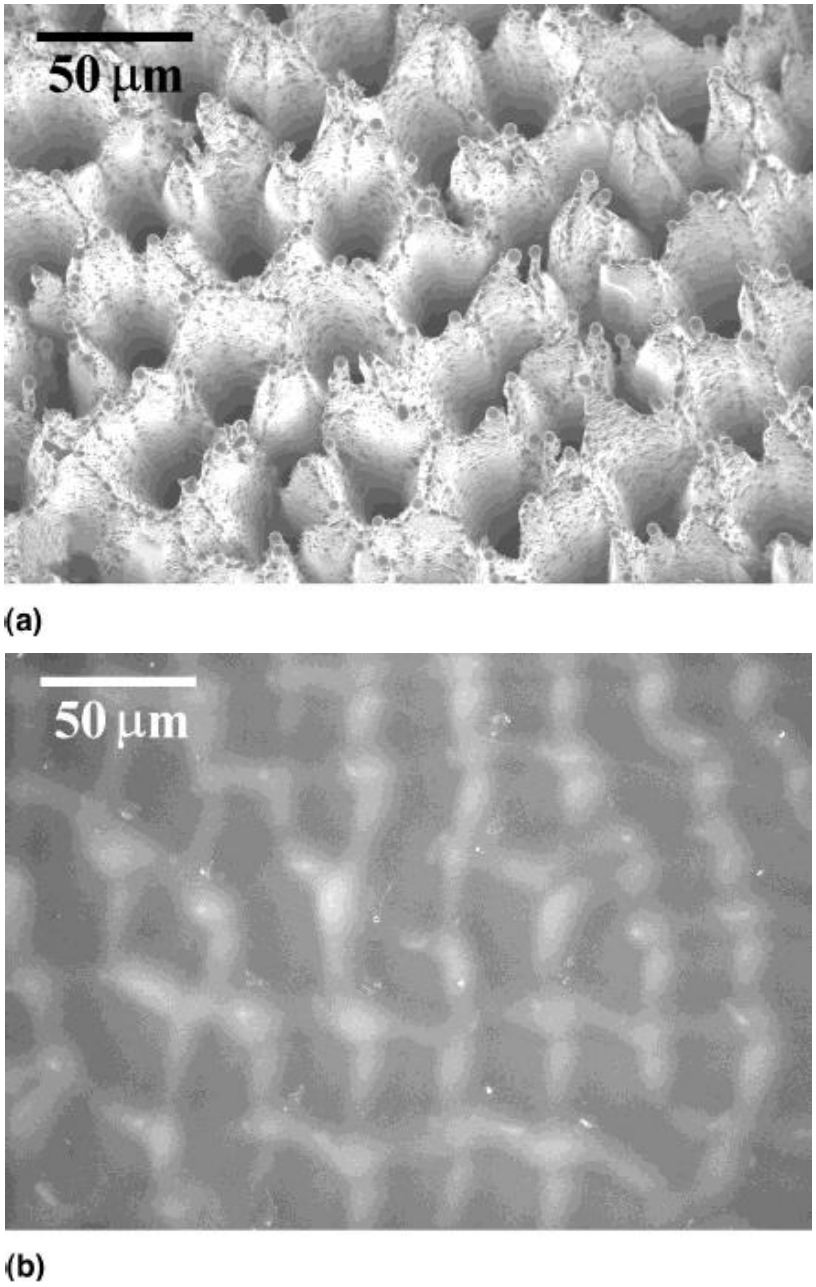

Figure 1.9 SEM images of (001) surfaces irradiated with 2000 pulses in (a) SF_6 and (b) vacuum. [49]

Source:
[49] A. J. Pedraza, S. Jesse, Y. F. Guan, and J. D. Fowlkes, *J. Mater. Res.* **16**(12), 3599 (2001)

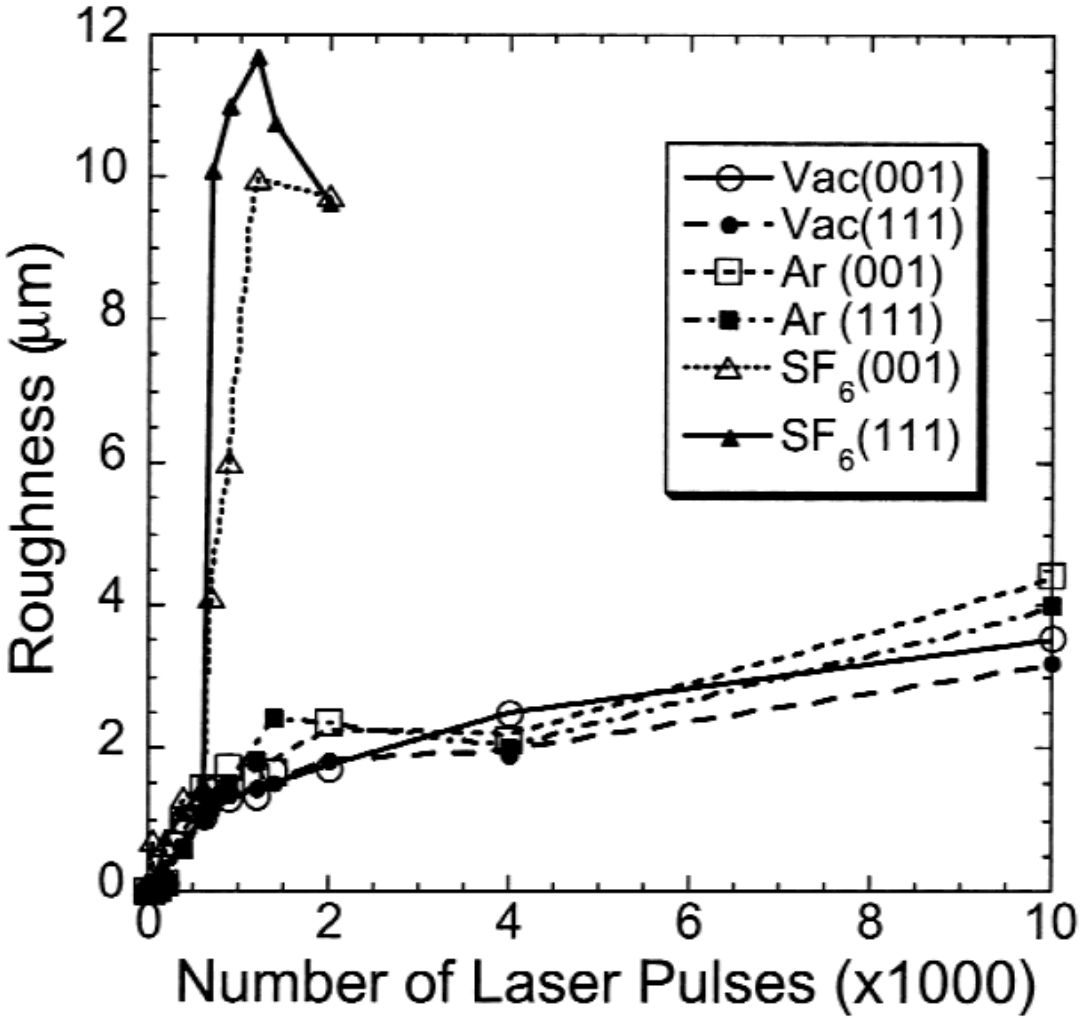

Figure 1.10 Silicon surface roughness of (111) and (001) surfaces as a function of the number of pulses for specimens irradiated at 3 J/cm^2 under SF_6, Ar, and vacuum atmospheres. [49]

Source:
[49] A. J. Pedraza, S. Jesse, Y. F. Guan, and J. D. Fowlkes, *J. Mater. Res.* **16**(12), 3599 (2001)

SF_6 clearly indicates a change in the mechanism causing the roughness boost. As seen in Figure 1.10, the silicon surface roughness produced under SF_6 ambient gas reaches the maximum at ~1300 pulses and decreases afterwards.

Several authors reported the formation of a dense array of high aspect ratio columns when irradiated in O_2-rich atmospheres, after 1000 laser pulses at an energy density of 3 J/cm^2 [41,44-45,50-55]. Sanchez et al. proposed that a hydrodynamic instability was responsible for the growth of columns in Si irradiated in air [41-42,55]. However, it has been pointed out that it was unlikely that straight columns, tens of micrometers tall, would grow by this mechanism [44].

Her et al. and Fowlkes et al. reported that under an SF_6 atmosphere an array of conical microstructures can be produced [40,43,56]. The conelike structures can form in a wide range of materials [57]. Foltyn had proposed a preferential etching mechanism to explain laser-induced cone formation [57]. However, Pedraza et al. pointed out that due to the fact that under sulfur hexafluoride (SF_6) atmospheres, the cone structures protrude above the initial surface, this mechanism is not applicable here [43,56]. Pedraza's group studied the relationship between the laser-induced silicon microstructures and the irradiation atmosphere [43,44,49,54,56], and found out that under the same irradiation conditions of wavelength, pulse fluence, and accumulated fluence, no columns are formed under inert gases such as nitrogen or argon [43-44]. By contrast, at high intensity, SF_6 will decompose, producing free fluorine. At high temperatures, free fluorine produced from the decomposition may then react with silicon at the surface, producing volatile SiF_2 [58]. The generation of a volatile species could enhance the laser plume, causing further decomposition of SF_6 [49]. So SF_6 fulfills two roles: 1) acts as an etcher

of silicon, and 2) exerts the background pressure that tends to restrict the expansion of the plume. Irradiation under Ar or vacuum, with similar conditions, does not induce a drastic increase in roughness supports the conclusion that the reactivity of SF_6 is the trigger for etching and the development of the associated plume [59].

After 600 pulses in SF_6 there is a change in the *cubic* morphology, which eventually produces the characteristic microhole-microcone microstructure. Figure 1.11(a) shows the transition from the shallow surface perturbation toward the microhole/microcone structure. The (001) specimen shown in Figure 1.11(a) has been irradiated under SF_6 with 750 pulses at a laser fluence of 2.6 J/cm^2. Clearly visible microholes have developed in some of the depressions. In other region the microstructure has evolved even further and microholes appear to pervade the depressed regions. In regions with well developed microholes, microcones started to form. Figure 1.11(b) shows the fully developed microcone/microhole structure after 1500 pulses.

Figure 1.12 is a cross sectional image of a silicon specimen irradiated with 2000 pulses that reveals the presence of very deep holes when the fluence is increased to 2.7 J/cm^2. The crest-valley distance in the figure is ~350 μm.

The mechanism proposed to explain these processes involves the ablation of silicon from regions surrounding the emerging features and the enhanced redeposition of silicon on top of them [43,44,49]. Thus, the deep grooves and pits between cones result from a laser-induced ablation phenomenon and this receding part of the surface surrounding each of the cones is the source of an intense flux of silicon-rich vapor. At variance with vapor-liquid-solid method (VLS) described in the literature [60-62], the laser process does not require the presence of a catalyst [44]. The pulsed-laser irradiation has two

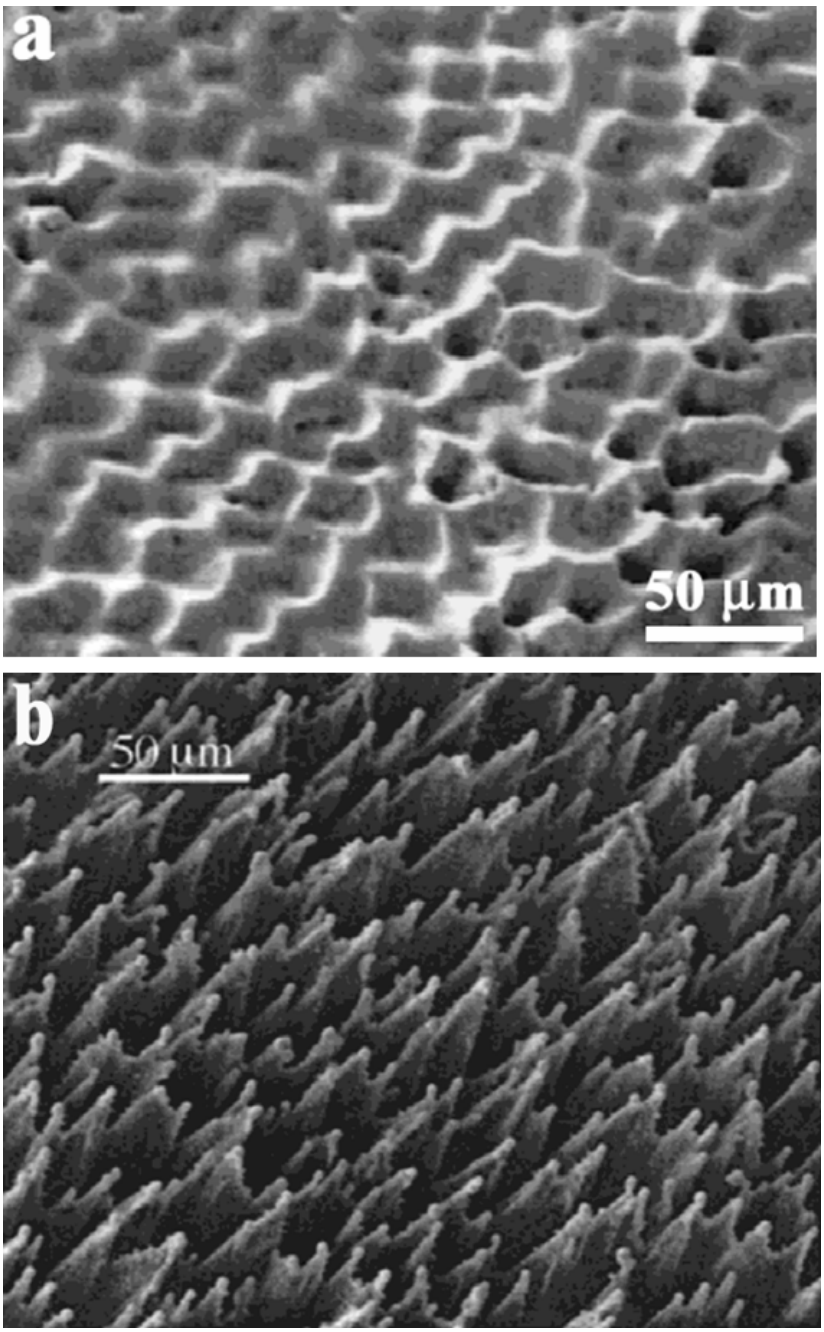

Figure 1.11 SEM images of (001) silicon surface morphology irradiated under SF_6 at 3 J/cm^2: (a) 750 pulses; (b) 1500 pulses. [32]

Source:

[32] Anthony J. Pedraza, Jason D. Fowlkes and Yingfeng Guan, "Surface Nanostructuring of Silicon", *Applied Physics A* **77**, 277-284 (2003).

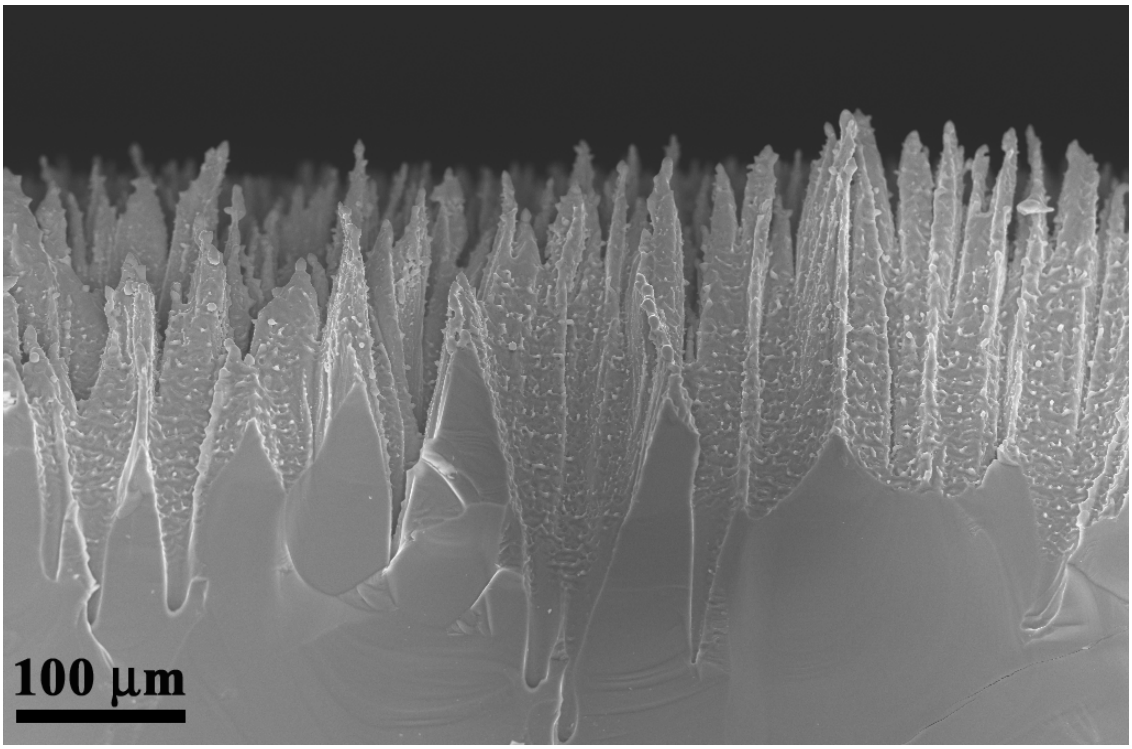

Figure 1.12 Cross sectional SEM image of a microcone/microhole structure. The silicon specimen was irradiated at a fluence of 2.7 J/cm^2 with 2000 pulses under an SF_6 background pressure of 0.5 bar.

simultaneous effects—the production of silicon flux and the melt of the tips of the cones. According to deposition theory a negligible super saturation is required to initiate the deposition on the liquid substrate [63]. The accommodation coefficient for molecules and atoms in a liquid is close to one [63]. For this reason the deposition takes place preferentially at the cone tips, which remain melted for a longer time than any other part of the cones, thence a very high axial growth rate could ensue. Another characteristic during the laser processing is the high reflectivity of a silicon surface to UV light and the formation of the cavity walls with steep slopes. Simulation shows that there is very strong concentration of laser energy at the bottom of the holes, due to multiple reflections which has been pointed out by Jesse [59]. Calculations show that according to this focusing effect, at the bottom of the microhole, a fourfold increase in the light intensity can be expected [59].

In situ studies using an ICCD camera established a relationship between the evolution of the fluorescent plume and the deepening of microholes [59]. Figure 1.13 shows the evolution sequence of silicon microstructure on a silicon surface under laser irradiation in SF_6. The ICCD images show that the production of microcones/microholes is closely correlated with the evolution of the laser-generated plume. This correlation is strong evidence that the silicon-rich material, which is removed by an ablation-etching process from the microholes feeds the growth of the cones near them, revealing the interplay between the deepening of microholes and growing of cones [59].

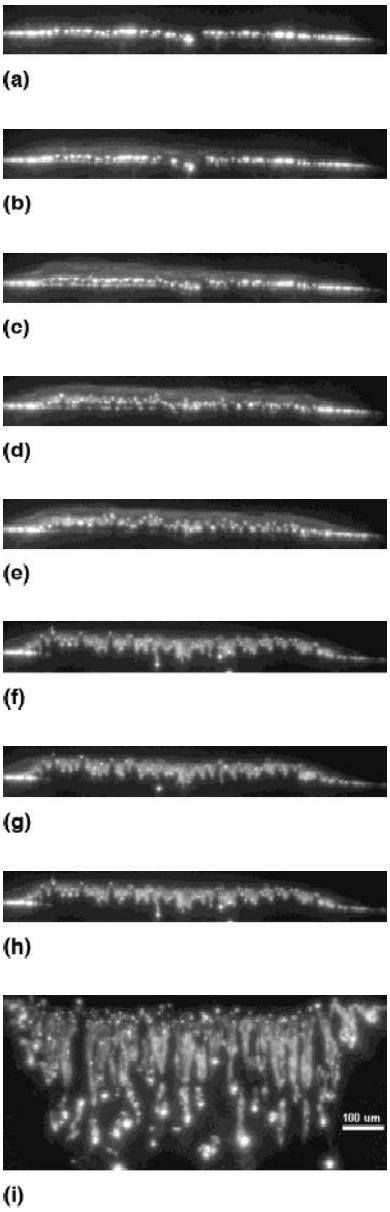

Figure 1.13 Evolution of microcones and microholes in Si irradiated at 3.1 J/cm^2 in SF_6 at a pressure of 0.5 bar. ICCD images were taken in continuous mode with a delay time of 55 ns. Parts (a) through (h) show the microstructure and the plume at 520, 550, 600, 700, 800, 900, 1300, 1700, and 22,000 sequential pulses, respectively. [59]

Source:
[59] S. Jesse, A. J. Pedraza, J. D. Fowlkes, J. D. Budai, *J. Mater. Res.,* **17**(5), 1002 (2002)

1.4 Laser-Induced Nanoparticulates

One of the most important characteristics of silicon nanoparticles is their luminescence properties. Extended research has been done in this area during the last decade or two. However, bulk silicon does not exhibit light emission due to its indirect gap. Canham reported bright visible photoluminescence and electroluminescence from porous Si [64], whose particle size is in the nanometer range. Similar results from other researchers confirmed his observation [65-70]. These results open the possibility of integrating Si nanostructures into future ultra-large-scale optoelectronic devices [71]. In this section, generation and alignment of silicon nanoparticles will be reviewed.

1.4.1 Photoluminescence from Si Nanostructures

The origin of the photoluminescence is still unclear. Different mechanisms have been proposed, such as radiative recombination through surface states [72], or through localized Si-O-Si states inside the oxide layer surrounding the crystallite core [73] or at the Si/SiO_2 interface [67-68,74-75]. However, the most plausive model involves quantum confinement effects [76-78]. Bulk silicon is an indirect band-gap semiconductor. Due to misaligned bands, the quantum efficiencies of bulk silicon are very low: $\sim 10^{-6}$. However, when the silicon particles are in the nanometer scale, quantum efficiencies of $\sim 10^{1}$-10^{2} can be realized, because the localization of carriers in nanometric crystallites, whose size is less than the exciton effective Bohr radius, leads to an increase in the energy gap and to more efficient radiative recombinations. Nanoscale silicon is, thus, also described as having a quasi direct band-gap.

Optical pumping through laser beam or a flash lamp can produce bound electron-hole pairs and is required for photoluminescence experiments. Milliseconds to nanoseconds decay rates have been observed during the PL experiments on optically pumped silicon nanoparticles [79].

Based on quantum confinement theory, a relationship between emission quanta energy and nanoparticle diameter has been established [77],

$$E_\lambda = E_0 + \frac{3.73}{d^{1.39}} \qquad 1.9$$

where E_λ is the energy (eV) of the emitted quanta, E_0 is the indirect band-gap energy of silicon (1.17 eV), and d is the diameter of silicon nanoparticle (nm). Many experimentally obtained PL maxima (eV) are consistent with the predictions of quantum confinement theory [75,80-84]. For example, Patrone et al. reported tuning the PL band within a large spectral region extended from near the UV to near the IR by varying the size of the Si nanoparticles [84].

1.4.2 Nanocluster Formation through Pulsed Laser Deposition (PLD)

Defects and impurities in the material can greatly change the PL properties. In order to increase the light-emission efficiency, it is necessary to suppress contaminants in the nanoparticle formation process. Currently, the commonly used techniques to synthesize nanoclusters are wet chemical methods, such as colloidal chemical techniques, which are suitable for porous Si or chain-like Si structures [66], and dry techniques such as chemical vapor deposition (usually using silane gas) [68,69], implantation of Si ions into dielectric hosts, strain induced island growth using molecular beam epitaxy and pulsed

laser deposition. Apparently, laser ablation process has advantages from the viewpoints of safety and compatibility with the environment. Also, the contamination, which is common to other techniques mentioned above, can be avoided in the laser ablation process. For this reason, PLA/PLD in inert background gases has been widely applied to the preparation of silicon nanocrystallites [81,85-88]. The particulate size and density strongly depend on the deposition parameters, such as the laser wavelength, laser power, laser spot size, and ambient gas pressure. Thus, by varying the experimental parameters, highly effective condensation of nanoclusters with reduced size dispersion can be obtained [70,89]. In this section, the relationship between experimental parameters and the accordingly produced nanoparticles will be introduced.

1.4.2.1 The Effect of Target Chemistry and Background Gases

Generally speaking, for most ceramic systems the compositions of both target and the PLD-produced particulates are the same. In binary metallic systems, on the other hand, exceptions have been reported. Chen [90] et al. pointed out that in such systems, the particulates are usually deficient in the element with lower melting temperature, and the difference is proportional to the particulate size.

If irradiation takes place in inert gases atmosphere, composition will be preserved. However, reactive background gases can modify the chemical composition of the produced nanoparticles [91]. For instance, ablating a Ti target in a nitrogen atmosphere can produce TiN nanoparticles.

Matsunawa et al. found that much smaller Si nanocrystals were obtained for ablation into He than into Ar [92].

1.4.2.2 The Effect of Ambient Gas Pressure

PLD processes in vacuum and in inert ambient gas give different result. Collisions between the ejected species and the ambient gas increase as the ambient gas pressure increases. However, when the PLD process is carried out in vacuum, there will be much less collisions between the ejected species until they reach the substrate. So the particulates formed during this process are mostly solidified liquid droplets expelled from the target by the recoiled pressure [93]. When the ambient gas is present, the vapor species can undergo enough collisions that nucleation and growth of particles can take place before they arrive at the substrate. Since the growth is controlled by diffusion, the particulate size is controlled by residence time of the particulate in the vapor. Because the residence time is proportional to the ambient gas pressure, larger particulate size can be expected at higher pressure.

However, the particle size is not a linear function of the ambient pressure. Lowndes et al. reported that the mean size of nanoparticles produced by ablation into a gas and collected at some fixed distance does not increase monotonically with the gas pressure, contrary to the observations of Yoshida and Makimura [81,88]. Comparison of their results can be found in Figure 1.14 [94]. Lowndes et al. found that the mean nanoparticle size reached a maximum at a pressure near 6 Torr in helium, with smaller nanoparticles found at both higher and lower pressures, with fixed target-substrate distances. Their

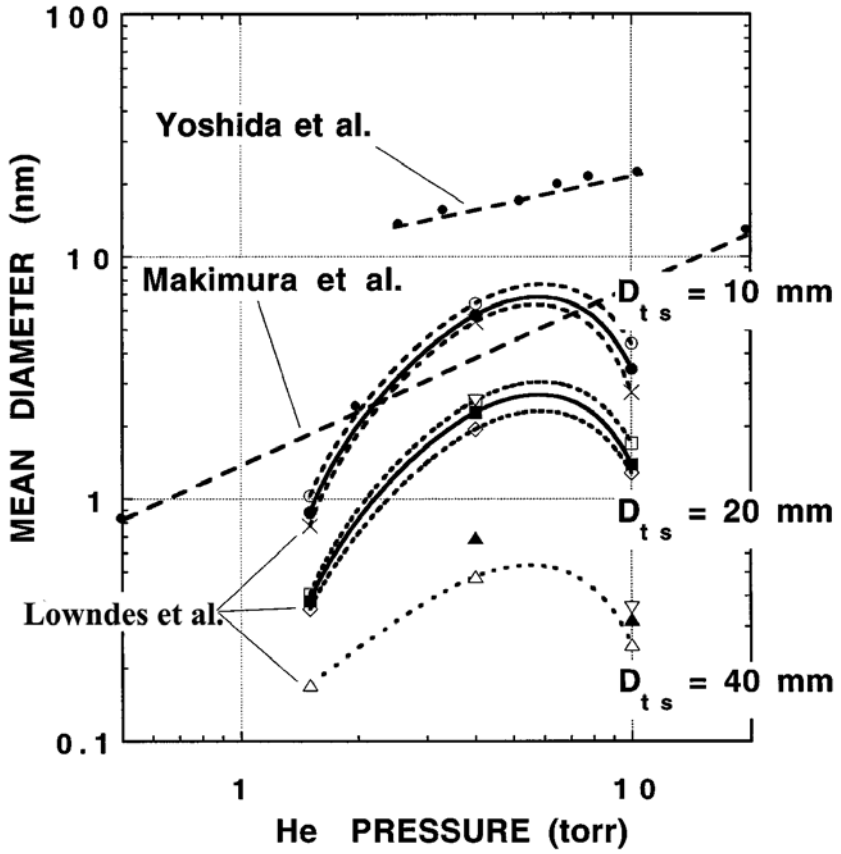

Figure 1.14 Average Si nanoparticle diameter (height) versus He gas pressure during ablation, at target-substrate separations Dts - 10, 20, and 40 mm. For each Dts value, size distributions were measured at two locations on each substrate, corresponding to the center and left-of-center of the ablation plume (open symbols and dashed lines). The average of these measurements is shown by the solid symbols and line. Results from Refs. 7 and 10 also are shown. [94]

Sourece:
[94] D. H. Lowndes, C. M. Rouleau, T. G. Thundat, G. Duscher, E. A. Kenik, and S. J. Pennycook, *J. Mater. Res.* **14**(2), 359 (1999)

explanation for this phenomenon is that at lower pressures, the mean free path of Si particles decreases as the background pressure increases, so that more collisions can be expected, which in turn can increase the nanoparticle size. However, there are already a lot of collisions at higher pressures, so only those experiencing fewer collisions can reach the substrate, i.e., when background pressure is larger than 6 Torr, nanoparticle size decreases as the background pressure increases.

1.4.2.3 The Effect of Laser Fluence

For a chosen material and a fixed laser wavelength, the laser fluence on the target has the most significant effect on the particulate size and density [93]. In general, there is a laser fluence threshold. Below the threshold the particulates are barely observable; above it the particulate number density increases rapidly with increasing fluence.

Normally, the nanoparticles are collected on the substrate. Actually, the target itself can also collect nanoparticles being reflected from the ambient gases. Observations of nanoparticle size as a function of laser fluence by Patrone et al. were based on the nanoparticles collected on the target [95]. The cluster size was characterized by AFM in tapping mode. Figure 1.15 [95] shows that the nanoparticle size distribution increases as the laser energy density increases from 1 to 3.9 J/cm^2. From the figure, a jump from 1.3 nm to 5-6 nm can be observed. This is strong evidence that the average nanoparticle size is proportional to the laser fluence.

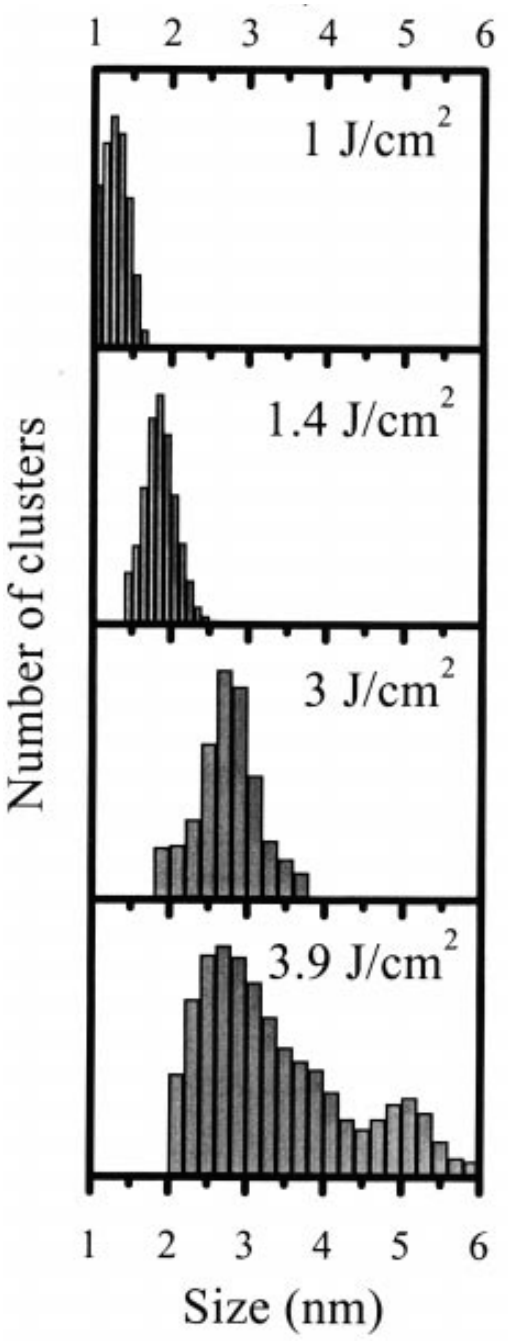

Figure 1.15 Cluster size distribution for deposits prepared at 4 Torr of He and at different laser fluences: 1 J=cm2, 1:4 J=cm2, 3 J=cm2, and 3:9 J=cm2. Size measurements were carried out by AFM on the clusters deposited at the center of the samples. [95]

Source:
[95] L. Patrone, D. Nelson, V. I. Safarov, S. Giorgio, M. Sentis, and W. Marine, *Appl. Phys. A* **69**[Suppl], S217 (1999)

1.4.2.4 The Effect of Target-to-Substrate Distance and Spatial Distribution

As the laser energy increases, the speed of the generated plume increases as well. Particle size and distribution depends on the target-substrate distance compared to the plume length. Dyer et al. [96] have shown that E/P_0 is the scaling parameter for plume range, where E is the laser-pulse energy, and P_0 is the background gas pressure. The plume length $L \propto (E/P_0)^{1/3\gamma}$, where γ is the ratio of specific heats of the elements in the plume. A very homogeneous distribution of particulate size and density can be obtained when the target-to-substrate distance is much smaller than L. Nishikawa [97] reported that as the target-to-substrate distance increases, the proportion of the smaller particulates decreases, and a few larger particulates appear, indicating smaller particulates merge during flight.

A number of reports indicate that the silicon particulate number density to be higher off the deposition axis [98-99], while Cheenne et al. [100] reported lower particulate densities off the deposition axis.

Lowndes et al. found that for Si, the largest nanoparticles were found closest to the ablation target, and the mean nanoparticle size decreased with increasing D_{ts} (distance between target and substrate) [94]. However, Makimura et al. observed that there is negligible nanoparticle deposition if the collection substrate is placed within the fluorescent part of the ablation plume; only at distances greater than the plume length L can the nanoparticles be formed [81]. He also reported an increase in the mean size of metallic nanoparticles formed by millisecond pulsed Nd: YAG laser ablation, which is in striking contrast with the observation of Lowndes et al. [94]. Figure 1.16 [94] shows the

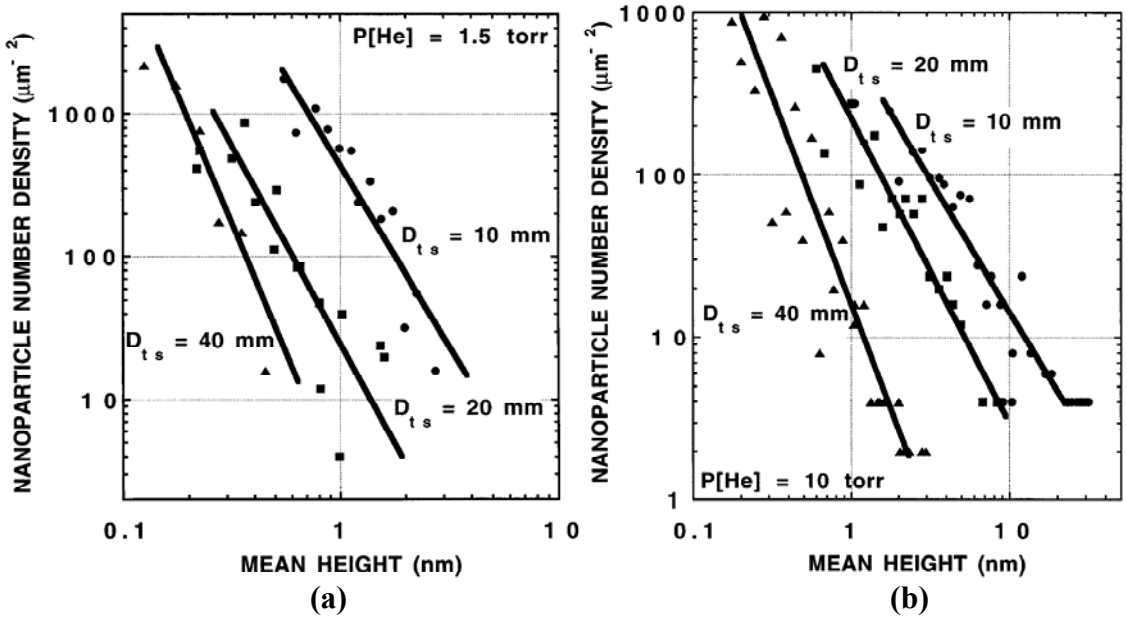

Figure 1.16 Area density of Si nanoparticles versus nanoparticle diameter at D_{ts} - 10, 20, and 40 mm for He pressures of (a) 1.5 Torr, and (b) 10 Torr, using 500 ArF laser pulses at 1.04 J/cm^2. This data was derived by analysis of AFM measurements, as described in the text. [94]

Source:
[94] D. H. Lowndes, C. M. Rouleau, T. G. Thundat, G. Duscher, E. A. Kenik, and S. J. Pennycook, *J. Mater. Res.* **14**(2), 359 (1999)

density of Si nanoparticles versus nanoparticle diameter as a function of D_{ts}. From the figure, we can see that the slope of 40 mm line is steeper than that of 10 mm line, which means a narrower size distribution at larger substrate-target distance. Also, the mean diameters for the 40 mm line are smaller than that for the 10 mm line, which indicates that at larger D_{ts}, the resulting average nanoparticle diameter is smaller (Figure 1.16). By comparing Figure 1.16a and Figure 1.16b, one can tell that higher ambient pressure leads to larger particle size, provided all the other experimental conditions remain the same. From the above results, larger target-substrate distance and lower ambient pressure should be used to obtain smaller particle size and narrower size distribution, which is critical to quantum confinement effect.

1.4.2.5 The Effect of Other Parameters

The laser wavelength λ plays an important role in determining the nanoparticle size. The absorption coefficient α decreases with decreasing λ. So for a shorter wavelength, the laser penetration depth is larger.

The laser duration time also makes a difference. Wu et al. compared the physical differences from ablation with nanosecond pulses and picosecond pulses [101]. They pointed out that shorter pulse durations result in higher peak power densities and therefore larger electric fields at comparable energy densities. Other potential advantages include that short pulses can decrease the thermal diffusion length into the target during the laser irradiation; the energy density threshold of picosecond pulsed laser is lower than that of nanosecond pulsed laser.

Target surface roughness and bulk density can have some effect on the particulate generation rate [93].

1.4.3 Time-Resolved in situ Imaging of Nanoparticle Evolution

Many methods to investigate the hydrodynamic flow or collisional phenomena during the nanoparticle production process have been reported. For example, the velocities of the particulates have been investigated by a number of groups. Gagliano and Geohegan used a high-speed camera to measure the velocities, respectively [102-103]; Dupendant used a rotating substrate device [104]; Murakami used laser beam deflection technique [105].

Among these techniques, in situ PL measurements can provide spatially and temporally resolved information about the connection between changes in plume hydrodynamics and the nucleation and growth of nanoparticles [106].

Chiu et al. attempted the first PL measurements of gas-suspended silicon nanocrystals [107]. Geohegan et al. reported the first time-resolved measurements of photoluminescence from gas-suspended nanoparticles by gated intensified CCD-array (ICCD). They compared the different silicon nanoparticle formation and dynamics in He and Ar. From Figure 1.17a, one can see that within 20 μs, the velocity of the nanoparticle drops from 2 cm/μs to 0.01 cm/μs. The deceleration is due to the collision with the background gas. Figure 1.17b shows the first detectable PL 3 ms after the initial ablation pulse when silicon was irradiated in 1 Torr argon gas, under 5-8 J/cm^2 laser fluence [106]. For the ablation in He gas, it only takes 0.15 ms to produce PL. Similar results were

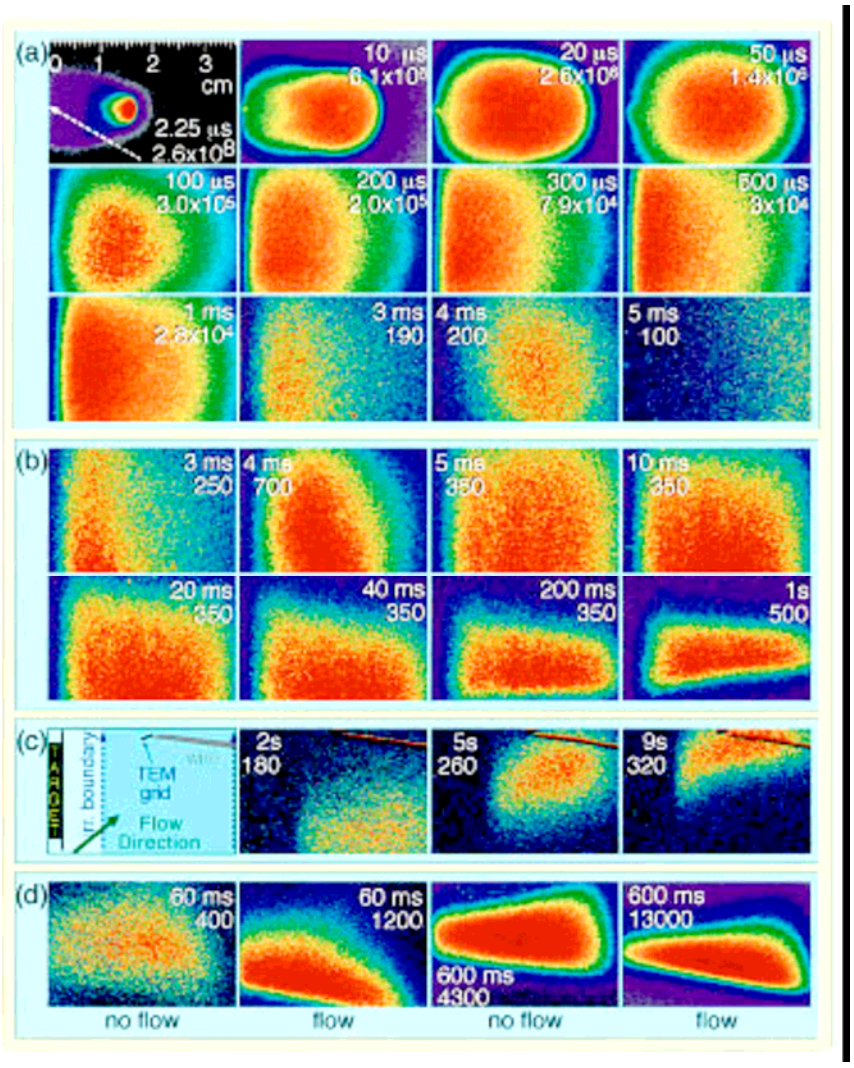

Figure 1.17 (A) Gated-ICCD photographs of the nascent visible plasma luminescence observed when a 2" c-Si wafer (left of frame) is laser-ablated (KrF, 28 ns FWHM pulse, incident at 30° as shown) into 1 Torr Ar (5 ns to 15 µs exposures). The time delay after ablation and the maximum intensity (red) of each image are listed. (B) 3 µs exposures of PL from nanoparticles after a XeCl-laser pulse (308 nm, 4.0 eV, 30 ns FWHM ~0.2 J/cm^2 in 3.5 cm x 0.15 cm beam) is directed vertically through the plume at the indicated times after laser ablation. (C) PL images of the nanoparticle cloud swept by the weak argon flow onto a TEM grid for subsequent analysis. (D) Rayleigh-scattered light from nanoparticles is imaged at two times (60 and 600 ms) after laser ablation into static (''no-flow'') or flowing (''flow'', 270 sccm) 1 Torr Ar. [106]

Source:
[106] D.B. Geohegan, A.A. Puretzky, G. Duscher, and S.J. Pennycook, *Appl. Phys. Lett.* **72**(23), 2987 (1998)

reported by Makimura, who observed the PL emission 1.2 ms after silicon ablation [108]. However, a different process was used in Makimura's experiments. PL was directly observed from the nanoparticles by Geohegan, while luminescence from the decomposed clusters through a second laser pulse was recorded by Makimura. Figure 1.18 shows spatial distributions of light emission at given laser duration τ_d [108].

As mentioned before, the ambient gases can affect the nanoparticle size and distribution. Figure 1.19 is the ICCD images of PL from nanoparticles produced by silicon ablation into 10 Torr He [106]. Because argon gas is much heavier than helium gas, only static, uniform cloud of nanoparticles are found in Figure 1.17, due to the collision between the nanoparticles and the heavy Ar gas. However, fewer collisions are expected in lighter He gas, so that smoke-ring of nanoparticles are observed throughout the chamber and finally encounter the silicon wafer (Figure 1.19) [106].

Other than Si nanoparticle, Geohegan et al. also studied in situ the formation, oxidation, and transportation of SiO_x nanoparticles by measuring their photoluminescence [109]. For the first time, the time-resolved PL from gas-suspended nanoparticles was measured. Together with other ex situ analyses techniques, the optical properties of isolated nanoparticles during synthesis can be modified. Time-resolved in situ imaging technique is not limited to silicon. It has been applied to superconductors as well [110-112]. Geohegan et al. determined the onset times and pressures for gas-phase $Y_1Ba_2Cu_3O_{7-d}$ (YBCO) nanoparticle formation by ICCD imaging process [110]. They also compared the laser ablation plumes of YBCO into vacuum and oxygen by photographing with an ICCD camera. Digitalized images of the visible plume emission have been used to investigate the laser plasma thermalization and the onset of shock

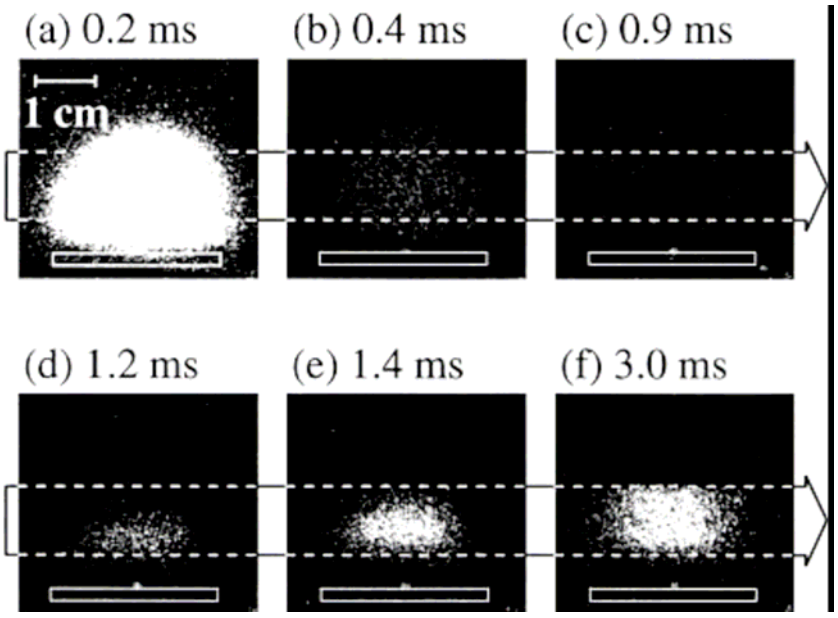

Figure 1.18a–f Light emission distributions in 5-Torr Ar gas at given delays. In distributions d–f, silicon nanoparticles are observed in the track of the decomposition laser light. [108]

Source:
[108] T. Makimura, T. Mizuta, and K. Murakami, *Appl. Phys. A* **69**[Suppl], S213 (1999)

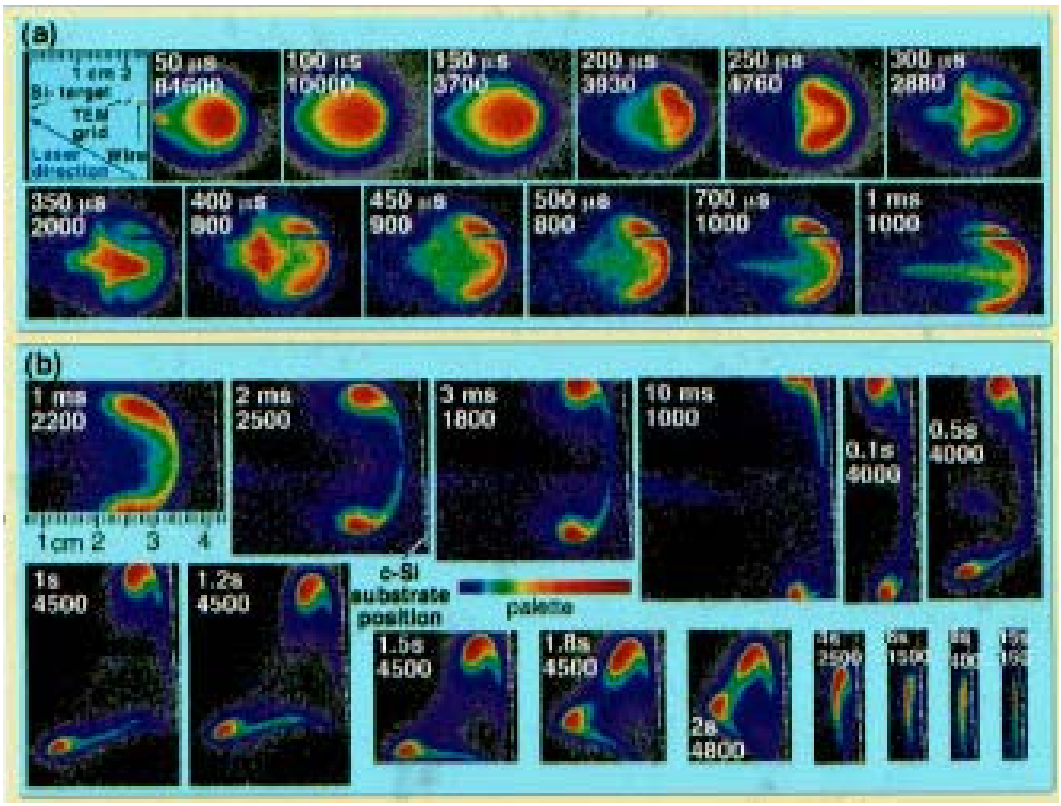

Figure 1.19 (A) ICCD images of plasma luminescence ($\Delta t<400$ μs) plus photoluminescence ($\Delta t>200$ μs) from nanoparticles produced by silicon ablation into 10 Torr He (3 μs exposures). (B) PL images at later times show the swirling smoke-ring of nanoparticles encountering a room-temperature silicon wafer (at the dashed line position). [106]

Source:
[106] D.B. Geohegan, A.A. Puretzky, G. Duscher, and S.J. Pennycook, *Appl. Phys. Lett.* **72**(23), 2987 (1998)

structures [111]. ICCD images of visible plume during ablation are correlated with both excited and ground states of Y and Y^+. Measurements from these photographs indicate the relationship between the target scattering due to ambient gas atoms and the plume-splitting in the background gases [112]. In recent years, Geohegan et al. have applied the in situ time-resolved technique to study the carbon nanotubes and come out with very important information [113-116].

1.5 Alignment of Nanoparticles

One of the challenges of nanoscience and technology is the manipulation of nanostructure into useful, organized and addressable spatial distributions for their applications in electronic materials, such as sensors. Lithography technique is the most common way for this purpose, but it is time consuming and the investment is huge. Other than that, few techniques exist to induce the aligned nanostructures [117-120]. One very attractive method is by using pulsed-laser ablation to produce nanoparticles into a self-organized array. Because the laser beam can cover a large area and ordering could be achieved in a very short time.

Energy density of the incident laser beam plays an important role in the process. In order to generate nanoparticles on the silicon surface, the energy density should be in the range of 0.6-1 J/cm^2 [121-122]. Fowlkes et al. reported that at irradiation with E_d=0.6 J/cm^2 nanoparticles as large as 80 nm were formed, while for E_d<0.6 J/cm^2 no nanoparticles were observed because too little energy was supplied to the substrate. At higher laser fluence—1.3 J/cm^2, the nanoparticles flattened and tended to fuse with the substrate [121].

As mentioned in the previous section, pulsed-laser deposition (PLD) is a simple and fast technique to grow nanoparticles [123-128]. During the PLD process, as a consequence of the continuous scattering, clusters and nanoparticles are formed ahead of the target and projected in the forward and backward directions, and can be collected on a substrate or redeposited on the target. The reviewed method here is similar to PLD, but employs pulsed-laser irradiation that not only produces silicon deposition but also induces the formation of sets of linear arrays of nanoparticles that extend over large areas. [121-122,129-130]

Fowlkes et al. reported several related methods to induce the aligned nanoparticles. The first is to use non-polarized light together with the microstructured surface to produce the linear arrays. The second one is to generate similar alignment by p-polarized laser beam on a smooth surface. Both processes were carried out in a vacuum chamber filled with inert gas, such as He. No nanoparticles were found in vacuum under otherwise the same experimental conditions.

There are several stages in the formation of aligned nanoparticles. The first stage is the film deposition. At laser fluence of 0.6-1 J/cm^2, with 100 pulses, ~10 nm thick thin film was observed at the substrate surface. Pedraza [130] pointed out that: 1. ablation occurs even at the low laser fluences used in the process; 2. the source of the deposited silicon film is the ablated material backscattered by the He atmosphere; 3. after continuing irradiation, not only ablation and film deposition occur but the film also tends to cluster, forming nanoparticles which are consisted of silicon cores covered with a thin sheath of oxide. The gas pressure is important in the process. It is reported that a sevenfold increase in total gas pressure can lead to a twofold increase in the nanoparticle

density [129]. If the inert background gas pressure is too low the amount of backscattered material may be insufficient to form a detectable film and no nanoparticles have been observed.

If a smooth surface was irradiated by a non-polarized laser light, only short-range alignment of silicon nanoparticles was reported [121-122,129-130]. As shown in Figure 1.20, nanoparticles, very uniform in size, become grouped into curvilinear strings distributed with a short-range ordering. After continuing irradiation, they change position, but their distinctive shape has been maintained and no additional particles aggregate to the strings (Figure 1.20).

The microcone/microhole structures reviewed in previous sections were used as a template to promote the alignment of nanoparticles. The production of long-range linear arrays of nanoparticles by irradiation was reported on surfaces partly covered with a well-developed microcone structure [121-122,129-130]. During the process, microstructure remained undisturbed due to the relatively low laser fluence. The aligned nanoparticles location relative to the microstructure can be seen in Figure 1.21. This figure illustrates the ordering of nanoparticles in a region adjacent to a pre-formed microstructure. As the microstructured area is approached, the completely aligned area (Figure 1.21a) changes to a non-aligned region (Figure 1.21b), to one with only thin silicon film (Figure 1.21c). The effect of microcone structure was attributed to its remarkable absorption of light [130]. Cone microstructure has long been recognized as a very good light absorber in a wide range of wavelengths, which include 248 nm [131]. The surface microstructure absorbs the light coming from every direction, including the incident laser light and the light scattered by the nanoparticles. All the scattered light from a semi-plane facing the

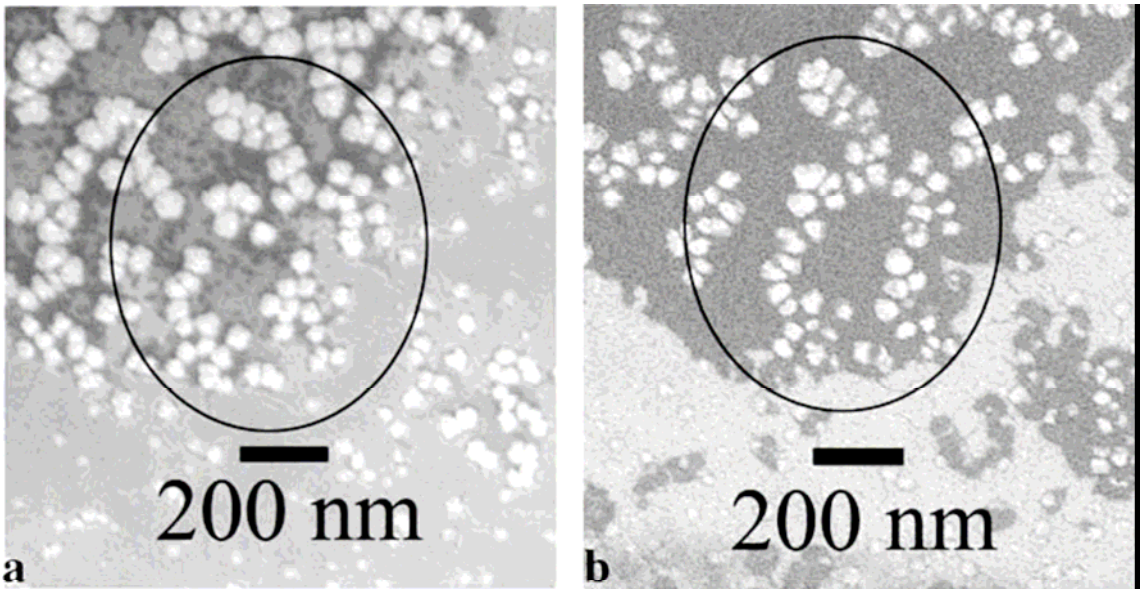

Figure 1.20 SEM images showing the short-range ordering of nanoparticles. Motion of nanoparticles can be observed inside encircled region. A. 500 pulses; B. 700 pulses. Fluence: 0.6 J/cm^2; He pressure: 100 Torr. [121]

Source:
[121] A. J. Pedraza, J. D. Fowlkes, Y. F. Guan, *Appl. Phys. A* **77**, 277 (2003)

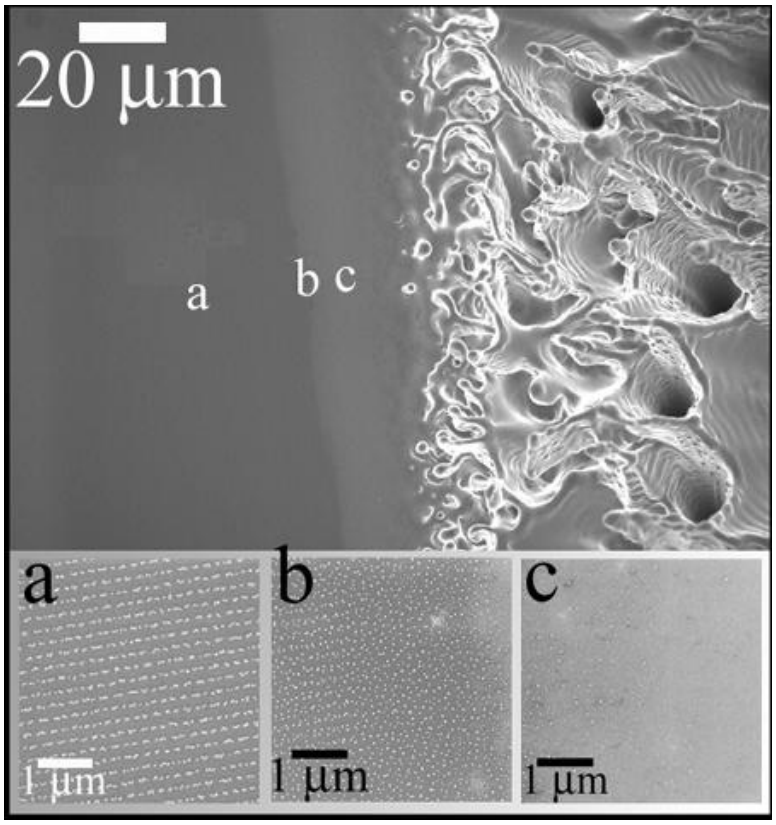

Figure 1.21 SEM images showing the alignment process of nanoparticles. First a Si microcone morphology was produced in the surface plane of a silicon substrate with 1500, Ed = 3.9 J/cm^2, in ½ atm SF_6. A second irradiation treatment of the microcones + the adjacent, flat substrate surface, with 200 pulses in 500 mTorr UHP He induces the formation of a thin Si film, the nucleation of Si nanoparticles and the eventual clustering and alignment of these nanoparticles. Shown above (top-most figure) is the irradiated region, up to 100 µm, adjacent to the microcone morphology and the stage of nanoparticle development of that specific region; a) total nanoparticle alignment (40 µm from the laser spot edge) , b) partial clustering and some film remnant (20 µm), and c) Si film. [122]

Source:
[122] A. J. Pedraza, J. D. Fowlkes, D. A. Blom and H. M. Meyer III, *J. Mater. Res.,* **17**(11), 2815 (2002)

cone microstructure would be eliminated due to this reason. So it is proposed that an obstacle in the incident non-polarized beam path can trigger the self-organization of nanoparticles [130].

When p-polarized light is used, similar long-range nanoparticle alignment can be produced [121-122,129-130]. Fowlkes et al. also studied the relationship between LIPSS and the aligned nanoparticles. They observed that when irradiation is performed at normal incidence, the distance between nanoparticles is equal to the wavelength of the laser beam λ. Figure 1.22a is the AFM image of the aligned sample. It can be seen clearly from Figure 1.22b that the nanoparticles are located in valleys of the LIPSS. The LIPSS is observed only in regions where nanoparticle alignment took place. This suggests the alignment of nanoparticles could be associated with the laser-induced periodic surface structure. The alignment process can then be explained as follows: the LIPSS evolution may precede the alignment of nanoparticles and the nanoparticles are trapped in the channels of the LIPSS, mostly narrower and shallower than the nanoparticle diameter. According to the LIPSS theory [132], the intensity maxima of the electromagnetic field are located in the surface valleys and the minima at the hilltops. So the initially small nanoparticles are dragged to the troughs where the intensity is higher. As the particles grow, they tend to negate the grating effect produced by the surface roughness, and after certain number of pulses, the nanoparticle lines obstruct any further LIPSS evolution and take control of the modulation dictating the positions of maxima and minima of the electromagnetic field [130].

Another way to align nanoparticles is by placing a thin wire in the path of the beam. Due to obstacle, there are two regions on the surface, one without irradiation and one can

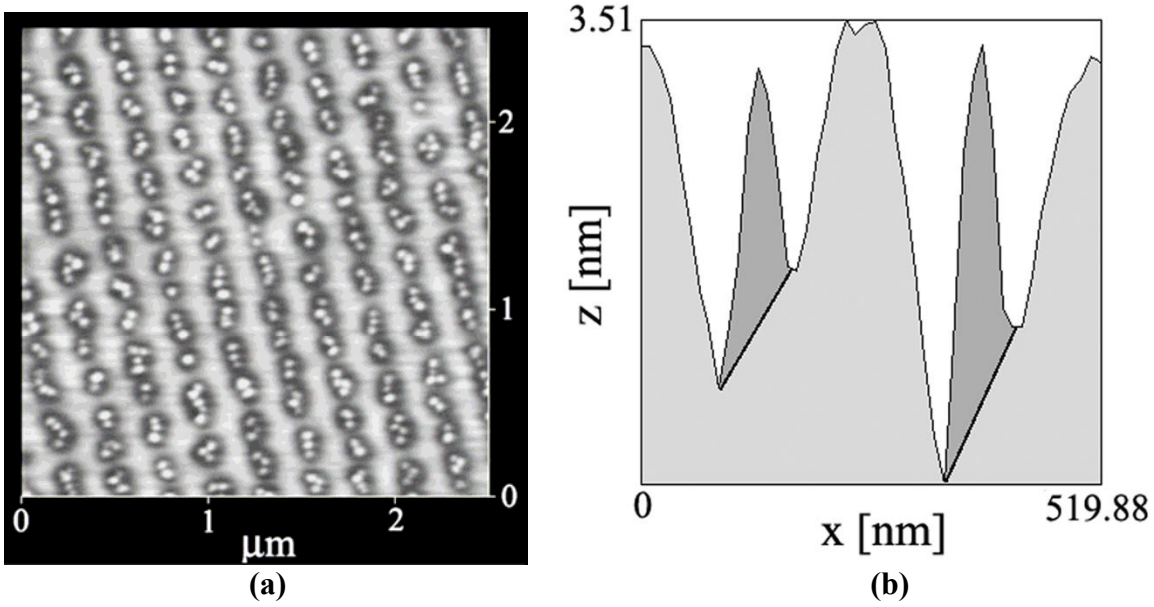

Figure 1.22 (a) AFM image showing the laser-induced nanoparticle linear array in the vicinity of a microstructured region of the surface. (b) Cross-section of an AFM image showing nanoparticles (darker shade of grey) located in the LIPSS troughs. Fluence: 1 J/cm^2; 0.5 Torr He; 200 pulses. [121,130]

Source:
[121] A. J. Pedraza, J. D. Fowlkes, Y. F. Guan, *Appl. Phys. A* **77**, 277 (2003)
[130] A. J. Pedraza, J. D. Fowlkes, D. A. Blom and H. M. Meyer III, *J. Mater. Res.*, **17**(11), 2815 (2002)

receive laser radiation. A thin continuous film of Si can be found along the region without laser radiation, while nucleation, growth, clustering and self-organization of nanoparticles took place in the region with laser irradiation [122].

1.6 Laser-induced periodic surface structures (LIPSS)

The spontaneous appearance of periodic surface structures, or ripples, whose spatial periods are closely related to the optical wavelength, is the result of illumination of a target surface with a laser beam at an energy density close to the melting threshold of the target. Such periodic structures were first observed in 1965, upon irradiation of Ge and Si semiconductors by ruby laser pulses [133]. Intensive experimental and theoretical investigations of the formation of surface gratings began approximately in 1980 [134-138]. LIPSS is a typical coherent structure. Upon irradiating with pulsed lasers of wavelength in the range of 10.6 to 0.193 μm, the formation of these gratings has been reported in metals [138-144], semiconductors [132-133,135-137,141,145,147-153], and insulators [154-156, 157-162] (including polymers [156,163-165]). The pulse duration in those experiments was submicrosecond, and the peak power varied from 100 MW/cm^2 to 10 GW/cm^2 [145]. In all the other experiments, performed in the visible or near infrared, the laser pulse was either in the nanosecond regime or in the picosecond region. However, Rozgonyi et al. reported that a cw argon ion laser can produce ripples on ion-implanted silicon [166]. The type of material, its structural form and its surface quality all play important roles in the production of a coherent ripple structure.

1.6.1 Detection of LIPSS

SEM and AFM are among the most frequently used methods to characterize LIPSS. Another important way to observe in situ the evolution of ripples is from the probing beam of a continuous laser in the far field on the periodically disturbed relief of the surface. This method has become in recent years the standard method for observing such perturbations and was first reported by Aksenov [146,167].

1.6.2 LIPSS Formation

The origin of LIPSS has been discussed extensively. The most accepted interpretation is that the development of the ripples is a result of the interference pattern of the incident or refracted light and scattered waves propagating parallel to the surface [133,145-147,168]. These interference patterns give rise to non-uniform, modulated heating which, in turn, can give rise to surface modifications that remain after the laser pulse is over and persist through the ensuing fast cooling.

1.6.2.1 Mathematic Derivation of the Equations Related to LIPSS

Before introducing in detail the existing theories about the LIPSS formation, let us derive the mathematic equations to describe the relationship between LIPSS characteristics and the controlling parameters. The patterns of ripples are very complex through a microscope, however, in Fourier space (reciprocal space) a lot of previously unappreciated information can be found in a simple, clear and neat formation.

In Fourier space, the spatial frequency of LIPSS as a function of the incident angle and laser polarization can be derived much more easily. The derivation follows closely that as provided by Bauerle [168].

A large number of experimental studies has been performed using linearly polarized light for the two possible directions of the electric field, $\boldsymbol{E_i}$, of the incident electromagnetic wave, commonly referred as p-polarized light ($\boldsymbol{E_i}$, lies in the plane of incidence) and s-polarized ($\boldsymbol{E_i}$ is normal to the plane of incidence). The equation of a grating for the case that reflected or transmitted scattered light propagates along the substrate surface is, for the first order of diffraction

$$\boldsymbol{k}_{//}^{\boldsymbol{s,a}} = \boldsymbol{k}_{//}^{\boldsymbol{i}} \mp \boldsymbol{q} \qquad 1.10$$

where the vectors $\boldsymbol{k}^{s,a}_{//}$ are the Stokes (-) and the anti-Stokes (+) diffracted beams, $\boldsymbol{k}^{i}_{//}$ is the projection of the wave-vector of the incident wave on the substrate surface, and $\boldsymbol{q}$ is the wave vector of the surface roughness. The direction of $\boldsymbol{k}^{i}_{//}$ is fixed and can be chosen to coincide with the x-axis, its modulus is $\left|\boldsymbol{k}_{//}^{\boldsymbol{i}}\right| = \frac{2\pi}{\lambda}\boldsymbol{\sin\theta_i}$, where λ is the wavelength of the incident laser light, and θ_i is the angle of incidence of the light [168]. The locus of all $\boldsymbol{q}$ values that satisfy the grating equation (equation 1.10) describe, in the reciprocal space, two circles of radius $\boldsymbol{k}^{s,a}_{//}$ whose origins are shifted from the origin by $q_x = \pm(2\pi/\lambda)\sin\theta_i$, as shown in Figure 1.23. Two of the most frequently observed ripples are those with $\boldsymbol{q}$ either parallel or normal to $\boldsymbol{k}^{i}_{//}$, and are indicated in Figure 1.23 as $\boldsymbol{q_1}$ and $\boldsymbol{q_2}$ for the parallel ones, and $\boldsymbol{q_3}$ for the perpendicular one. Their magnitude is given by

$$\frac{2\pi}{\Lambda_{1,2}} = \left|\boldsymbol{q}_{1,2}\right| = \left|\boldsymbol{k}_{//}^{\boldsymbol{s,a}}\right| \pm \frac{2\pi}{\lambda}\boldsymbol{\sin\theta_i} \qquad 1.11$$

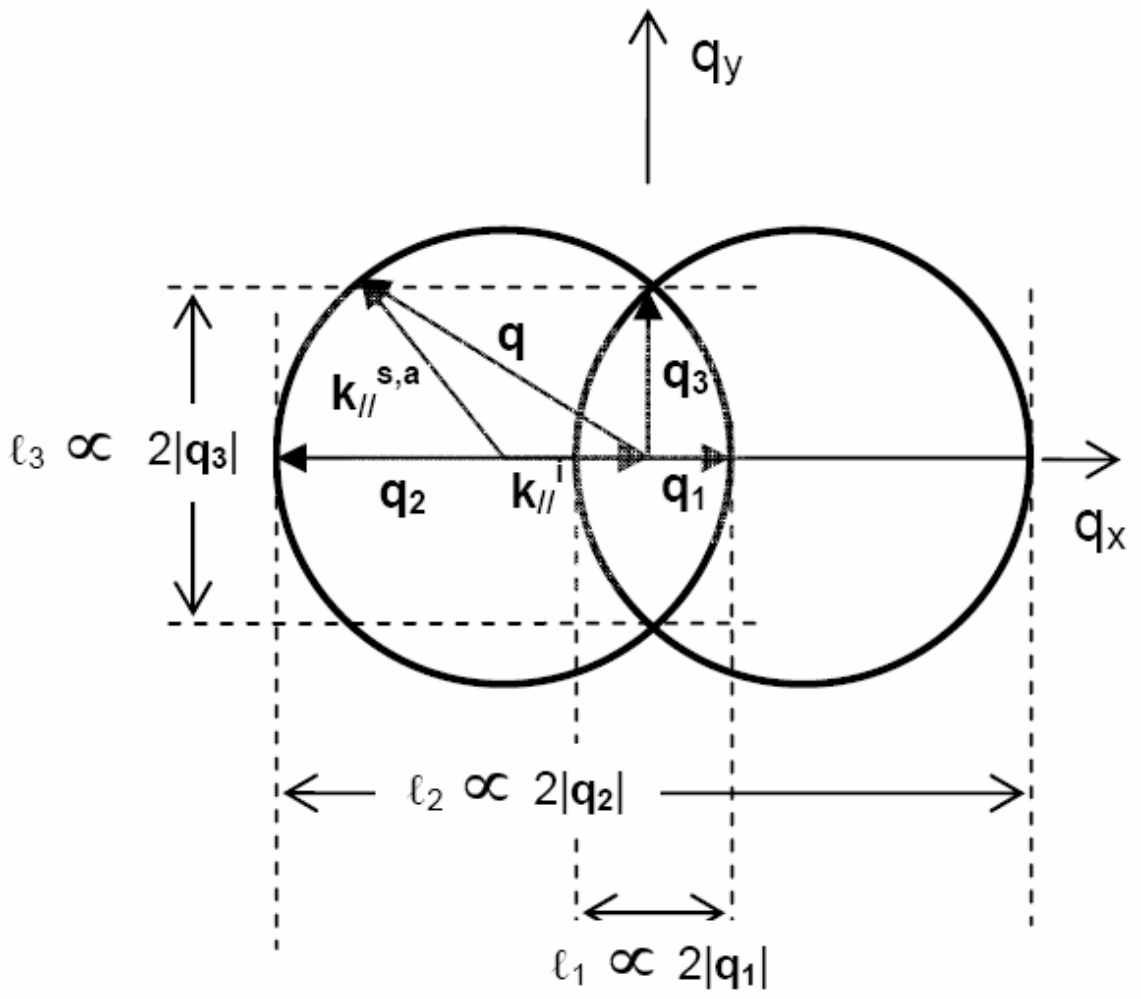

Figure 1.23 Reciprocal space of the substrate surface. The direction of the incident light projected on the substrate surface defines the direction of positive q_x. ℓ_1, ℓ_2, and ℓ_3 are experimentally measurable lengths proportional to $|q_1|$, $|q_2|$ and $|q_3|$, respectively. [217]

Source:

[217] A. J. Pedraza, Y. F. Guan, J. D. Fowlkes and D. A. Smith, to be published in *J. Vac. Sci. Technol. B* Vol. **22**, No. 6 (2004)

and

$$\frac{2\pi}{\Lambda_3} = |q_3| = \sqrt{\left|k_{//}^{s,a}\right|^2 - \left(\frac{2\pi}{\lambda}\right)^2 \sin^2\theta_i} \qquad 1.12$$

For the wave scattered in reflection,

$$\left|k_{//}^{s,a}\right| = \frac{2\pi}{\lambda} \qquad 1.13$$

while for the wave scattered in transmission,

$$\left|k_{//}^{s,a}\right| = \frac{2\pi}{\lambda} n \qquad 1.14$$

In metals and molten semiconductors with a dielectric permittivity $\varepsilon=\varepsilon_1+ i\varepsilon_2$, surface electromagnetic waves (SEW) with a wave-vector k^{SEW} can be excited during the scattering process; this vector satisfies the relation [139,168-169]

$$\left|k_{//}^{SEW}\right| = \left(\frac{|\varepsilon_1|}{|\varepsilon_1| - 1}\right)^{1/2} \frac{2\pi}{\lambda} = \left|k_{//}^{s,a}\right| \qquad 1.15$$

The grating spacing Λ of most of the ripples reported in the literature are obtained by substituting equations 1.13, 1.14, or 1.15 into 1.11 or 1.12.

The amplitude of the SEW can be approximated by [169]

$$E_{s,a} \approx 2k_i \Delta h \frac{\varepsilon_1}{\varepsilon_2} E_{//}^i \qquad 1.16$$

where $2\Delta h$ is the grating height, $E_{s,a}$ is the amplitude of the Stokes and anti-Stokes scattered waves and $E_{//}^i$ is the projection of the electric field vector E_i on the substrate. For the case of liquid silicon, $\varepsilon_1 = -8.75$ and $\varepsilon_2 = 6.9$ at the photon energy of 5eV used in

this work [170]. Substituting these values and a grating height of 10 nm into equation 1.16 yields

$$E_{s,a} \approx 0.32 E_{//}^{i} \qquad 1.17$$

which shows that a very significant portion of the incoming laser beam is scattered in the surface.

1.6.2.2 Existing Theories on LIPSS Formation

Numerous theoretical investigations have been stimulated by experiments on optically induced surface periodic structures [135-136,145,150,171-176]. The physics behind the generation of periodic structures has now been largely formulated. The mechanisms of the formation of surface structures can be different for different materials, different wavelengths, and different laser radiation intensities. Many experimental results indicate that the amplitudes of the starting nonuniformities do not play a significant role in the formation of laser-induced periodic structures [132,177].

Emmony et al. [158] first suggested that a scattering center on the surface might be the reason for the observed ripples. Leamy et al. [178] later developed this model by adding that, the melting threshold was periodically exceeded as a consequence of these intensity fringes, leaving alternating regions of different crystallinity, provided that the average temperature of the surface is close to the melting temperature.

Several authors have suggested that surface plasmons or surface polaritons could produce the ripples. Vechten, Rendell and Ngai [179-180] suggested that ripples may occur as a consequence of the condensation of plasmons in very high carrier-density

regions. Keilmann and Bai [155] produced some evidence for a dispersive behavior of the ripple period, and attributed that phenomenon to the action of surface polaritons.

Zhou et al. proposed the corrugated surface model [145]. In their model, initial surface disturbances scatter part of the incident beam at almost grazing incidence; the interference between the scattered optical wave and the incident beam can modulate the absorbed power, so that only one Fourier component is reinforced and grows. The most likely initial perturbation is the existing surface roughness, because even in polished samples the surface is far from ideally flat. The complex dielectric function determines the growth coefficient. Surface melting of the semiconductor is necessary, because growth will be much faster if the material is metallic like, that is, for $\varepsilon_r < 0$.

Because the LIPSS spacing is a function of the incident angle, Zhou concluded that the surface ripples must be produced by interference of the incident laser beam with an optical wave traveling along the surface with a velocity of light in free space. They also explained the reasons for the existence of an optical wave traveling along the surface. The surface roughness can be decomposed into components of spatial period Λ_i. Any initial period can thus produce an interference pattern on the surface which may cause optically induced growth of that component.

Similarly, Young et al [181] suggested the initial evolution of LIPSS was due to light propagating along the surface. However, they criticized the "surface scattered wave" model, by indicating that for semiconductors, the wave propagating parallel to the surface with any wavelength λ, does not satisfy the Maxwell boundary conditions across the interface. Instead, they proposed that radiation remnants, which are the scattered electromagnetic waves traveling parallel to the surface, are responsible for the formation

of the LIPSS. In certain directions, they found the Fourier components of a surface source are particularly effective in creating electric fields in the medium below, where LIPSS can be produced.

1.6.3 LIPSS Growth

1.6.3.1 Growth and Propagation

Either single laser shot or multiple laser shots can produce ripples. The fluence threshold for formation of ripples under multiple laser irradiations is much less than that required for single-shot ripple formation [137,155,182].

1.6.3.2 Spacing and Polarization

At normal incidence, the ripple spacing $\Lambda = \lambda$ (wavelength) can be observed. However, exceptions have been reported [155,183-184], for example, in one case, the material is distributed by a standing acoustic wave, whose patterns are not consistent with an interference effect at optical frequencies.

Linearly polarized light of the p-type (the incident electric field is in the plane of incidence), incident on the surface at an angle θ, will produce a ripple pattern with one or the other of two spacings Λ given by

$$\Lambda = \frac{\lambda}{1 \pm \sin\theta} \qquad 1.18$$

where θ is the angle of incidence measured from the normal to the surface. The occurrence of these two spacings is random and irregular, and the factors determining

which spacing will occur are still unknown. Only in very rare occasions, did both ripples intermingle in the same area.

For oblique incident with s-polarized light, there are two different conclusions. Zhou [145] et al observed that the spacing remains equal to the wavelength, while for many others the spacing obeys the following relationship.

$$\Lambda = \frac{\lambda}{\cos\theta} \qquad 1.19$$

For circular polarization no ripples are observed. In a few instances, ripples running both perpendicular and parallel to the incident electric field have been observed [137,155,182,185].

Ripples introduced above are irreversible gratings, because they remain after the laser irradiation is gone. Nevertheless, in some cases reversible ripples have been found on liquid metals [140] and melts of semiconductors [186], which can only exist for the duration of the laser pulses [187-188]. In order to obtain irreversible gratings, a positive feedback during the laser irradiation process is required.

1.6.3.3 Feedback Mechanisms

A positive feedback is established between the incoming laser light and the roughness having a wave vector that follows the grating equation. Once the correct spacing is established, as the number of laser pulses increases further and the laser intensity is in the range that favors the formation of LIPSS, the ripples propagate. During the propagation, material can be moved from one place to the other to form elevations. The displacement of material can only take place while silicon is liquid. A possible

mechanism that can drive the liquid is the gradient of surface tension (Marangoni effect). This gradient is due to the existence of a thermal gradient and the fact that the surface tension of silicon decreases as the temperature increases.

However, several researchers have proposed some other feedback mechanisms, most of which are related to capillary waves. The following is a brief review of some of those mechanisms.

Akhmanov [169] pointed out that in the presence of spatially uniform surface melt two instabilities exist: the capillary wave (CW) instability [144,172-173] and the interference spatially nonuniform evaporation instability (IEI) [174-176,189]. Three key factors are included in his proposed mechanism: 1. thermocapillary forces can build up CW; 2. the recoil pressure makes an additional contribution to building up of CW; 3. nonuniform evaporation increases the amplitude of the modulation of the relief [169].

Zhou et al. [145] pointed out that those periodic grating components, whose periods were given by Eq. 1.18 or Eq. 1.19, will diffract light from the incident beam along the surface, and one can expect the longest and strongest interaction between the diffracted light and the scattered light, when its grating periods are identical to those of the diffracted light.

Figure 1.24 illustrates an initial sinusoidal temperature disturbance of period Λ at a surface illuminated under normal incidence. Because the index of refraction is temperature dependent, it will follow similar periodic variation. Since the light intensity and the absorbed power are related to the index of refraction, they become modulated with the same period as the sinusoidal wave. Two extreme cases can be expected: 1. If the power absorbed is given by the solid line, regions that are already warmer will

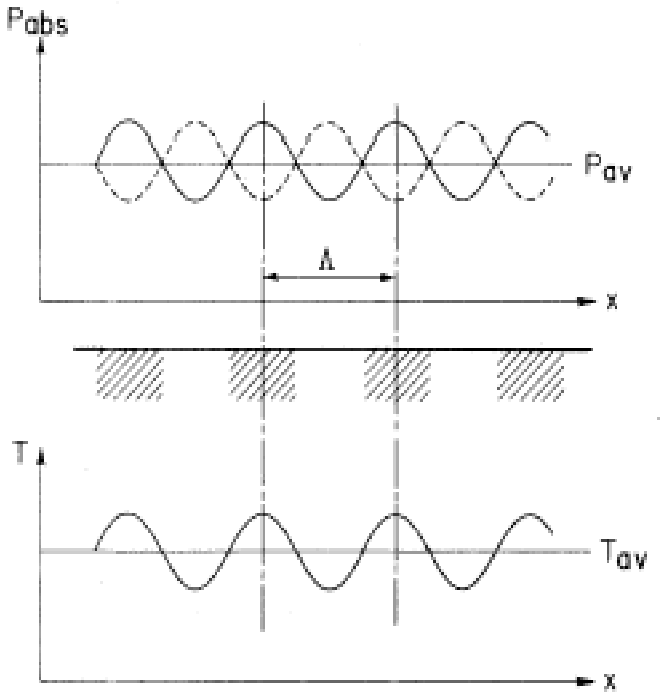

Figure 1.24 Schematic image showing both the positive and negative feedback for a sinusoidal temperature variation. T_{av} represents the average surface temperature. The dashed regions correspond to $T>T_{av}$. Solid and dashed lines represent positive and negative feedback respectively. [145]

Source:

[145] Zhou Guosheng, P.M. Fauchet, and E. Siegman, Growth of spontaneous periodic surface structures on solids during laser illumination, Phys. Rev. B 26, 5366-5381 (1982)

experience a faster rate of temperature increase, and the temperature difference between the shaded and nonshaded regions will increase as well as the variation of the refraction index. So the diffraction is stronger, and the intensity fringes are more pronounced, which means the positive feedback has been established and growth occurs; 2. On the other hand, if the power absorbed is given be the dashed line, more power will flow into regions that were initially colder and any initial perturbation will soon be erased, resulting in a no-growth situation.

P_c is the alternating current (ac) part of the absorbed power normalized to the "intrinsic" absorbed power. In Figure 1.25, P_c is plotted as a function of the relative spatial period Λ/λ for a TM wave at normal incidence on a corrugated silicon surface. According to the geometry of Figure 1.24, $P_c<0$ corresponds to more energy being absorbed in the "hills" than in the "valleys", while $P_c>0$ corresponds to the opposite situation. If thermal expansion is responsible for the ripples, then $P_c<0$ yields the desired positive feedback. Otherwise, $P_c>0$ yields positive feedback if the temperature dependence of the surface tension causes the ripples to grow. In that case more energy is absorbed in the "valleys" where the temperature is the highest, while the surface tension of the liquid is the lowest. The periodic variation of the surface tension pulls the liquid away from the valleys and positive feedback is established.

Young et al. considered both low E_d and high E_d situation. They used the iterative feedback technique to demonstrate that localized melting of a solid semiconductor and preferential etching of a liquid-semiconductor surface both provide feedback mechanisms. Their paper explains the mechanism of transforming surface region into a grating morphology by mass transportations, through partial melting or capillary waves. They

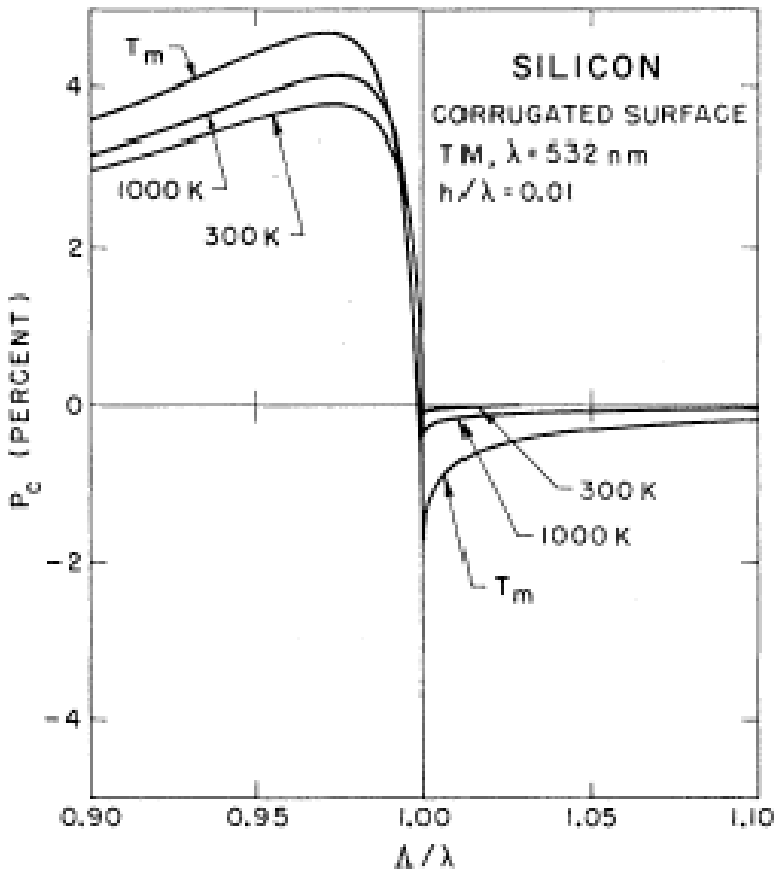

Figure 1.25 Relationship between Pc (Pc is the ac part of the absorbed power normalized to the "intrinsic" absorbed power) and Λ/λ for solid silicon at different temperatures: 300 K, 1000 K, and melting temperature. [145]

Source:

[145] Zhou Guosheng, P.M. Fauchet, and E. Siegman, Growth of spontaneous periodic surface structures on solids during laser illumination, Phys. Rev. B 26, 5366-5381 (1982)

also criticized the models proposed by Zhou [145] and Ehrlich [147], by indicating that their models did not distinguish structures produced in higher E_d and lower E_d. At higher E_d, Young et al. attributed the periodic structure to the capillary waves generated at the vapor/liquid interface. However, at lower E_d, there will be no uniform-melting, the hypothesis is not applicable to the gratings formed at low fluences. Ehrlich et al. didn't consider capillary waves at all, while Zhou et al. attributed the LIPSS formation to an inhomogeneous thermal-expansion mechanism, which is not consistent with the fact that the mechanism requires more energy to be deposited on top of the ripples rather than the bottom. While Young's mechanism requires more energy to be deposited in the valleys, which is closer to reality, thus supports their preferential etching mechanism.

1.7 Lloyd's Mirror Interferometer and Its Application in Formation of Surface Gratings

Humphry Lloyd published an article in 1837, describing a device that can demonstrate interference. Figure 1.26 is a schematic image of a Lloyd's Mirror interferometer [190]. The light is reflected by the mirror to the substrate and interferes with the direct beam. An interference pattern is formed on the screen AA' due to the fields from the source S_1 and its virtual image S_1'. If the angle of incidence on the mirror is small enough, then $\theta_1 \approx \theta_2 \approx \theta$ and the grating spacing $\Lambda = \lambda/(2\sin\theta)$.

Interferometric lithography (IL) technique is based on Lloyd's Mirror interferometer. Compared with e-beam and photo lithography, IL allows the production of fine features without the need for complicated imaging and masks systems. IL can be used for

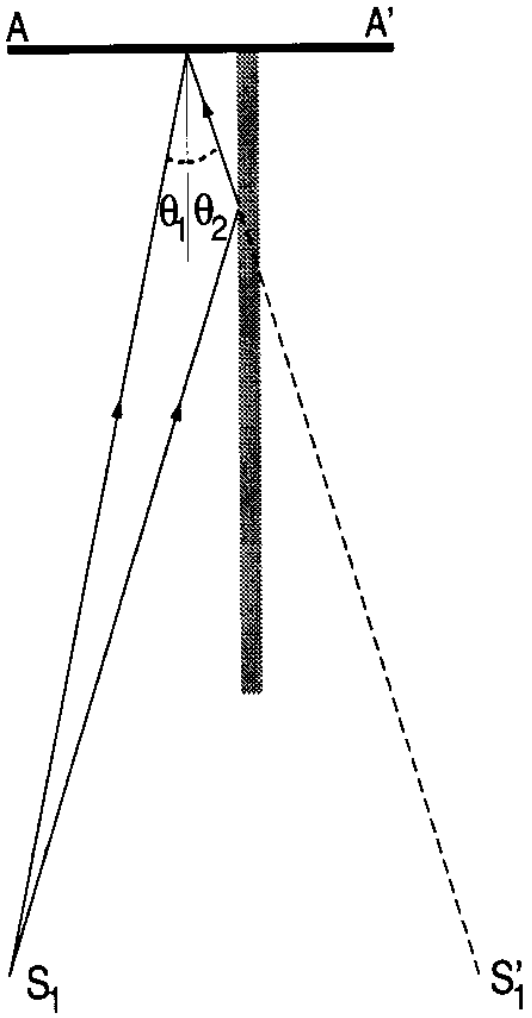

Figure 1.26 Schematic image of a simple Lloyd's Mirror configuration with a point source S1. An interference pattern is formed on the screen AA' due to the interference of the direct incident beam and the reflected beam from the mirror. S1' is a virtual image of S1. [190]

Source:

[190] H. H. Solak, D. He, W. Li, S. Singh-Gasson, F. Cerrina, B. H. Sohn, X. M. Yang, and P. Nealey, *Appl. Phys. Lett.* **75**(15), 2328 (1999)

production of gratings, grids and sometimes two dimensional features over large areas.

Figure 1.27 is the SEM image of interference patterns generated in positive resist [191]. The line spacing is 125 nm, and each line is 50 nm wide. Compared with conventional EUV exposure, the nearly vertical side walls are of high quality.

1.8 General Techniques for Fabricating Large Arrays of Nanowires

1.8.1 Surface Patterning plus Oblique Metal Evaporation

A general and relatively simple technique has been applied to generate large arrays of parallel metallic nanowires ranging from 20-120 nm in width. Jorritsama et al [192] reported patterning of InP substrates surface by holographic laser interference exposure of photoresist and anisotropic etching. The metal is next evaporated at an angle onto the V-shaped grooves, resulting in thousands of ultra-narrow parallel metallic wires. Figure 1.28 [192] shows the schematic image of the evaporation of metal at a grazing angle onto the patterned substrate, and Figure 1.29 [192] is the SEM image of the nanowires formed afterwards. The width of the nanowires formed by this method can be adjusted by changing the grazing angle. Pd, Au and Ta nanowires have been successfully produced.

Similar results have been reported by Prober et al [193], who used surface-relief steps to make 30 nm wide Au-Pd lines shown in Figure 1.30 [193], and by Olson et al [194], who used a shadow evaporation technique to produce 15-nm-wide Pd wires. Olson also remarked that if diffusion takes place during the process, angle evaporations may fail to leave “shadowed” (or uncovered) regions. In order to prevent the smearing of the edge

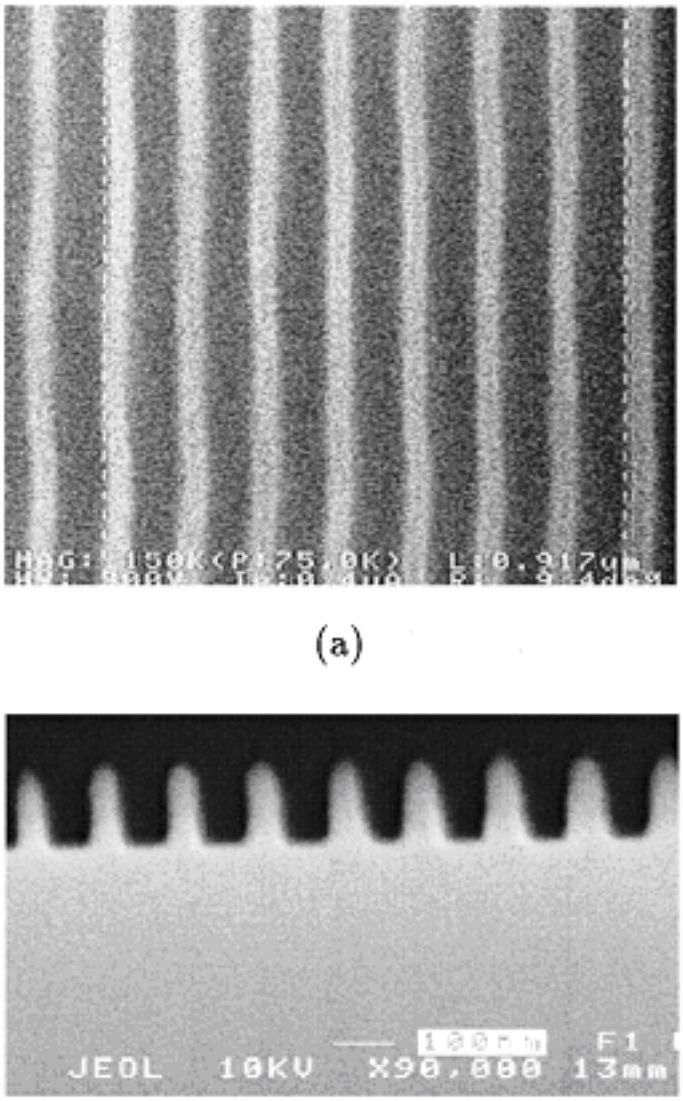

Figure 1.27 SEM images of interference patterns produced in positive resist UV-6 by lithography interferometry based on a Lloyd's Mirror configuration. The line width is 50 nm and the line spacing is 125 nm. (a) Top view; (b) Cross-section. [191]

Source:

[191] H. H. Solak, D. He, W. Li, and F. Cerrina, J. Vac. Sci. Technol. B 17(6), 3052 (1999)

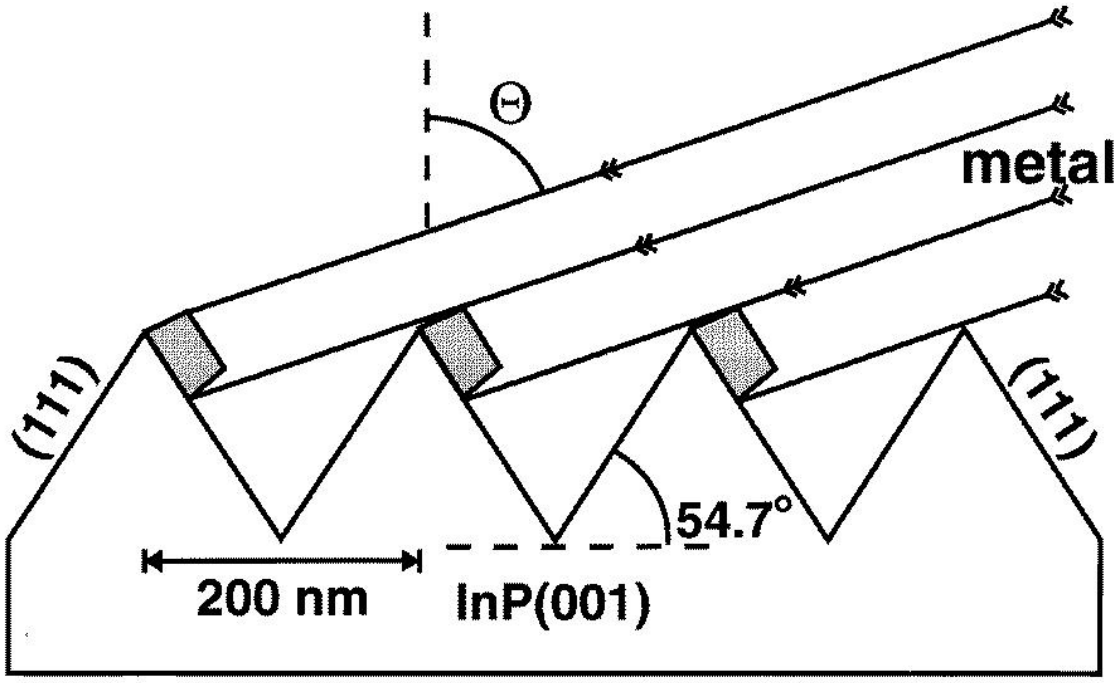

Figure 1.28 Schematic picture of the oblique evaporation of metal onto V-grooved InP(001) substrates. [192]

Source:

[192] J Jorritsma, M A M Gijs J M Kerkhof and J G H Stienen. General technique for fabricating large arrays of nanowires. Nanotechnology 7, 263-265. 1996.

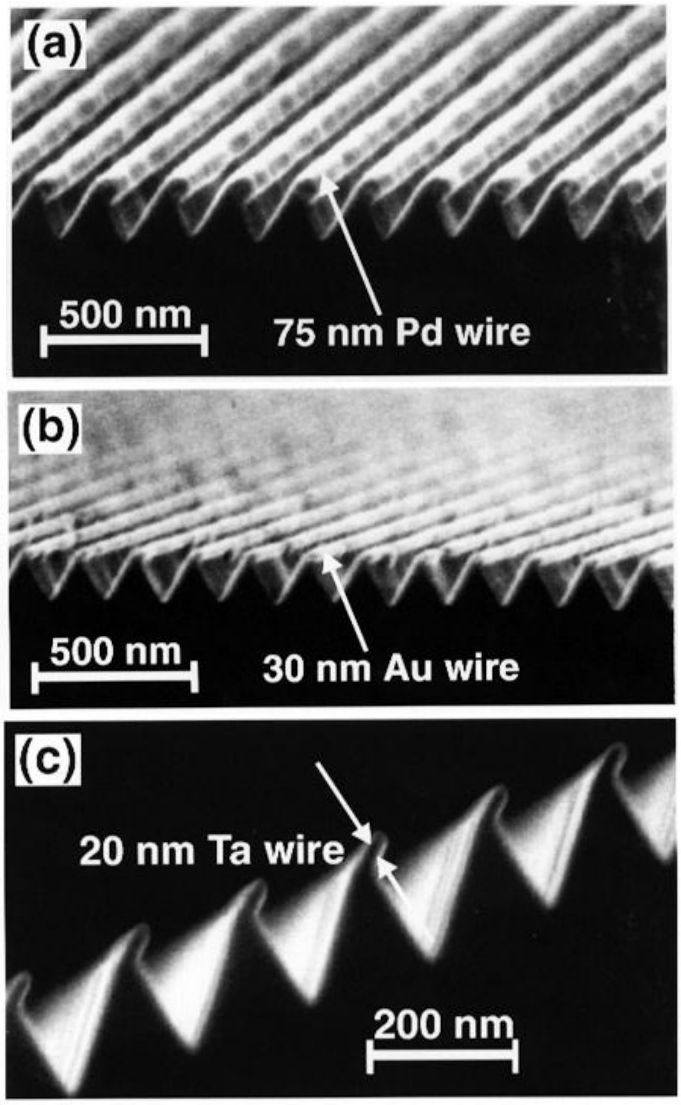

Figure 1.29 SEM micrographs of metallic nanowires on V-groove InP substrates obtained at different evaporation angles θ. (a) Tilted view on an array of 75 nm wide Pd wires (θ=75˚). (b) A similar micrograph showing an array of 30 nm wide Au wires (θ=85˚). (c) Cross section of a V-grooved InP substrate after evaporation of Ta (θ=86˚). The protrusions visible on one side of the V grooves are cross sections of 20 nm wide Ta wires. [192]

Source:

[192] J Jorritsma, M A M Gijs J M Kerkhof and J G H Stienen. General technique for fabricating large arrays of nanowires. Nanotechnology 7, 263-265. 1996.

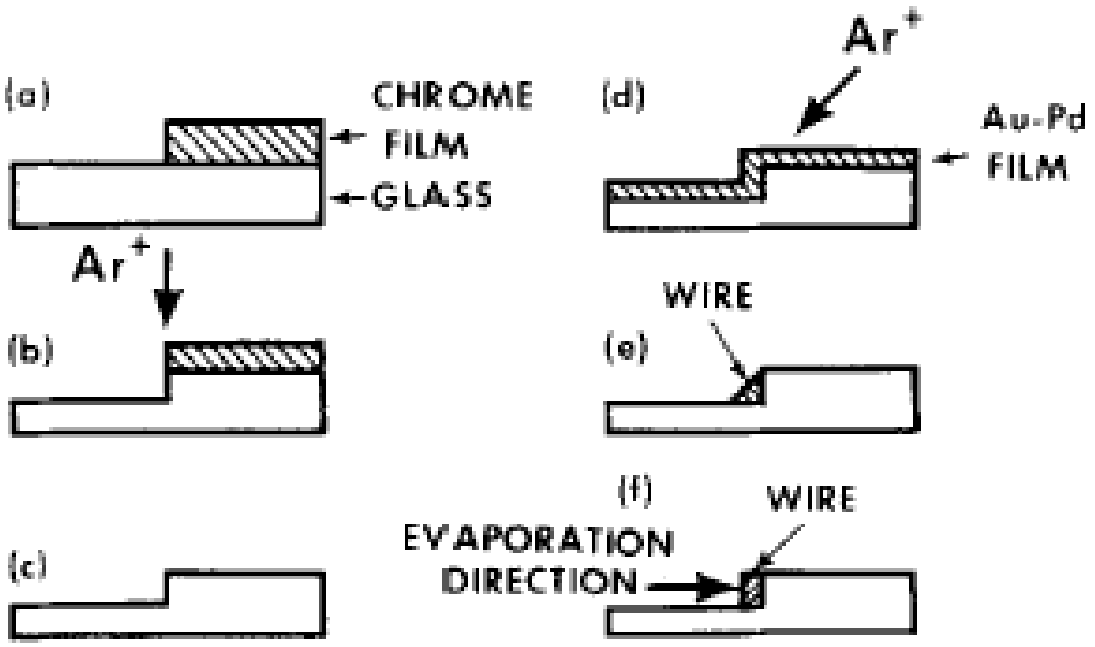

Figure 1.30 Fabrication procedures for production of fine metal wires. The substrate is a microscope cover glass, shown in side view. Procedures a-c are the same for both process A and process B. (a) Half the substrate is coated with a thin chrome film. (b) The substrate is ion etched to produce a square step. (c) The chrome film is removed with a chemical etch. Process A: (d) The substrate is coated with the metal film (e.g. Au-Pd), and ion etched at an angle until (e) A nearly triangular wire is formed along the step edge. Process B: (f) The metal film is evaporated parallel to the substrate to coat only the step edge. A subsequent ion etching normal to the substrate may be required to remove the light coating on the rest of the substrate. [193]

Source:

[193] D.E.Prober, M. D. Feuer and N. Giordano. Fabrication of 300A metal lines with substrate-step techniques. Appl.Phys.Lett. 37[1], 94-96. 1980.

of the shadowed region due to the spreading of the angle of the incoming atoms, they collimated the beam of evaporant by passing it through a long, narrow tube [194].

The above methods all used oblique evaporation. With the help of well-controlled wet etching process, 30-nm-wide Au wires can be obtained without film deposition at a grazing angle. Figure 1.31 shows the whole process [195].

1.8.2 Gold Nanowires from Silicon Nanowire Templates

Due to the good electrical conductivity and stability in oxidizing environments, the production of Au nanowires (AuNWs) has been widely studied [196-201]. Other than the oblique evaporation of metal on prestructured substrates mentioned above, both electrochemical fabrication [196-198] and scanning tunneling microscope (STM) [199] have been reported to successfully synthesize AuNWs. Wong et al [202] reported furnace annealing of Au-coated SiNWs to synthesize crystalline AuNWs embedded in a SiO_x sheath. SiNWs were first prepared by thermal decomposition of pure SiO powders, followed by gold deposition by argon ion sputtering. Figure 1.32 and Figure 1.33 [202] show the AuNWs after furnace annealing at 500 ˚C and 880 ˚C respectively. The AuNWs formation was attributed to the softening of SiNWs upon oxidation and the enhanced Au diffusion at elevated temperatures, as shown in Figure 1.34 [202].

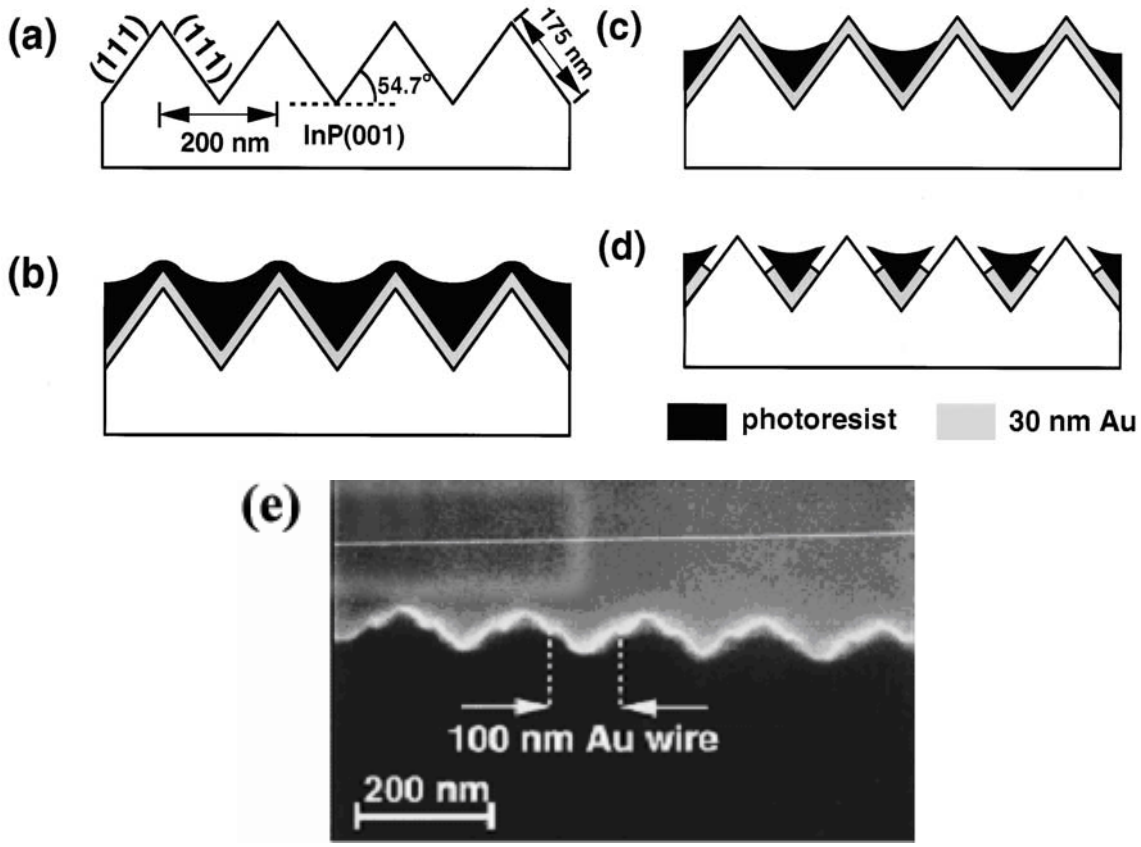

Figure 1.31 Schematic representation of the process used to fabricate Au nanowires on V-grooved InP(001) substrates. (a) The V-grooved InP substrate. (b) The V-grooved InP substrate after evaporation of 30 nm Au and spin coating with diluted photoresist. (c) The substrate structure after the photoresist is etched back during a short oxygen plasma. (d) The Au wires obtained in the V grooves after wet etching of the Au film. (e) SEM cross sectional image showing the contours of 100 nm wide Au wires contained in the V grooves. [195]

Source:

[195] J.Jorritsma, M. A. M. Gijs C. Schonenberger and J. G. H. Stienen. Fabrication of large arrays of metallic nanowires on V-grooved substrates. Appl.Phys.Lett. 67[10], 1489-1491. 1995.

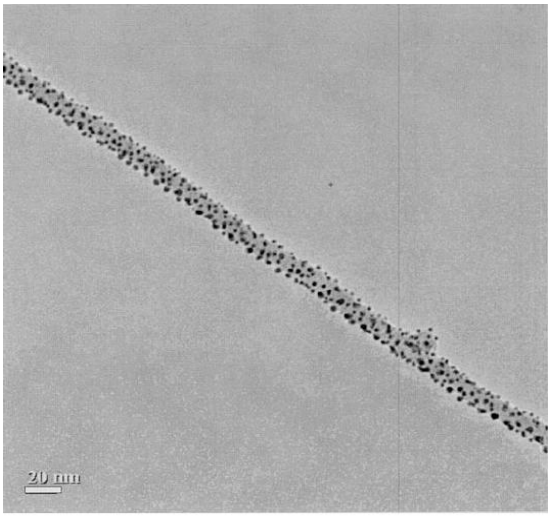

(a)

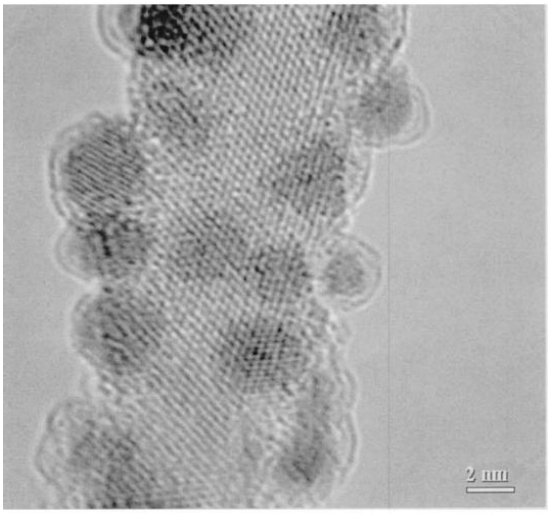

(b)

Figure 1.32 (a) TEM image of Au nanoparticles attached on the surface of SiNWs after annealing at 500 ˚C for 1 h at 10^{-2} Torr, and (b) the corresponding HRTEM image. [202]

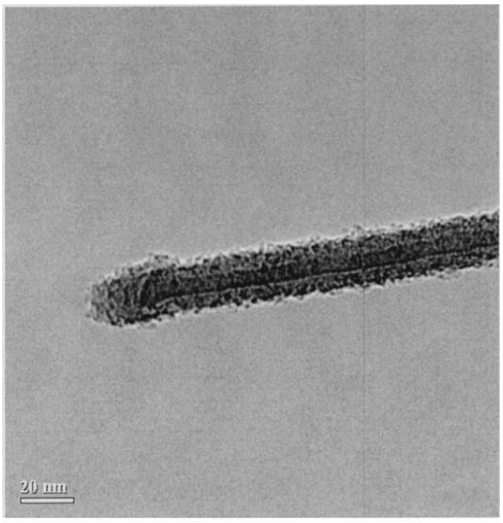

(a)

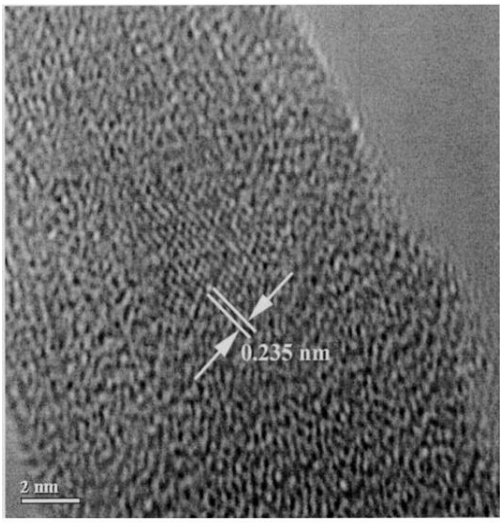

(b)

Figure 1.33 (a) TEM image of AuNW inside a SiO_x sheath formed by the annealing of the Au-coated SiNW at (b) 880˚C for 1h at 10^{-2} Torr, and (b) the corresponding HRTEM image showing the Au core. [202]

Source:

[202] T.C.Wong, C. P. Li R. Q. Zhang and S. T. Lee. Gold nanowires from silicon nanowire templates. Appl.Phys.Lett. 84[3], 407-409. 2004.

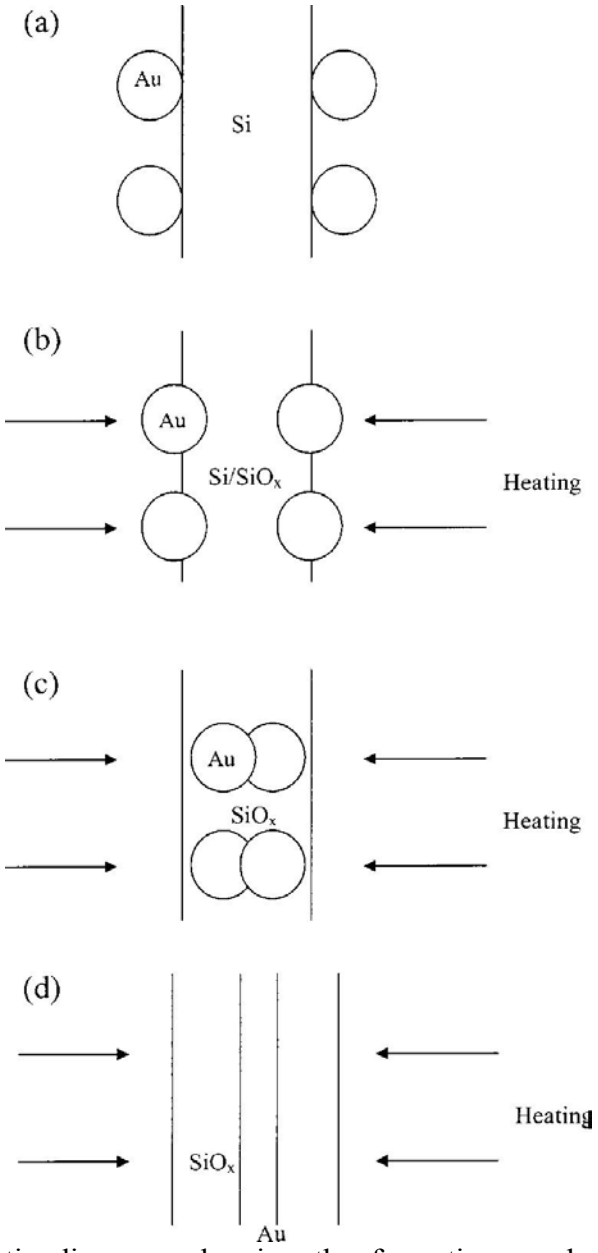

Figure 1.34 Schematic diagrams showing the formation mechanism of AuNWs by furnace annealing: (a) Au nanoparticles deposited by argon ion sputtering are attached on the surface of a SiNW, (b) oxidation of SiNWs and diffusion of Au nanoparticles into SiNWs under heating, (c) diffusion of Au nanoparticles in the SiO*x* matrix of the nanowire at elevated temperature (e.g., 880 °C), and (d) formation of AuNW in the SiO*x* matrix. [202]

Source:

[202] T.C.Wong, C. P. Li R. Q. Zhang and S. T. Lee. Gold nanowires from silicon nanowire templates. Appl.Phys.Lett. 84[3], 407-409. 2004.

CHAPTER 2

EXPERIMENTAL PROCEDURE

2.1 Sample Preparation Procedure

In this research, different test grade silicon wafers have been used. They came from two companies: Transition Technology International (TTI) and Wafer World Inc. Both (001) and (111) wafer orientations have been used. The diameter of the as-received silicon wafers is four inches, and their thickness was between 475 and 575 μm. Boron doped p-type and phosphorous n-type wafers, having resistivities in the range of 1 to 100 Ω.cm, were employed. Figure 2.1 is a schematic image indicating the relationship between the flats on the wafer and the orientation of the wafer [203]. Normally, the largest/primary flat is related to a specific crystal orientation. For example, for the p-type (111) wafer, the flat indicates the <110> direction. The purpose of primary flat is to serve as a locator to position the wafer, while the secondary flat serves to indicate both the wafer orientation and the conductivity type of the wafer.

The wafers were cut to different sizes and shapes for different experimental purposes. Normally, a 1x1 cm^2 rectangular specimen was the default shape. Only one side of the wafer was polished. In order to cut it to its final shape, it was scribed on the unpolished surface by a diamond knife with sharp edges. After this, a slight force was applied to the wafer along the scribe to cleave the sample.

Prior to any treatment, there was a thin native silicon oxide layer on top of the surface, which was around 2-3 nm-thick. In order to study the effects of the oxide, samples with and without oxide layer were prepared. For the samples with oxide, sample

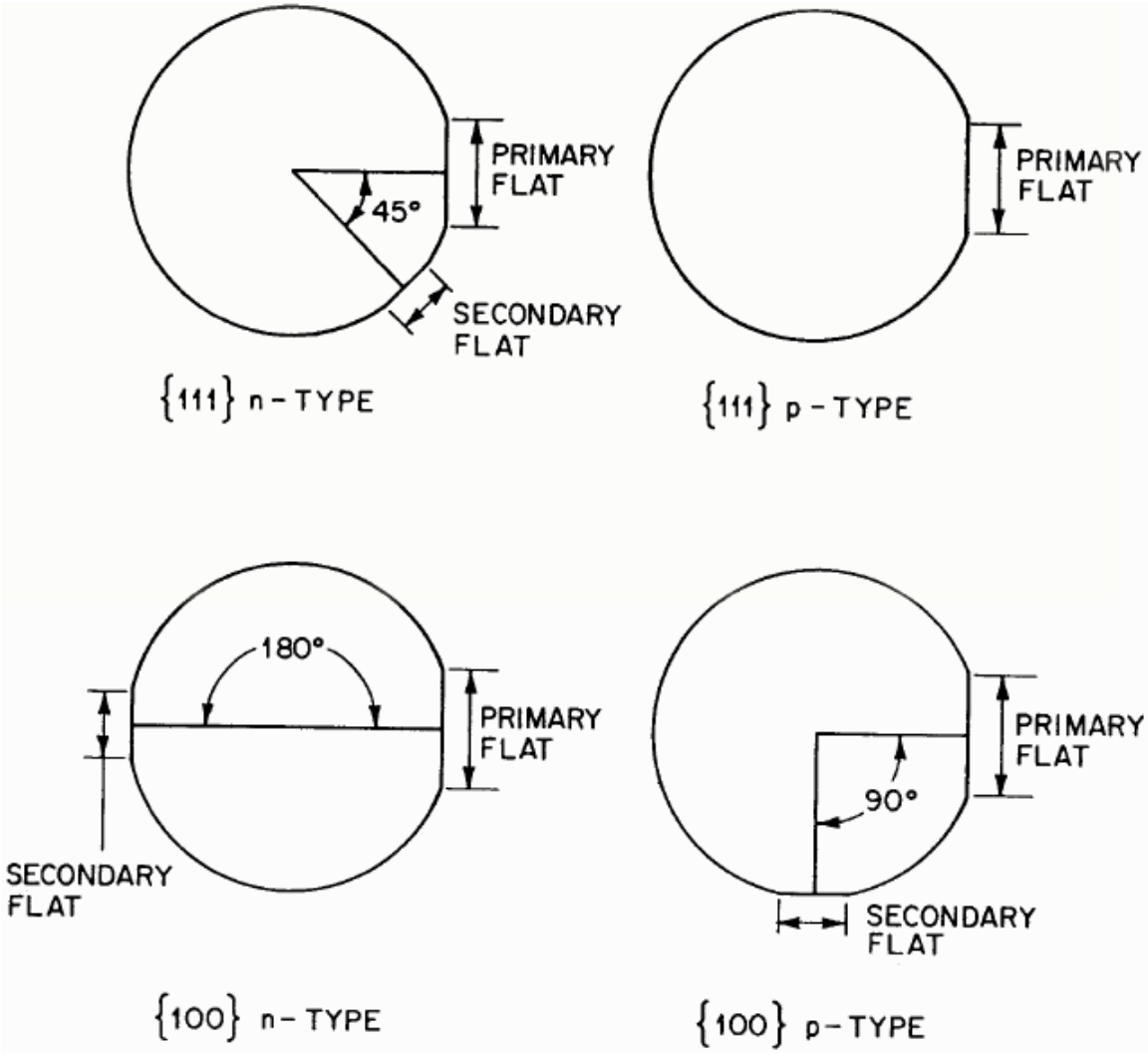

Figure 2.1 Schematic image showing the relationship between conductivity type, orientation of the wafer and the flat on the surface. [203]

rinsing in acetone followed by distilled water was applied to remove the grease and other contaminations off the surface. 10% HF dip was used to remove the oxide layer. Samples were placed in 10% HF solution for five minutes. Right afterward, the HF remainder on the surface was washed away with methanol leaving stabilizing hydrogen bonds terminating the Si substrate. The methanol was in turn washed away with distilled water and blown dry with pure Ar gas before introducing the specimen into the vacuum chamber. This process guarantees that no oxide will form on the surface in a short period of time.

Several ambient atmospheres were employed in this research. Air, SF_6, noble gases and vacuum were used as well. The normal pumping procedure was to start with a mechanical pump to pump the pressure down to $1x10^{-2}$ Torr and then flush the vacuum chamber several times with UHP Ar or He, so that the residual oxygen could be removed. Finally, a low pressure of $1x10^{-7}$ Torr was attained with a turbomolecular pump.

2.2 Laser Irradiation Procedure

The specimens were irradiated with a 248 nm-wavelength light from a Lambda Physik LPX-305i excimer laser. Figure 2.2 shows the optical configuration. The laser beam can be homogenized by passing through the aperture. The energy of the incoming laser beam can be adjusted not only by altering the high voltage discharge in the excimer gas tube, but also by using a beam attenuator. Figure 2.3 shows the transmission percentage of the attenuator as a function of the angle of incidence. When the incident angle is less than 5˚, only 10% of the incoming beam can pass through.

Figure 2.2 Images taken at different angles showing the optical configuration used in the experiments.

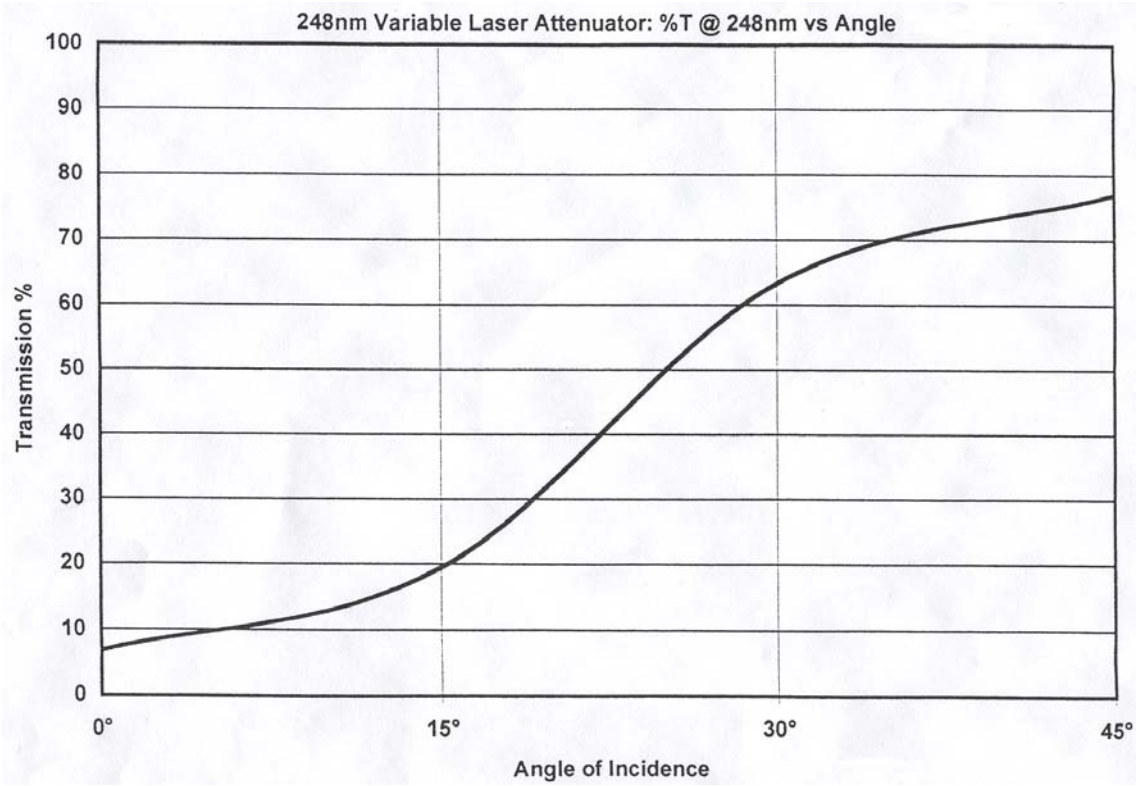

Figure 2.3 The attenuator light transmission as a function of the angle of incidence.

In this thesis, an important parameter is the polarization of the laser beam. In order to get s or p polarized light, a polarizing cube was employed. Figure 2.4 is a schematic image of the UV laser polarizing beamsplitter. After passing the non-polarized beam into the polarizer, the outcoming radiation is separated into s and p polarized beams. By directing either the s or the p polarized light onto the substrate, we can test the effect of laser polarization on the formation of nanostructures.

Mirrors can change the beam delivery pathway from the excimer laser cavity to the substrate fixed on the sample holder. By adjusting the distance between the lens and the substrate, the laser beam spot size can be controlled and the designated energy density of the beam can be obtained.

Experiments were also carried out in the vacuum chamber, where different ambient atmospheres and pressures can be tested. Figure 2.5 shows the vacuum chamber used to prepare nanoparticles. The pressure and gas flow is controlled by the vacuum gauge and mass flow controller from MKS shown in the figure. Both a Varian ionization gauge at high vacuum ($1x10^{-3}$ to $1x10^{-8}$ Torr) and Boc dial gauge at high pressure (5 to 760 Torr) were used to monitor the pressure change in the vacuum chamber. The laser beam enters the stainless steel vacuum chamber through a 2" fused silica window, which is transparent to UV light. Energy deposited on the sample was measured with a volume absorber calorimeter (AD30) from Scientech Astral. Due to the size of the calorimeter, it cannot be reached inside the chamber, so the energy was measured right before the chamber window. Since, there is a 10% energy loss when the light passes through the window, it is necessary to consider this energy loss as well. The energy density on the substrate was calculated by measuring the incoming beam energy and the area of the laser

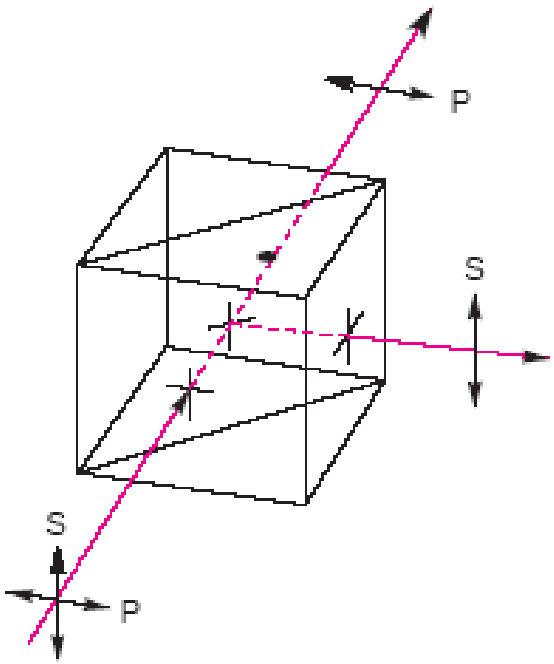

(a)

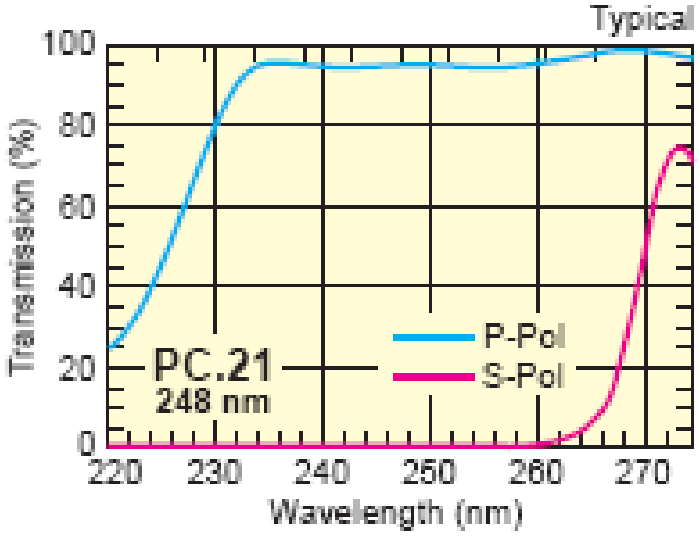

(b)

Figure 2.4 (a) Schematic image showing the UV laser line polarizing cube beamsplitter used in the experiments. (b) Transmission percentage of p- and s-polarized light as a function of laser wavelength. [206]

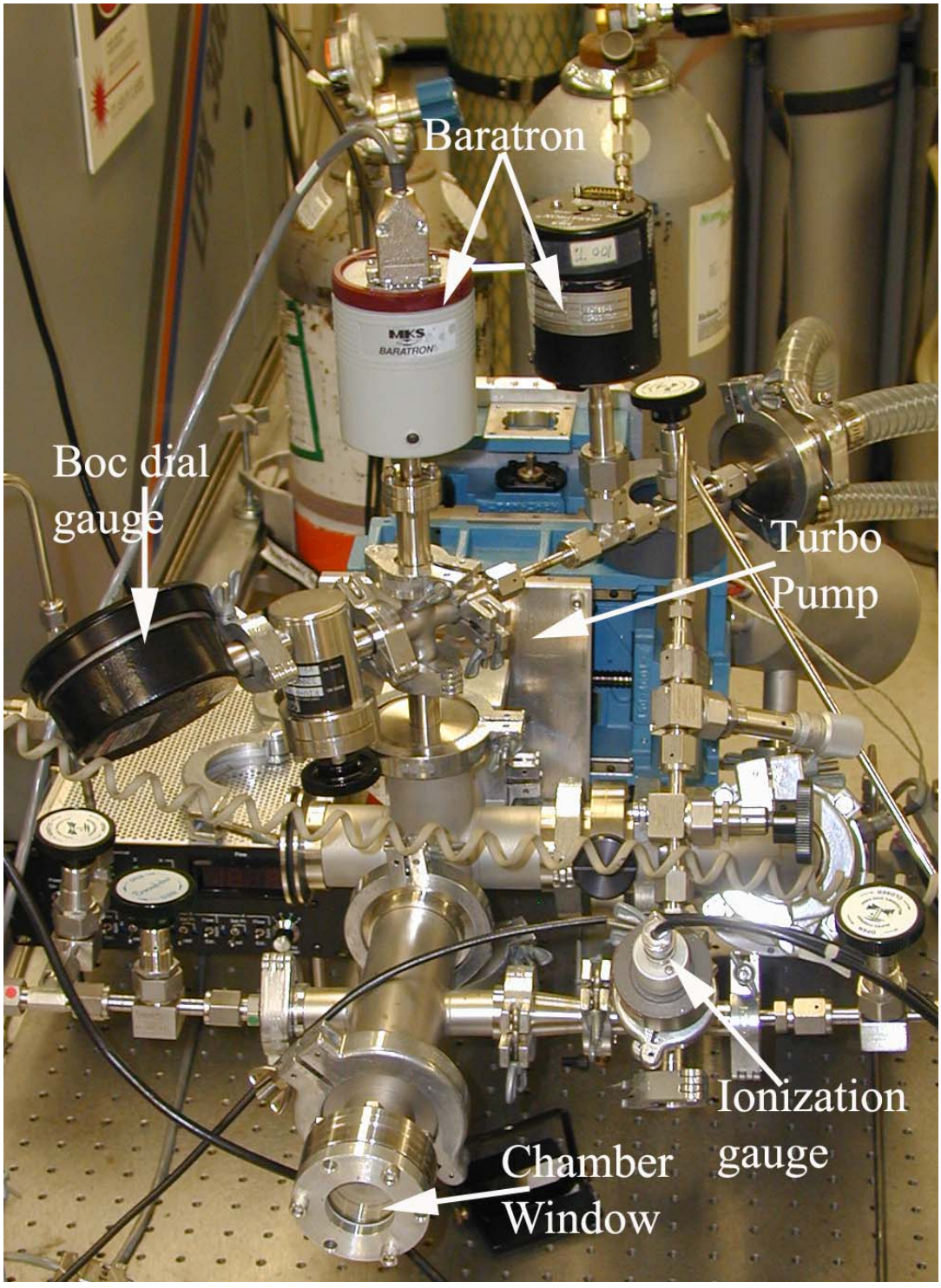

Figure 2.5 Digital image showing the stainless steel vacuum chamber used to house samples under vacuum or specific gas types. Main components attached to the chamber are labeled.

spot produced on a thermal paper. The energy density can be increased by decreasing the laser spot area.

In order to produce nanoscale structures on the surface of silicon, the energy density used was less than 1 J/cm^2. The number of laser pulses required to produce designated nanostructures spanned from 100 to 10000 pulses. The nanoscale structures induced here were found to be insensitive to laser pulse repetition rate; so, unless otherwise indicated, the repetition rate was 10 Hz.

2.3 Ex-Situ Surface Characterization Techniques

2.3.1 Scanning Electron Microscopy

Two high resolution scanning electron microscopes were used: Hitachi S4300-SE Schottky emitter SEM and Leo 1525. LEO 1525 has a field emission cathode. The advantage of a field emission SEM lies in the improved resolution (1.5 nm at 20 kV acceleration voltages). Both microscopes utilize secondary electron emission from a sample irradiated with 5 – 20 keV electrons to produce high resolution images of the laser treated surface. The default working distance was 5 mm. Unless otherwise indicated, the sample surface in all of our studies was normal to the electron beam. Sometimes, samples were tilted in order to get a better viewing.

2.3.2 Atomic Force Microscopy

An atomic force microscope— Dimension 3100 from Digital Instruments (Veeco) was employed to study the surface morphology of the laser irradiated samples. The

system has a standard scanner head, which includes a piezoelectric tube scanner, a laser, and a quadrature optical detector. Due to its high resolution in the z-direction, the surface roughness has been imaged very precisely. The AFM was working under the tapping mode using a very high frequency tapping of the AFM tip along the surface. Figure 2.6 shows the actual AFM tip used in the research. Low to high magnification images of the tip are shown from a to c.

The reason for the high z-direction resolution is that as the cantilever flexes, the light from the laser is reflected onto the split photo-diode. By measuring the difference signal, changes in the bending of the cantilever can be measured. A very small roughness on the surface can be drastically magnified by this mechanism. During the measurement, a pre-determined force is set and the electronic feedback can alter the tip-sample distance so that the force can be kept constant. Under the tapping mode the cantilever oscillates at its resonant frequency ~ 300 KHz, so that during its oscillation period, it only taps the surface occasionally, which can decrease the lateral forces during the scan. This can decrease the *dragging* phenomenon, especially when the bonding between an imaged particle and the substrate is weak.

However, horizontal resolution of the AFM is limited by the sharpness of the scanning tip. Figure 2.6d shows how the tip can change the real shape of a particle. Tip broadening happens when the radius of the curvature of the tip is greater than, or comparable with, the size of the feature to be measured. The figure shows schematically how this happens. When the tip scans over the sample, the sides of the tip make contact with the specimen before the apex, and the microscope begins to respond to the feature. Lowndes et al. studied the dimension effects of the AFM tip on the size measured from

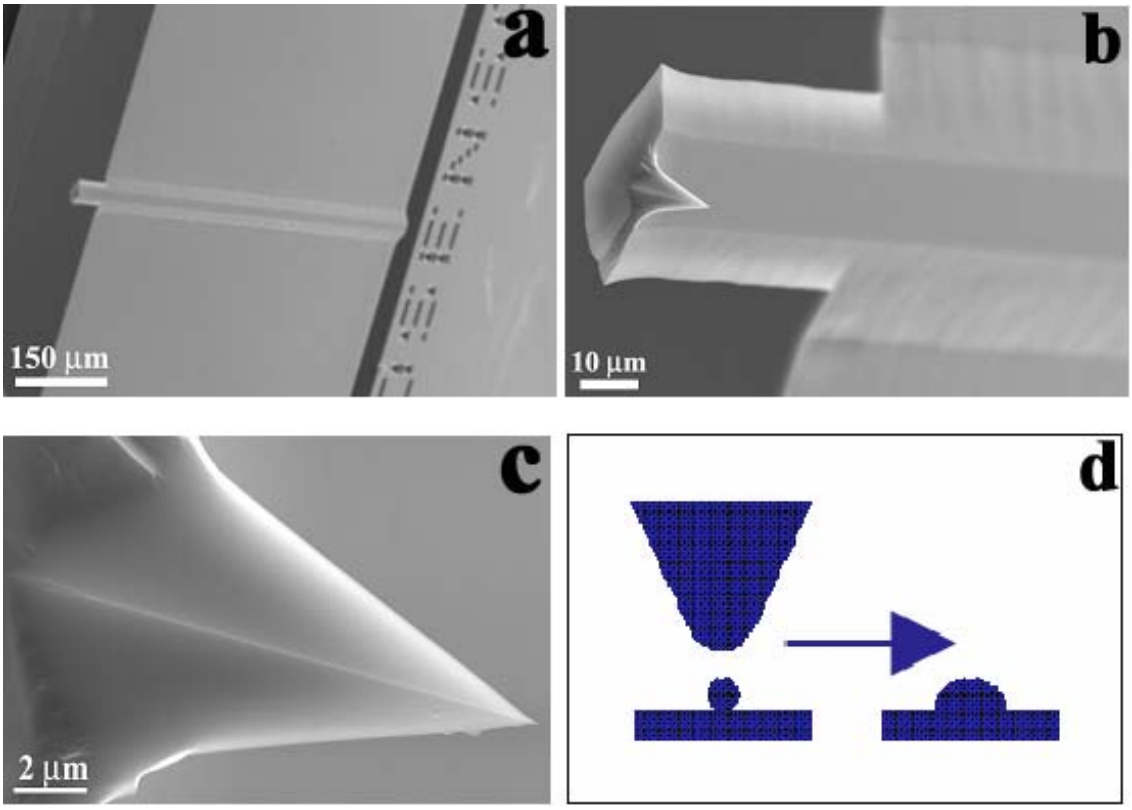

Figure 2.6 SEM and schematic images of the AFM tip. (a) Low magnification SEM image showing mostly the cantilever. (b) Relative position of the AFM tip to the cantilever. (c) High magnification SEM image showing the sharp edge of the AFM tip. For a brand new tip the dimension is around 10-15 nm. (d) Schematic image comparing the real-space sphere and its AFM image. The difference is due to the shape of the AFM tip.

the AFM image [94]. They proposed that the apparent width W of an imaged nanoparticle is proportional to $4(R_1R_2)^{1/2}$, where R_1 is the tip radius and R_2 is the nanoparticle radius. For example, the AFM tip we used for measurements has a 10-nm tip, thus a 5-nm diameter nanoparticle can have an apparent width W ~ 28 nm. Hence, in this research the diameter of a nanoparticle was taken to be its measured height.

CHAPTER 3

EXPERIMENTAL RESULTS

3.1 Formation of 3-D Non-Coherent Silicon Nanostructures in Microstructured Substrate

Laser-generated silicon microcone arrays were used as templates for the growth of nanocolumns using laser irradiation. Laser energy density, ambient atmosphere and number of laser pulses were found play important roles in the formation of nanocolumns. It was shown that under laser irradiation silicon nanocolumns were not produced on smooth surfaces.

3.1.1 Formation of Silicon Nanocolumns on Microstructured Template

A two-step procedure is required to form the nanocolumns. First, a microcone/microhole structure is formed by irradiating a silicon specimen in SF_6 at a fluence of 2.5 J/cm^2. In the second step the microstructured surface is irradiated at a much lower laser fluence, in an inert ambient at low background pressure.

After irradiating the microhole/microcone microstructure with 1000 pulses at a fluence of 0.48 J/cm^2 in a 10 Torr He atmosphere, a small protrusion appears at the top of the cones (Figure 3.1). At this initial stage the protrusions are very short, having a 150 nm diameter and a height of less than 20 nm (Figure 3.1b). The protrusions change little even after 2000 pulses (Figure 3.1c). After 2000 pulses, as the number of laser pulses increases the nanocolumns start to lengthen, while maintaining their diameter constant.

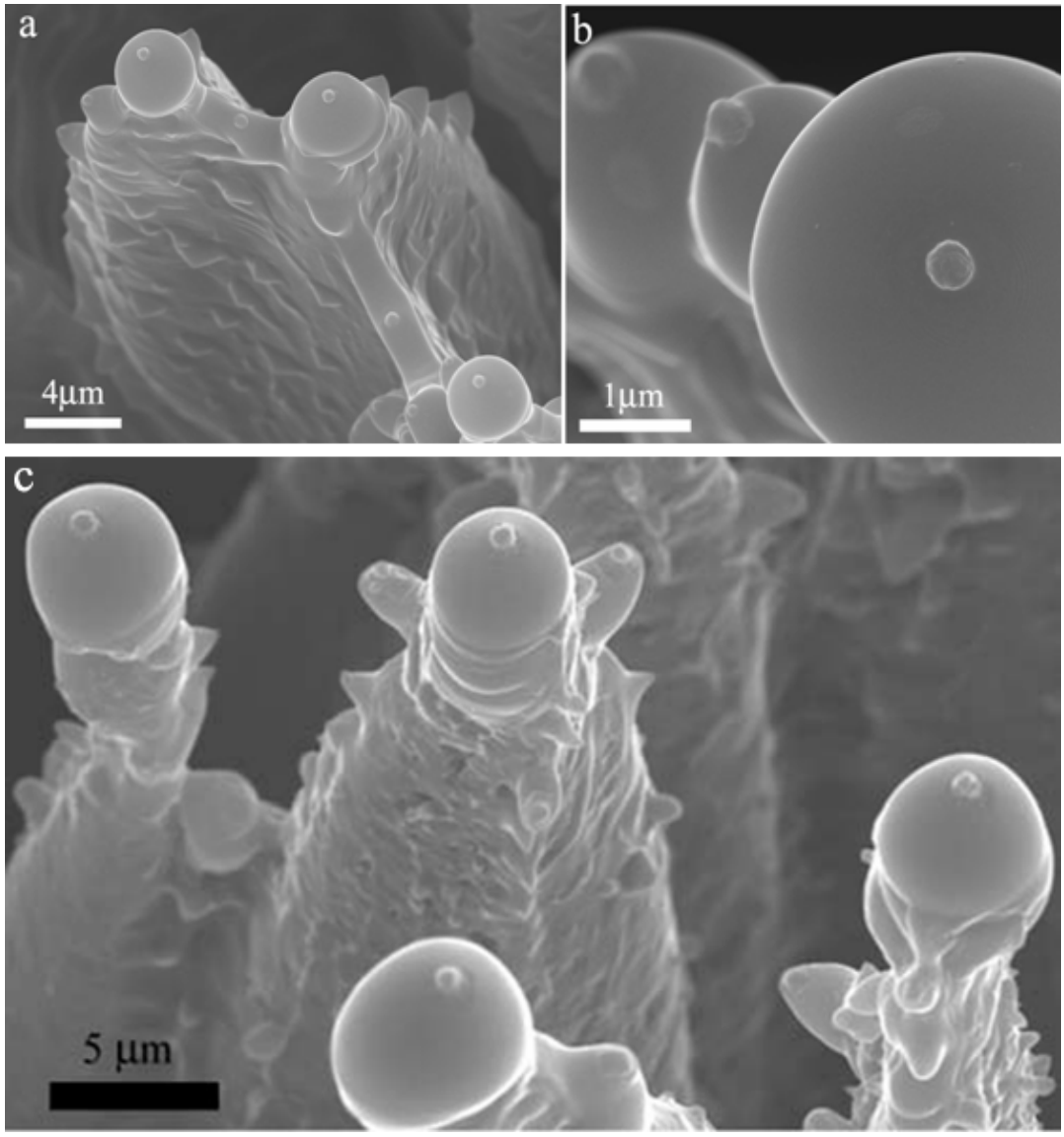

Figure 3.1 SEM images of the early stage of the nanocolumns atop a laser-induced microcone template. Small tips shown in (a) and (b) are formed at 0.5 J/cm^2, in 10 Torr He after 1000 laser pulses. (c) Tips' morphology after 2000 pulses.

The growth of a single nanocolumn was followed with the help of similar sample holders installed in the processing chamber and in the scanning electron microscope (SEM). In this way, the same region could be imaged after successive irradiations. An example of this technique is shown in Figure 3.2, where the evolution of an individual nanocolumn was imaged after 1000, 2500, 5000, 8000 and 10000 pulses. Figure 3.2a shows the cone tip of the initial microstructured surface from which the nanocolumn growth was followed. We always observed a small tip at the top of the microcones, and as we continued the irradiation at low energy, the protrusion grew and a flat depression was formed around it (Figure 3.2b and c). Figure 3.3 shows the high resolution SEM images of the nanocolumns after 2500, 5000, 8000 and 10000 pulses. A careful examination of the high resolution images shows that the low-energy irradiation only produced melting at the very top of the cone tip. As the irradiation was continued, the depression around the protrusion disappeared (Figure 3.3b-d), and the protrusion developed into a nanocolumn, while a multitude of very small protrusions appeared at its base (Figure 3.3c). Finally, after 10000 pulses the nanocolumn had a height of 3.1 μm and a diameter of 200 nm, giving an aspect ratio of 15. The top of the microcones is not the only place that nanocolumns can be found. Sometimes nanocolumns can be found on the "bridge" connecting the microcones (Figure 3.4).

The growth rate of nanocolumn was measured as a function of number of laser pulses and appears to have three different stages (Figure 3.5). Up to 2500 the growth rate is almost negligible, but then it rapidly increases and reaches a steady state of 0.2 nm/pulse after 4000 pulses. After 10000 pulses, the nanocolumn has an aspect ratio of 15, which is double that of the microcones.

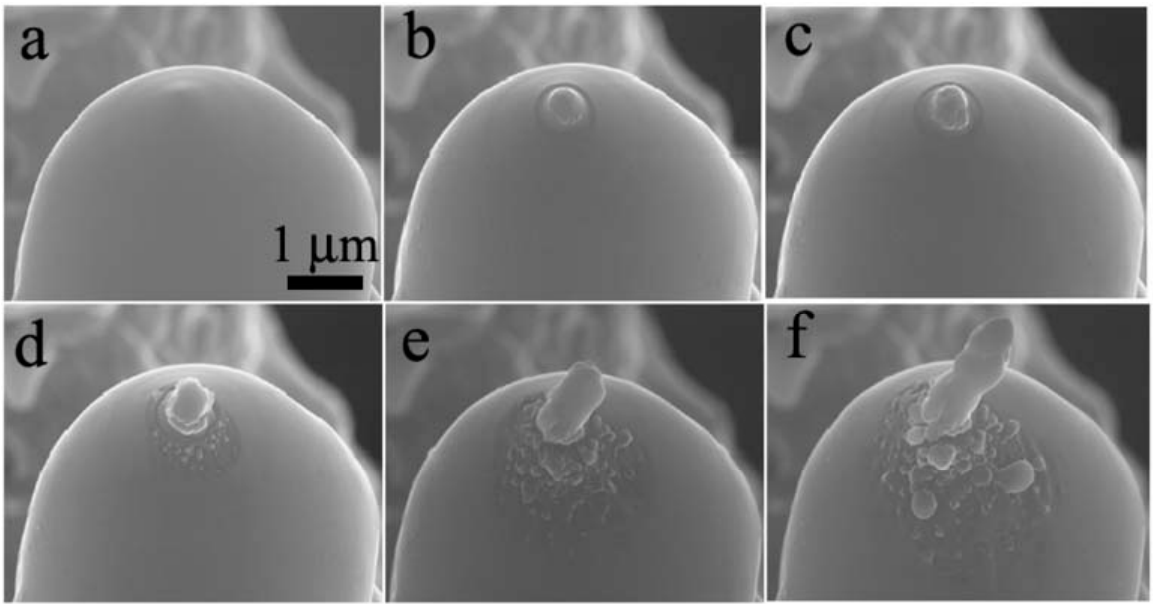

Figure 3.2 Nanocolumn evolution upon laser irradiation at 0.5 J/cm^2 in 10 Torr He. (a) Initial cone tip; (b) after 1000 pulses; (c) after 2500 pulses; (d) after 5000 pulses; (e) after 8000 pulses; (f) after 10000 pulses.

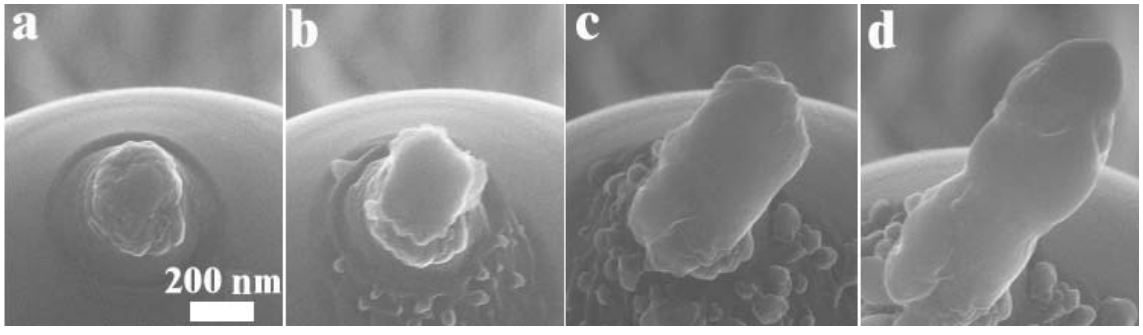

Figure 3.3 Higher SEM images showing the nanocolumn evolution upon pulsed laser irradiation at 0.5 J/cm^2, in 10 Torr He. (a) after 2500 pulses; (b) after 5000 pulses; (c) after 8000 pulses; (d) after 10000 pulses.

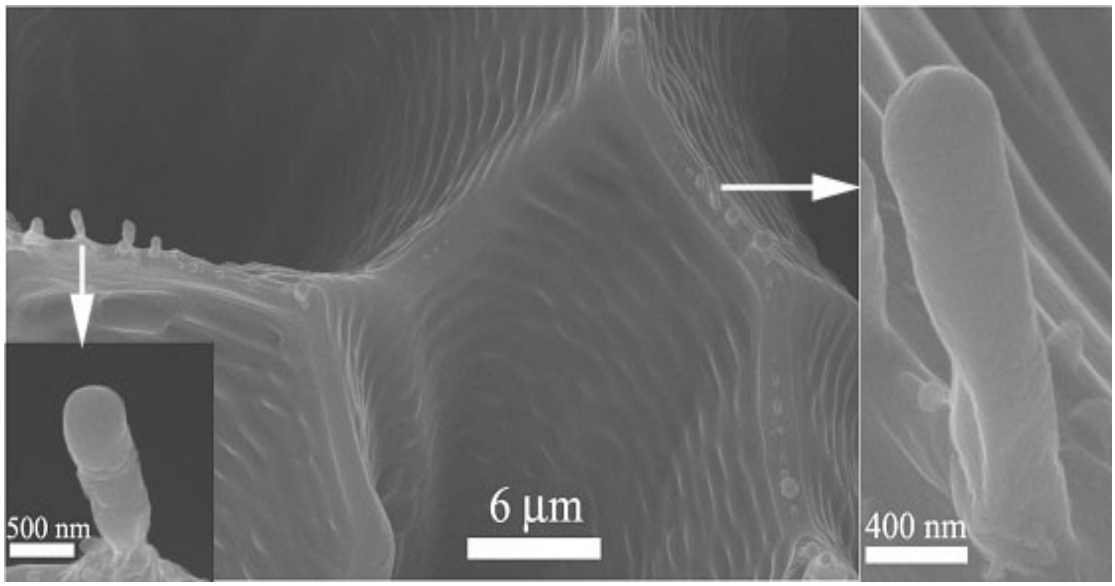

Figure 3.4 Nanocolumns formed on the "bridge" of the microstructured template. The sample was irradiated with 6000 laser pulses at a fluence of 0.5 J/cm^2 in 10Torr SF_6.

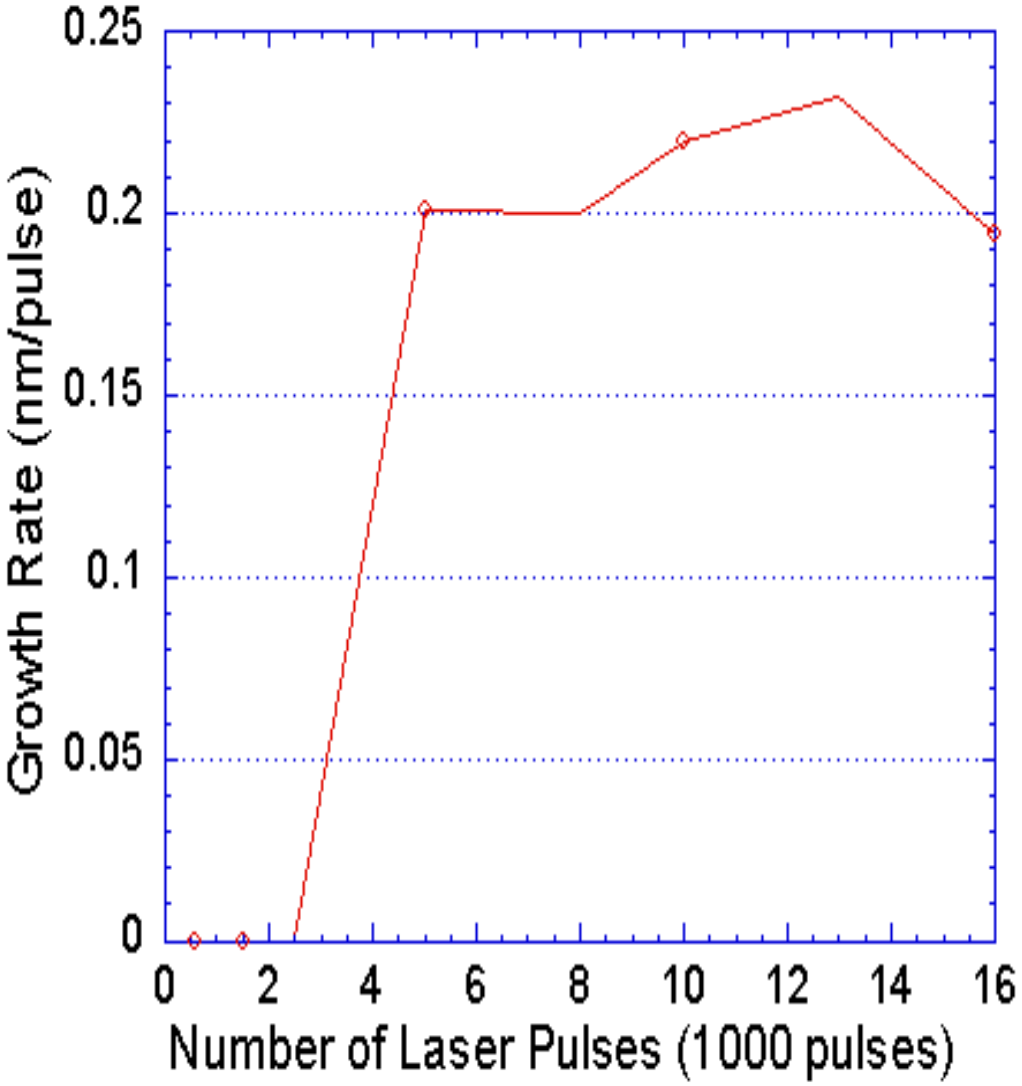

Figure 3.5 Growth rate of nanocolumns vs. number of laser pulses in He atmosphere at the fluence of 0.5 J/cm^2.

The chemical composition of the nanocolumns grown in He was measured using the electron beam of an SEM focused at the center of the nanocolumn in a spot of 150-nm-diameter. Only the chemical composition of the nanocolumn was measured, because the probe region extends to ~1.5 μm in depth, which is significantly less than the column height. It was found that the nanocolumns were made of silicon with less than 2 at % of oxygen, while the oxygen measured in the substrate was less than 1 %. The error in the electron dispersion X-ray spectroscopy measurements was on the order of 1 %.

In order to study the effect of laser fluence on the resulting nanocolumn evolution, microstructured samples were irradiated at 0.3 J/cm^2, 0.5 J/cm^2 and 1.0 J/cm^2, under otherwise similar experimental conditions. Figure 3.6 shows the different morphologies after 1000 laser pulses. These results indicate that melting is required to form the first protrusions because the melting threshold of silicon is ~0.5 J/cm^2 [28].

The effect of the background atmosphere on nanocolumn growth was investigated by irradiating microstructured specimens in He, vacuum, and SF_6. Figure 3.7 shows the results of the experiments performed under these three different atmospheres at the same fluence and after 5000 pulses. Irradiation in vacuum cannot generate the nanocolumns, while under SF_6 and He, the nanocolumns grow up to several microns. In vacuum, it is more difficult to trap the ablated material because there is no buffer gas atmosphere. However, small protrusions similar to those shown in Figure 3.2 are formed at the top of the microcones, but these protrusions do not grow additionally in vacuum and after 10000 pulses they tend to flatten.

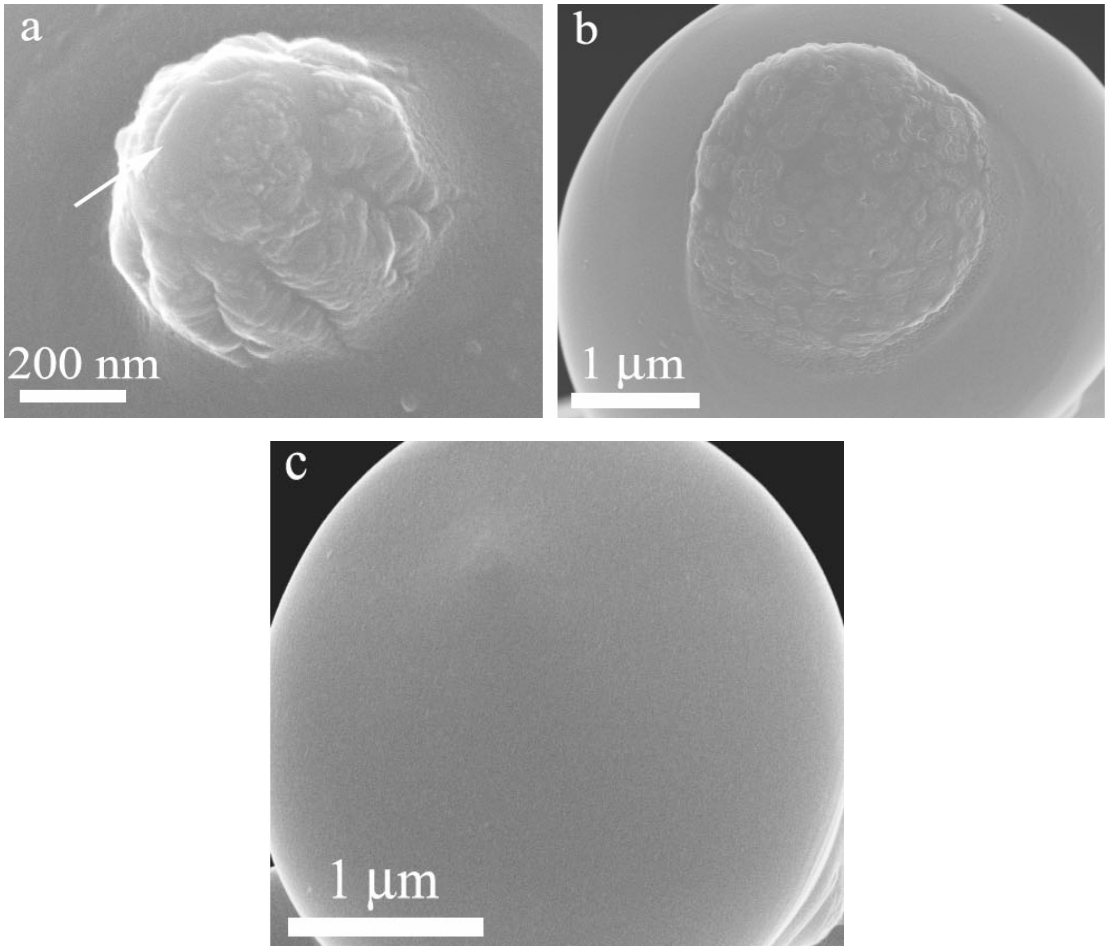

Figure 3.6 SEM images of cone tip after 1000 pulses at different laser fluences in 10 Torr He atmosphere. (a) 0.5 J/cm^2; (b) 1.0 J/cm^2; (c) 0.3 J/cm^2.

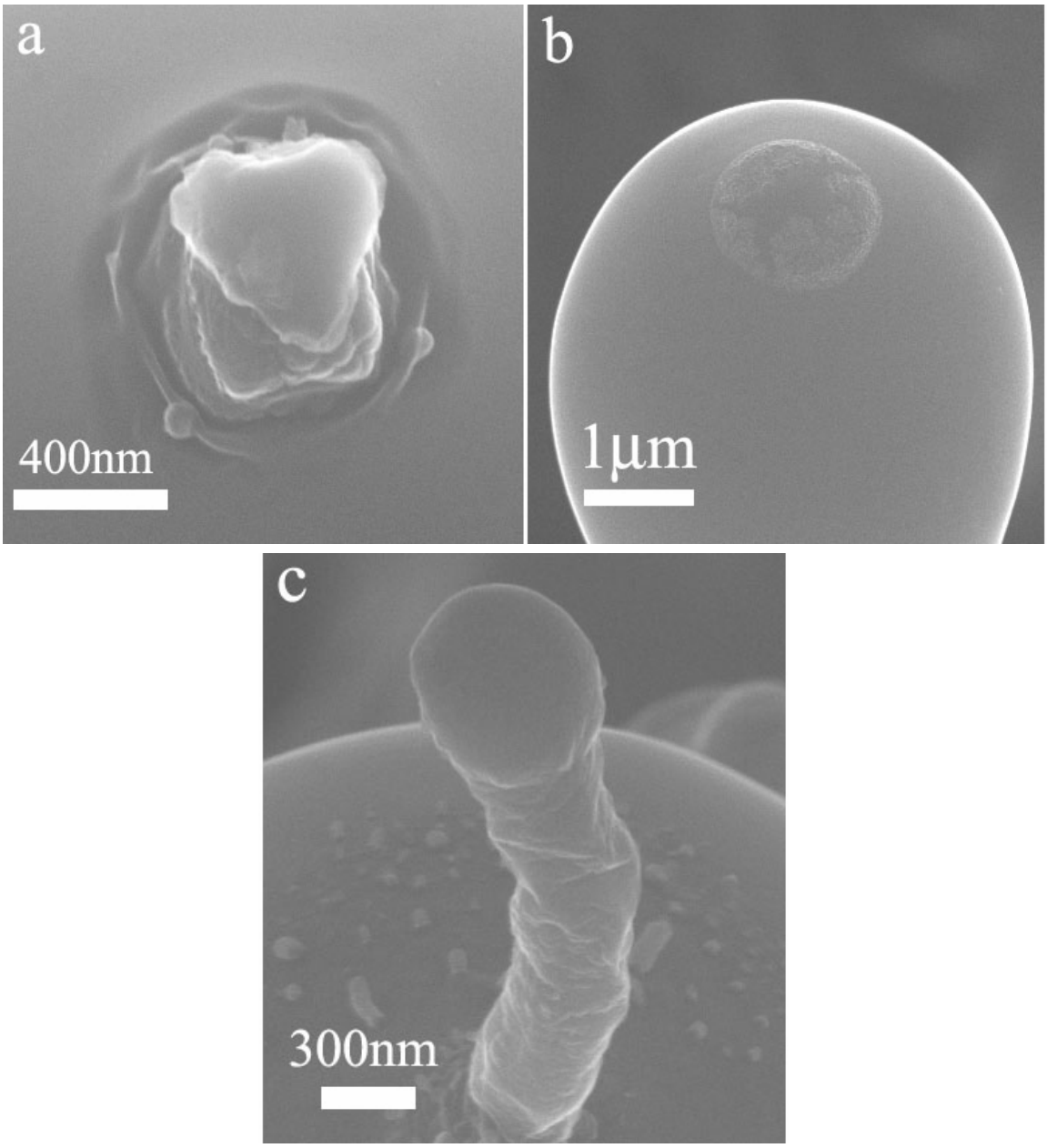

Figure 3.7 SEM images of growth structures at cone tip after 5000 pulses in different background atmospheres at 0.5 J/cm^2 laser fluence. (a) 10 Torr He; (b) Vacuum (2.6x10^{-7} Torr); (c) 10 Torr SF_6.

The process of deposition is clearly visible after 15000 pulses because a film covers a large portion of the substrate. Also, after 15000 pulses the diameter at the top of the nanocolumns increases significantly, and further evidence of the deposition process is lent by the multiple small protrusions that cover the nanocolumn tip proper (Figure 3.8).

3.1.2 Measurement of Field Emission Properties

Field emission (FE) was measured using a small-diameter (2 mm) moveable probe. The sample probe distance was determined by stepping the probe tip into the sample surface with 10 VDC applied to the probe tip. Once a current was detected, a Z=0 (height) position was defined [204]. The Z-axis was then stepped up to a nominal position of 15 μm. Since the sample at the position of touch down was likely damaged in the process, the X- or Y-axis was moved to a position of approximately 50 μm – 100 μm from the touch down position. The DC voltage was then ramped up to a value that yields a current of 1 nA. I-V sweeps were also performed on the samples.

The collected I-V emission data were analyzed by the Fowler Nordheim (F-N) equation [205] giving the relation between local current density J, local applied electric field E, work function Φ, and field enhancement factor β as follows

$$J = \frac{A\beta^2 E^2}{\Phi} \exp\left(-\frac{B\Phi^{3/2}}{\beta E}\right)$$

where A and B are constant. If the F-N relation is plotted as a logarithmic function, $\ln(J/E^2) = f(1/E)$, the work function Φ and field enhancement factor β can be compared independently from the probe-sample distance d for different samples.

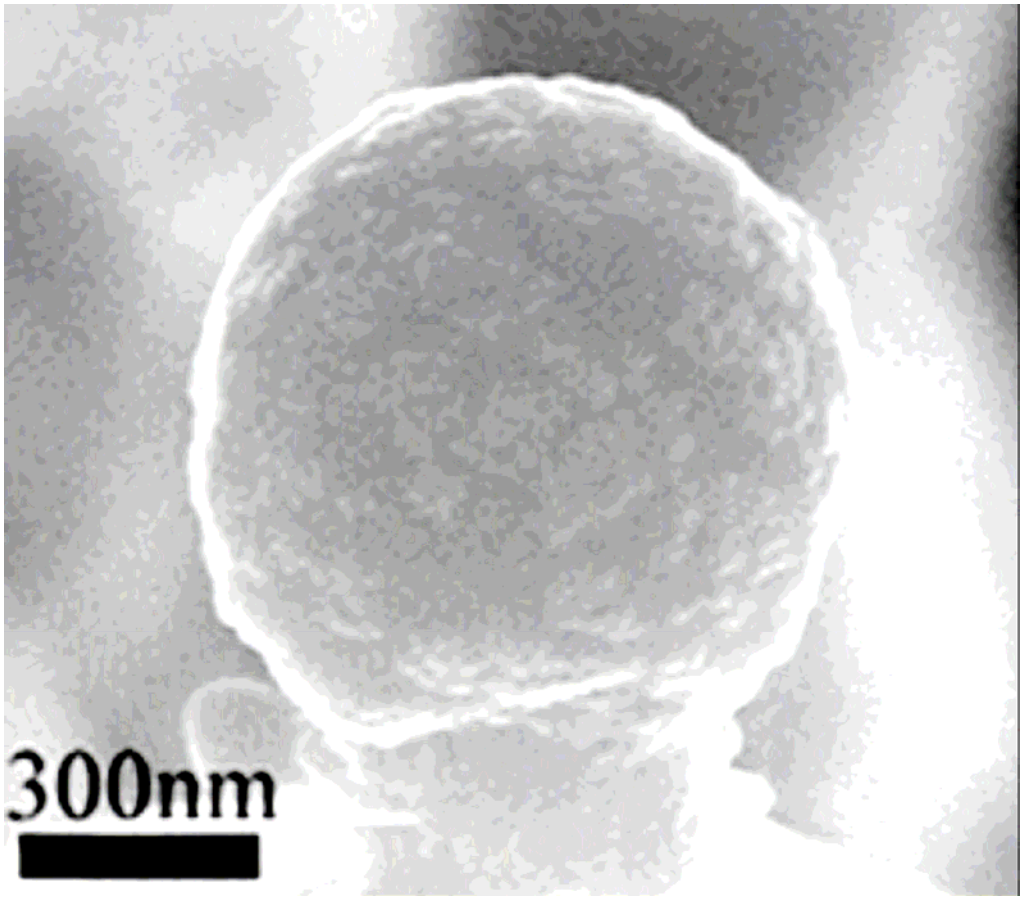

Figure 3.8 SEM image showing the tip of same nanocolumn as shown in Figure 3.2 and 3.3, after 15000 pulses.

The threshold field of the sample with microcones alone is around 55 V/μm. The same measurement was done on the sample with nanocolumns. The threshold field we got is 35 V/μm, which is significantly lower than that of the microcone sample. Figure 3.9a shows the I-V sweep for the sample with microcones and Figure 3.9b shows the I-V sweep for the sample with nanocolumns. The Fowler-Nordheim (FN) plots in both figures show linearity, indicating that the measured current is indeed from field emission. The emission threshold field depends on the geometric aspect ratio of the micro/nano structures.

Stability tests of the nanocolumns suggest that they are likely to have a long emission lifetime at expected device-operation currents. Figure 3.10 shows the result of such longevity test. A constant emission current of 100 nA was maintained from the typical nanocolumns for over 2300 seconds.

3.2 Formation of Laser Induced Periodic Surface Structures (LIPSS) under Single-Beam Irradiation

Single beam irradiation was done using p-polarized laser light. Under single beam illumination, only 1-D gratings were generated on the substrate surface. The grating lines were perpendicular to the projection of the electric field of the incident light on the substrate surface.

Different experimental conditions have been tested to find out what factors effect the formation of LIPSS. The incident angle of laser beam, the ambient atmospheres, the

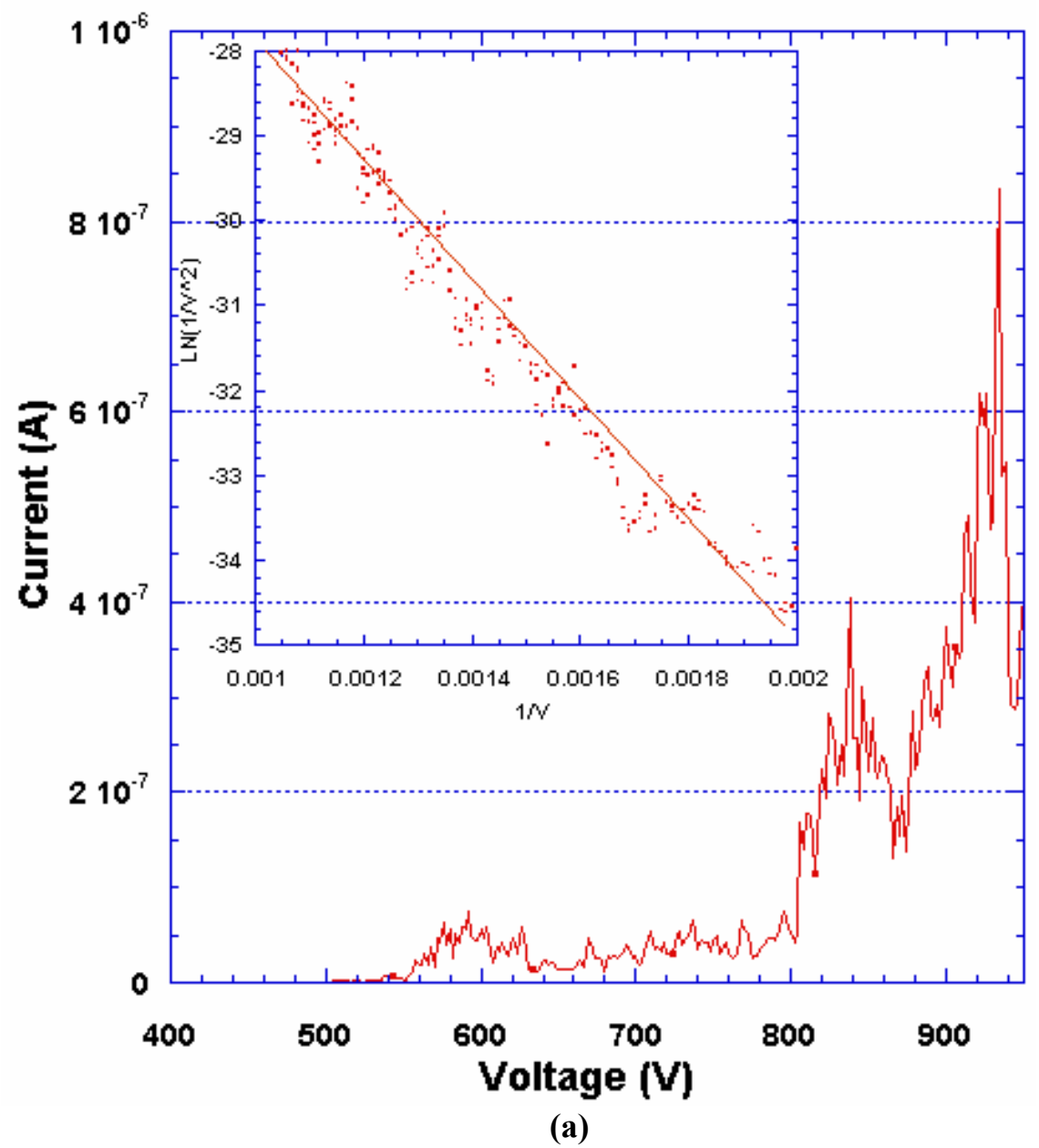

(a)

Figure 3.9a Emission (I-V) curve and FN plot (inset) of sample with microcones only. The probe height was set at 8.6μm.

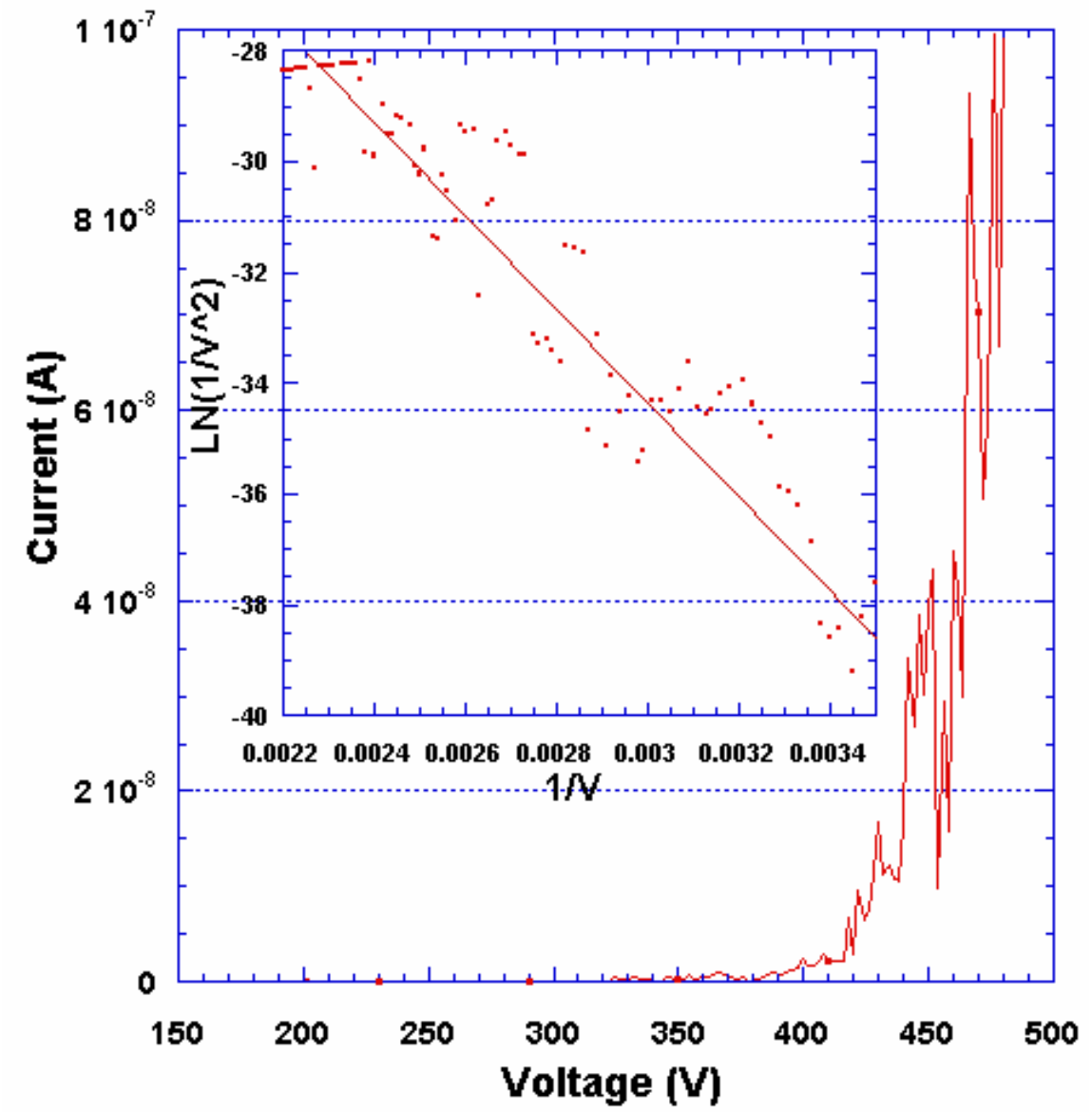

(b)

Figure 3.9b Emission (I-V) curve and FN plot (inset) of the same specimen as in Figure 3.9a with nanocolumns. The probe height was set at 7.6μm.

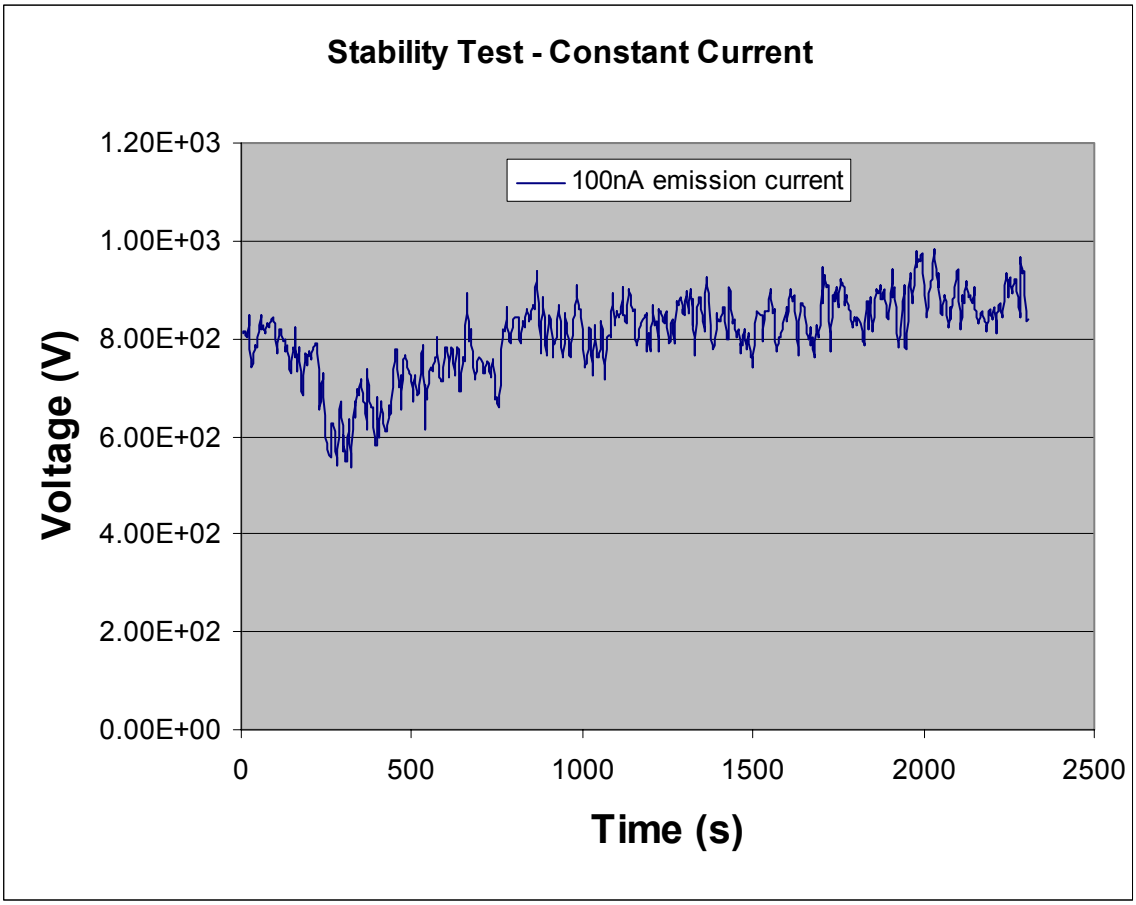

Figure 3.10 Plot of the applied electric field required to maintain a 100 nA steady-state emission current from the nanocolumns of the same specimen tested in Figure 3.9 for a 2300 seconds period.

energy density of the laser beam, and polarization of the light have been tested. Ex situ characterization of the samples was conducted mainly by AFM.

3.2.1 Effect of Laser Polarization

According to the characteristics of the KrF laser we were using, the light coming out of the cavity was non-polarized. When the smooth silicon specimen was irradiated by the non-polarized laser beam, a root-mean-square (RMS) value of roughness of 0.047 nm was produced in the surface plane, with a maximum height of only 0.6 nm. No periodic ripples structures were found at the surface no matter what angle of incidence was used. Figure 3.11 is the AFM image of a sample irradiated with non-polarized light at an incident angle of 38˚. The sample was irradiated in vacuum at a laser fluence of 0.8 J/cm^2 with 400 laser pulses. The same fluence, atmosphere and number of pulses were used later on for irradiation with p-polarized laser light, yielding LIPSS.

Schematic image of the UV laser polarizing beamsplitter used in the experiments is shown in Figure 2.4. By directing either the s or the p polarized light onto the substrate, we can test the effect of laser polarization on the formation of LIPSS.

Periodic ripples (LIPSS) were observed when the irradiation was performed with p-polarized laser light, under the same atmosphere, at the same fluence and with the same number of pulses as used in the experiments described above. On the other hand, s-polarized light did not produce ripples.

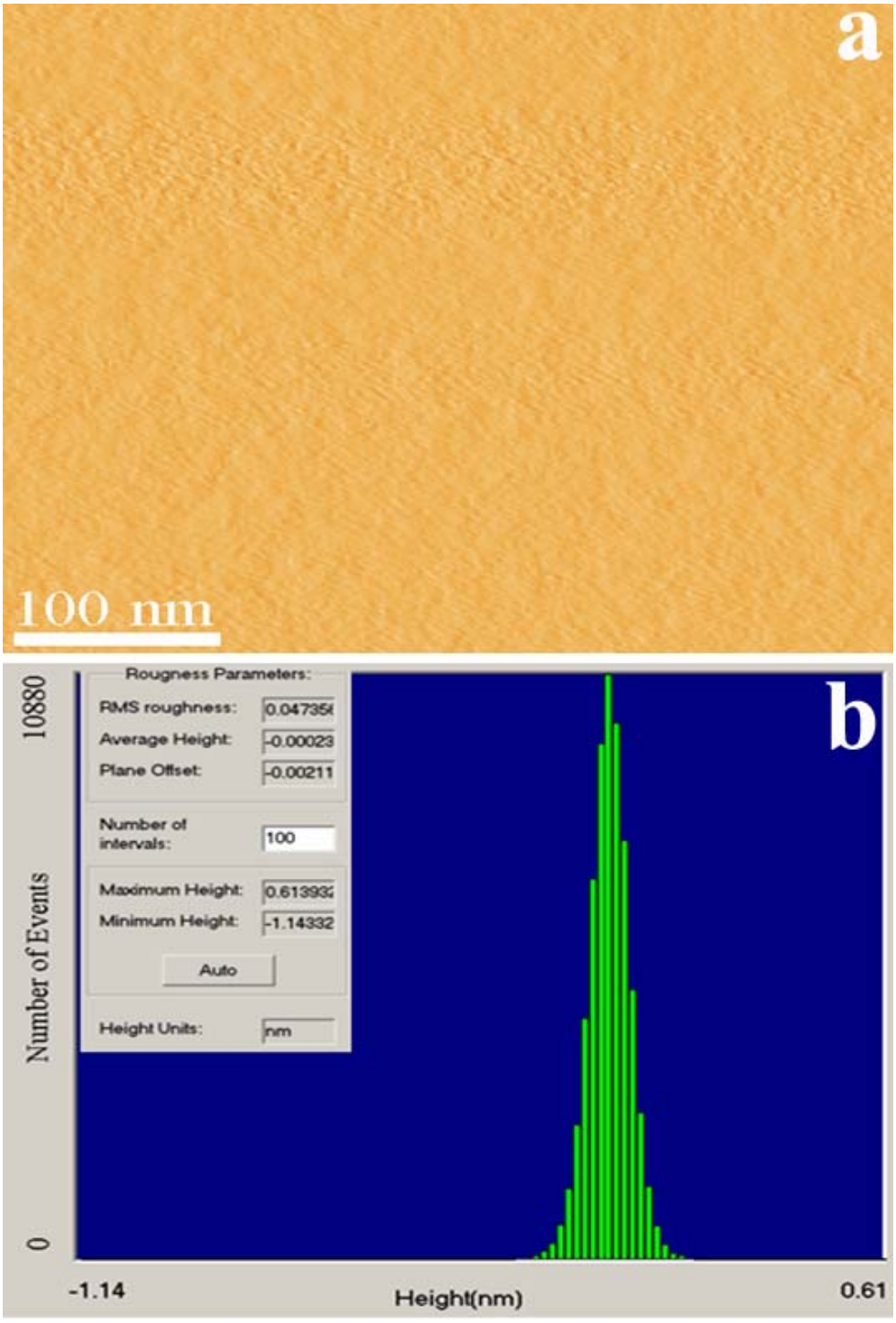

Figure 3.11 (a) AFM image showing the surface of a sample irradiated with non-polarized laser beam after 400 pulses at a laser fluence of 0.8 J/cm^2 in vacuum. (b) Roughness analysis results showing the smoothness of the surface.

3.2.2 Line Spacing of LIPSS as a Function of Incident Angle

Under single beam illumination, it was found that the LIPSS line spacing Λ and the incident angle θ follow the sine law:

$$\Lambda_{1,2} = \lambda/(1 \pm \sin\theta) \qquad 3.1$$

where Λ_1 is for the subtraction and Λ_2 for the addition, and λ is the laser wavelength, in our case λ=248 nm.

The 2-D and 3-D AFM images of a sample irradiated in Ar after 2000 pulses at a laser fluence of 0.64 J/cm^2, and an angle of incidence of 38˚ are shown in Figure 3.12. The measured line spacing is 153 nm, which agrees with the theoretical value Λ_2 calculated using eq. 3.1.

The crest-to-trough weight is 7.08 nm, with an RMS value of 1, which is 20 times larger than the RMS value for the specimen irradiated with non-polarized light.

From the measured profile (Figure 3.12b) and 3-D AFM image (Figure 3.12d), we found the presence of *sub*-ripples with identical line spacing but whose heights are ~ ¼ of the main ripples.

A similar relation has been found in a sample irradiated at a 45˚ incident angle. Figure 3.13 shows the corresponding plane view image of the sample surface (a) and the profile (b) along the line traced in Figure 3.13a. The measured line spacing between ripples is 146 nm, and the calculated incident angle is 44.3˚. Once again, we clearly discerned the occurrence of *sub*-ripples.

In a large number of experiments we found that the most widely represented relationship between ripple line spacing and angle of incidence of the light is given by eq.

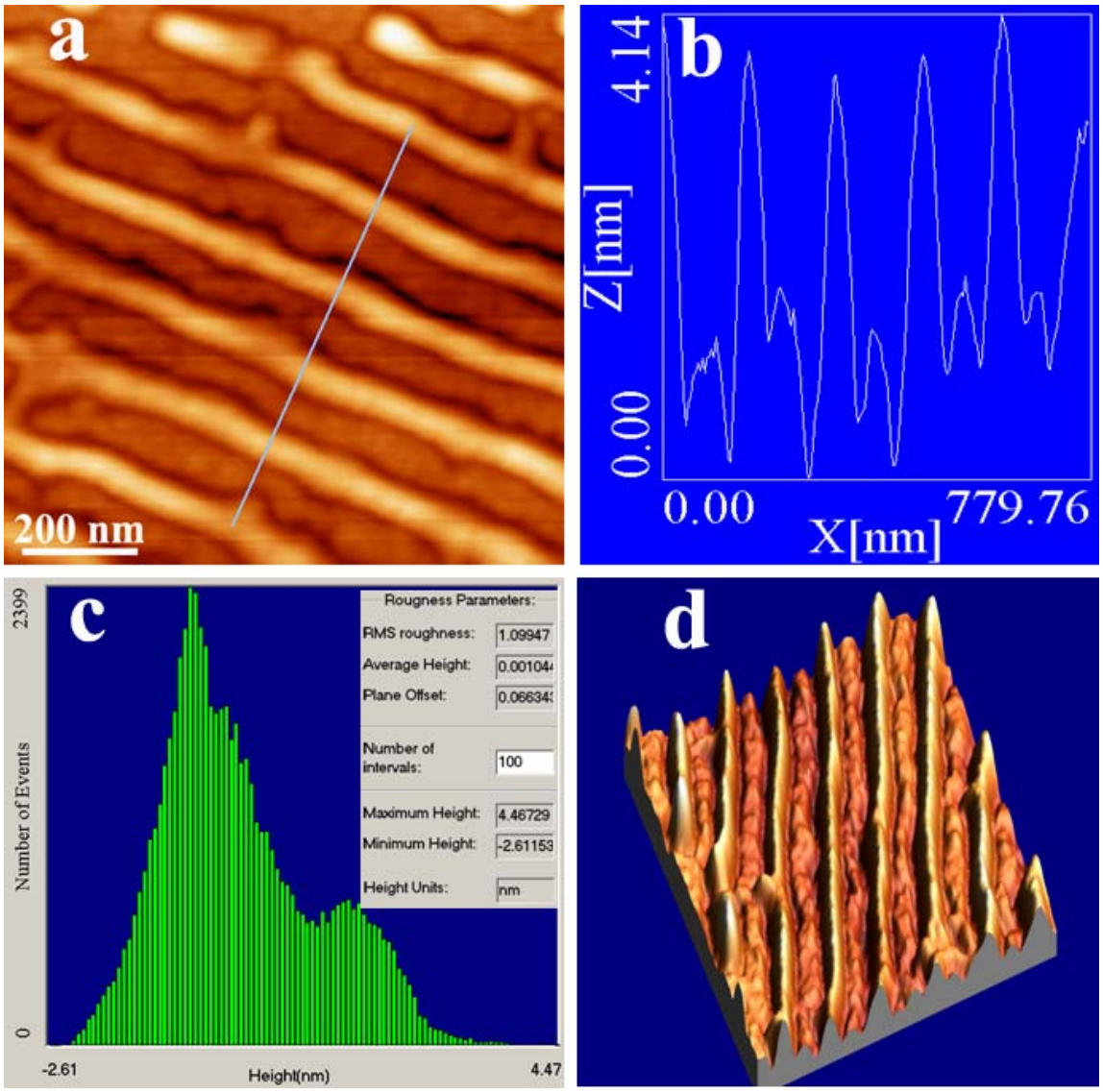

Figure 3.12 AFM image of a sample surface irradiated in 0.1 Torr Ar after 2000 pulses at a laser fluence of 0.64 J/cm^2 with an incident angle of ~38˚. (a) Plane view of the sample; (b) Profile of the line traced in (a) showing that the line spacing of the ripples is ~ 153 nm; (c) Roughness analysis of the sample showing that the RMS is ~1 and the maximum height is 4.47 nm; (d) 3-D view of the sample.

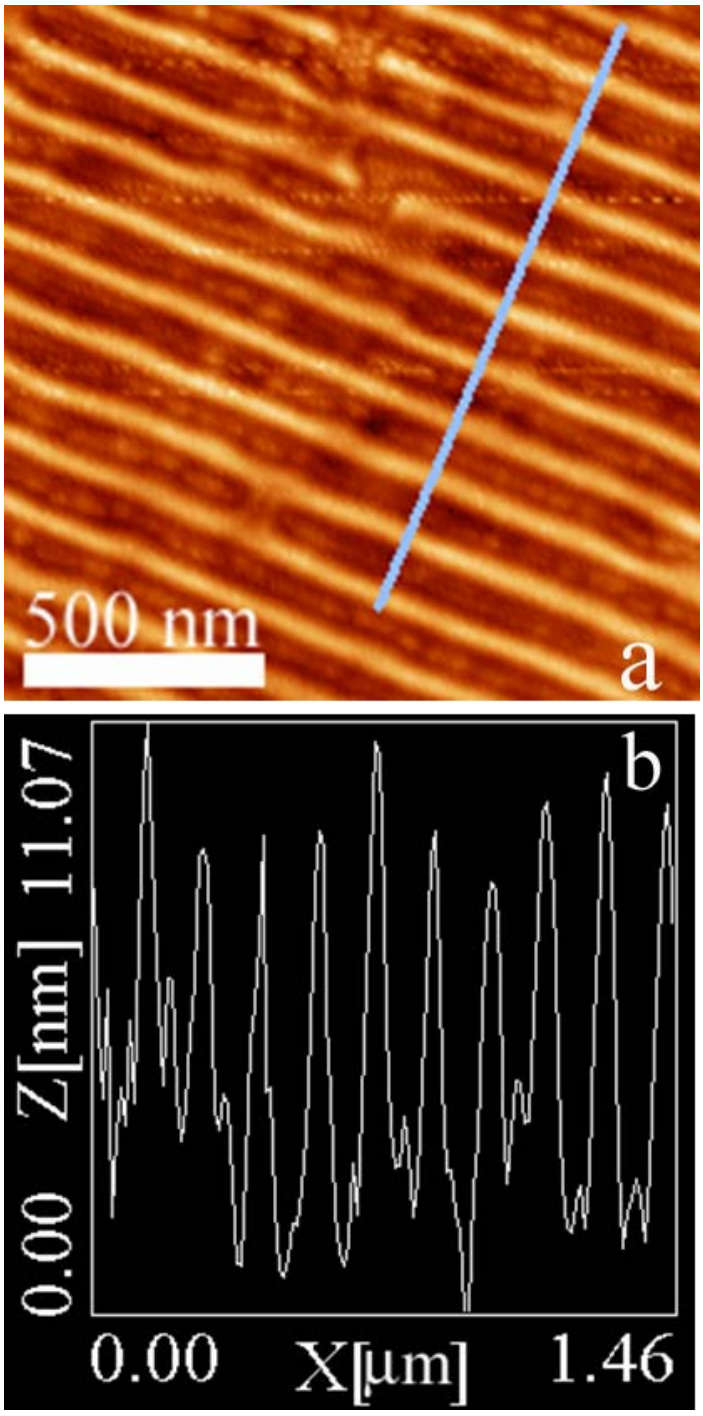

Figure 3.13 AFM image of a sample surface irradiated in 0.1 Torr Ar after 2000 pulses at a laser fluence of 0.64 J/cm^2 with an incident angle ~45˚. (a) Plane view of the sample; (b) Profile of the line traced in (a) covering ten ripples, showing a line spacing of the ripples of ~ 146 nm.

3.1 for Λ_1.

Figure 3.14 was taken on the same sample as Figure 3.12, but in different regions. From the profile in Figure 3.14b we noticed a drastic increase in the line spacing. The measured value is ~ 648 nm. From Figure 3.12, we previously calculated an incident angle of 38.4˚. The calculated line spacing following equation 3.1 should be 654 nm. The difference between theoretically predicted value and the experimentally determined value is 0.9%.

A comparison of the profiles in 3.12b and 3.14b, taken on the same specimen, shows that the ripples spaced according to Λ_1 are significantly taller than those spaced according to Λ_2.

Figure 3.15 is another sample irradiated at 0.6 J/cm^2 in Ar after 2000 pulses. The angle of incidence is 38˚. The actually measured line spacing from the AFM is 621 nm, yielding a calculated angle of incidence according to equation 3.1 of 36.9˚.

In both Figure 3.15b and 3.15c, sub-ripples can be observed between dominant ripples. The dominant ripples are approximately sine wave. The sub-ripples can then be described as sine wave, which is 180˚ phase shifted from the original wave.

The profile accompanying Figure 3.15a exhibits an asymmetry, whereby one side smoothly increases in steps as it goes from the valley to the crest and the other side decreases more abruptly. It can be reasoned that, since the fringes are normal to the plane of incidence and the incident beam stroked the surface at an angle, the fringes and the generated roughness cast a narrow shadow into the valley. This shadowing would have decreased the light intensity in one side relative to the other, possibly producing the noted asymmetry.

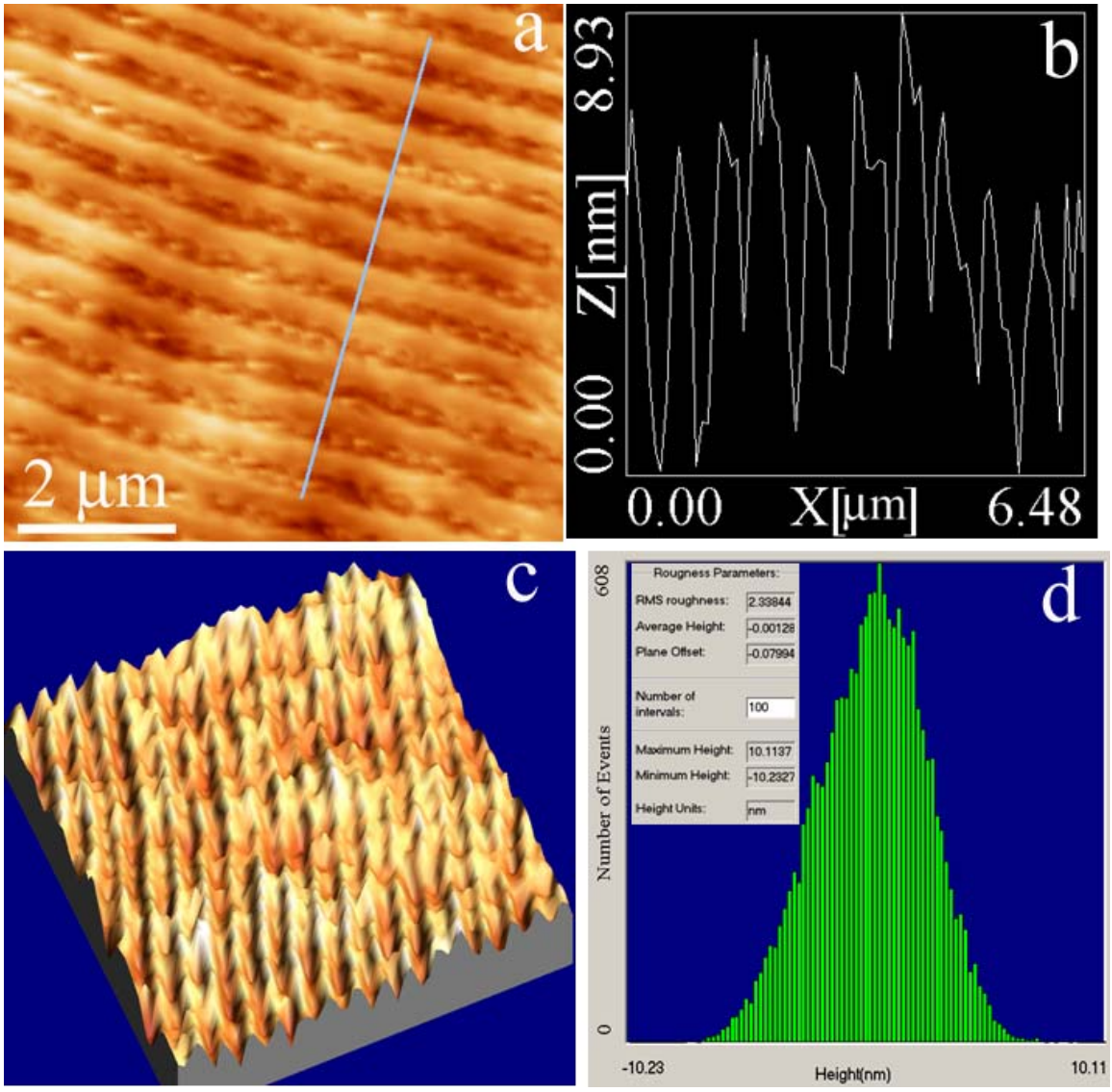

Figure 3.14 AFM image of a sample surface irradiated in 0.1 Torr Ar after 2000 pulses at a laser fluence of 0.64 J/cm^2 with an incident angle ~38˚. (a) Plane view of the sample; (b) Profile of the line traced in (a) covering ten ripples showing a line spacing of the ripples of ~ 648 nm; (c) 3-D view of the sample; (d) Roughness analysis of the sample surface. The RMS is 2.34, and the maximum height is ~10 nm.

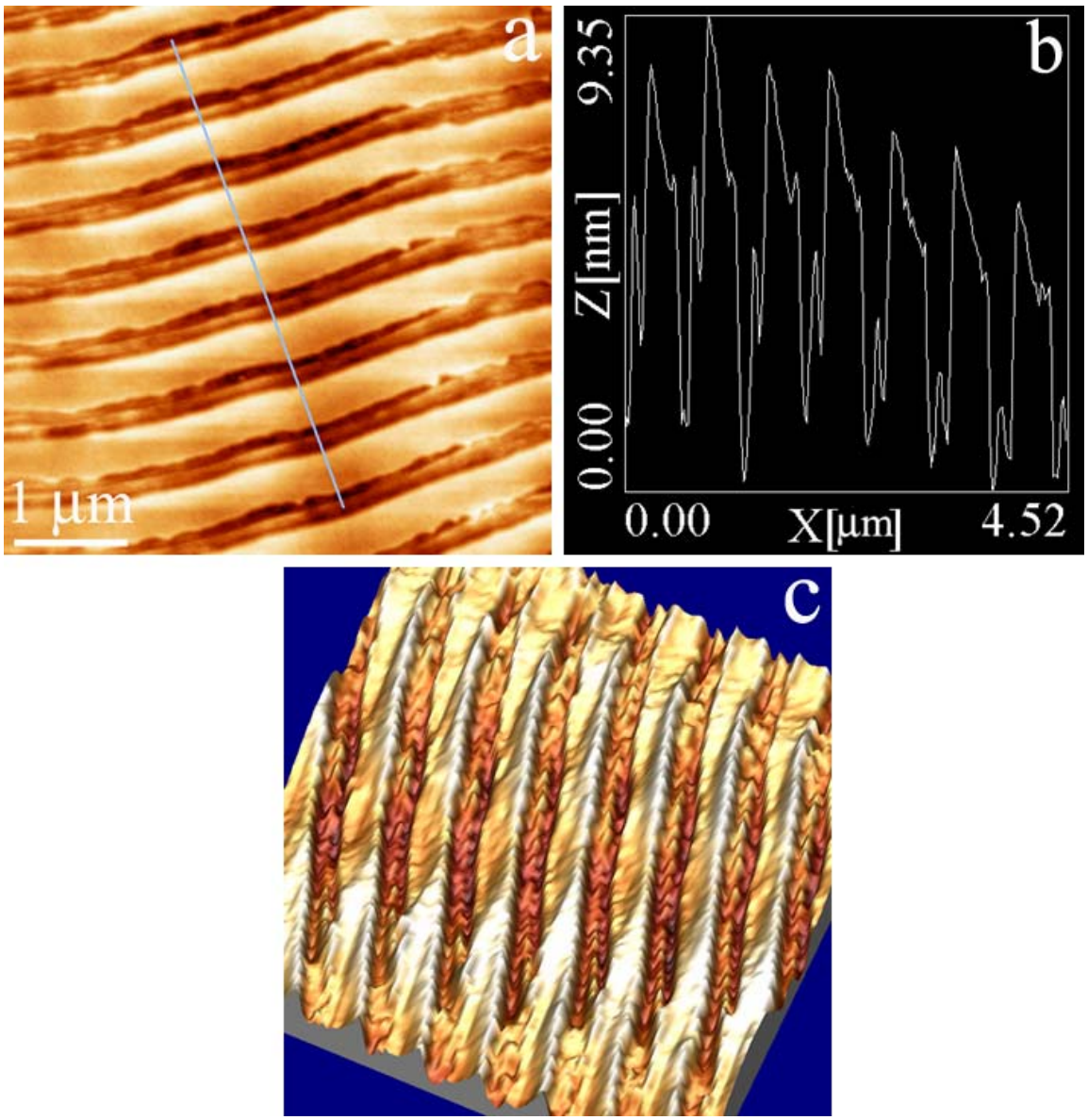

Figure 3.15 AFM image of a sample surface irradiated in 0.1 Torr Ar after 2000 pulses at a laser fluence of 0.6 J/cm^2 with an incident angle ~38˚. (a) Plane view of the sample; (b) Profile of the line traced in (a) covering seven ripples. The calculated line spacing of the ripples is ~ 621.4 nm. Notice asymmetry in fringe profile; (c) 3-D view of the sample. Sub ripples can clearly be seen between dominant ripples.

Figure 3.16 is the AFM image showing a substrate irradiated at <1˚ off normal incidence with 400 p-polarized laser pulses exhibiting ripples with a line spacing of 250 nm. The ripples formed under normal incidence are seen to be straighter than those formed at larger incident angles. The sub-ripple height is almost half that of the dominant ripples.

Table 3.1 summarizes the relationship between angle of incidence and the ripple line spacing. The data in the table are plotted in Figure 3.17, together with the functional dependencies given by eq. 3.1, showing that the data follow eq. 3.1.

3.2.3 Evolution of LIPSS under Single Beam Illumination

Unlike previously reported for longer wavelength gratings, and depending on the specific irradiation conditions, in our experiments several tens and, in some cases, hundreds of laser pulses are required to initiate formation of submicron wavelength periodic structures in silicon. For instance, after several hundred pulses a rather diffuse rippled structure was formed at the center of a silicon substrate. The ripple amplitude was very small reaching a maximum value of 0.5 nm; in the AFM image (Figure 3.18), the ripples are clearly delineated but lack a complete ordering and have a wavelength that varies considerably depending on the region. This initial period is difficult to quantify because, most probably, it depends on unpredictable variables such as surface defects that could trigger the initiation process. A general trend is that the number of pulses required to initiating the periodic ripple structure increases as the ripple line spacing decreases.

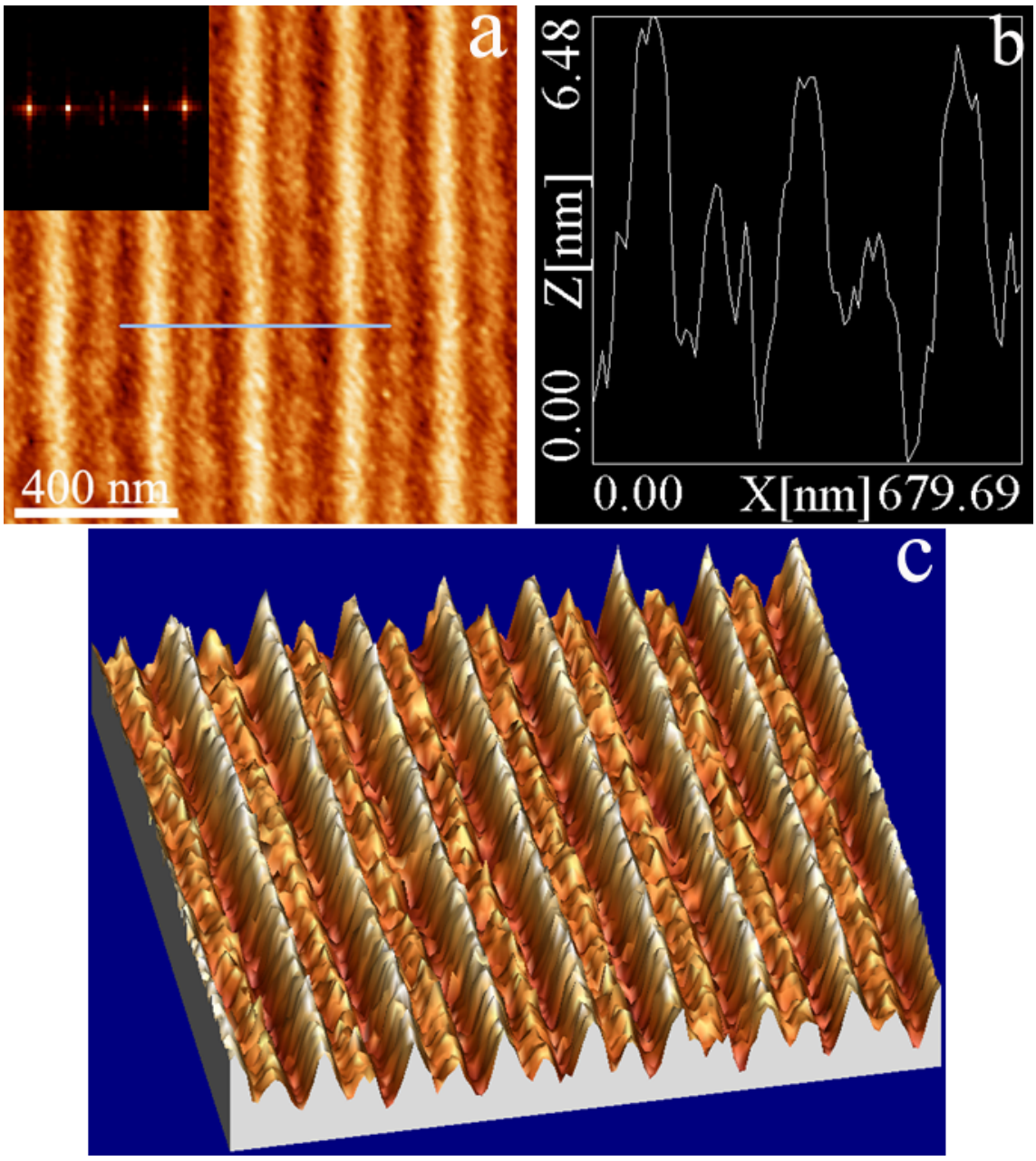

Figure 3.16 LIPSS generated at normal incidence on the surface of laser irradiated silicon after 400 laser pulses at a laser fluence of 0.8 J/cm^2. (a) 2-D AFM image, the inset is the FFT of the pattern, from the FFT the measured line spacing between those ripples is ~250 nm. (b) Cross-section of the ripples marked by the trace line in (a). The average crest to trough distance for these LIPSS is 6 nm ± 0.5 nm. (c) 3-D AFM image showing the relative positions of dominant and of sub ripples in the surface.

Table 3.1 Angle of incidence vs. line spacing of ripples

Angle of incidence	Line spacing of ripples (nm)
0	248
33	545
37	621
38.1	648
38.4	153
40	694
44.3	146

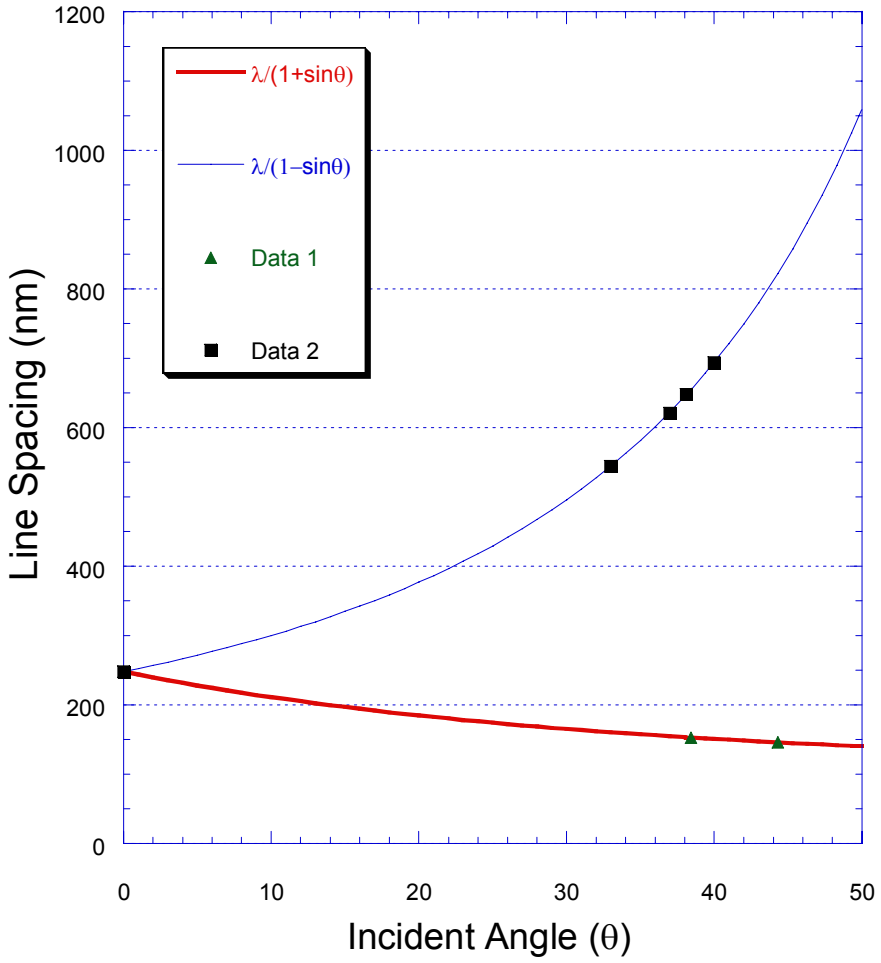

Figure 3.17 Line spacing vs. incident angle, for ripples formed under single beam illumination. Data are listed in Table 3.1. Experimental data points superimposed on the figure follow the relationships indicated in the legend. Most of the data follow $\Lambda = \lambda/(1-\sin\theta)$.

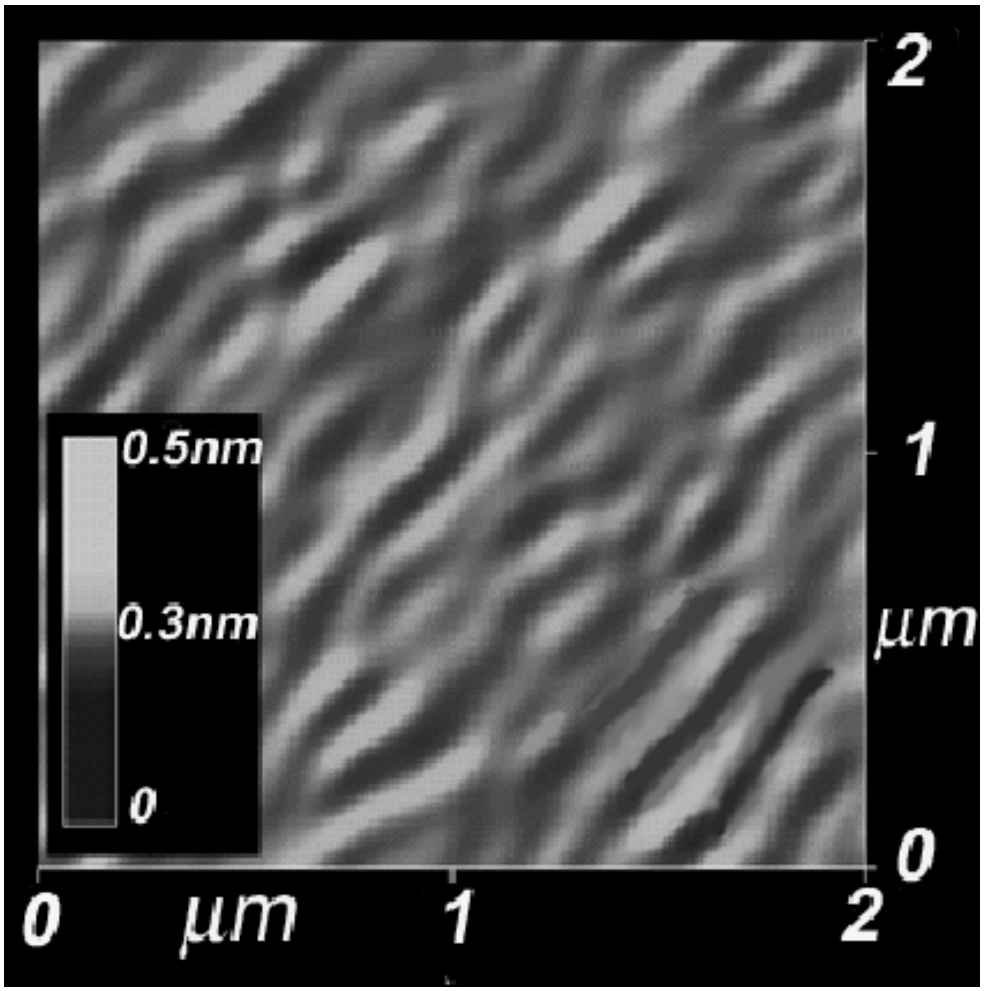

Figure 3.18 Early stage of ripple formation. AFM image suggesting an evolution of the surface with increasing number of laser pulses, until the proper conditions are achieved for the ripples to propagate. Specimen irradiated with 400 pulses of a single beam of p-polarized light incident at 8°. Laser fluence of 0.8 J/cm^2; He atmosphere pressure of 100 Torr.

Another aspect relevant to the formation of laser induced periodic surface structures is the strong dependence on the laser fluence. Studies performed with a laser beam incident at 38˚ showed that fringes form only in the fluence range of 0.4-0.8 J/cm^2. As described in section 2, this fluence is the average value incident on the surface. The ripples tend to be concentrated at the center of the laser spot for laser fluences of around 0.4 J/cm^2 and extend from the center towards the edges as the laser fluence is increased. This is due to the Gaussian distribution in intensity of our laser beam. At a laser fluence of 0.5 J/cm^2 the ripples covered the irradiated spot almost completely except for the edges where the fluence was less.

In order to examine the effect of the native oxide layer two types of experiments were performed initially using the same conditions: 2000 pulses of p-polarized laser light at an angle of incidence of 14˚, a fluence of 0.7 J/cm^2 and a vacuum pressure of 5x10^{-6} Torr. In one of the experiments the native oxide was removed from the surface of the silicon prior to the irradiation, while in the other specimens having their as-received native oxide were irradiated without undergoing any surface conditioning. These experiments consistently showed that the oxide layer stabilizes the ripples, e.g. the ripple's height is larger if this layer has not been removed. All the experiments described in this section were performed on silicon with the native oxide film.

Figure 3.19 shows three sets of ripples that are identifiable as three vertical stripes. In the group at the left the maxima and minima are clearly delineated with elongated holes forming in the valley. In the middle stripe the peak to trough vertical distance is significantly smaller than that in the left one and decreases from the center to the upper part, and in the lower part some holes start appearing. The right-most stripe is only faintly

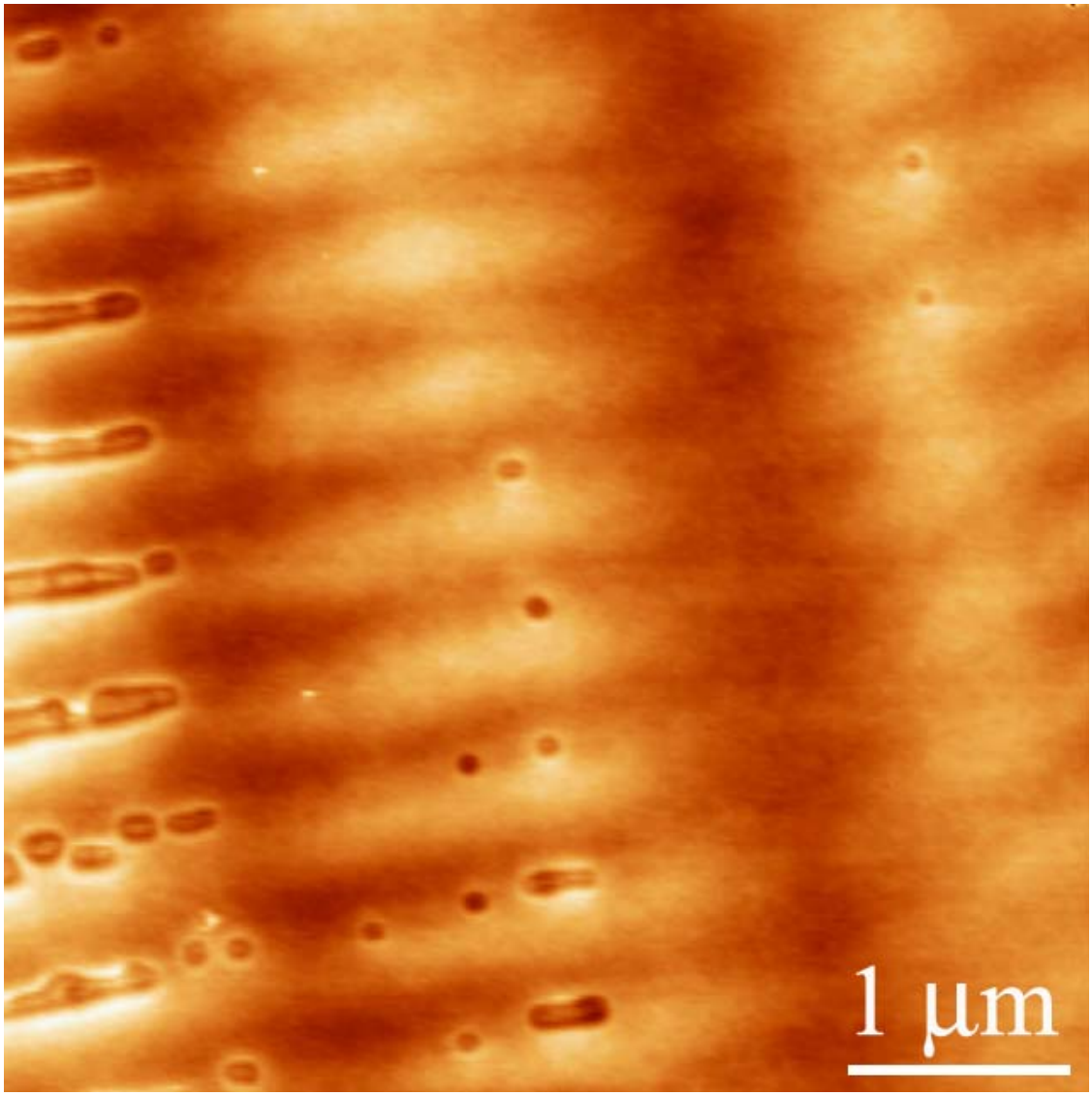

Figure 3.19 AFM image of a specimen edge where incipient LIPSS can be observed. Laser fluence is 0.7 J/cm^2.

delineated. These three stripes appear as though they have been initiated independently because their minima and maxima do not relate to each other, but they are parallel because they must lie in the direction of the light polarization vector.

From several observations it appears that the gratings evolve with the number of pulses. For instance, ripples detected after 50 pulses at a laser fluence of 0.7 J/cm^2 and at an angle of incidence of 38˚ had a peak to trough height of 8 to 14.5 nm. The appearance of the ripples was irregular because they seemed to have formed independently as very narrow bands, like in the previous case, and when they merged many misalignments occurred. After 2000 pulses a peak to trough vertical distance is significantly larger, ~20 nm was measured across the ripples shown in Figure 3.20. Also, it can be seen that a process of coalescence of different bands took place. This image illustrates the case of ripples that seem to have been independently initiated from several sites creating a defective structure as they propagated and coalesced. Furthermore, it also suggests that the rippled structure tends to propagate faster in the direction parallel to the polarization vector than in a direction normal to it. Defective structures with bending lines have been frequently observed in our experiments. Figure 3.21 is another example of this behavior. Figure 3.21 shows a larger region irradiated with p-polarized laser light at an incident angle of 40˚. The measured line spacing is 697 nm.

A high magnification view of another specimen irradiated with 50 pulses at a fluence of 0.7 J/cm^2 and angle of incidence of 38.5˚ is shown in Figure 3.22. The silhouette of the lower part of the fringes in this image clearly suggests displacement of liquid moving uphill and leaving in its path tiny liquid fingers. Likewise, the profiles accompanying both figures also exhibit an asymmetry.

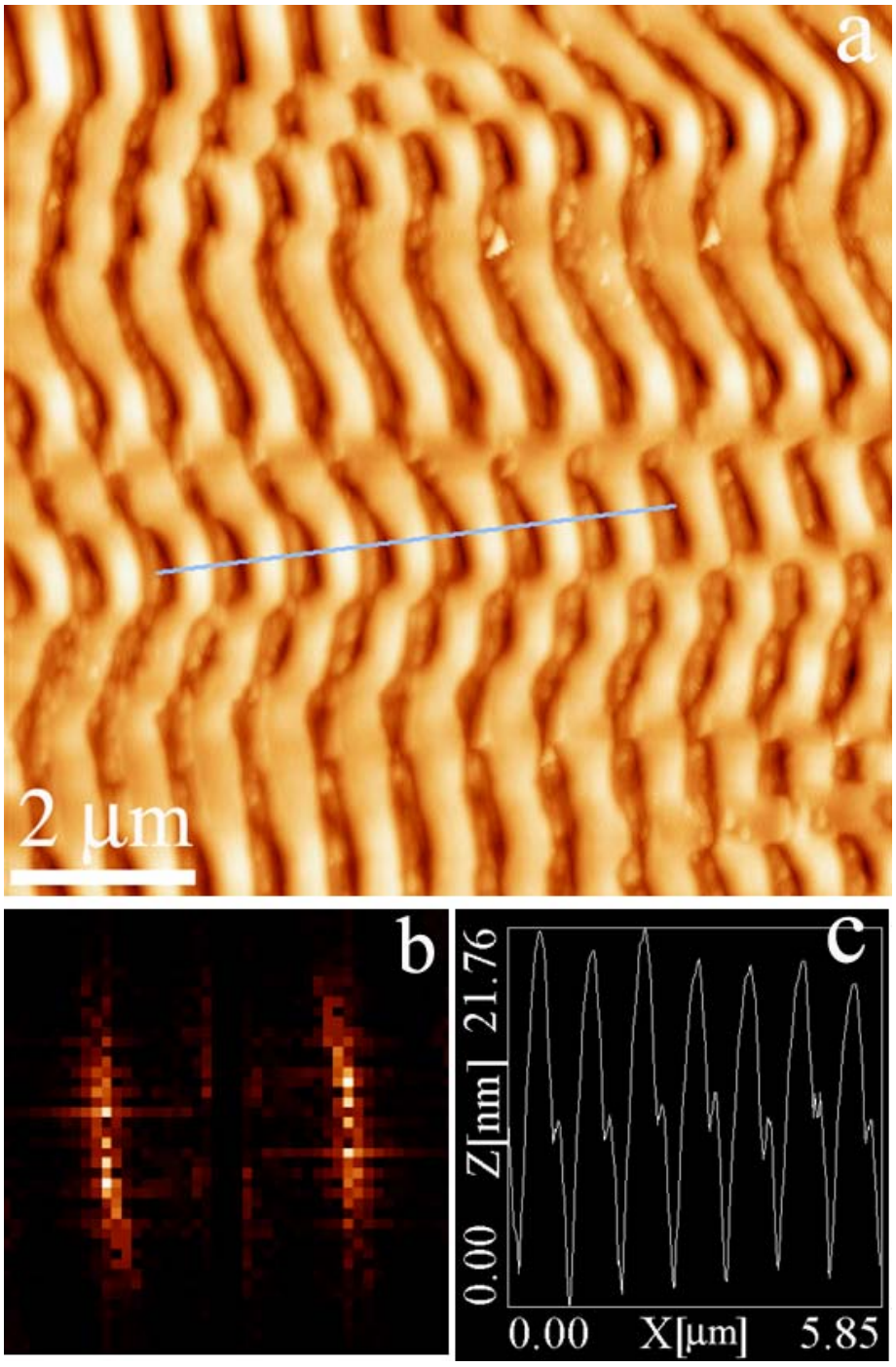

Figure 3.20 AFM image of sample irradiated with 2000 pulses at a laser fluence of 0.7 J/cm^2, using a p-polarized single beam at an incident angle of 44°. (a) Plane view. (b) FFT of the image shows two short arcs that reveal a rotation of the q vector (Figure 1.23). (c) Profile of the trace line marked in (a). The spacing measured in the profile is 811 nm, in very good agreement with formula 3.1 and with the value of $|\boldsymbol{q}_1|$ obtained from the FFT.

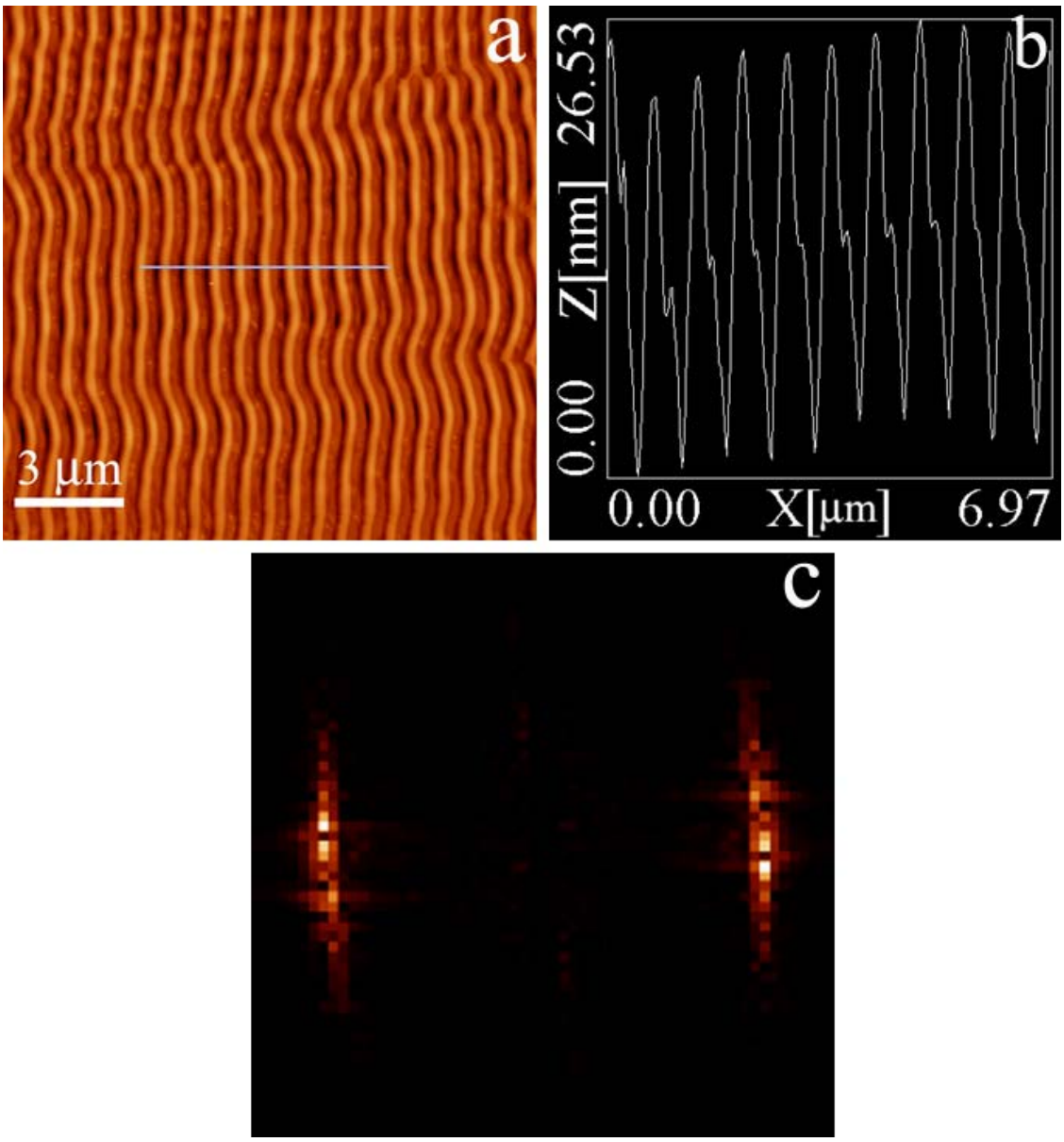

Figure 3.21 AFM image of sample irradiated with 2000 pulses at a laser fluence of 0.7 J/cm^2, using a p-polarized single beam at an incident angle of 40°. (a) Plane view. (b) Profile of the trace line marked in (a). The spacing measured in the lower right profile is 798 nm. (c) FFT of the image.

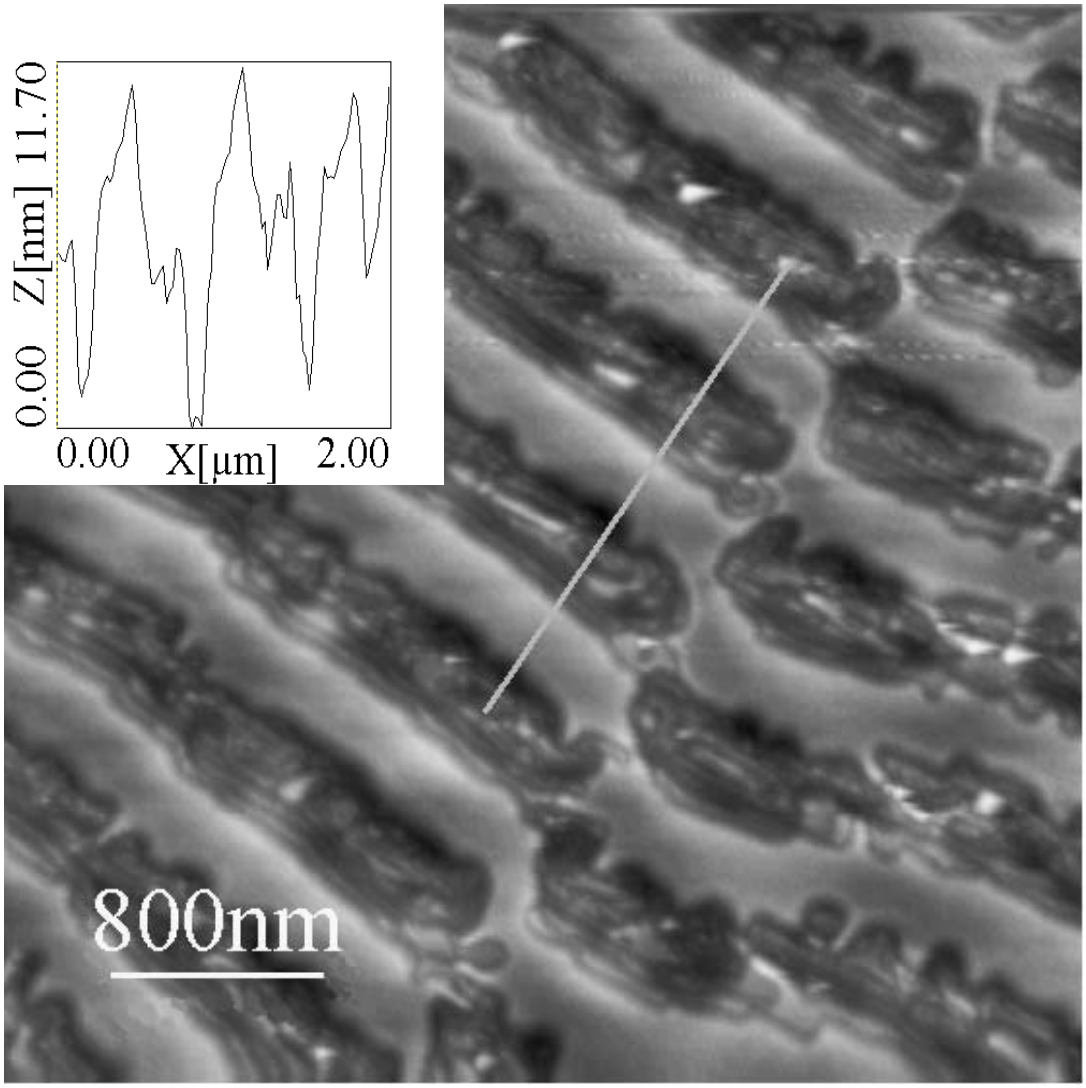

Figure 3.22 AFM image of sample irradiated with 50 pulses at a laser fluence of 0.7 J/cm^2. Ripples produced using a p-polarized single beam at an incident angle of 38.5^o. Λ= 673 nm. Notice tiny little "fingers" in lower rim of fringes and asymmetry in fringe profile taken.

This image in Figure 3.23 was taken in a region close to the edge of the laser spot and the average laser energy probably was insufficient to produce ripples at the lower edge. However, at the lower left part of the image parallel lines are faintly delineated. A profile taken from the lower to the upper end of the line traced in the image reveals an increase in the ripple amplitude. The FFT of the image shows two intense short arcs which are part of two circles that can be completed with the much fainter arcs close to the origin. The spacing measured in the profile is 153 nm, in very good agreement with equation 3.1. The value of $|\boldsymbol{q}_2|$ derived from the FFT also gives a spacing value in good agreement with this figure. Several profiles across the faint region enclosed by the rectangle in Figure 3.23 are presented in Figure 3.24. They show that the roughness in this region follows the same pattern as that of the ripples further up but only very shallow depressions with an average depth of 0.7 nm can be resolved. The profiles B and C across the holes show that the material removed from them has accumulated at both sides next to them. Figure 3.23 thus suggests that the propagation of the ripples ahead of the already developed structure took place first by the formation of faint grooves followed by the production of elongated holes, and finally by the coalescence of the holes forming the characteristic grated structure. Moreover, due to the nanosecond processing time most probably silicon was displaced while in the melted state, consistent with other observations (see for instance Figure 3.22).

Nanoripples with a line spacing following equation 3.1 were the only nanostructures formed using polarized light. No ripples were found with a spacing that obeys other than equation 3.1. Defective structures as that shown in Figure 3.20 and 3.21 were very often

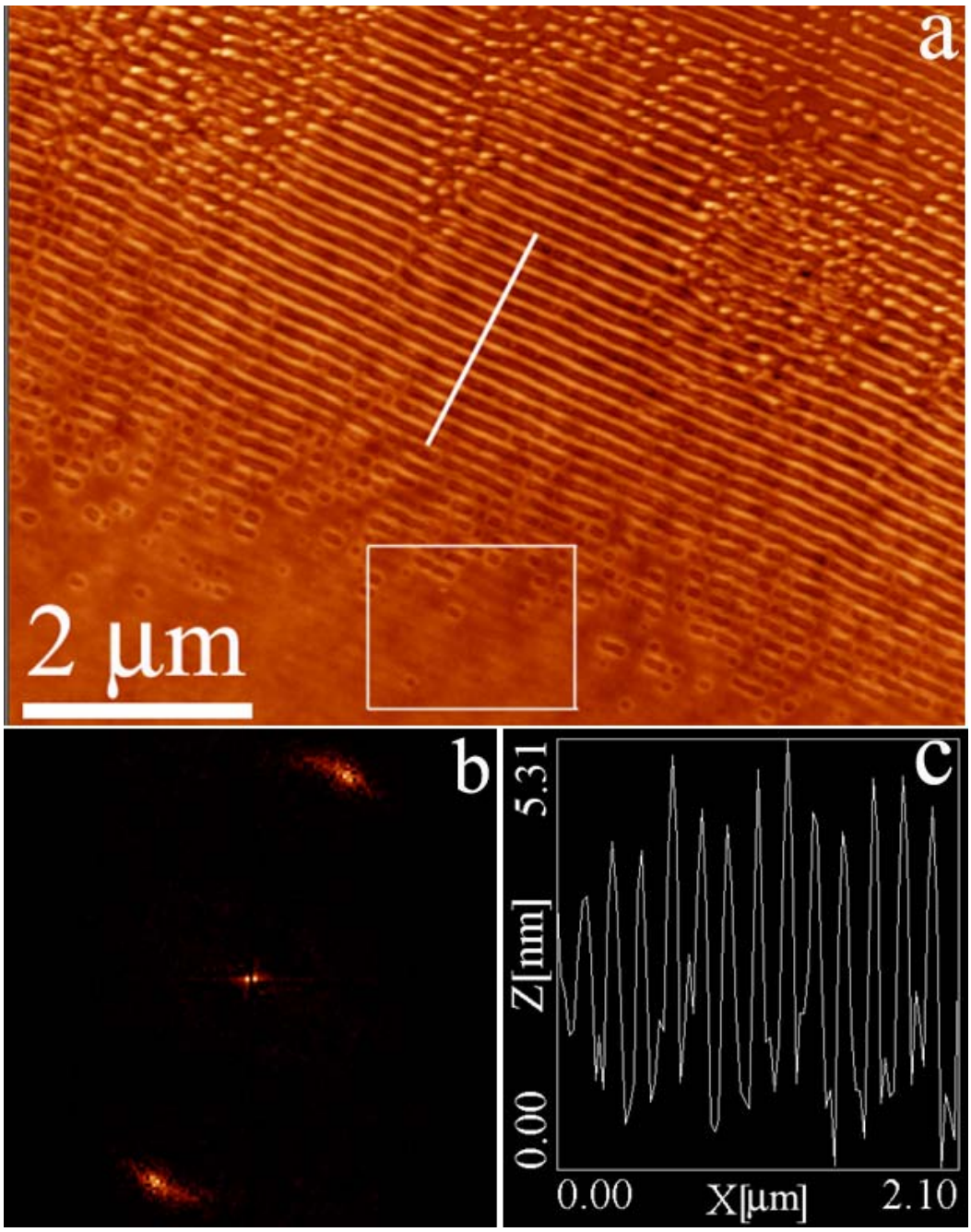

Figure 3.23 AFM image of sample irradiated with 2000 pulses of a p-polarized single beam at an incident angle of 38.5˚. Laser fluence: 0.7 J/cm^2. (a) 2-D AFM image. (b) FFT of the image showing two intense short arcs which are part of two circles that can be completed with the much fainter arcs close to the origin. A vector from the origin to any of the strong spots is proportional to the magnitude of the vector $\boldsymbol{q}_2$ (Figure 1.23). (c) Profile from the lower to upper end along line shown in image. Notice the increase in the ripple amplitude. Measured spacing is 153 nm, in very good agreement with equation 3.1 for Λ_2. This spacing agrees with the value of $|\boldsymbol{q}_2|$ derived from the FFT.

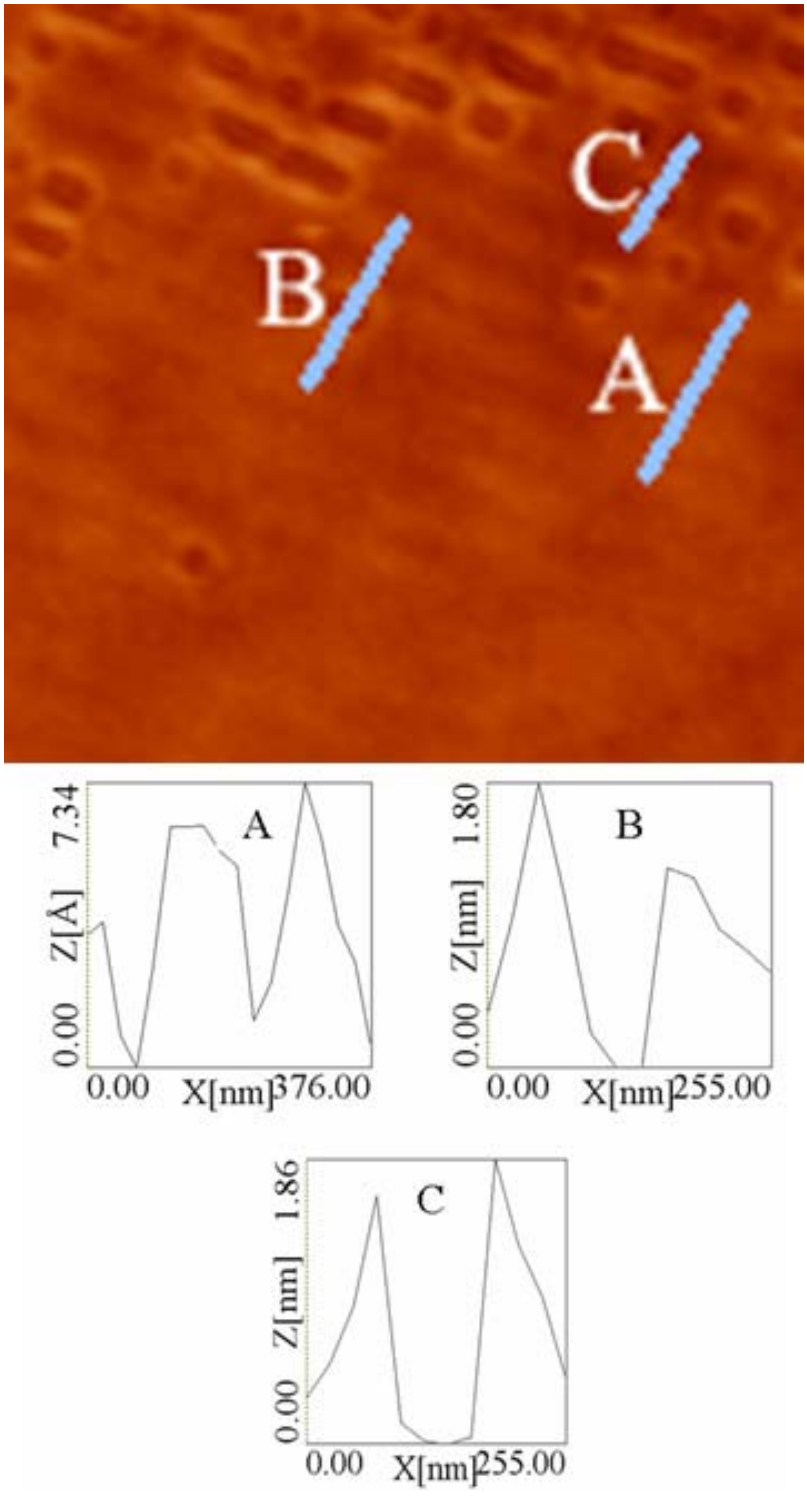

Figure 3.24 Magnified image of the region enclosed by a rectangle in Figure 3.23. This region reveals the propagation of ripples (downward in the figure) from the region of fully developed ripples. The three profiles show ripple evolution at three different stages characterized by the groove depth (Notice different scale in the ordinate of A).

encountered although in some cases the ripple structure extended a few hundred microns without defects.

3.3 Formation of LIPSS by Illumination using a Lloyd's Mirror Configuration

A Lloyd's mirror arrangement was installed to produce modulated structures using a two-beam irradiation. This system consists of a sample holder with an attached mirror so that mirror and substrate are in contact along an edge which is set perpendicular to the two surface normals, as depicted in Figure 3.25. Both mirror and substrate are illuminated by the same laser beam. The substrate is thus irradiated with two beams at the same time, the incident beam and the beam reflected by the mirror. The angle of incidence for both beams is the same but they are on opposite sides of the surface normal, in the same plane of incidence. If the beam had sufficient spatial and temporal coherency an interference pattern between the two beams should have developed. The modulated intensity that results from this interference pattern would have a wavelength:

$$\Lambda_{interf} = \frac{\lambda}{2\sin\theta_i} \qquad 3.2$$

This is possibly the simplest system that can be set to produce an interference pattern in the substrate [207].

The 248 nm excimer laser source used in these experiments has a very short coherency length (<80 μm). For this reason, a narrow aperture was located at the focal point where the beam was shaped as a fairly small football prior to its expansion. In addition, owing to the pulsating nature of this source, the temporal coherency is relatively poor as well. The mirror/substrate pair was set in two orientations relative to

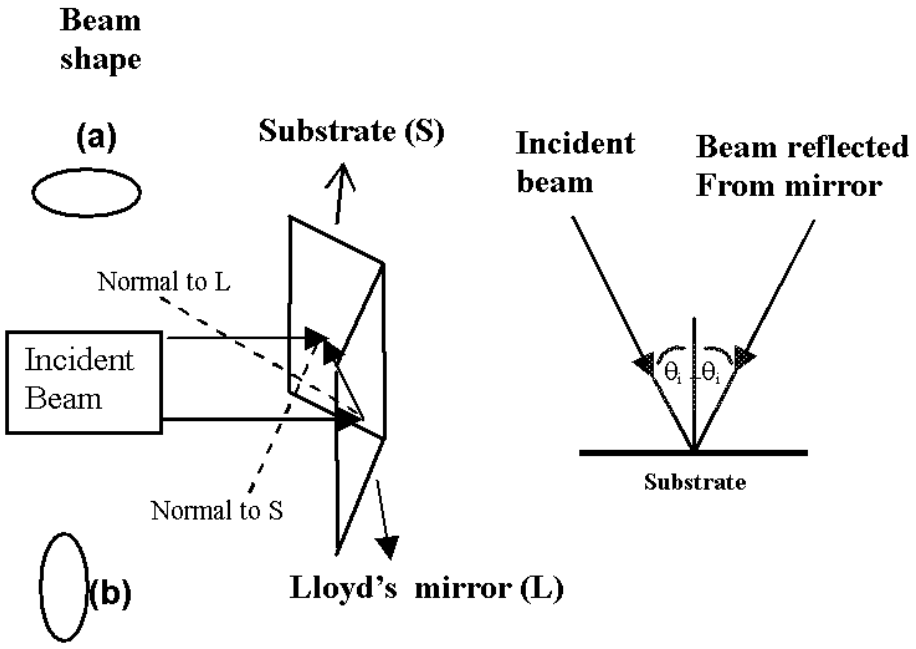

(A)

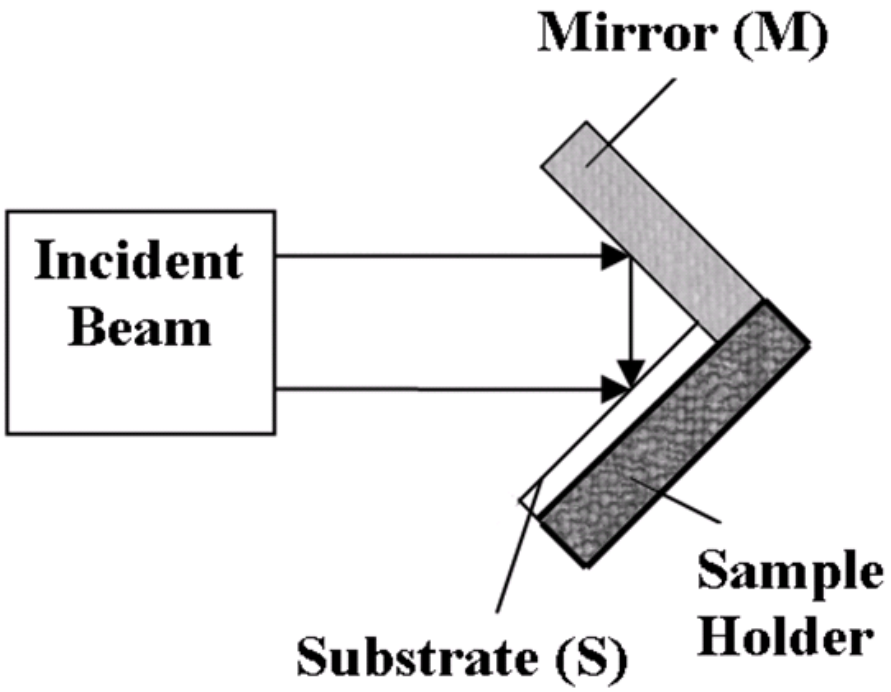

(B)

Figure 3.25 (a) Schematics of the two orientations of the beam shape for a Lloyd's mirror configuration: (a)—Horizontal; (b)—Vertical. (b) Cross-section of the Lloyd's mirror. Notice both substrate and mirror in the experiments are made of smooth silicon wafer.

the direction of maximum diameter of the beam, either parallel (a) or normal (b) to this direction. Owing to the poor spectral and temporal coherency of the source, an interference pattern described by equation 3.2 was only produced when the beam was directed as in (a) ('horizontal') in Figure 3.25A, and in a region very close to the edge. This can only be attributed to the laser characteristics. The most remarkable consequence of using this arrangement was that ripple formation was greatly enhanced in general, notwithstanding the absence of an interference pattern due to the mirror.

3.3.1 LIPSS Formation by Two-Beam Illumination with p-Polarized Light using Lloyd's Mirror Configuration

Similar to the single-beam illumination setting, s-polarized light failed to induce ripple formation under Lloyd's mirror configuration. However, p-polarized light is able to form LIPSS under Lloyd's mirror configuration. Figure 3.26 shows a single set of ripples produced using p-polarized light. This grating is remarkably straight and exhibits a nearly sinusoidal profile, as can be seen in Figure 3.26b. The ripple spacing is 310 nm, obtained as an average over 15 ripples. This spacing is closely fitted using

$$\Lambda_3 = \frac{\lambda}{\cos\theta_i} \qquad 3.3$$

which can be derived substituting equation 1.13 for $\boldsymbol{k}^{s,a}_{//}$ in equation 1.12. For the angle $\theta_i = 33°$ used in this experiment, equation 3.5 gives $\Lambda_3 = 296$ nm which is within <5% of the measured spacing. The FFT of the surface relief (Figure 3.26d) shows two bright

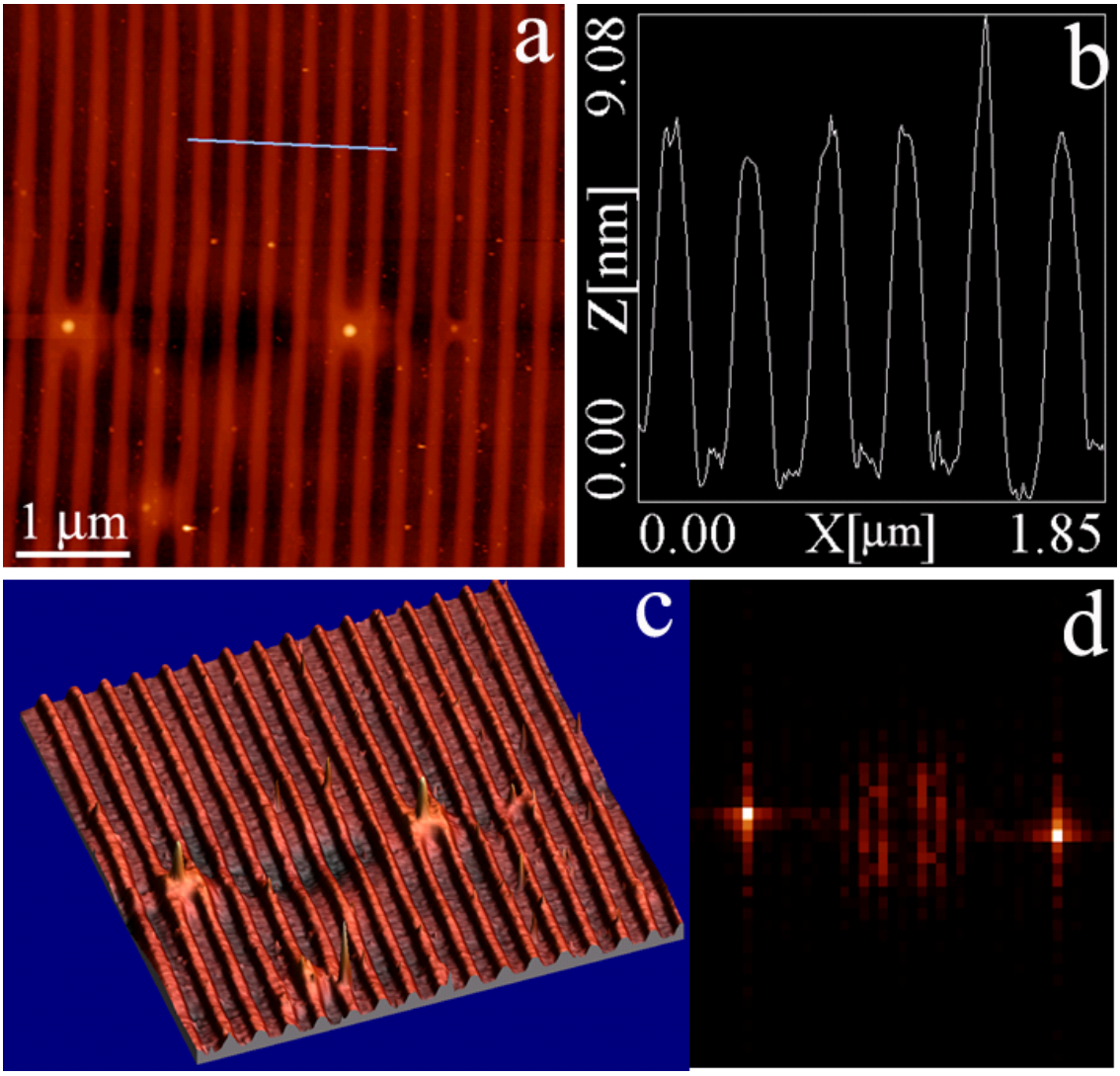

Figure 3.26 Ripple structure obtained after 1000 laser pulses using a Lloyd's mirror; edge orientation relative to beam (horizontal) is illustrated in Figure 3.25, (a) 2-D AFM image showing the surface morphology after irradiation by p-polarized light incident at an angle of 33°. (b) Profile from trace marked on the AFM image. (c) 3-D AFM image. (d) FFT of the AFM image. Ripple spacing derived from FFT is 310 nm.

spots whose separation can then be related to the length of the vector $\boldsymbol{q}_3$ in Figure 1.23. From the 3-D AFM image (Figure 3.26c) and the profile along the traced line, we noticed that there are no sub-ripples between the dominant ripples. This is a big difference between the cosine ripples and the sine ripples.

Figure 3.27 is another AFM image taken at higher magnification on the same sample but in a different region. As mentioned before, in the Lloyd's mirror system used here, both the substrate and the mirror are made of smooth silicon wafers. In theory, the substrate and the mirror are interchangeable. However, for the sample shown in both, Figure 3.27 and Figure 3.26, LIPSS can only be found on the substrate (side 1), where the incident angle is 33°. Assuming that the beams directed to the substrate and the mirror are parallel, then the incident angle on the mirror is 57° (side 2). The projection area on side 1 is proportional to cos 33° and the projection area on side 2 is proportional to cos 57°, so for the same laser beam the energy density on side 1 is larger than that on side 2. This may explain why the LIPSS can only be found on the substrate surface and not on the Lloyd's mirror surface. As mentioned in section 3.2, LIPSS formation is very sensitive to laser fluence. The ratio of energy density on substrate to energy density on mirror would be cos 33°/cos 57°. The measured laser fluence on side 1 is ~0.6 J/cm^2, so the corresponding laser fluence on side 2 is ~0.39 J/cm^2, which is below the LIPSS formation threshold. In this sense, in order to form LIPSS on both substrate and mirror, the laser fluence on both sides should be close to each other and in the range of LIPSS formation, which is between 0.6 and 1 J/cm^2. For example, when the angle of incidence is 45°, LIPSS have been found on both sides.

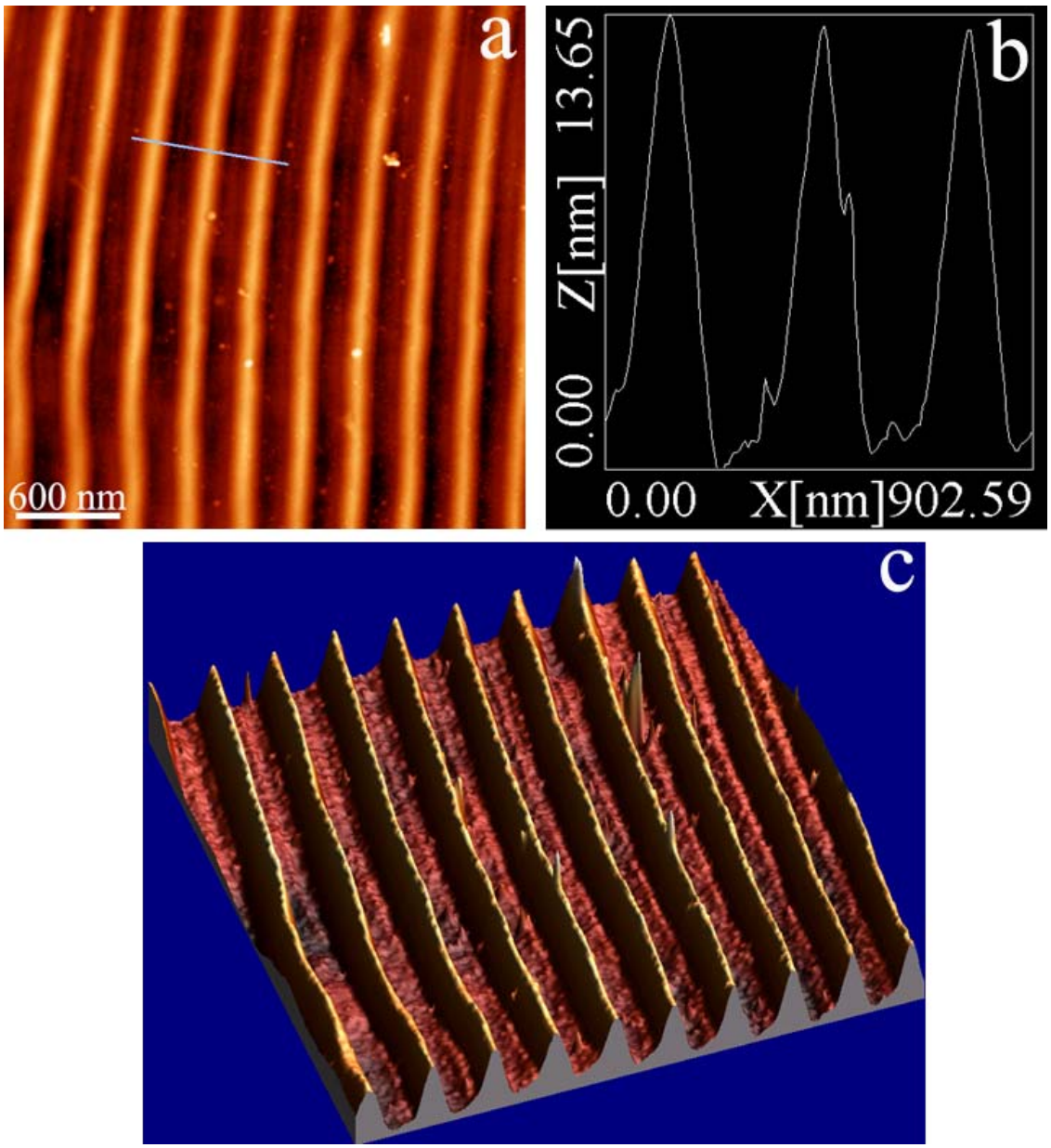

Figure 3.27 Ripple structure obtained under the same conditions as in sample shown in Figure 3.26. (a) 2-D AFM image showing the surface morphology after irradiation by p-polarized light incident at an angle of 33^{o}. (b) Profile from trace marked on the AFM image. (c) 3-D AFM image.

The 1-D cosine LIPSS have been observed by SEM as well. Figure 3.28 shows the extended ripples following equation 3.3. The image illustrates the straight lines parallel to each other without disturbance. SEM images taken at lower magnification show that the ripples produced by p-polarized laser light cover almost the whole laser irradiated region. No defects were found in the ripple periodicity.

2-D orthogonal ripples structures following both equations 3.2 and 3.3 are formed on the surface after p-polarized laser irradiation under Lloyd's mirror configuration. Figure 3.29 shows two orthogonal intercepting ripples. Arrow A in the figure is parallel to the cosine ripples and the orientation of arrow B is parallel to the interference pattern. The measured line spacings of both structures are 296 nm and 227 nm respectively, which are consistent with the calculated values at incident angle of 33˚.

LIPSS that follow equations 3.2 and 3.3 are the only two structures observed during irradiation with p-polarized laser light. However, other LIPSS have been observed under the same configuration by non-polarized light.

3.3.2 LIPSS Formation by Non-Polarized Laser Light under Lloyd's Mirror Configuration

3.3.2.1 Formation of Intercepting Ripples Patterns

Unlike the case of single beam illumination, non-polarized light also produced ripples. The most extraordinary structures are two sets of intercepting ripples. We found the following combinations of intercepting ripples: 1. Interference pattern that follows

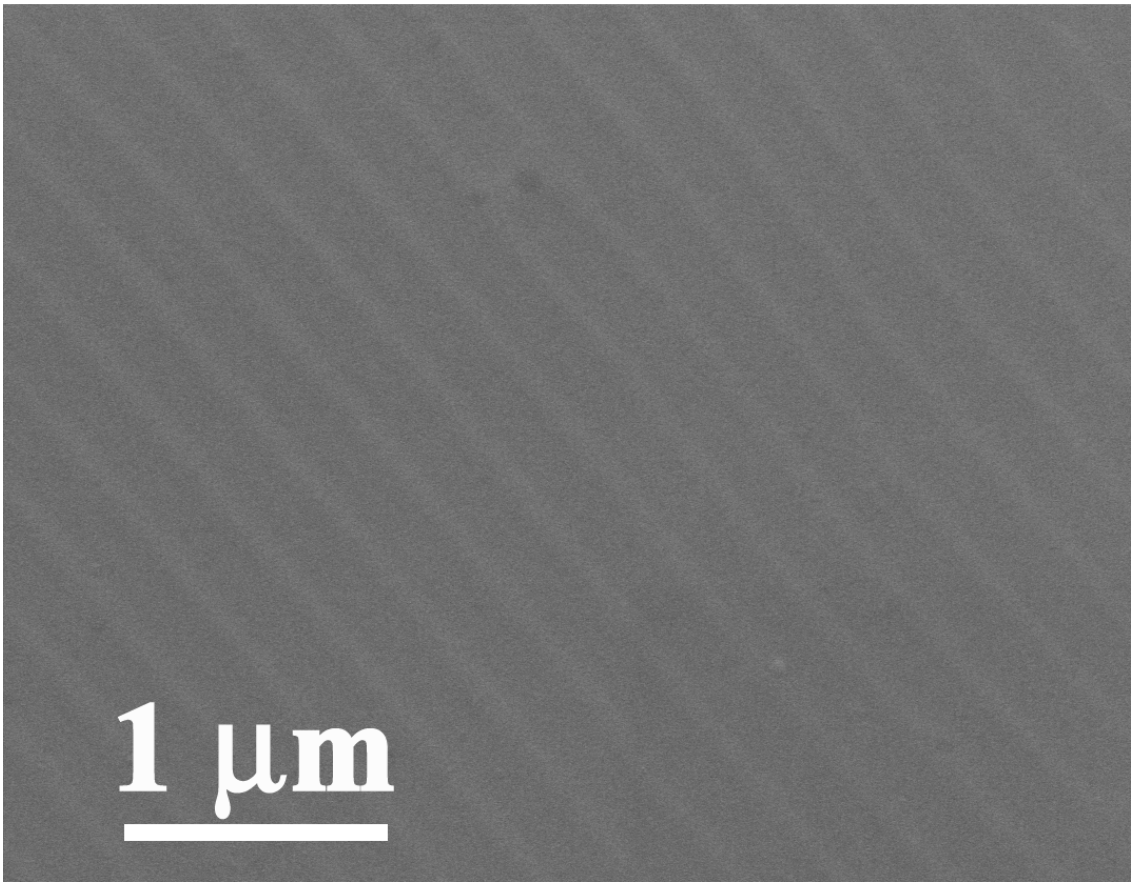

Figure 3.28 SEM image showing the ripple structure with a spacing following equation 3.3. The cosine LIPSS extended all over the laser irradiated region.

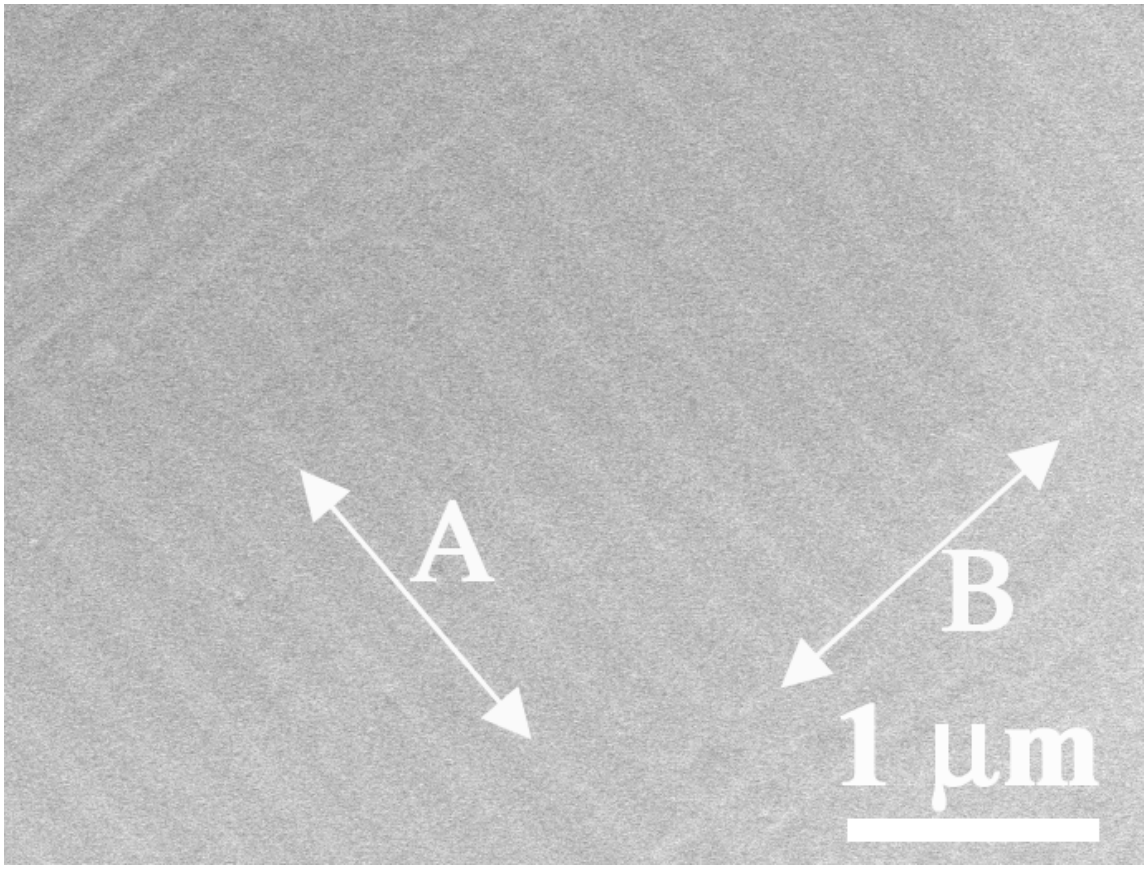

Figure 3.29 SEM image showing two orthogonal ripples following equations 3.2 and 3.3 respectively. Arrow A represents the cosine ripples, and arrow B represents the interference pattern. The measured line spacing between cosine ripples is ~296 nm, and that of the interference pattern is 227 nm, both are in good agreement with the equations.

equation 3.2 and cosine ripples following equation 3.3; 2. Cosine ripples that follow equation 3.3 and sine ripples following equation 3.1.

I. Combination of interference pattern and cosine ripples

Figure 3.30 is an SEM image of a region very close to the substrate/mirror edge after irradiating at θ_i=33°. The direction of the edge is indicated in the image with a double arrow, revealing that the orientation of the lines is well defined relative to the edge. The spacing of the set parallel to the edge is 212 nm, while the spacing of the set perpendicular to it is 296 nm. The latter is in excellent agreement with the value calculated using equation 3.3, while the other spacing is close to that calculated using equation 3.2 (228 nm), which corresponds to the spacing defined by the light interference pattern. In none of the remaining observations to be described, the ripples parallel to the substrate/mirror edge were related to the interference pattern described by equation 3.2.

II. Combination of ripples from different orientations

In many instances the intercepting ripples are orthogonal to each other, but in other cases they are not. In general, the grating equation establishes the relationship between ripple spacing Λ, the angle of incidence θ, and the angle α that the ripple wavevector makes with the surface projection of the light wavevector.

Using the cosine theorem it can be derived that,

$$\sin^2\theta + \left(\frac{\lambda}{\Lambda}\right)^2 - 2\left(\frac{\lambda}{\Lambda}\right)\sin\theta\cos\alpha - n^2 = 0$$

When ripples of two orientations are present on the surface, images from SEM or AFM allow us to determine the values of the two ripples' spacing, Λ_a and Λ_b, and the angle

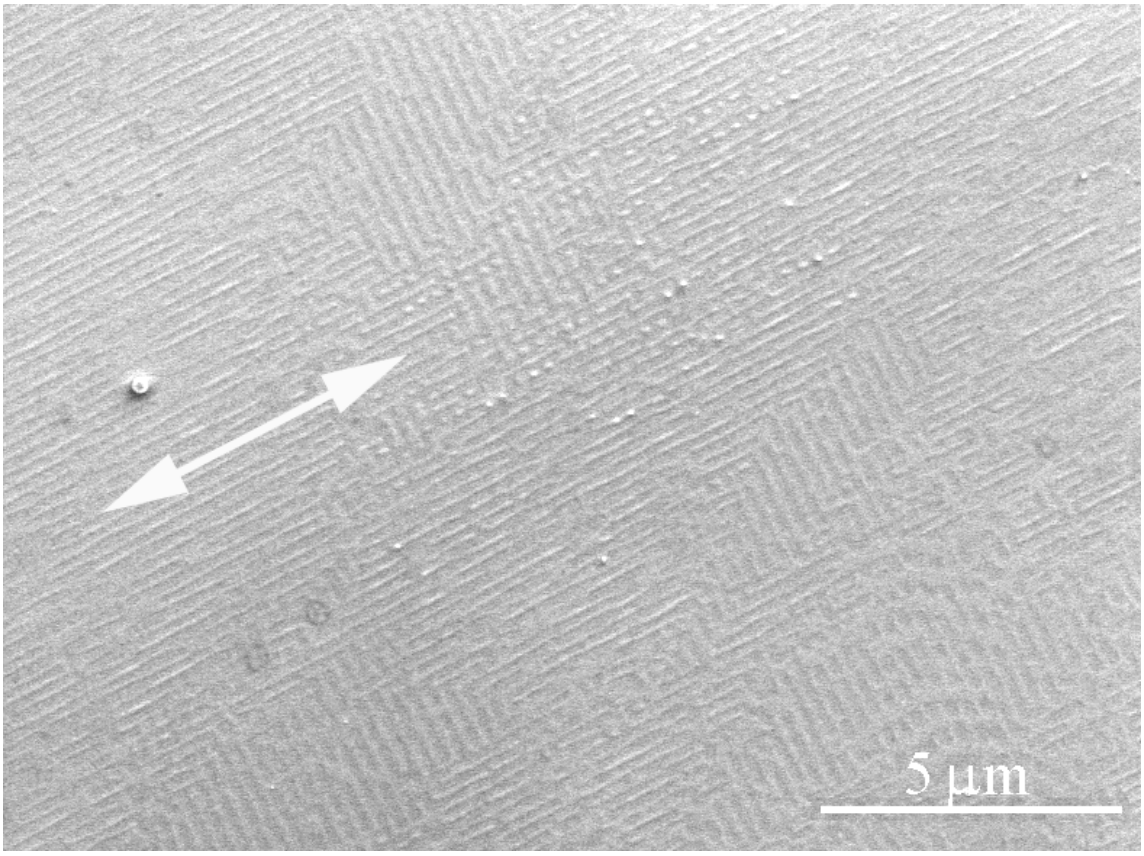

Figure 3.30 Ripples obtained after 1000 pulses using a Lloyd's mirror; configuration illustrated in Figure 3.25A-a. Non-polarized laser light incident at θ_i =33˚.

between them α_a-α_b. The angle of incidence can then be determined by α_a and α_b in such a way that the calculated α_a-α_b equals the measured α_a-α_b. For the case shown in the SEM images of Figure 3.31, α_a-α_b=56.5˚, Λ_a=1323 nm and Λ_b=413 nm, yielding a value of θ=66˚.

When this experiment was performed, the available setting did not allow an exact measurement of θ, but it was close to 70˚, which agrees with the value obtained from the SEM image. The AFM images (Figure 3.32) renders an angle of incidence of 64˚ that, within the error involved in the measurement, is consistent with the value obtained from the SEM image.

3.3.2.2 Formation of Two Different Kinds of Parallel Ripples

Ripples formed in the surface are not always intercepting with each other. Sometimes, ripples with same orientation but different line spacings have been observed. Figure 3.33 indicates such situation. Two different kinds of sine ripples, which follow Λ_1 and Λ_2 in equation 3.1 respectively, were formed in the same sample at an angle of incidence of 10˚. Figure 3.33 is the SEM image showing the "1-sinθ" ripples and Figure 3.34 is the AFM image describing the "1+sinθ" ripples. Both ripples are parallel to the mirror/substrate edge, but located in different regions. It is still unclear what determines the appearance of either ripple. It seems that the formation of "1+sinθ" ripples is very random, but the "1-sinθ" ripples can be found most of the time. According to equation 3.1, the line spacings for the sine ripples formed at an incident angle of 10˚ are Λ_1=300

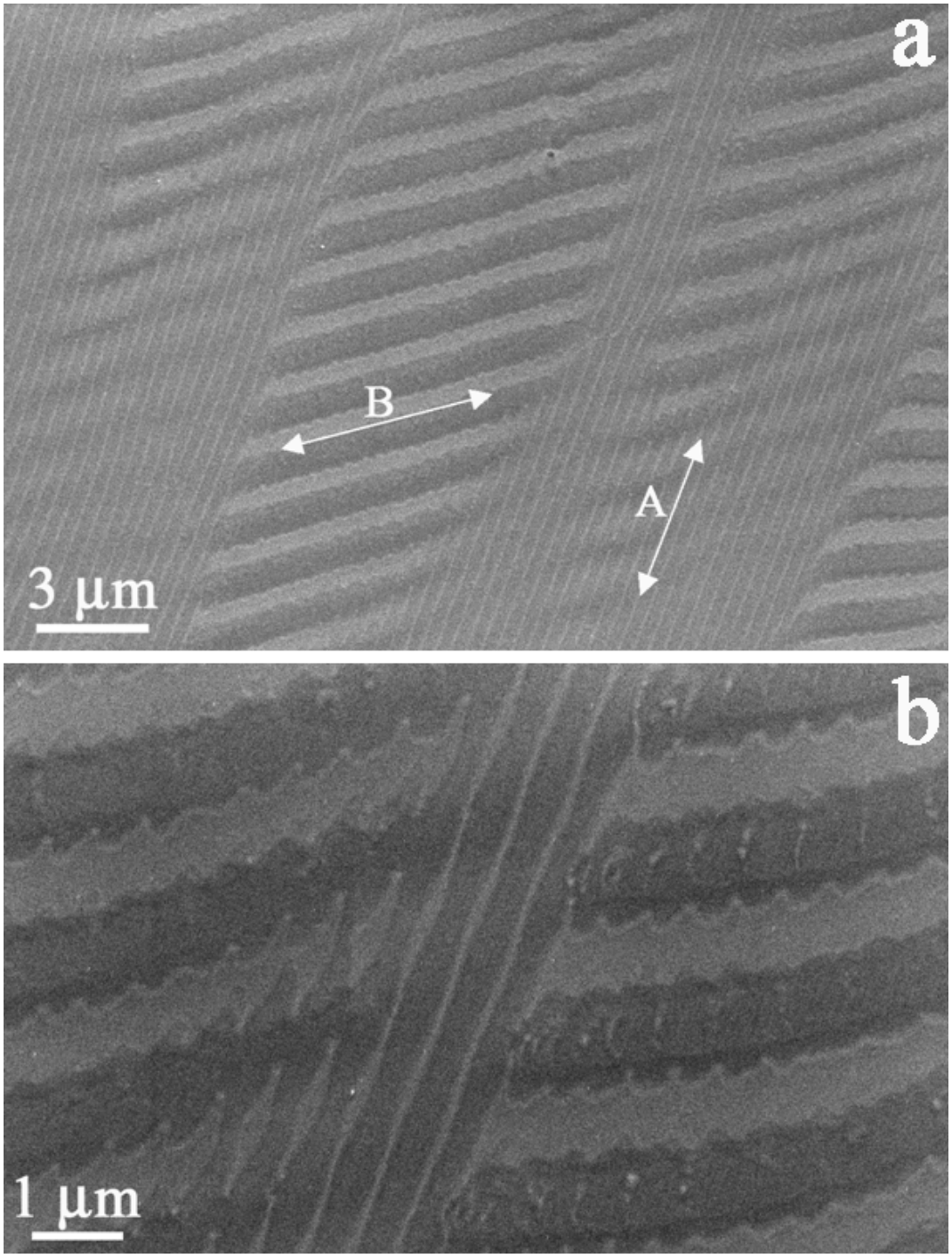

Figure 3.31 SEM images showing two kinds of ripples intercepting with each other on the sample surface irradiated with 1000 pulses by non-polarized laser beam using Lloyd's mirror. (a) Arrow A is parallel to the ripples whose line spacing is 413 nm and arrow B is parallel to the ripples with a line spacing of 1323 nm. (b) Higher magnification SEM image showing that the cosine ripples are separated into bundles by the other ripples.

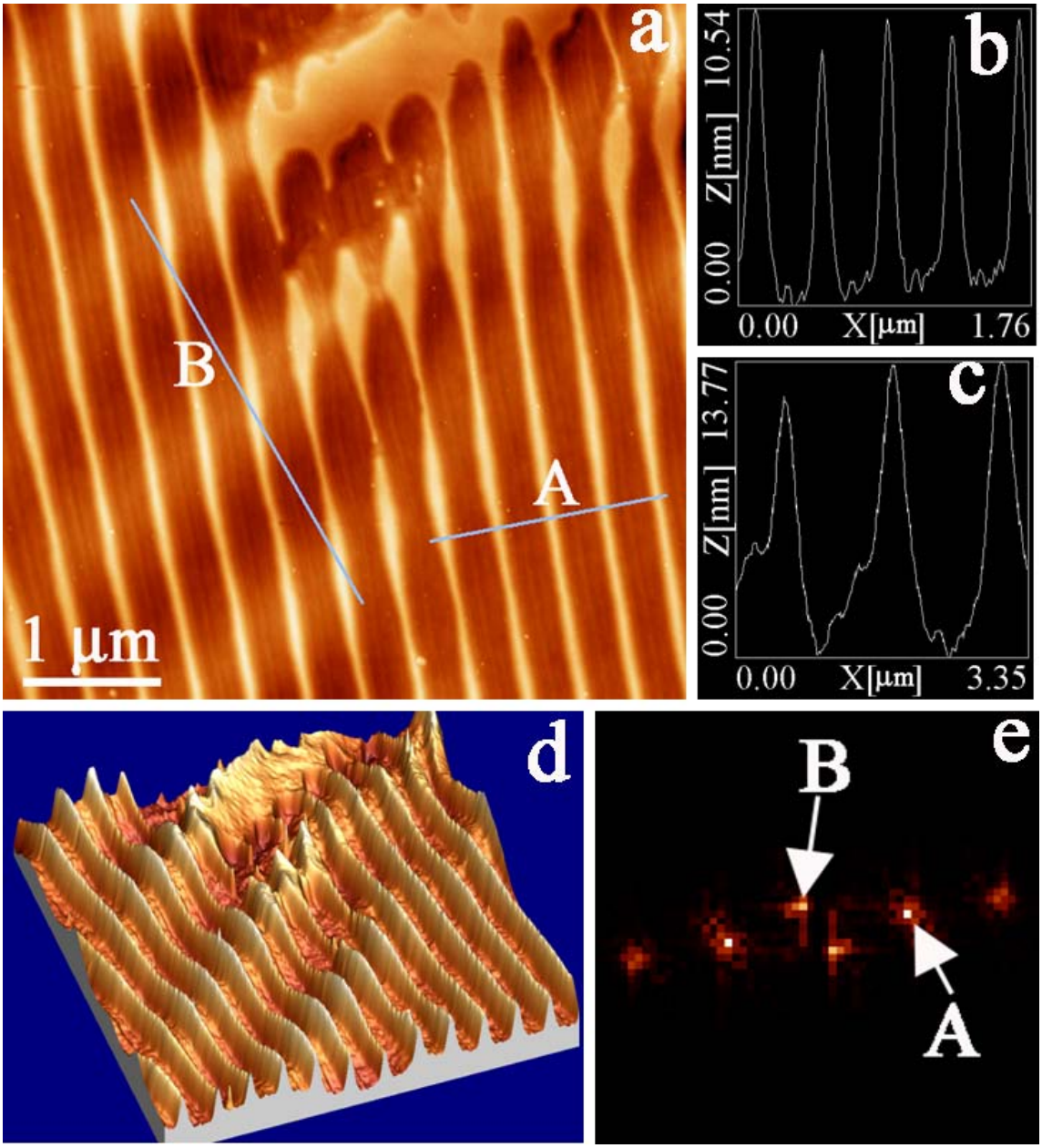

Figure 3.32 AFM image taken on the same sample as Figure 3.31. (a) 2-D top view. Trace line A is orthogonal to the cosine ripples and trace line B is normal to the other ripples. (b) Profile along line A marked in Figure a. (c) Profile along line B marked in Figure a. Notice the difference between the line spacings. (d) 3-D AFM image showing the interal relationship between the two ripples embedded on the surface. (e) FFT of the 2-D image. Point A represents the cosine ripples in reciprocal space, and point B represents the other ripples after fast Fourier transformation. Intercepting angle between these two ripples can be measured as well.

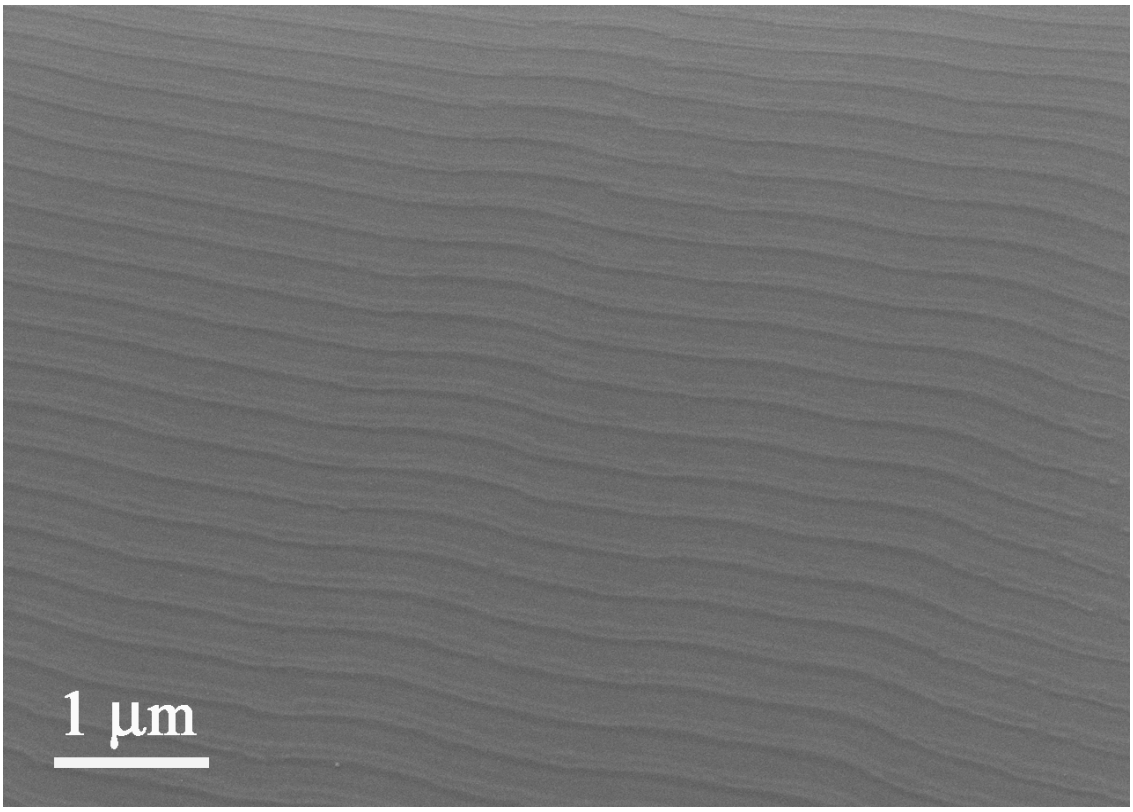

Figure 3.33 SEM image showing the ripple structures produced at an angle of incidence of 10˚ with 1000 non-polarized laser pulses under a Lloyd's mirror configuration. The ripples formed here follow equation 3.1 for Λ_1. Calculated and measured line spacings are 300 nm and 303 nm respectively.

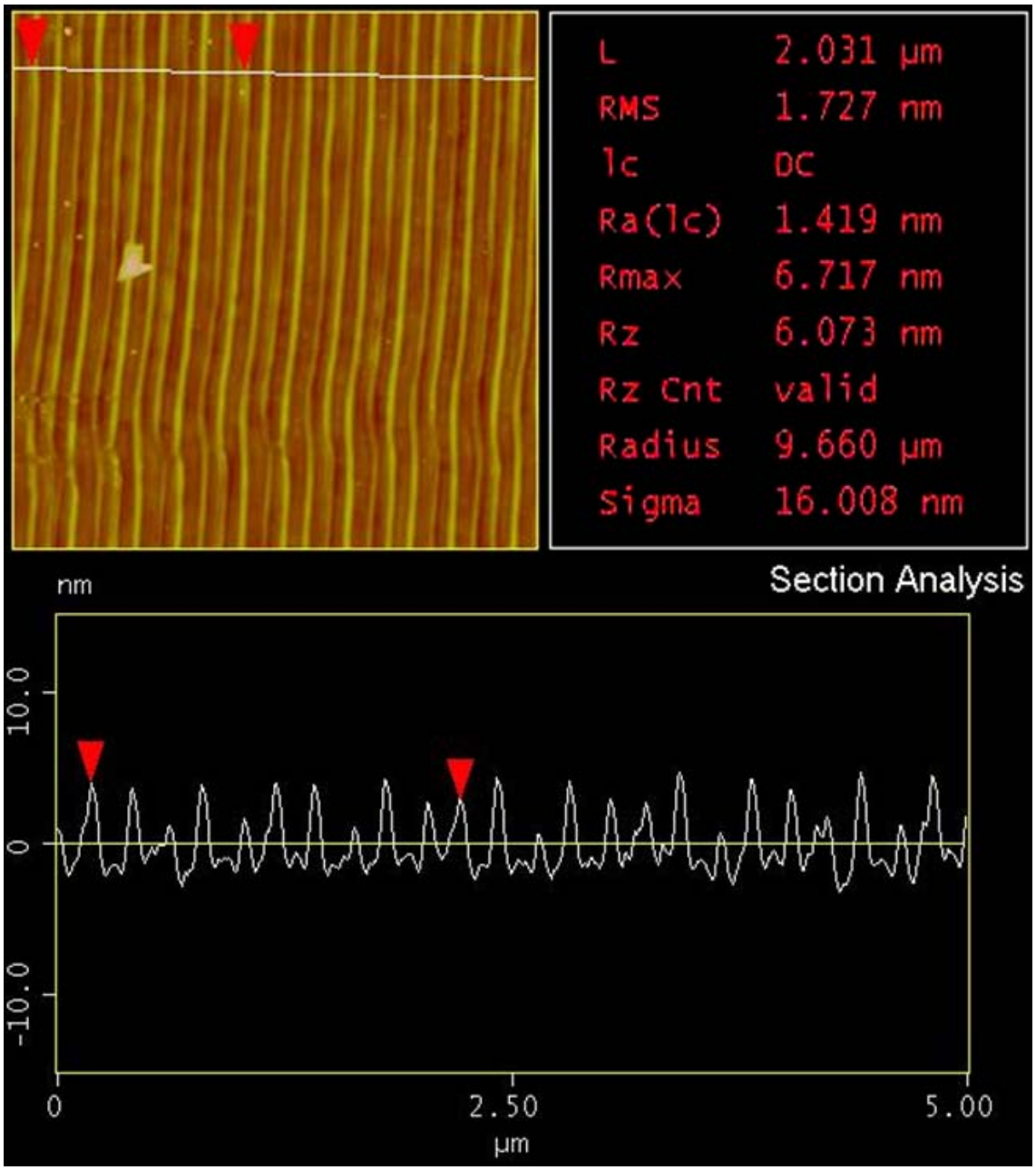

Figure 3.34 AFM image taken from a different region of the same sample as in Figure 3.33. The ripple structures shown here follow equation 3.1 with Λ_2. Lower part of the image is the profile of the trace line covering ten ripples in the 2-D AFM image. From the upper right chart, the measured line spacing is 203 nm, while the calculated value is 211 nm.

nm and Λ_2=211.3 nm respectively. Those values are very close to the measurements from the SEM and AFM images, which are 303 nm and 203 nm.

Another example is shown in Figure 3.35, where two sine ripples coexist. The sample was irradiated by non-polarized laser light under Lloyd's mirror configuration at an angle of incidence of 22˚. Arrow A represents the ripples that follow Λ_2 in equation 3.1, and arrow B represents Λ_1 ripples (equation 3.1). The calculated and measured line spacings for ripple "A" are 180 nm and 182 nm respectively, and calculated and measured line spacings for ripple "B" are 397 nm and 390 nm.

3.3.2.3 Formation of 1-D Gratings

Not only 2-D gratings have been formed by non-polarized light, 1-D gratings, especially those follow equation 3.3 have also been observed in the sample irradiated using Lloyd's mirror configuration. The 1-D straight cosine ripples extend over a large area without any disruption or dislocations. They form at both low and high angles of incidence.

Figure 3.36 shows the AFM image of cosine 1-D gratings produced at an angle of incidence of 56˚ after 1000 non-polarized laser pulses. The line spacing of the ripples measured from the profile in Figure 3.36b is 448 nm, while the calculation from equation 3.3 gives a value of 443 nm. FFT in Figure 3.36d indicates clearly that the only pattern found in the AFM image is the cosine ripples running parallel to each other. 3-D AFM image in Figure 3.36c makes it clear that no sub-ripples exist between the dominant ripples.

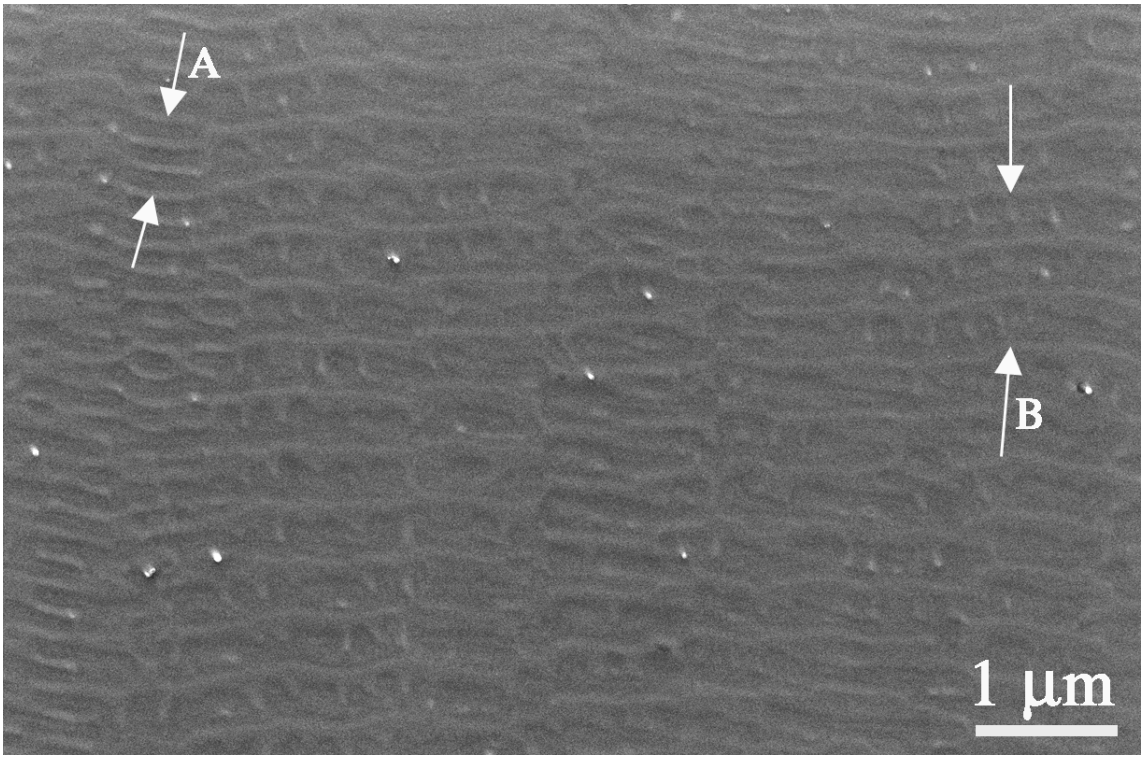

Figure 3.35 SEM image of sample irradiated by non-polarized laser light at an incident angle of 22˚ using the Lloyd's mirror. Two kinds of sine ripples following equation 3.1 can be found on the surface. Arrow A points to "1+sinθ" ripples and arrow B points to "1-sinθ" ripples. The calculated and measured values for "1+sinθ" ripples are 180 nm and 182 nm respectively. And the corresponding values for "1-sinθ" ripples are 397 nm and 390 nm.

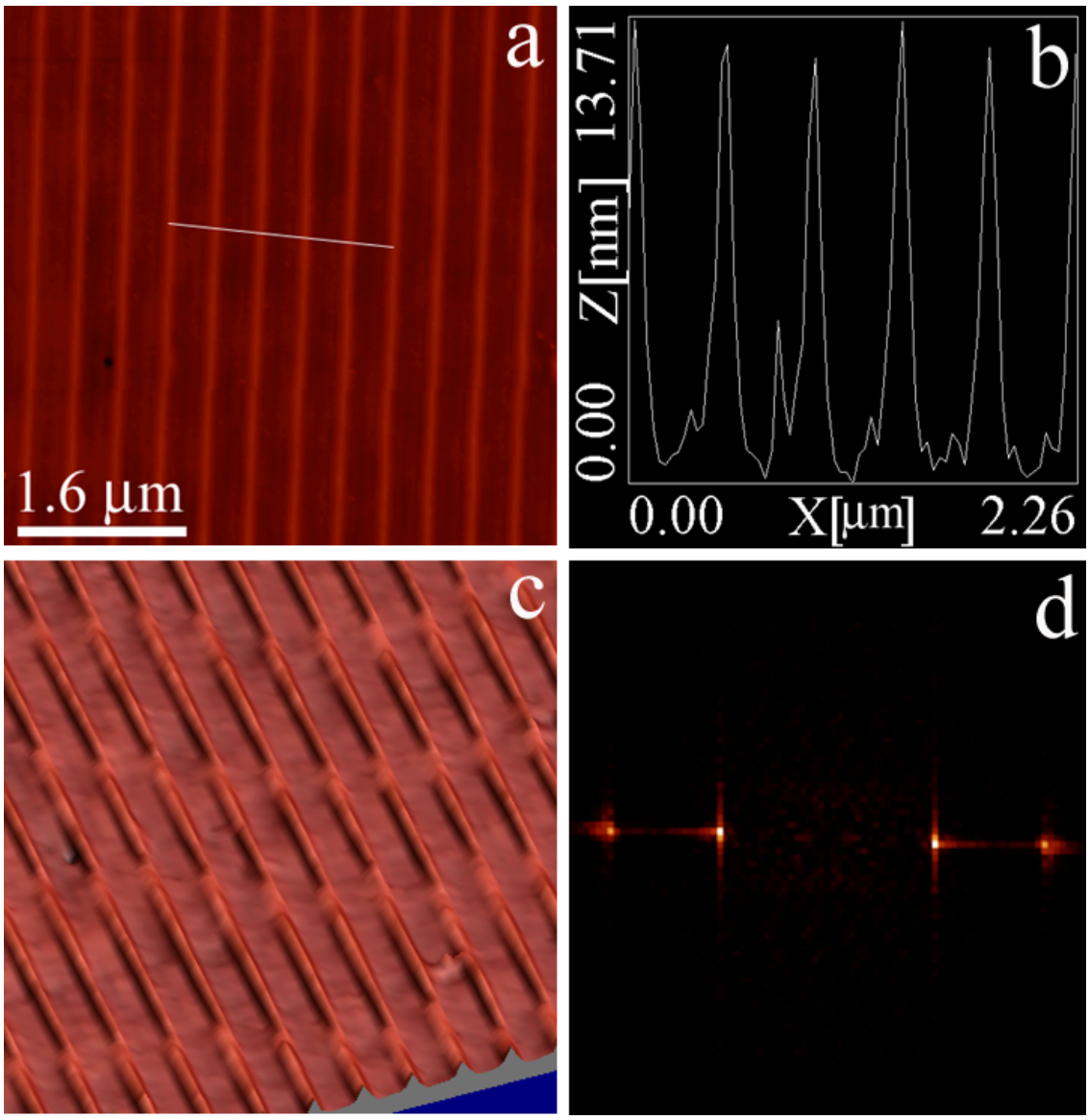

Figure 3.36 AFM image showing the straight cosine ripples produced by non-polarized laser light after 1000 pulses. The angle of incidence is ~56˚. (a) 2-D AFM image. Trace line covers five ripples. (b) The profile of the trace line in Figure a. The measured line spacing is ~448 nm. (c) 3-D AFM image. (d) FFT of the AFM image.

When the angle of incidence decreases to 42˚, as we can expect, the line spacing between the ripples decreases accordingly. Figure 3.37 shows the surface morphology of sample irradiated under the same conditions as the sample shown in Figure 3.36 but at a lower incident angle. Figure 3.37a is the top view of the sample surface, and profile of the trace line B covering ten ripples is shown in Figure 3.37b. Trace line A coves only one single ripple, and its profile together with several others are shown in Figure 3.40. As shown in Figure 3.37b, the measured line spacing is 335 nm. The calculated value for an incident angle of 42˚ is 333 nm. Figure 3.37c is the surface pattern's FFT, which shows how the morphology looks like in the reciprocal space. Once again, FFT indicates that there is only one orientation in the surface, which is normal to the mirror/substrate edge. And this is the case for all the cosine ripples produced in the surface.

Figure 3.38 is an SEM image indicating the straight cosine ripples extend in a large surface area. The ripples were produced after 800 pulses at an energy density of 0.8 J/cm^2. The angle of incidence for this sample is 40˚. Measurement from the image gives a line spacing value of 319 nm.

Finally, in order to study how the cosine ripples change as a function of the angle of incidence, we put the Lloyd's mirror in such a position that the incident angle is 36˚. Figure 3.39 shows the AFM image of sample surface irradiated after 1000 pulses. The measured and calculated values for the line spacings are 305 nm and 307 nm respectively.

Figure 3.40 compares the width of the cosine ripples as a function of the angle of incidence. Figure 3.40a shows the profile of a single ripple shown in Figure 3.36, and the width of this ripple is 125 nm. Similarly, Figure 3.40b and 3.40c represent the profiles of

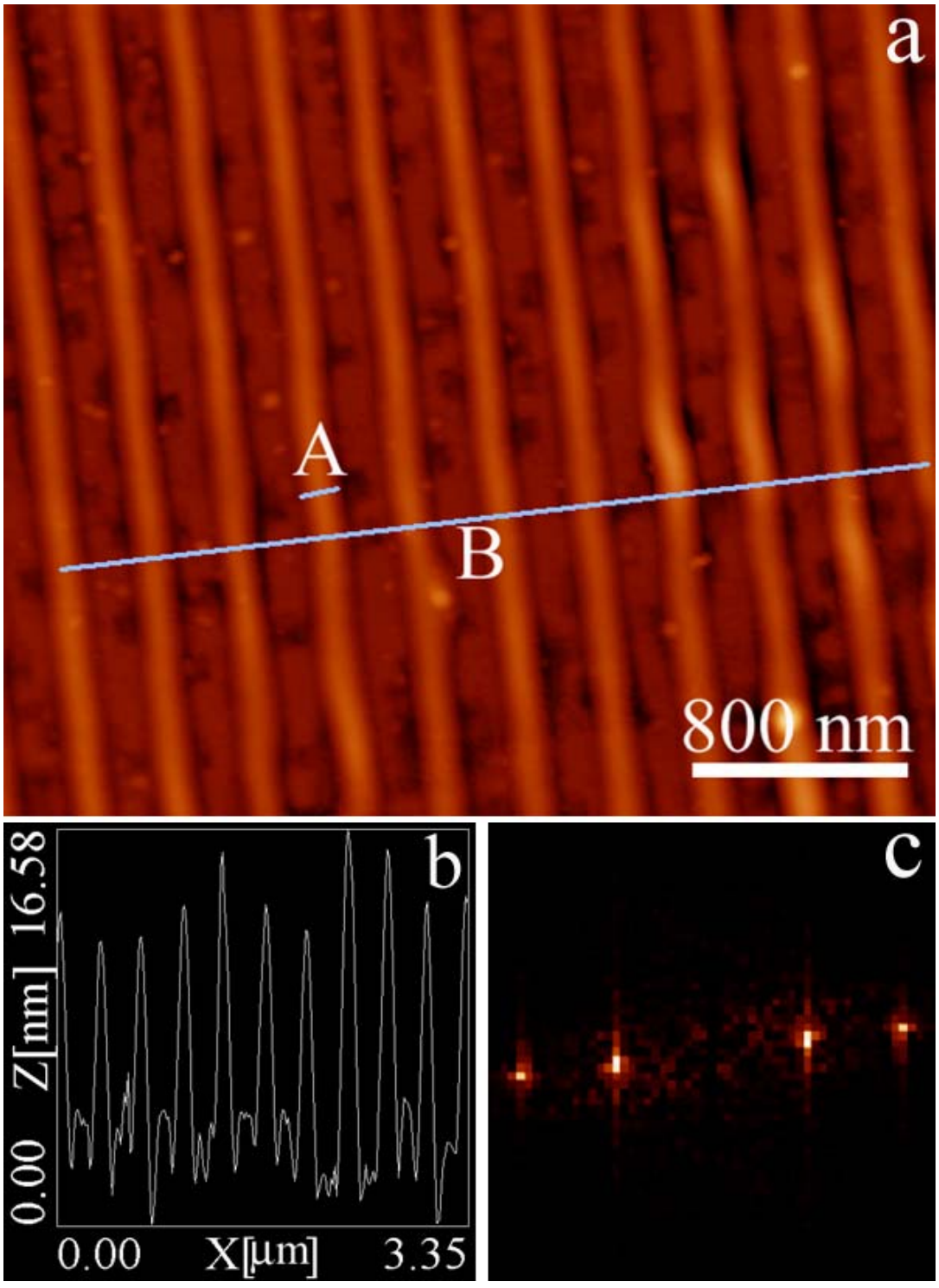

Figure 3.37 AFM image showing the straight cosine ripples produced by non-polarized laser light after 1000 pulses. The angle of incidence is ~42˚. (a) 2-D AFM image. Trace line A covers a single ripple and B covers ten ripples. (b) The profile of the trace line B in Figure a. The measured line spacing is ~335 nm. (c) FFT of the AFM image.

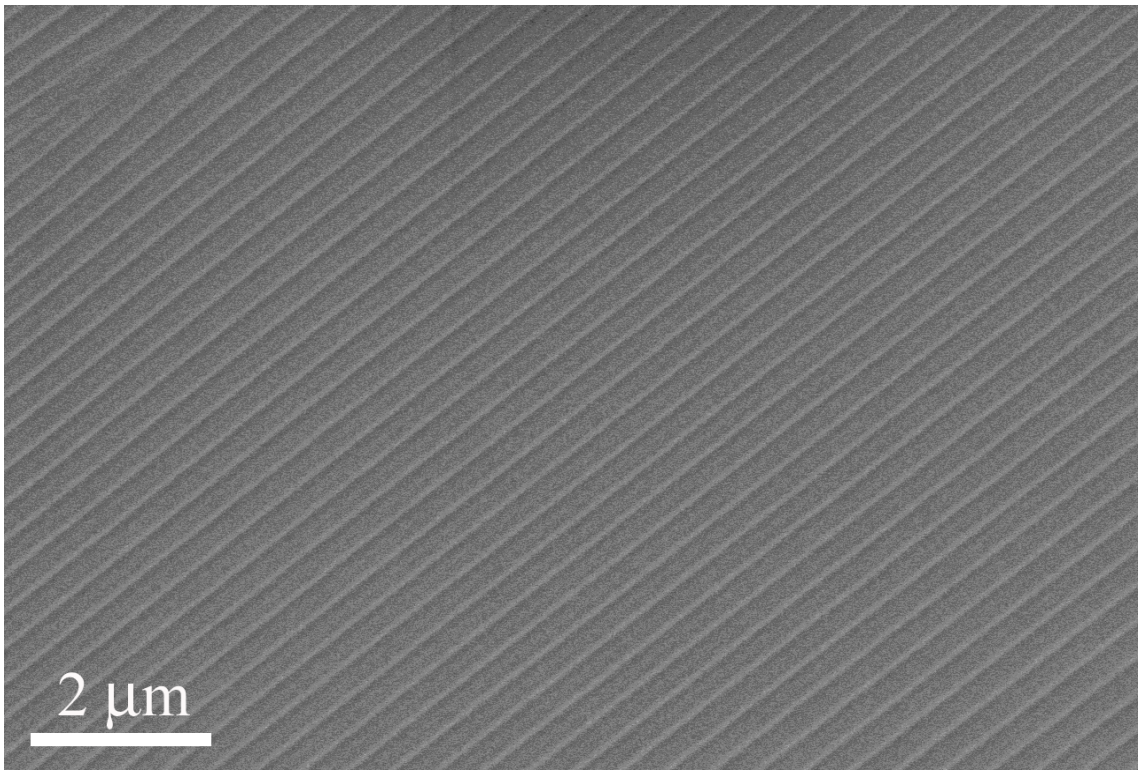

Figure 3.38 SEM image showing straight cosine ripples running normal to the mirror/substrate edge of the Lloyd's mirror configuration. The angle of incidence is ~40˚, and the measured line spacing from the image is ~319 nm. From the image we can see that the ripple structure covers the entire surface area.

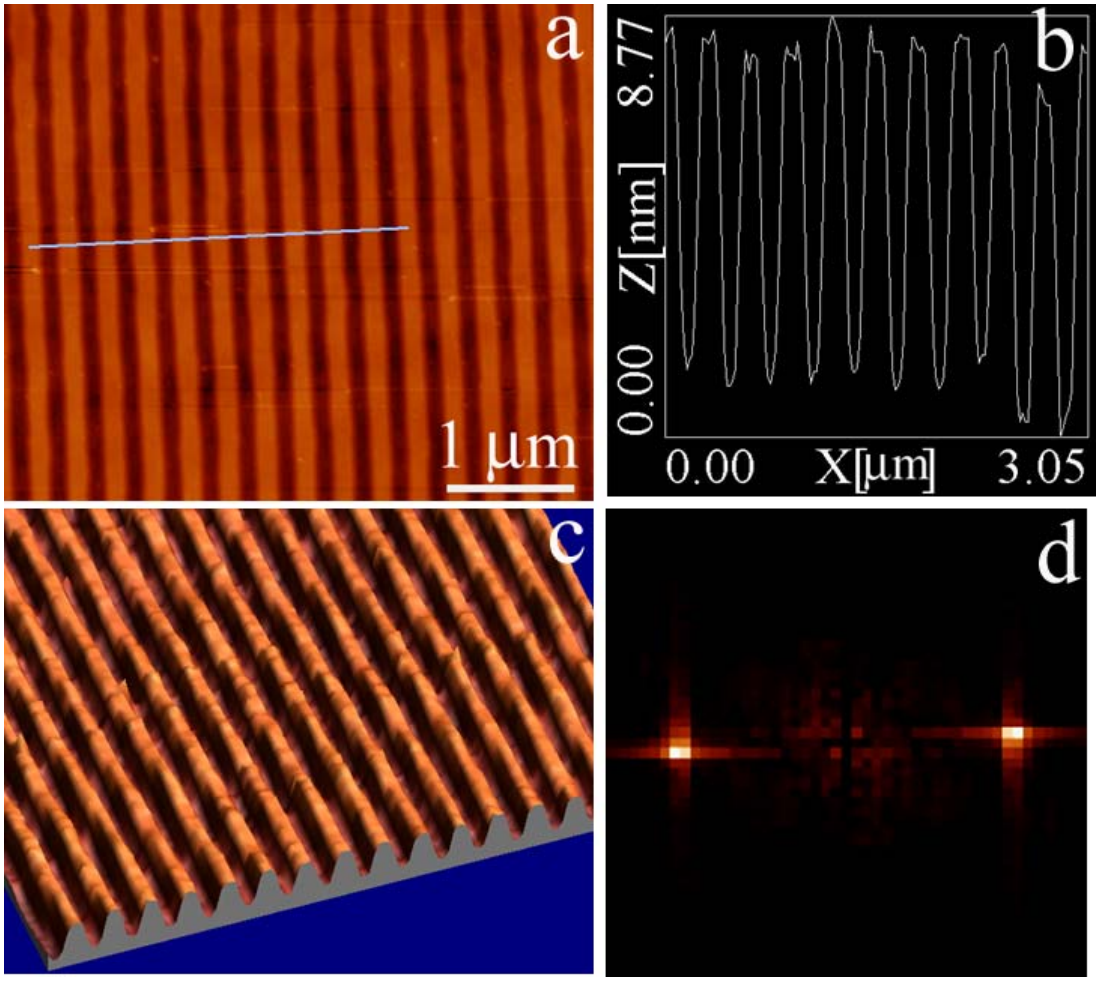

Figure 3.39 AFM image showing the straight cosine ripples produced by non-polarized laser light after 1000 pulses. The angle of incidence is ~36˚. (a) 2-D AFM image. Trace line covers ten ripples. (b) The profile of the trace line in Figure a. The measured line spacing is ~305 nm. (c) 3-D AFM image. (d) FFT of the AFM image.

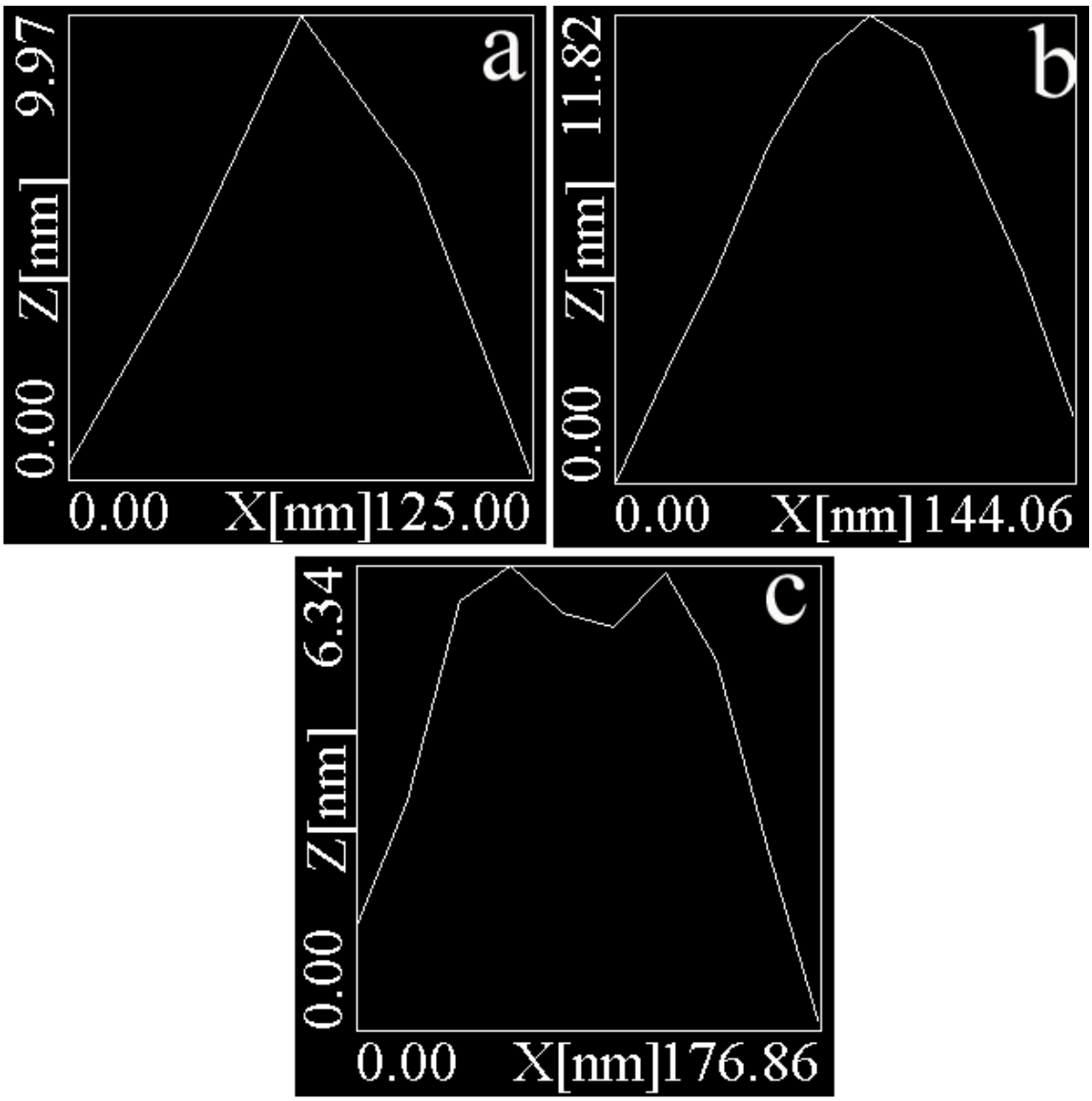

Figure 3.40 Profiles of single ripples from samples irradiated by non-polarized laser light at different angles of incidence using a Lloyd's mirror. (a) Profile from sample shown in Figure 3.36 (θ=56˚); the ripple width is 125 nm. (b) Profile from sample shown in Figure 3.37 (θ=42˚), with a width of 144 nm. (c) Profile from sample shown in Figure 3.39 (θ=36˚), whose ripple width is 177 nm. Notice that the width of the cosine ripples increases as the angle of incidence decreases.

ripples shown in Figure 3.37 and Figure 3.39 respectively. The widths of these two ripples are 144 nm and 177 nm. So there is a clear tendency for the ripple's width to grow as the angle of incidence decreases, i.e. the line spacing decreases as well. Another interesting phenomenon is that when the incident angle decreases, the crest of the ripples becomes flatter. Figure 3.40a shows a very sharp crest, while the top part of the ripples shown in Figure 3.40c is much flatter than Figure 3.40a and b.

Table 3.2 summarizes the line spacing and width of the cosine ripples as a function of the angle of incidence.

3.3.2.4 Formation of *Random* Gratings

So far we have illustrated that the non-polarized light together with Lloyd's mirror configuration can produce 1-D and 2-D gratings. Four different kinds of ripples whose line spacings follow equation 3.1, 3.2 and 3.3 respectively have been found: "1+sinθ" and "1-sinθ" ripples, interference pattern, and cosine ripples. The orientations of the first three ripples are parallel to the mirror/substrate edge, and the only one that runs normal to the edge is the cosine ripples. Images exhibiting an apparently more irregular pattern than the commonly observed single or double gratings were seen in some instances. Thus, as shown in Figure 3.41a, the ripple contours are bent, kinked, and rotated, and in some places describe arcs. This complex structure can be interpreted more clearly through the FFT pattern, presented in Figure 3.41b. This transform image is easily recognized as part of the q-space depicted in Figure 1.23, the arcs of the circumferences enclosing the intersecting areas of the two circles, where the distance between the

Table 3.2 Line spacing of cosine ripples produced by non-polarized laser light vs. angle of incidence

Angle of incidence	Measured line spacing (nm)	Calculated line spacing (nm)	Difference between measurement and calculation (%)	Width of the cosine ripple (nm)
56˚	448	443	1.1	125
42˚	335	333	0.6	144
40˚	319	324	1.6	N/A
36˚	305	307	0.7	177

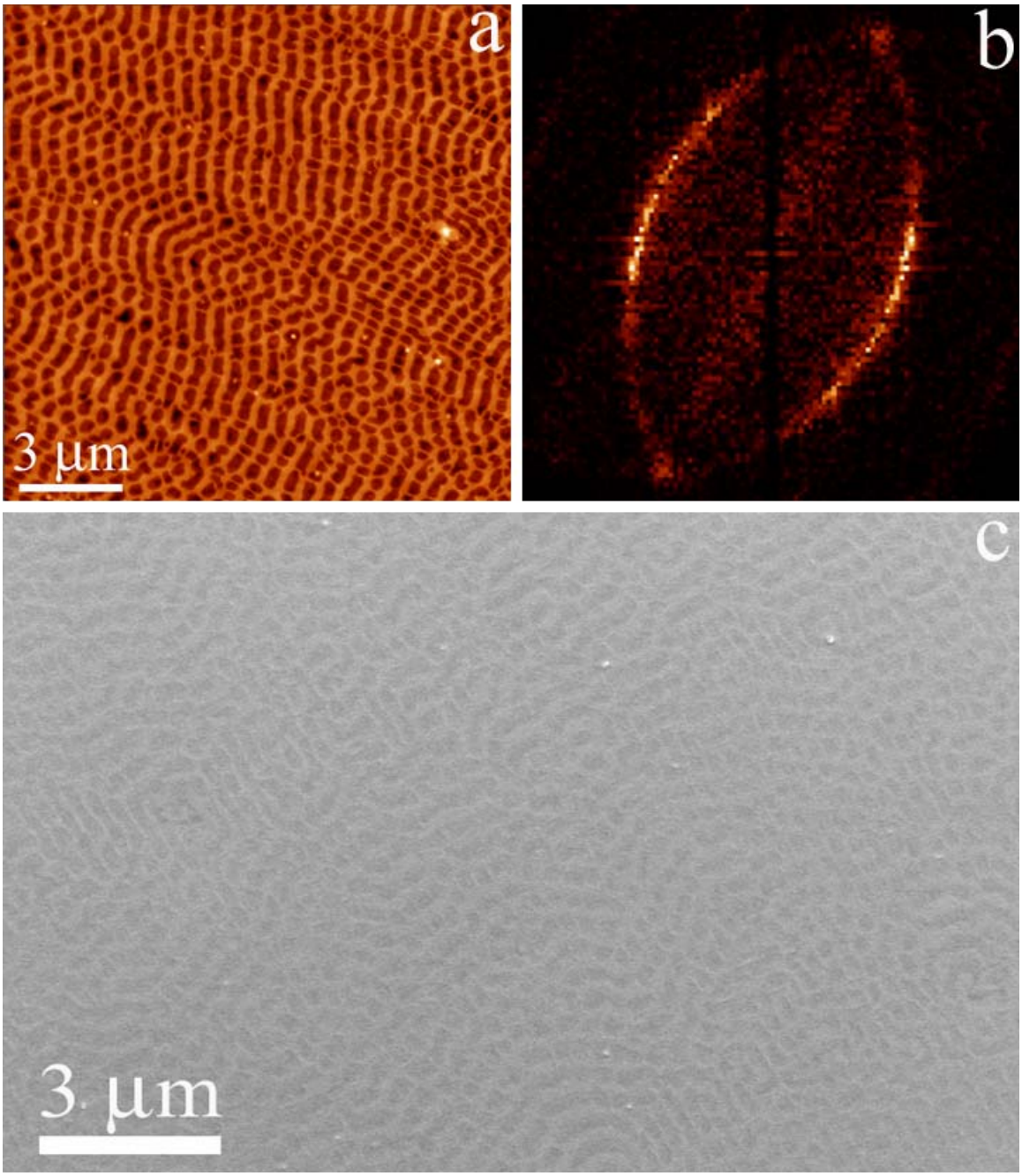

Figure 3.41 (a) AFM image of region displaying a much distorted ripple structure produced at $\theta_i = 33^\circ$, using a Lloyd's mirror arrangement. (b) The FFT image shows that the q-vectors follow the grating equation and a significant number of them are present clearly outlining part of the allowed q-space shown in Figure 1.23. The extra faint arcs shown in the FFT are harmonics of the Fourier transform. The values of ℓ_3 and ℓ_1 have been used to derive the Λ-values and check the value of θ_i (Table 3.3). (c) SEM image of the same sample.

intersecting points ℓ_3 is proportional to $|\boldsymbol{q_3}|$ and the distance of the normal to this line at its widest ℓ_1 is proportional to $|\boldsymbol{q_1}|$. Figure 3.41c is the SEM image of the same sample, showing a larger area of the surface.

An even more complex pattern is shown in Figure 3.42a. Here, the ripple lines appear to be broken into short segments and the lines seem to run along several different directions. More details can be found in Figure 3.42b. Again, the FFT of this image helps to interpret the apparently chaotic pattern. As can be seen in Figure 3.42c, this transform is the same as the schematics drawn in Figure 1.23. In this case, the interference of scattered and incident light took place in most of the possible directions. The two intense spots at the intersections of the two circumferences are equivalent to the two single spots obtained in Figure 3.26d. In the case of the structure shown in Figure 3.26, a grating wave vector perpendicular to $k_i^{//}$ is the predominant and only direction where the interference pattern has materialized into ripples.

Similar case is indicated in Figure 3.43. Figure 3.43a is the top view of the sample surface, FFT of the image is shown in Figure 3.43b, where two circumferences have been found.

The angle of incidence, and the wavelengths Λ_1, Λ_2, and Λ_3 can be determined from the FFT pattern by measuring the lengths ℓ_1, ℓ_2, and ℓ_3 that have been defined in Figure 1.23. ℓ_1, ℓ_2, and ℓ_3 are marked by the arrows in Figure 3.43b. Taking the ratio

$$\boldsymbol{r_{3,2}} = \frac{\ell_3}{\ell_2} \qquad 3.4$$

or the ratio

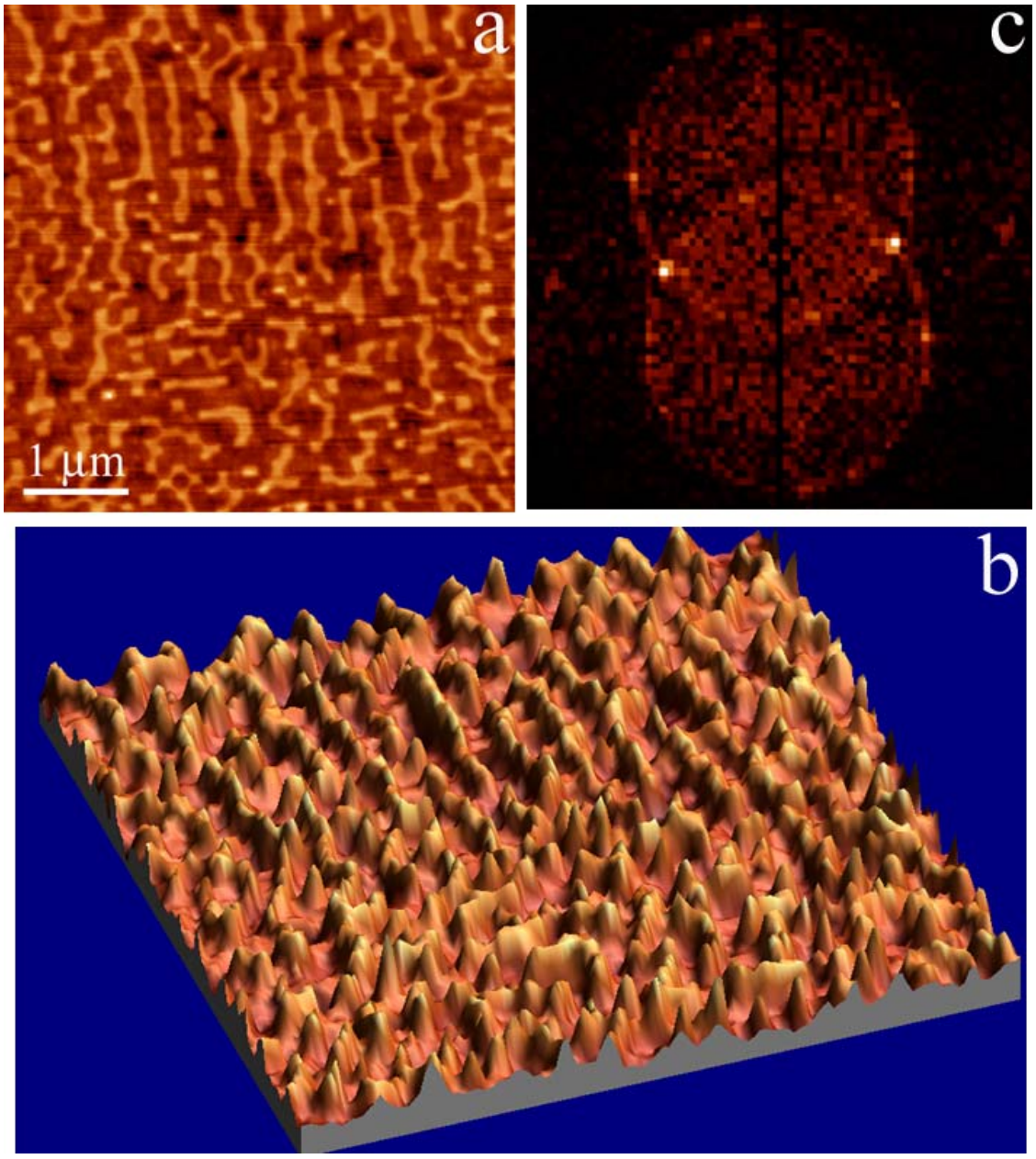

Figure 3.42 AFM image of region displaying a fractured ripple structure produced at θ_i= 35˚, using a Lloyd's mirror arrangement. (a) Top view of the sample surface. (b) 3-D AFM image. (c) The FFT image shows that the q-vectors follow the grating equation and a significant number of them are present in order to clearly delineate all of the allowed q-space shown in Figure 1.23. The values of ℓ_3 and ℓ_1 have been used to derive the Λ-values and check the value of θ_i (Table 3.3).

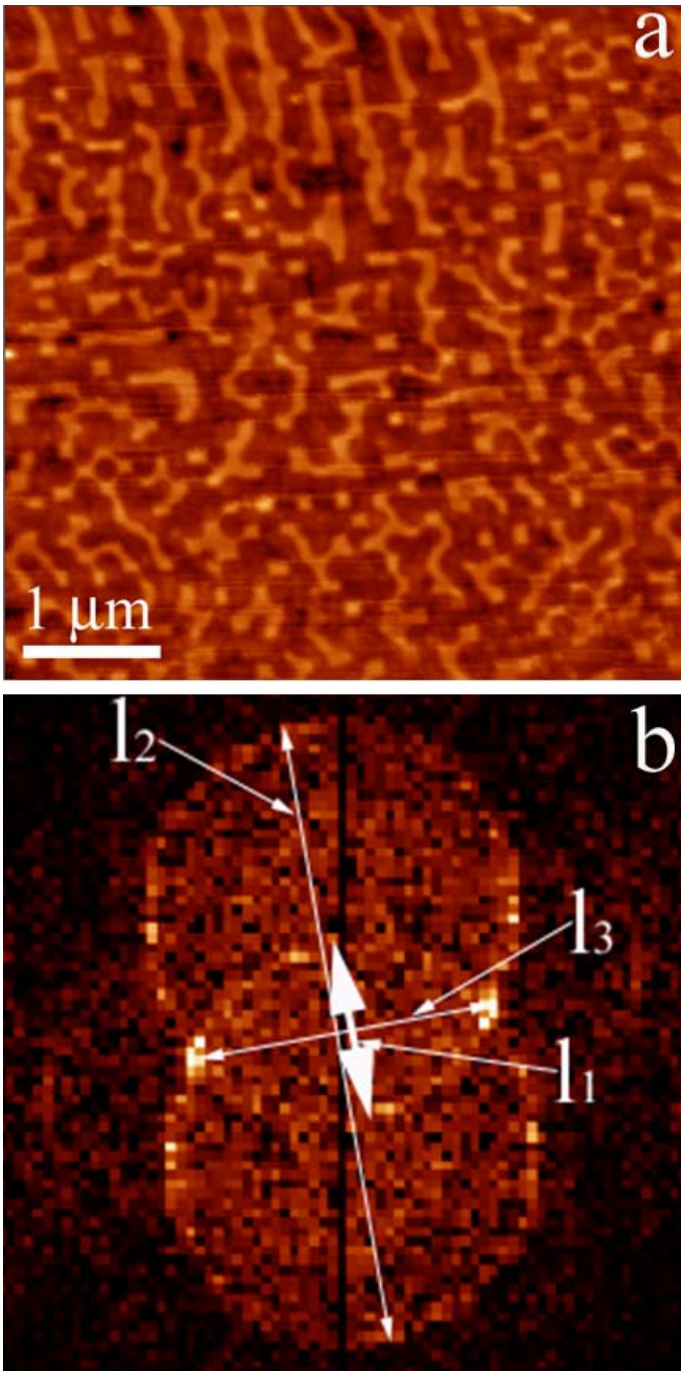

Figure 3.43 AFM image of a sample irradiated by non-polarized light under Lloyd's mirror configuration. The production procedure is similar to the sample shown in Figure 3.42. The angle of incidence is ~ 35°, with 1000 laser pulses. (a) Top view of the sample surface. (b) The FFT image shows that the q-vectors follow the grating equation and a significant number of them are present in order to clearly delineate all of the allowed q-space shown in Figure 1.23. ℓ_1, ℓ_2, and ℓ_3 are marked by the arrows. The values of ℓ_3 and ℓ_1 have been used to derive the Λ-values and check the value of θ_i (Table 3.3).

$$r_{3,1} = \frac{\ell_3}{\ell_1} \tag{3.5}$$

the corresponding values of the ripple spacing are respectively given by

$$\Lambda_2 = \frac{\lambda}{2}\left(r_{3,2}^2 + 1\right) \tag{3.6}$$

$$\Lambda_1 = \frac{\Lambda_2}{r_{3,2}^2} \tag{3.7}$$

$$\Lambda_3 = \frac{\Lambda_2}{r_{3,2}} \tag{3.8}$$

or

$$\Lambda_3 = \frac{\lambda}{2}\left(\frac{r_{3,1}^2 + 1}{r_{3,1}}\right) \tag{3.9}$$

$$\Lambda_1 = \Lambda_3 * r_{3,1} \tag{3.10}$$

$$\Lambda_2 = \frac{\Lambda_3}{r_{3,1}} \tag{3.11}$$

Assuming that equation 1.13 holds the angle of incidence can independently be calculated from the transcendental equation

$$r_{3,2} \times (1 + \sin\theta_i) = \cos\theta_i \tag{3.12}$$

or from

$$r_{3,1} \times (1 - \sin\theta_i) = \cos\theta_i \tag{3.13}$$

The values of ℓ_2 and ℓ_3 were measured using the FFT in Figure 3.43b, and the ratio $\boldsymbol{r}_{3,2}$ calculated using equation 3.4. The three spacings were next calculated using equations 3.6 to 3.8. Similar calculations were conducted using the pertinent equations for Figure 3.41b and other experiments where the FFT was similar to it.

Normally, values of ℓ_1 and ℓ_3 can be measured from the FFT easily. So that $\boldsymbol{r}_{3,1}$ can be calculated. By using equations 3.9, 3.10, 3.11 and 3.13 all three spacing and the angle of incidence can be obtained (See Figures 3.44 to 3.48 for details).

However, sometimes only values of ℓ_1 and ℓ_2 can be measured from the FFT. And that is the case shown in Figure 3.49. In order to calculate the spacing, we must know the value of ℓ_3; if it is absent, no more information can be obtained. In Figure 3.50 the only value we can measure is ℓ_1.

Part of the results mentioned above is tabulated in Table 3.3. The angle of incidence could then be calculated using 3.12 or 3.13, however $|\boldsymbol{k}_{//}^{s,a}|$ may obey either of the equations 1.13, 1.14, or 1.15. It was found that the values of θ_i calculated using 3.12 or 3.13 with $|\boldsymbol{k}_{//}^{s,a}|=2\pi/\lambda$ agree excellently with the experimentally measured angles listed in Table 3.3. These results show that, in addition to self-consistency, the FFT of the original image is a very good way of measuring ripple spacings. All three possible fringe spacings have been calculated and listed in Table 3.3 even though, as noted, fringes spaced by Λ_2 have not been observed in every case.

The spacing values measured from images acquired with AFM and SEM are plotted as a function of the measured angle of incidence in Figure 3.51 and listed in Table 3.4. Values derived from the FFT images and recorded in Table 3.3 have been

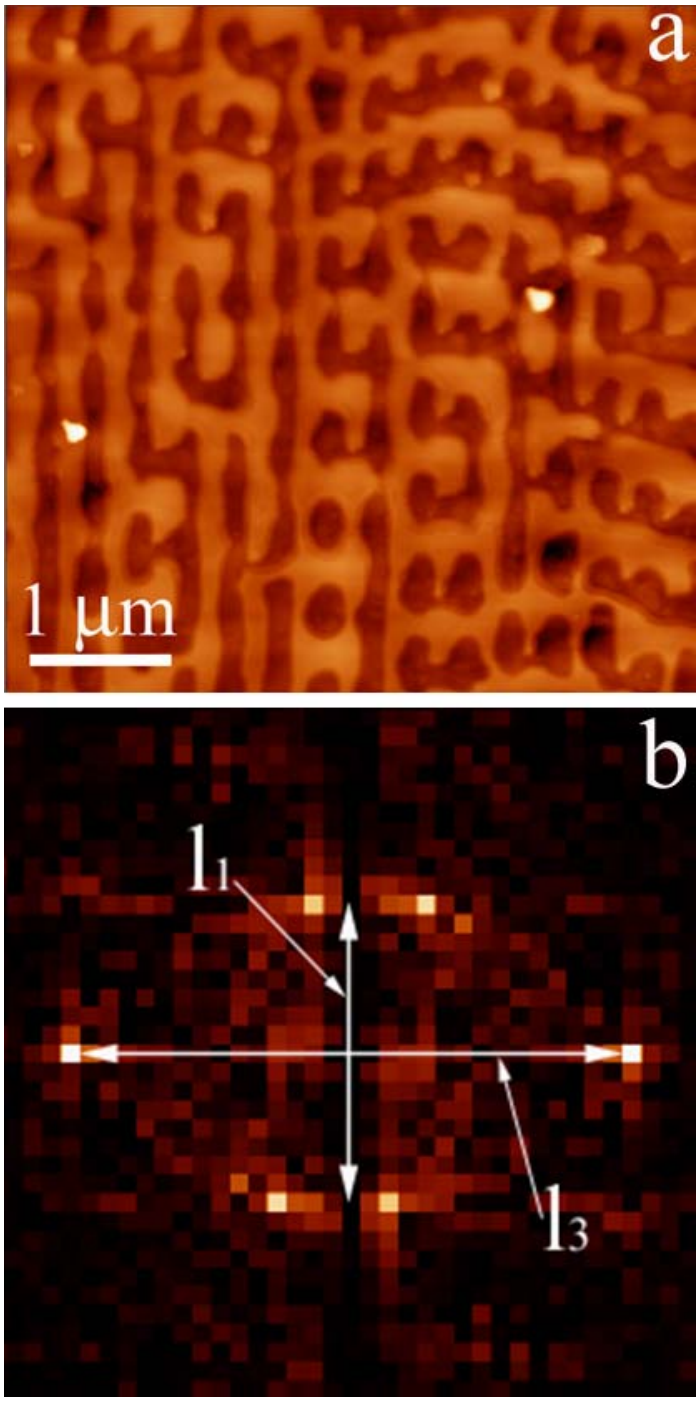

Figure 3.44 AFM image of a sample irradiated by non-polarized light under Lloyd's mirror configuration. The angle of incidence is ~ 51°, with 1000 laser pulses. (a) Top view of the sample surface. (b) The FFT image shows that the q-vectors follow the grating equation and a significant number of them are present clearly outlining part of the allowed q-space shown in Figure 1.23. The values of ℓ_3 and ℓ_1 have been used to derive the Λ-values.

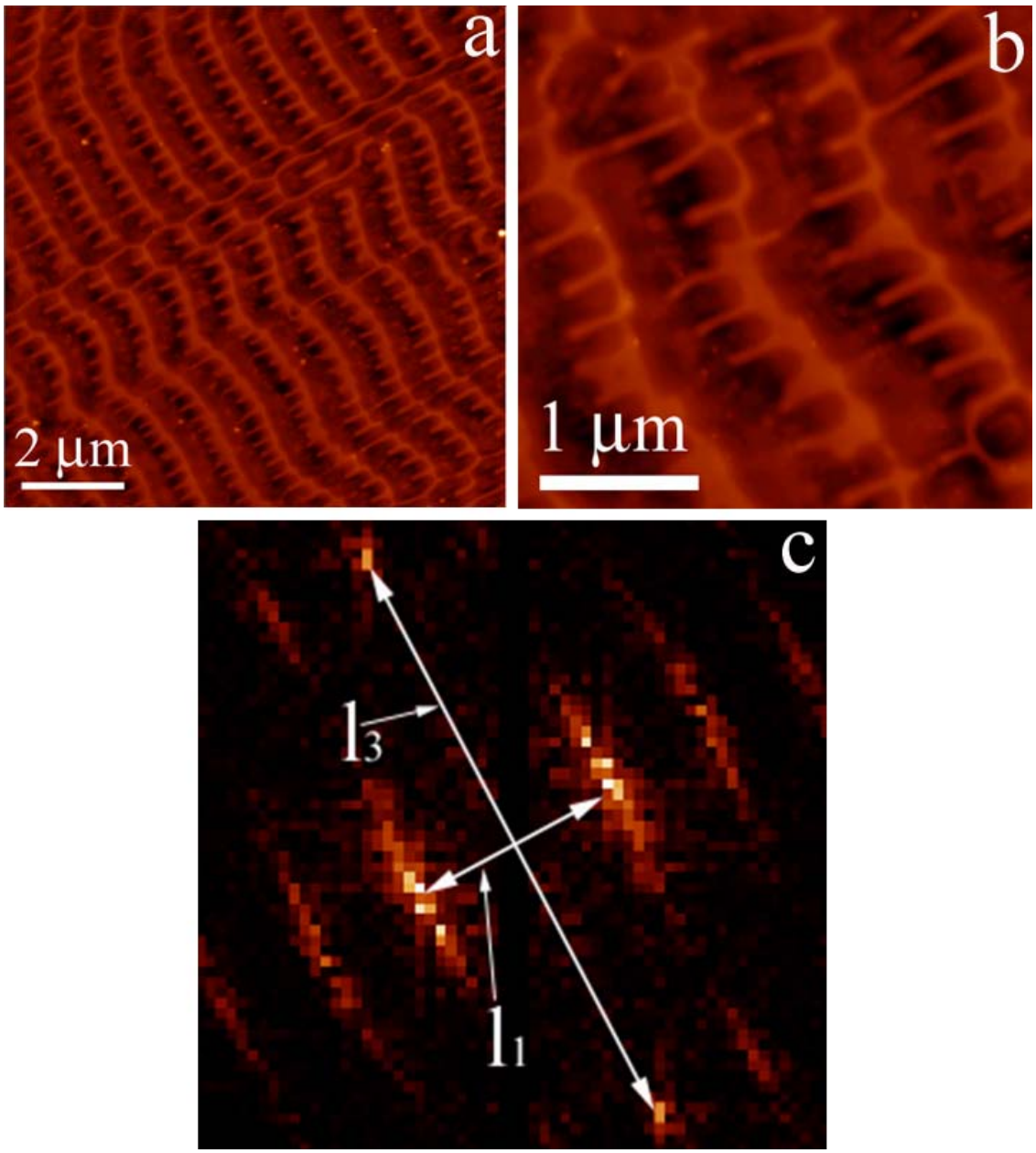

Figure 3.45 AFM image of a sample irradiated by non-polarized light under Lloyd's mirror configuration with 1000 laser pulses. The angle of incidence is ~ 45˚, with 1000 laser pulses. (a) Top view of the sample surface. (b) High resolution AFM image of the same region as in Figure a. (c) The FFT image shows that the q-vectors follow the grating equation and a significant number of them are present in order to clearly delineate all of the allowed q-space shown in Figure 1.23. ℓ_1 and ℓ_3 are marked by the arrows.

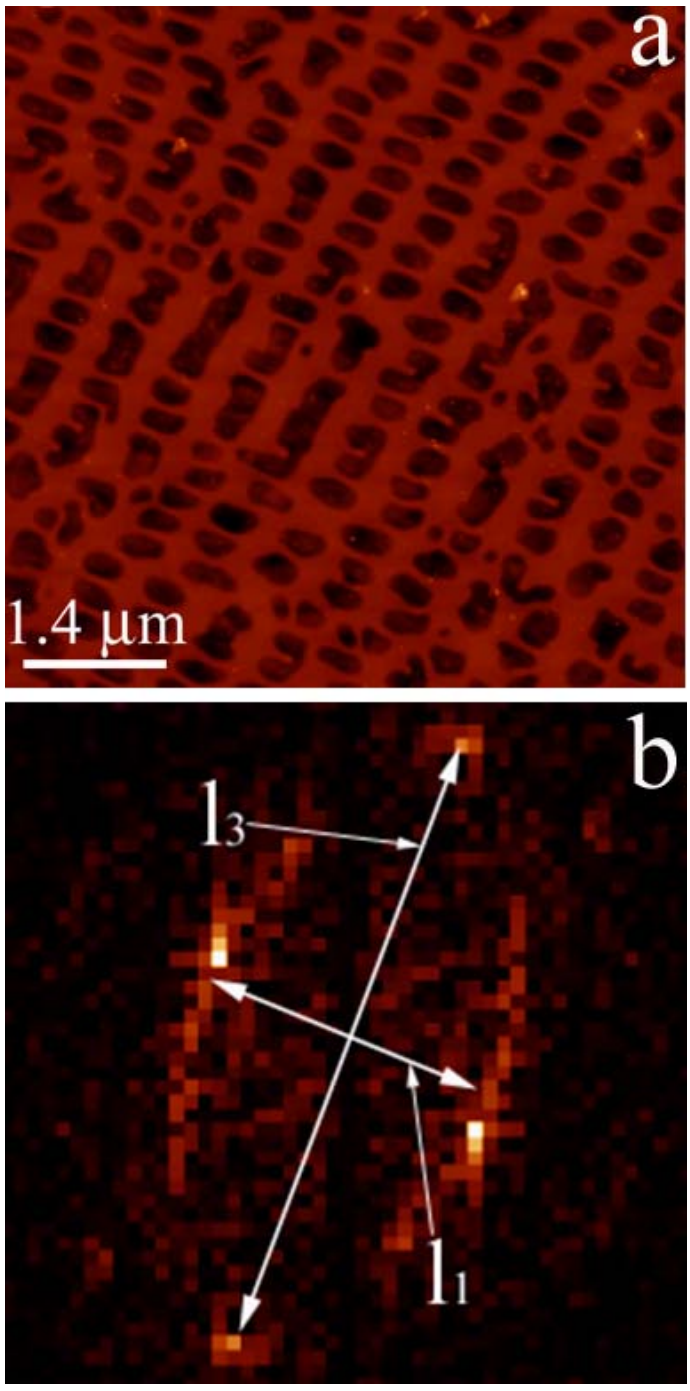

Figure 3.46 AFM image of a sample irradiated by non-polarized light under Lloyd's mirror configuration with 1000 laser pulses. The angle of incidence is ~ 33˚. (a) Top view of the sample surface. (b) The FFT image shows that the q-vectors follow the grating equation and a significant number of them are present clearly outlining part of the allowed q-space shown in Figure 1.23. The values of ℓ_3 and ℓ_1 have been used to derive the Λ-values.

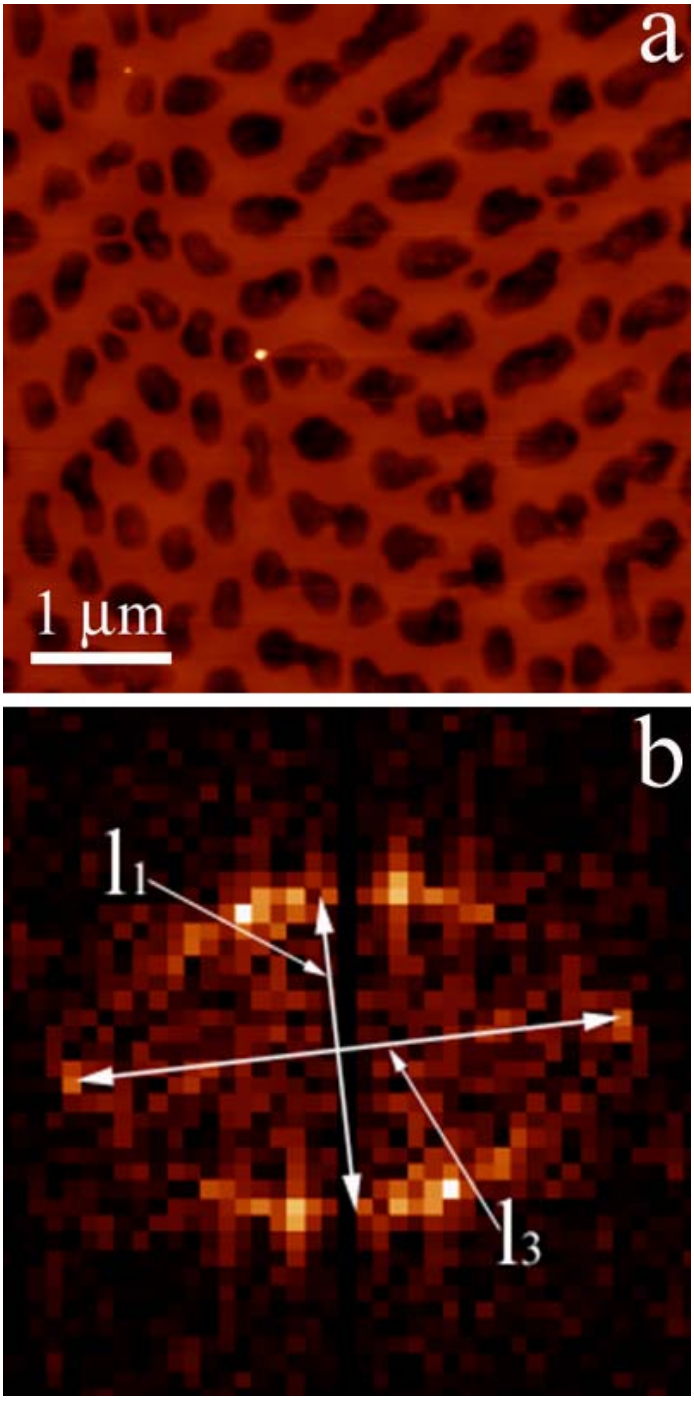

Figure 3.47 AFM image of a sample irradiated by non-polarized light under Lloyd's mirror configuration with 1000 laser pulses. The angle of incidence is ~ 35˚. (a) Top view of the sample surface. (b) The FFT image shows that the q-vectors follow the grating equation and a significant number of them are present clearly outlining part of the allowed q-space shown in Figure 1.23. The values of ℓ_3 and ℓ_1 have been used to derive the Λ-values.

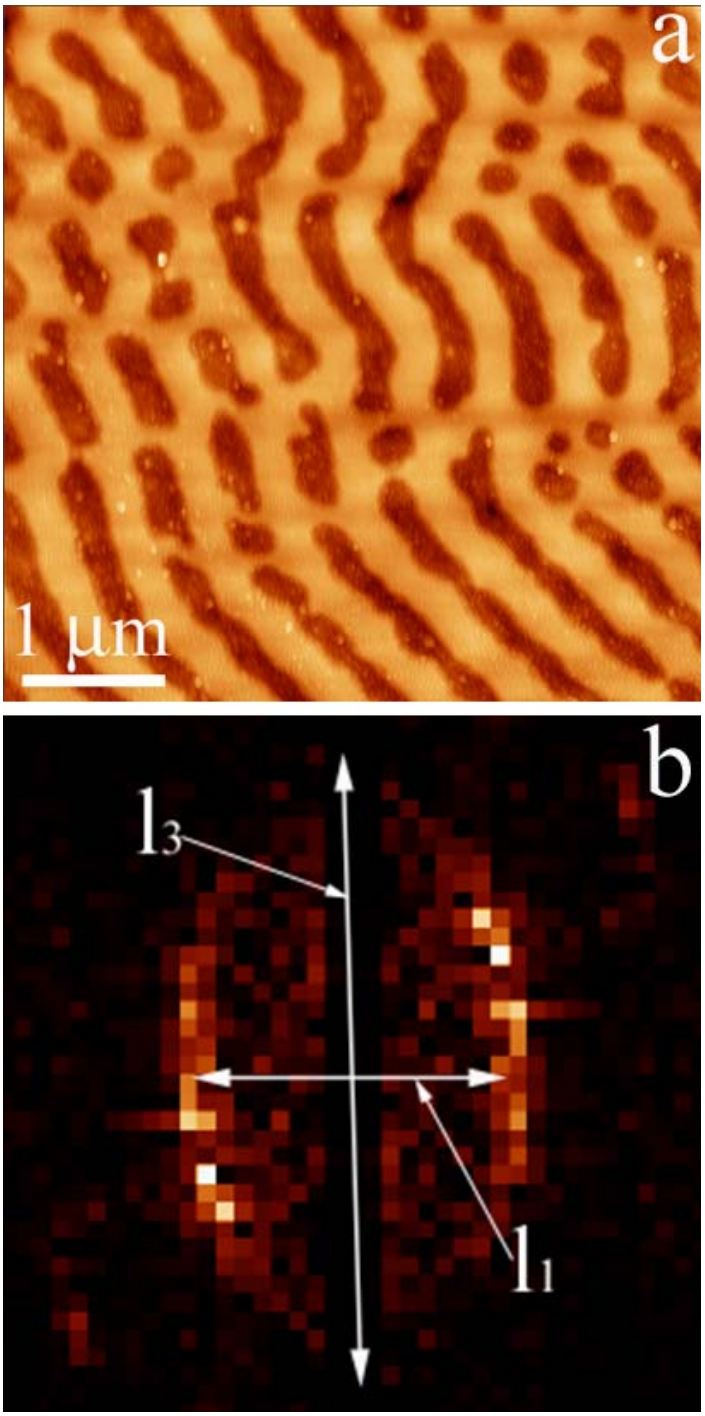

Figure 3.48 AFM image of a sample irradiated by non-polarized light under Lloyd's mirror configuration with 1000 laser pulses. The angle of incidence is ~ 35˚. (a) Top view of the sample surface. (b) The FFT image shows that the q-vectors follow the grating equation and a significant number of them are present clearly outlining part of the allowed q-space shown in Figure 1.23. The values of ℓ_3 and ℓ_1 have been used to derive the Λ-values.

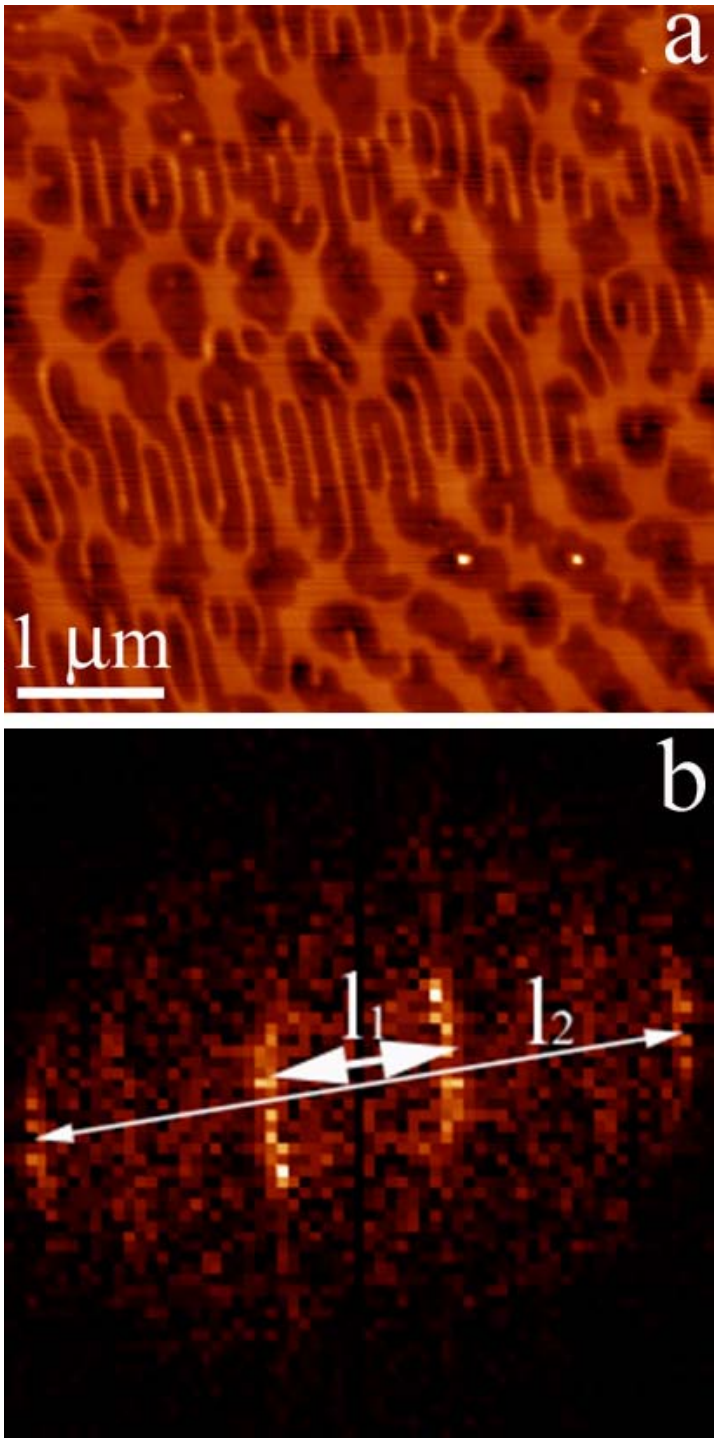

Figure 3.49 AFM image of a sample irradiated by non-polarized light under Lloyd's mirror configuration with 1000 laser pulses. The angle of incidence is ~ 35˚. (a) Top view of the sample surface. (b) The FFT image shows that the q-vectors follow the grating equation and part of them are present clearly outlining part of the allowed q-space shown in Figure 1.23. The values of ℓ_1 and ℓ_2 have been used to derive the Λ-values.

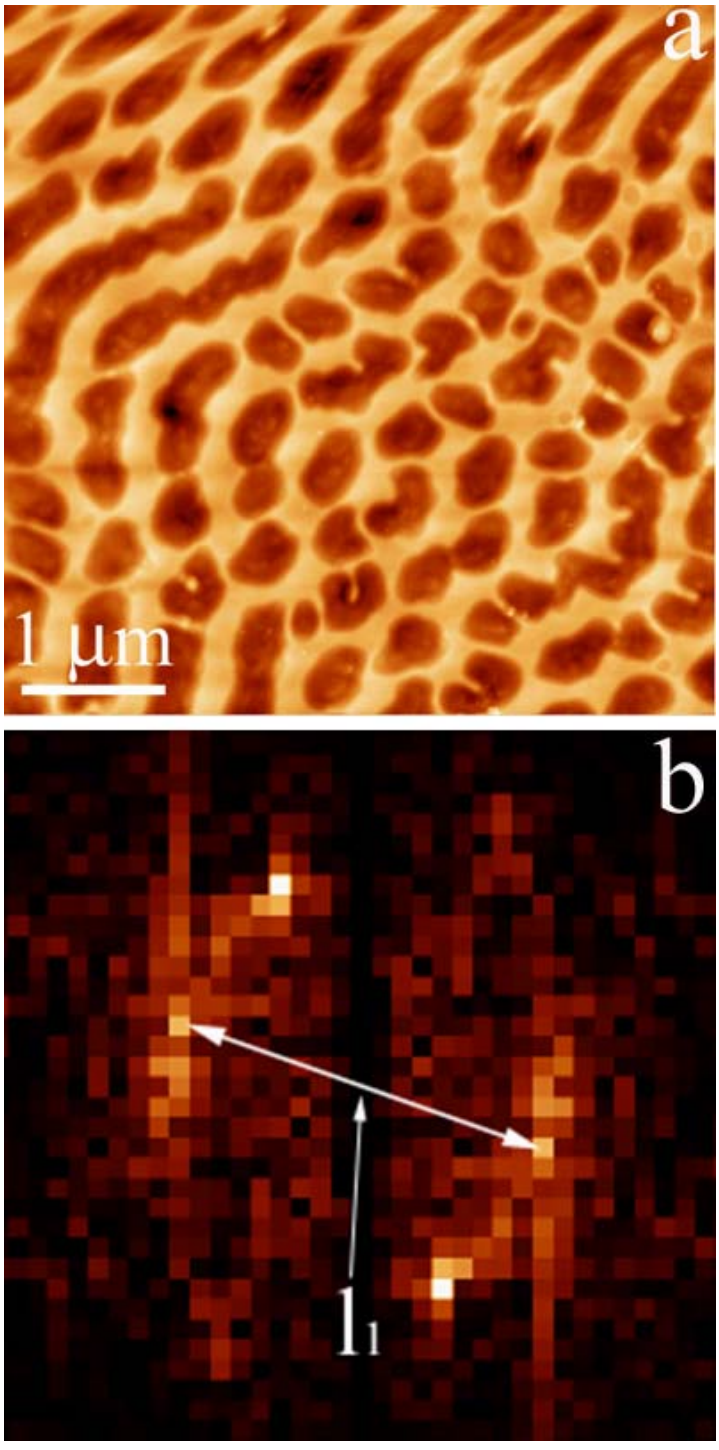

Figure 3.50 AFM image of a sample irradiated by non-polarized light under Lloyd's mirror configuration with 1000 laser pulses. The angle of incidence is ~ 33˚. (a) Top view of the sample surface. (b) The FFT image shows that the q-vectors follow the grating equation and only part of them are present outlining part of the allowed q-space shown in Figure 1.23. From the FFT only ℓ_1 can be measured.

Table 3.3 Ripple Spacings and Angles of Incidence Derived from FFT Images vs. Calculated Spacings and Experimentally Measured Angles

Specimen	r ratios	FFT- determined Spacings [nm]			Calc θ_i	Meas θ_i	Calculated Spacings [nm]		
		Λ_1	Λ_2	Λ_3			Λ_1	Λ_2	Λ_3
V-16	$r_{3,2}$=0.51	597	157	306	35.8	35	582	158	303
V-18	$r_{3,1}$=2.14	692	N/O†	323	40	40	694	151	324
iii-52	$r_{3,1}$=1.85	548	N/O†	296	33	33	544	160	296

† Not observed

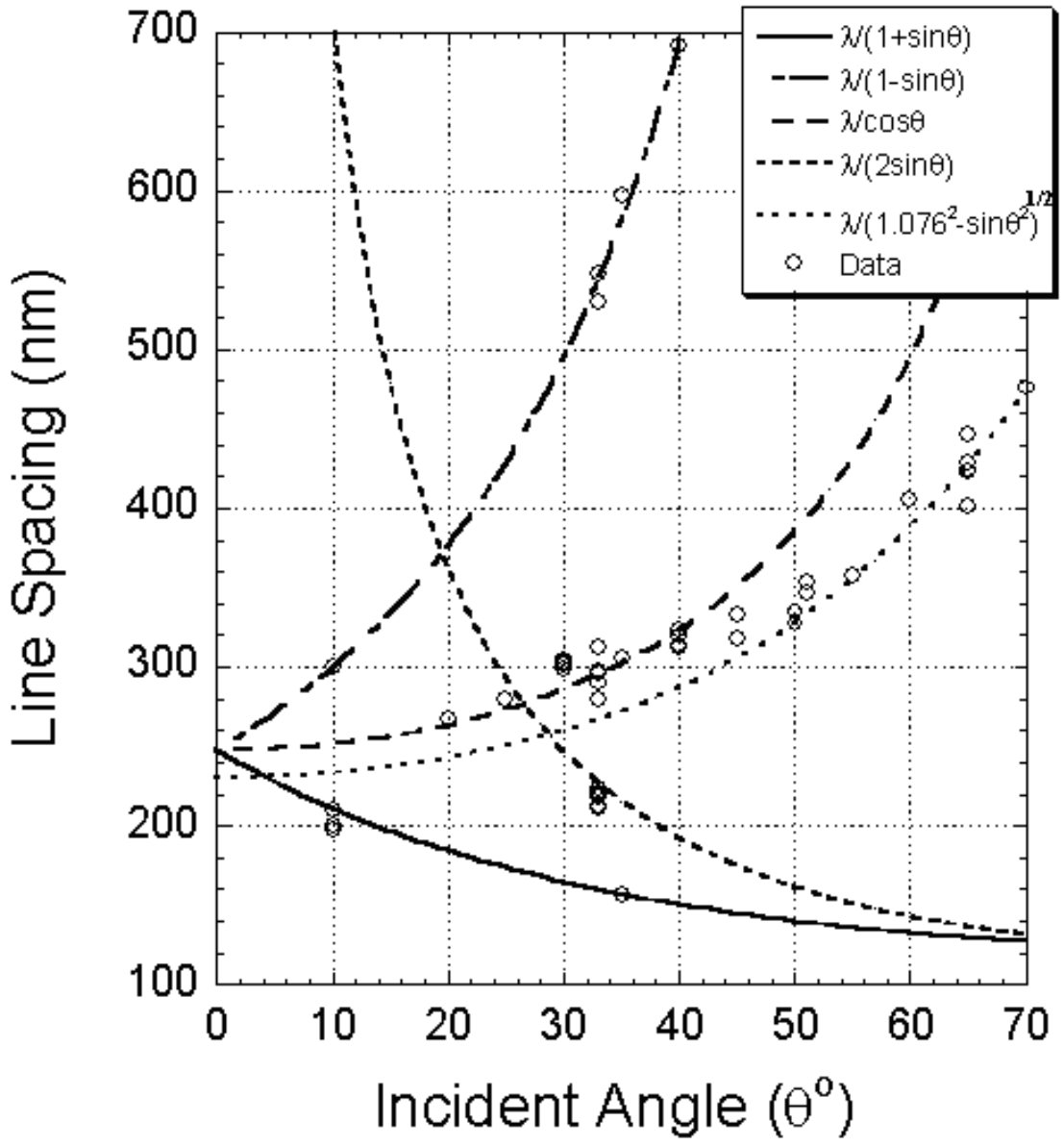

Figure 3.51 Line spacing vs. incident angle, for ripples formed using Lloyd's mirror. Data are listed in Table 3.4. Notice occurrence of ripples characterized by only one set of possible values at $\theta>40^{\circ}$, those that run normal to the substrate/mirror edge. A transition can be seen to occur gradually between $\theta=40^{\circ}$ and $\theta=50^{\circ}$.

Table 3.4 Nano-fringe spacing at various angles of incidence of the laser beam on substrates, with Lloyd's mirror attached– Total number of pulses: 1000

Specimen Identification	Angle of incidence of laser beam [deg]	Fringe Spacing[§] [nm]	Lloyd's mirror setting*, Image acquisition**, Measurement method***
iii.40	10	197,200,210,300	V, SEM
V33	20	267	V, SEM
V34	25	280	V, SEM
V-17	30	299,301,303,305	V,
iii-55	33[†]	313	H, AFM, D
iii-52	33	298 and 530	H, AFM, D
iii-52	33[‡]	296 and 548	H, AFM, FFT
iii-52	33	223,220,221,211,218,212 and 290, 280,297,290	H, SEM
V-16	35	157, 597 and 306	V, AFM, FFT
V-18	40	323 and 692	V, AFM, FFT
V-19	40	313, 314, 320	V, AFM, D
V-21	45	318	V, AFM, D
V-22	45	333	V, AFM, D
V-20	50	328, 334, 335	V, AFM, D
iii-53	51	347, 353	H, AFM, D
V-31	55	358	V, SEM
V-30	60	405	V, SEM
V-24	65	429	V, SEM
V-25	65	424	V, SEM
V-23	65	402, 447, 423	V, AFM, D
V-28	70	476	V, SEM

† P-polarized light. ‡ Angle from FFT same as experimental.

§ Multiple values indicate measurements done at different locations in the surface images. The conjunction 'and' separates sets of perpendicular ripples.

*Lloyd's mirror Setting: H: horizontal (Figure 3.25a-a); V: vertical (Figure 3.25a-b).

** Image Acquisition: SEM or AFM.

*** Measurement: D: from direct image; FFT: from fast Fourier transform of image.

added in the figure, as well. The curves plotted in the figure correspond to equations 3.1 and 3.3 with $|\boldsymbol{k}_{//}^{s,a}|$ given by equation 1.13. Also equation 3.2 for Λ_{interf} has been plotted since, as reported earlier, some of the measured spacings closely agreed with this equation suggesting the presence and effectiveness of an interference pattern produced by the Lloyd's mirror configuration.

As can be seen in Figure 3.51, when the angle of incidence exceeded 40°, the measured spacing departed significantly from the curves plotted using $|\boldsymbol{k}_{//}^{s,a}|=2\pi/\lambda$.

Instead, they were seen to change towards and be fitted at θ_i >45° by another curve that also is described by equation 3.3 but with $|\boldsymbol{k}_{//}^{s,a}|$ given by equation 1.14, for a value of n=1.07.

3.3.3 Summary of LIPSS Formation by Using Lloyd's Mirror Arrangement

The Lloyd's mirror set up strongly enhances the formation of ripples and in particular those that are characterized by a $\boldsymbol{q}_3$ wave vector. These ripples, that we never obtained using a single laser beam, are much straighter than those described by either $\boldsymbol{q}_1$ or $\boldsymbol{q}_2$ vectors. At angles of incidence larger than 45^o they extend over the whole irradiated area, that covers several millimeters wide.

When two sets of ripples intersect there is a clear tendency to break each other's lines. Each set of ripples forces a modulation on the other. In general, the set that has the longer wavelength tends to dominate, forcing its modulation on the set that has the smaller value of Λ. In some cases, it can be observed that the broken line ends with a

droplet-like shape, suggesting the quenching of a retreating liquid line, see for instance Figure 3.46.

3.4 Formation of Nanoprotrusions by Illuminating under a Lloyd's Mirror Configuration

A new nanostructure was seen to evolve at the same laser fluences as required for nanoripple formation, but commonly requiring a larger number of pulses. This structure is characterized by steep elevations, 40 to 70 nm in height, and ~ 60 to 100 nm in diameter at their base, organized into lines separated by a precise spacing, and placed on top of a subjacent ripple structure.

Figure 3.52 is a typical view of this structure, showing the elevations as an array of dots that can extend for many hundreds of micrometers, and sometimes millimeters, covering a large portion of the irradiated region. The specimen in the figure was irradiated at 0.45 J/cm^2, and at 35° angle of incidence. The adjoined profile corresponds to a scan along the shorter of the two segments traced in Figure 3.52a, and it reveals a regular spacing and an average height of ~70 nm. The 3-D image of Figure 3.52b is an amplified image of the upper left area of 3.52a, and shows the elevations mounted atop a 10 nm-high ripple structure. Very bright short segments can be seen in the fast Fourier transform (FFT) presented in Figure 3.52c, certifying the regularity of the 'dot' array seen in the planar view. The two diffuse arcs at the side of the short segments indicate that the dots have some ordering within each line. The line spacing, taken as an average over 30 lines parallel to the longer segment traced in Figure 3.52a, is Λ=300 nm. Using

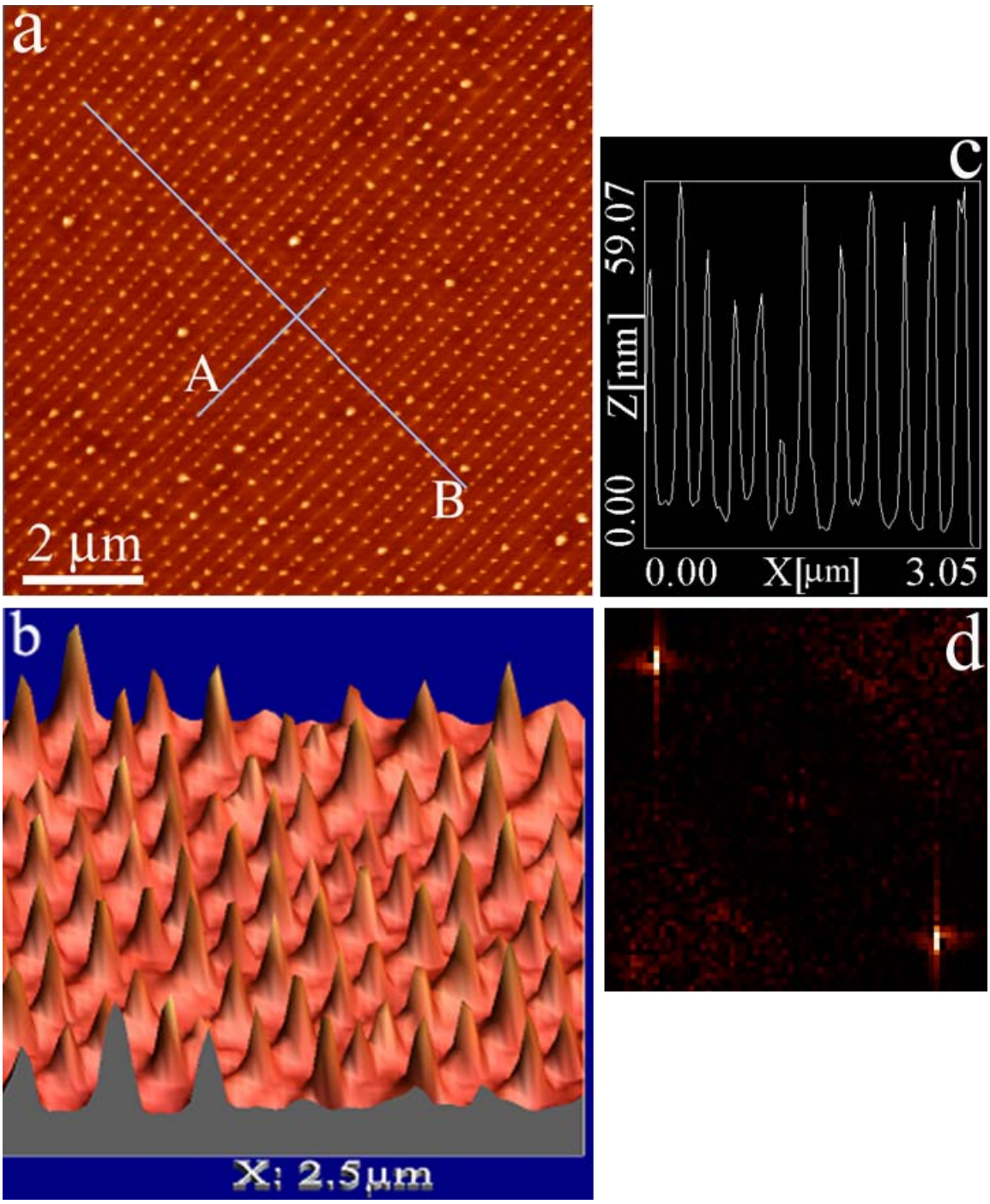

Figure 3.52 Nanoprotrusions formed on the silicon specimen surface upon irradiation at 0.7 J/cm^2, with 1000 pulses. Angle of incidence: 35º. (a) Planar view. Notice misalignment along longer segment "B". (b) 3-D image of upper left of (a). (c) Profile along shorter segment "A" in Figure a. (d) FFT of image in (a) showing regularity of the array spacing between lines spanned in the profile.

equation 3.3, the value of θ_i = 34.2° is calculated, in excellent agreement with the experimental value. These elevations will be called nanoprotrusions.

Figure 3.53 shows the AFM image of nanoprotrusions taken at higher magnification. From these AFM images, we can see more clearly that the nanoprotrusions are sitting on top of the nanoripples. The nanoprotrusions double images are due to the scanning rate of AFM tip. At higher magnification, it takes the AFM tip longer time to scan a certain region, so the nanoprotrusions have a tendency to be dragged away from its original position.

In many cases, in the same specimen we have observed some regions covered with ripples and other regions with protrusions. In these specimens, an interfacial area can be found where both surface structures coexist. Figure 3.54 is an AFM image taken from a specimen irradiated at an angle of incidence of 44º with 1000 pulses, using a fluence of 0.7 J/cm^2. On the left side of this image, the ripple structure started to evolve with the formation of cavities resulting from displacement of material (Profile 1). The coalescence of cavities to form the troughs of the ripples has been introduced in chapter 3.3, and is also seen in Figure 3.54. On the right side of the image, the ripple elevations seen in Profiles 2 and 3 of Figure 3.54 show the ripples' tendency to become thinner and taller as they approach the region where nanoprotrusions emerge. The protrusions formed on top of the subjacent ripple structure which tended to disappear as the protrusions grew taller (Profiles 4 and 5). Together with Figure 3.54, the 3D-image shown in Figure 3.55 clearly reveals that the nanoprotrusion structure was evolving and

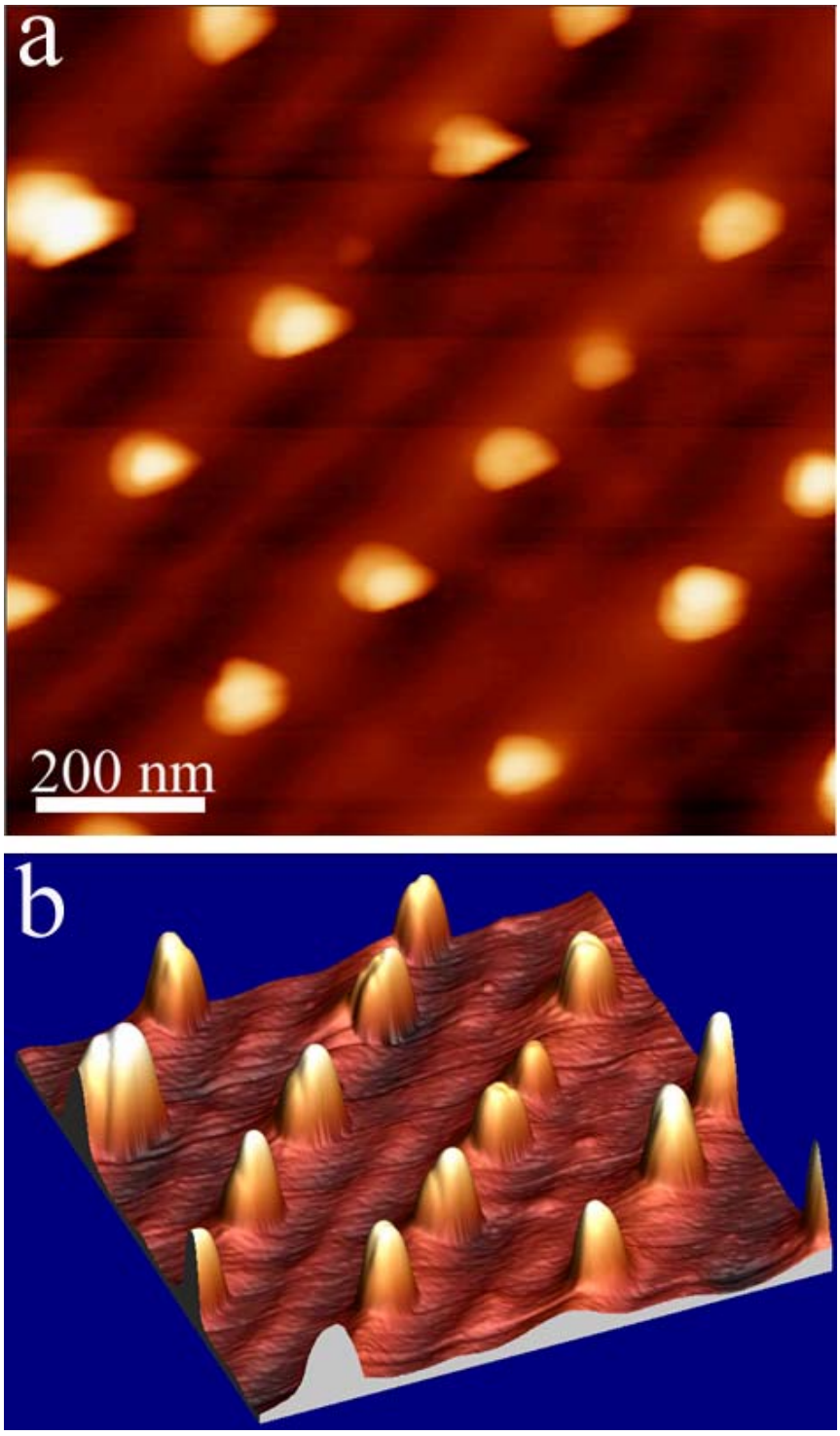

Figure 3.53 Higher magnification AFM images of nanoprotrusions formed on the silicon specimen surface upon irradiation, using the same experimental conditions as for sample shown in Figure 3.52. (a) Planar view. (b) 3-D image of the sample.

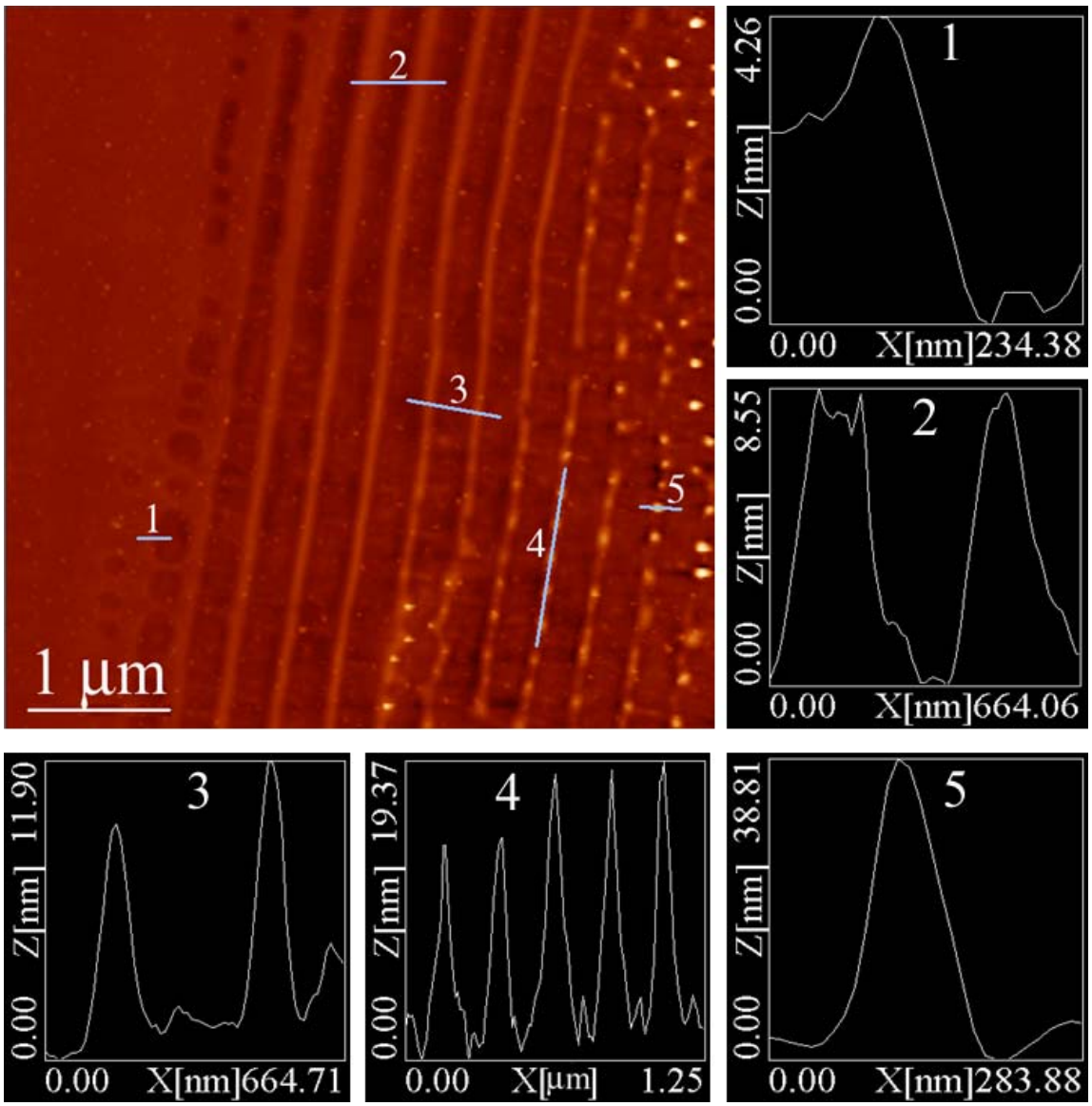

Figure 3.54 AFM image revealing development of nanoripples and their transition to nanoprotrusions. Ripples tend to become thinner and taller as the nanostructure evolves toward protrusions. Notice different axes scales in the profiles from 1 to 5. Specimen irradiated at 0.7 J/cm^2, with 1000 pulses. Angle of incidence: 44º.

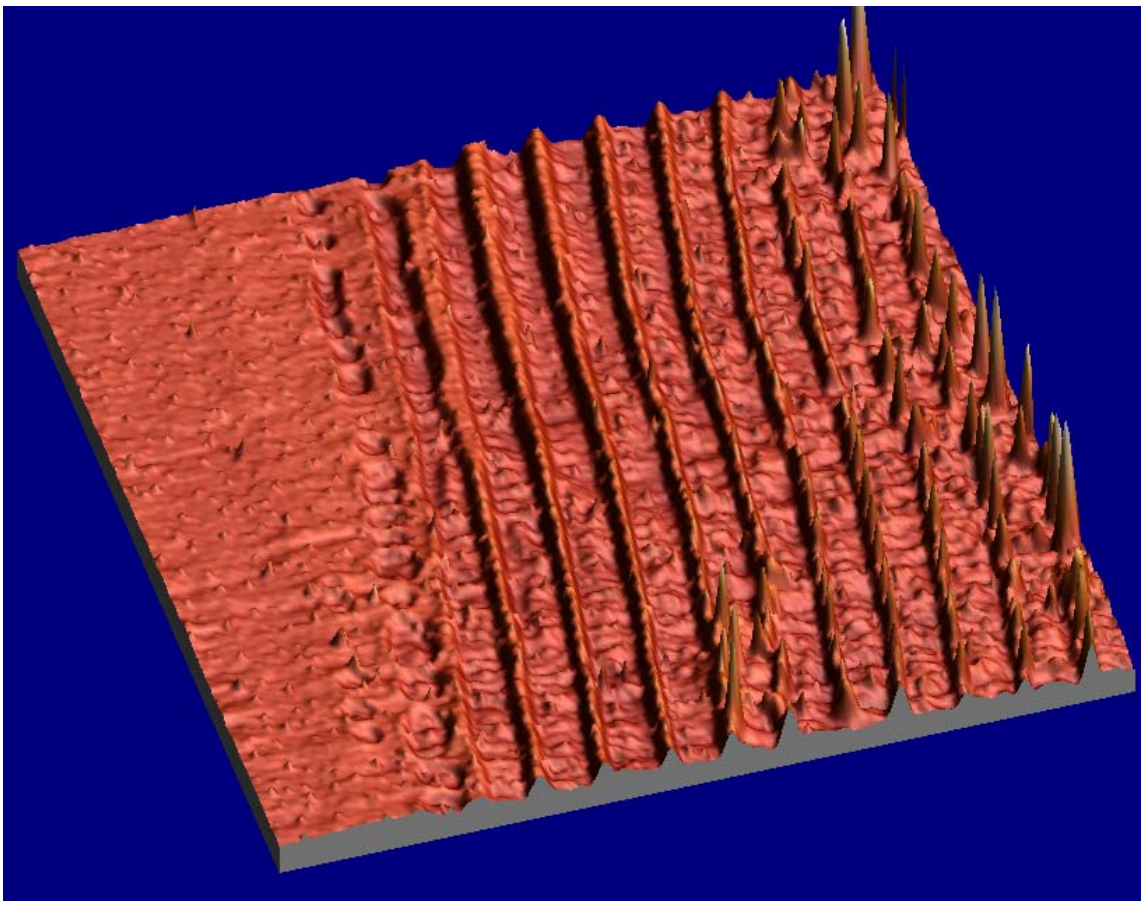

Figure 3.55 3-D image of the same specimen surface shown in planar view in Figure 3.54, demonstrating nanoripple evolution and transition to aligned nanoripple structure.

propagating, similar to the observations done on protrusion-free ripples, as explained in previous section.

It should be stressed that this is a common observation, viz. ripples form, become thinner and increase their height, and end up in nanoprotrusions mounted atop the subjacent initial ripple structure which gradually tends to disappear as the nanoprotrusions grow. Figure 3.56 shows such situation. Figure 3.56a is the top view of a sample, where the transition from nanoripples to nanoprotrusions can be observed. The 3-D AFM image in Figure 3.56c indicates the increase in height as a result of the evolution. In Figure 3.56b, we found that the base of the profile on the left is wider than that on the right by comparing the leftmost and rightmost peaks, respectively.

The evolution of nanoprotrusions seems to be independent of the irradiation atmosphere. All the experiments previously described were carried out in air and the native oxide layer on the sample surface was not removed. In order to asses the importance of the native oxide in the growth of nanoprotrusions a specimen was irradiated under a pressure of $1x10^{-6}$ Torr. The native oxide had been previously stripped by immersing the specimen in a 10% HF solution. After 1000 pulses, nanoprotrusions as high as 80 nm were observed, indicating that the native oxide in the presence of oxygen in the irradiation atmosphere plays a minor role, if any.

Another ripple/nanoprotrusion transitional region is shown in Figure 3.58. Figure 3.58a is the top view of the sample, which has been irradiated under the same conditions as the sample shown in Figure 3.57. Profiles of the trace line “A” and “B” are shown on the right. Profile “A” shows that the ripples have more than doubled their height as they near the nanoprotrusion area.

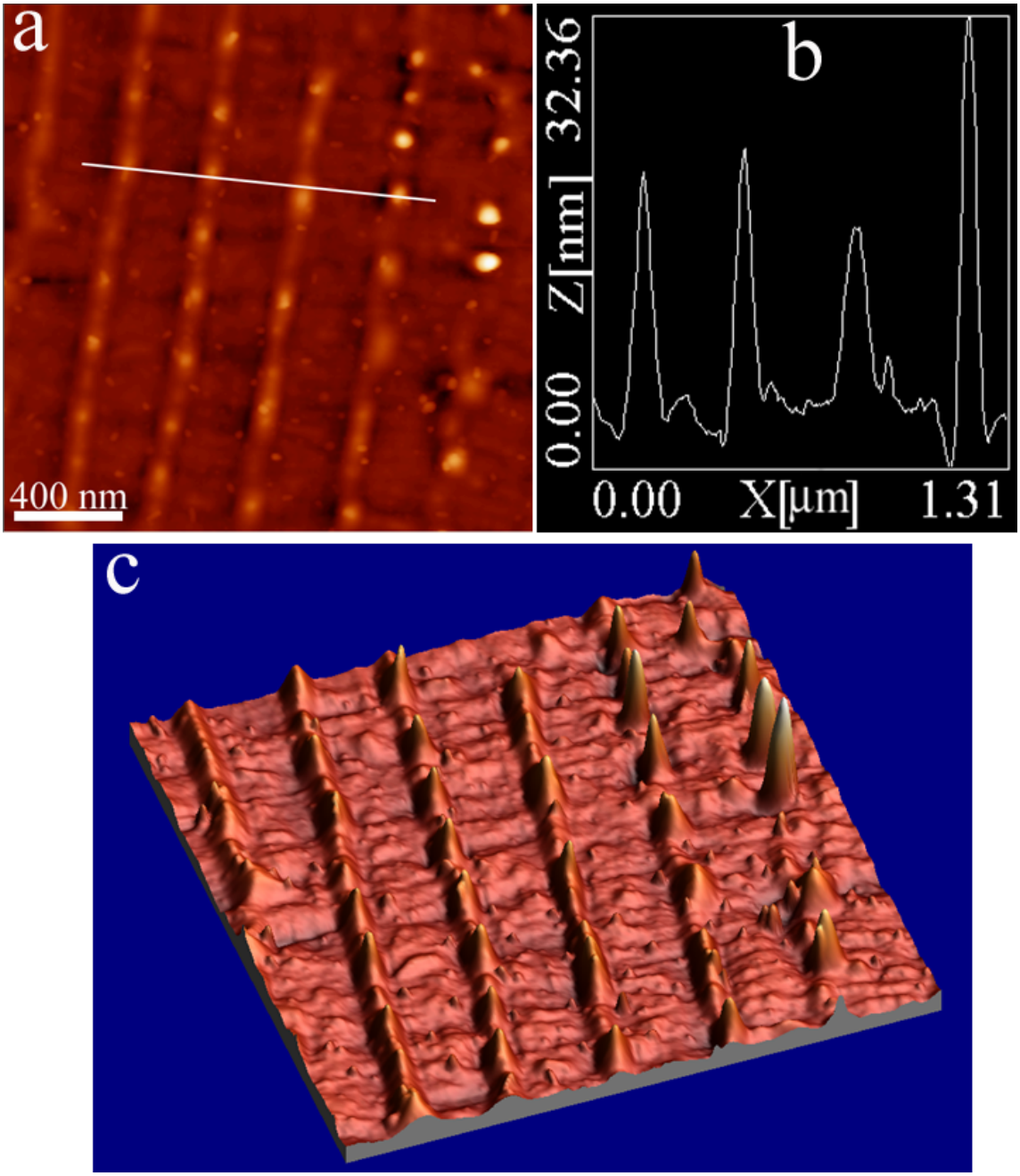

Figure 3.56 AFM images showing the evolution of nanoprotrusions as a result of 1000 laser pulses using non-polarized light and a Lloyd's mirror configuration. The angle of incidence is ~43˚. (a) Top view of the sample surface. (b) Profile along the trace line marked in (a). (c) 3-D AFM image showing the relative heights of the protrusions as they grow from nanoripples.

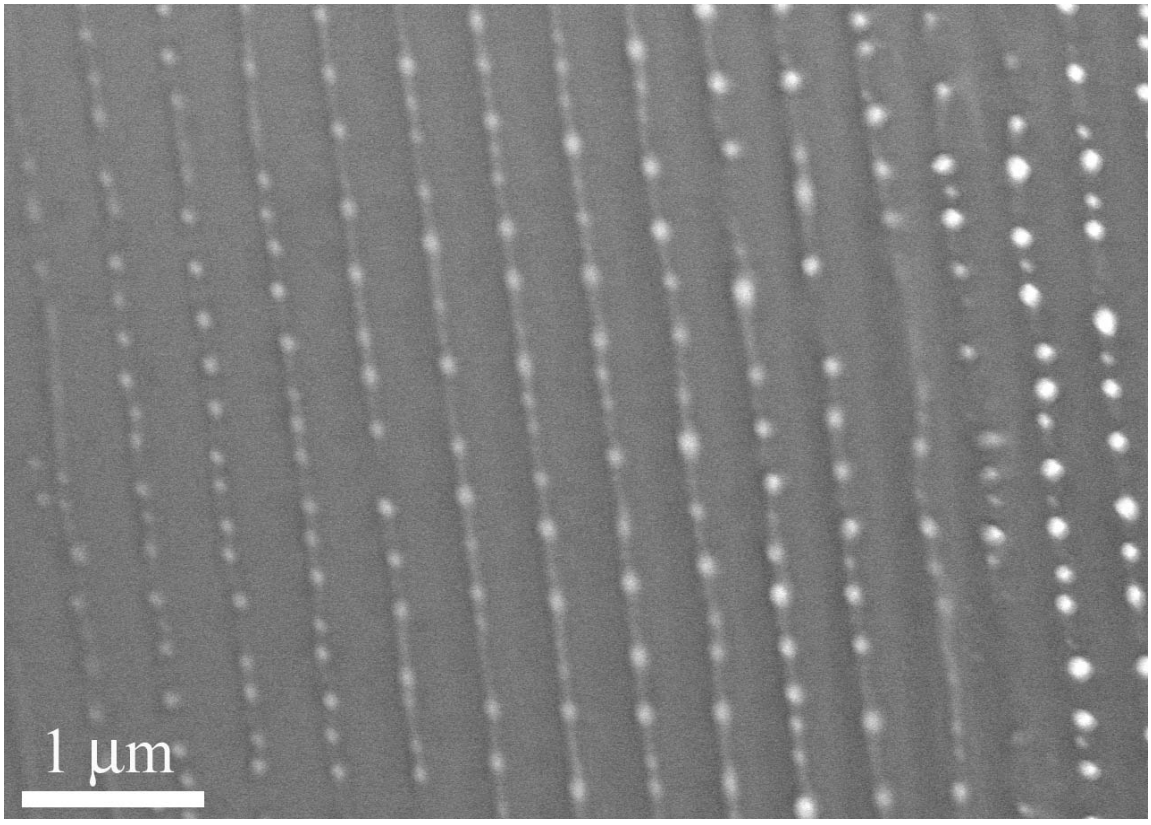

Figure 3.57 SEM image showing a sample surface irradiated with 1000 pulses of non-polarized laser light. The angle of incidence is ~65˚. The native oxide layer on the silicon surface was removed by rinsing the sample in 10% HF solution for 5 minutes. The treated sample was then put into the irradiation chamber, which was evacuated to a base pressure of $1x10^{-6}$ Torr.

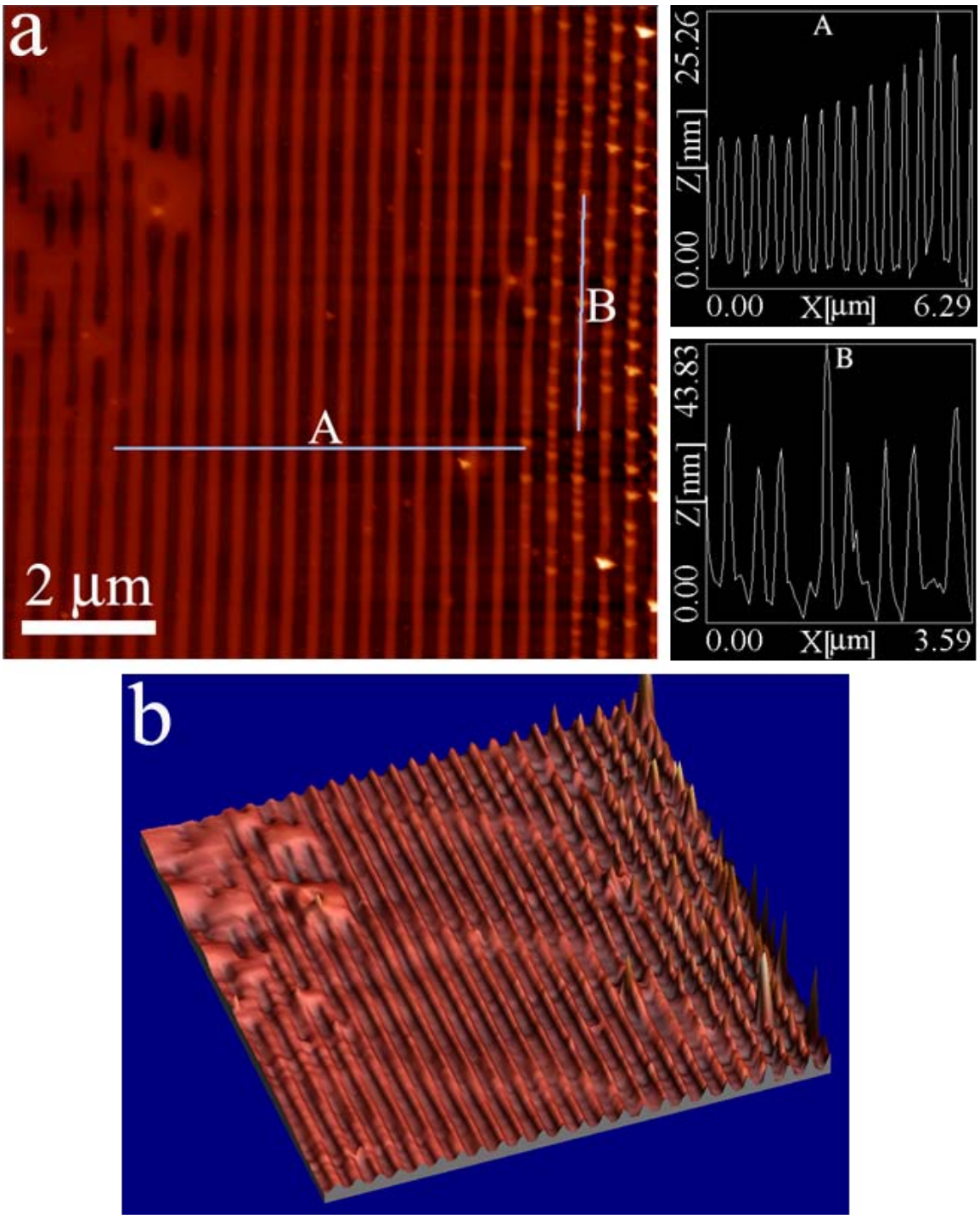

Figure 3.58 Nanoripple to nanoprotrusion transition region. Planar view of specimen irradiated at 0.7 J/cm^2, with 1000 pulses. Angle of incidence: 65˚. Left profile reveals pronounced increase in height and decrease in width of ripples from left to right, as nanoprotrusion region is approached.

The nanoprotrusions mentioned above were generated on 1-D grating, which means they are aligned along one direction only.

However, as found earlier, the Lloyd's mirror set up not only enhances the evolution of ripples but also induces the formation of 2-D structures. These 2-D structures are formed by the intersection of two orthogonal ripple systems that break each other's lines forming sets of streaks and dots. Figure 3.59 illustrates these intersecting sets for a specimen irradiated at 35º, one set exhibiting a spacing fitted by equation 3.3 and the other, fitted by equation 3.4. These streaks are the sites where the nanoprotrusions grow and form, in turn, a 2-D structure.

Figure 3.60 is an SEM image of a specimen under the same irradiation conditions as Figure 3.59 but after 2000 pulses. In this image the 2-D streak lattice of has been transformed into a 2-D nanopotrusion lattice. In other regions streaks capped with nanoprotrusions are visible. As observed earlier, the subjacent structure tends to disappear as the nanoprotrusions grow. Arrow A in both Figure 3.60a and 3.60b represents the direction of interference patterns. And arrow B is parallel to the direction of cosine ripples in both Figure a and b. In both cases, all the nanoprotrusions align very well along these two orthogonal directions.

However, the perfect alignment along both orientations can not be observed all the time. Figure 3.61 shows situations similar to Figure 3.60, but the perfect alignment can only be found in one direction, which is parallel to the cosine ripples. In the direction orthogonal to the cosine ripples, another grating can be observed, which is parallel to the pattern formed by interference under Lloyd's mirror configuration. Due to the poor coherency of the laser we are using, the interference pattern is not strong enough, and

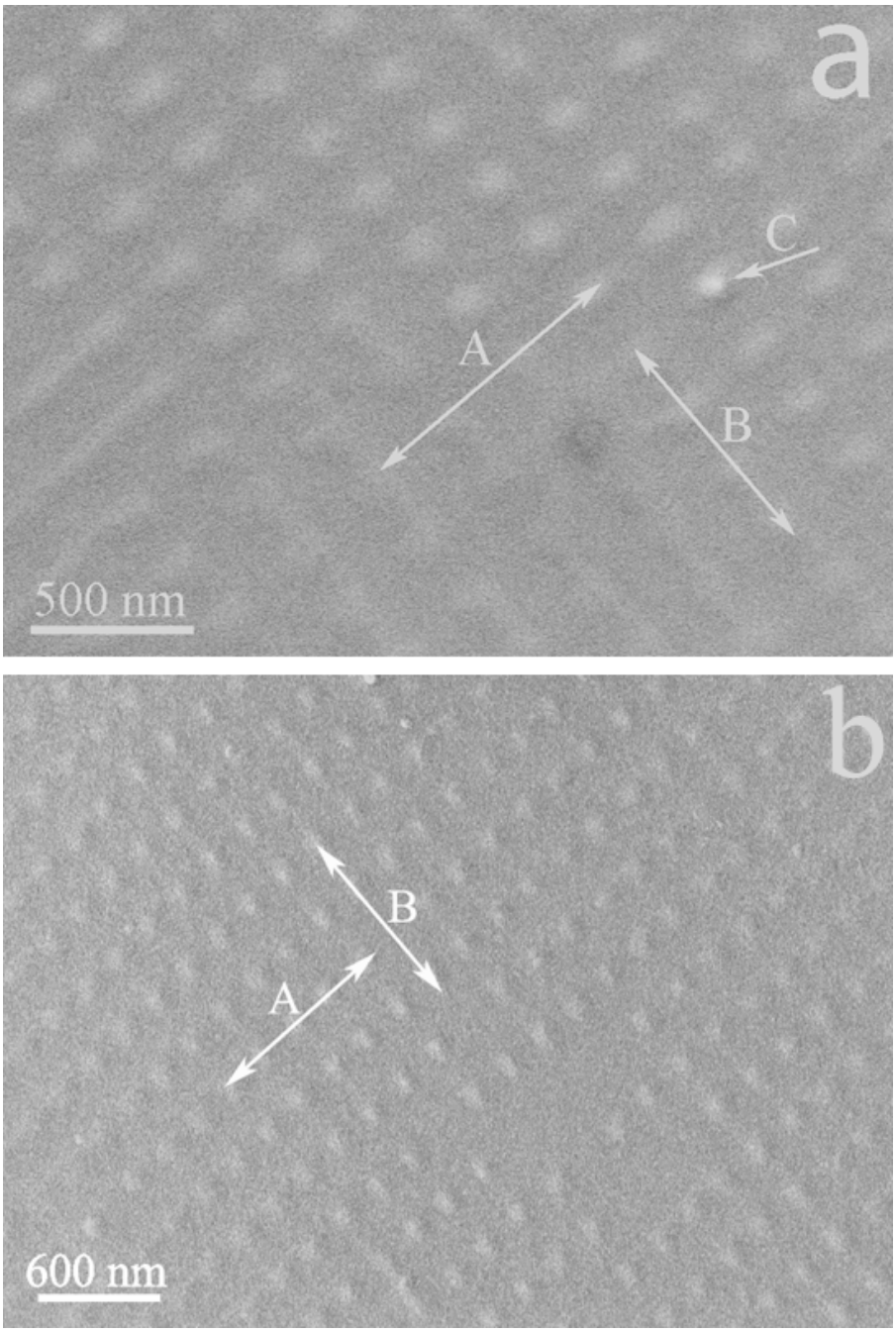

Figure 3.59 (a) SEM image showing the initial stage of nanoprotrusions that are produced by orthogonal intercepting of nano-LIPSS. Condition: 500 laser pulses in air using a Lloyd's mirror configuration. E_d= 0.7 J/cm^2. Incident angle of the non-polarized laser light is 35˚. Arrow A is parallel to the interference pattern, whose line spacing is 216 nm, and arrow B is parallel to the cosine LIPSS, whose line spacing is close to ~297 nm. Arrow C points to a protrusion starting to grow. (b) SEM image taken at lower magnification than Figure a, showing broader region with orthogonal nanoripples.

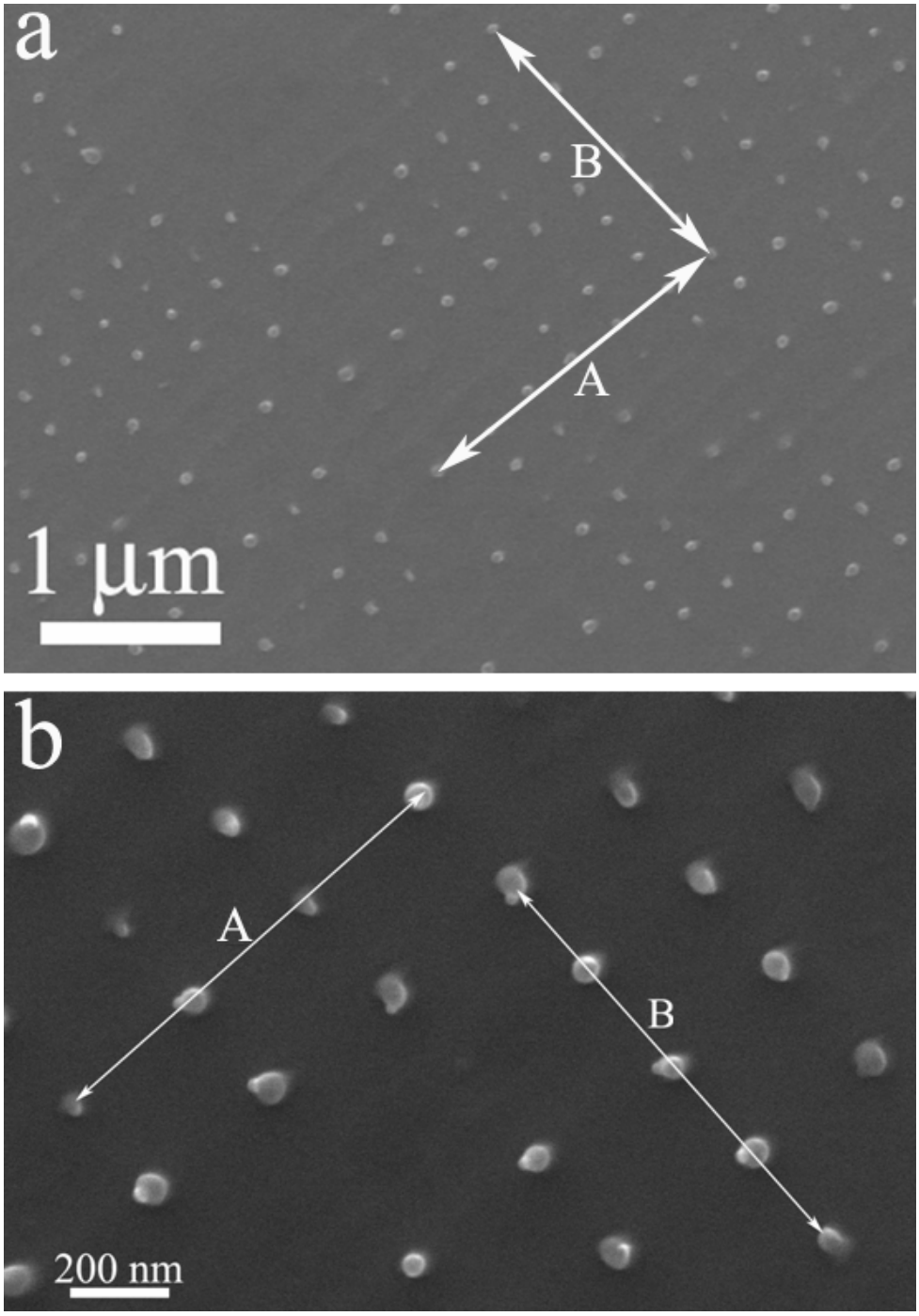

Figure 3.60 SEM images showing the nanoprotrusions formed using Lloyd's mirror. Same fluence and angle of incidence as those in Figure 6.68, but after 2000 pulses. Arrow A direction is parallel to the 1-D pattern formed by interference, while arrow B is parallel to the orientation of cosine LIPSS. (a) Lower magnification image showing a broader region with orthogonal nanoprotrusions. (b) High resolution SEM image showing the 2-D gratings following exactly cosine ripples and interference patterns.

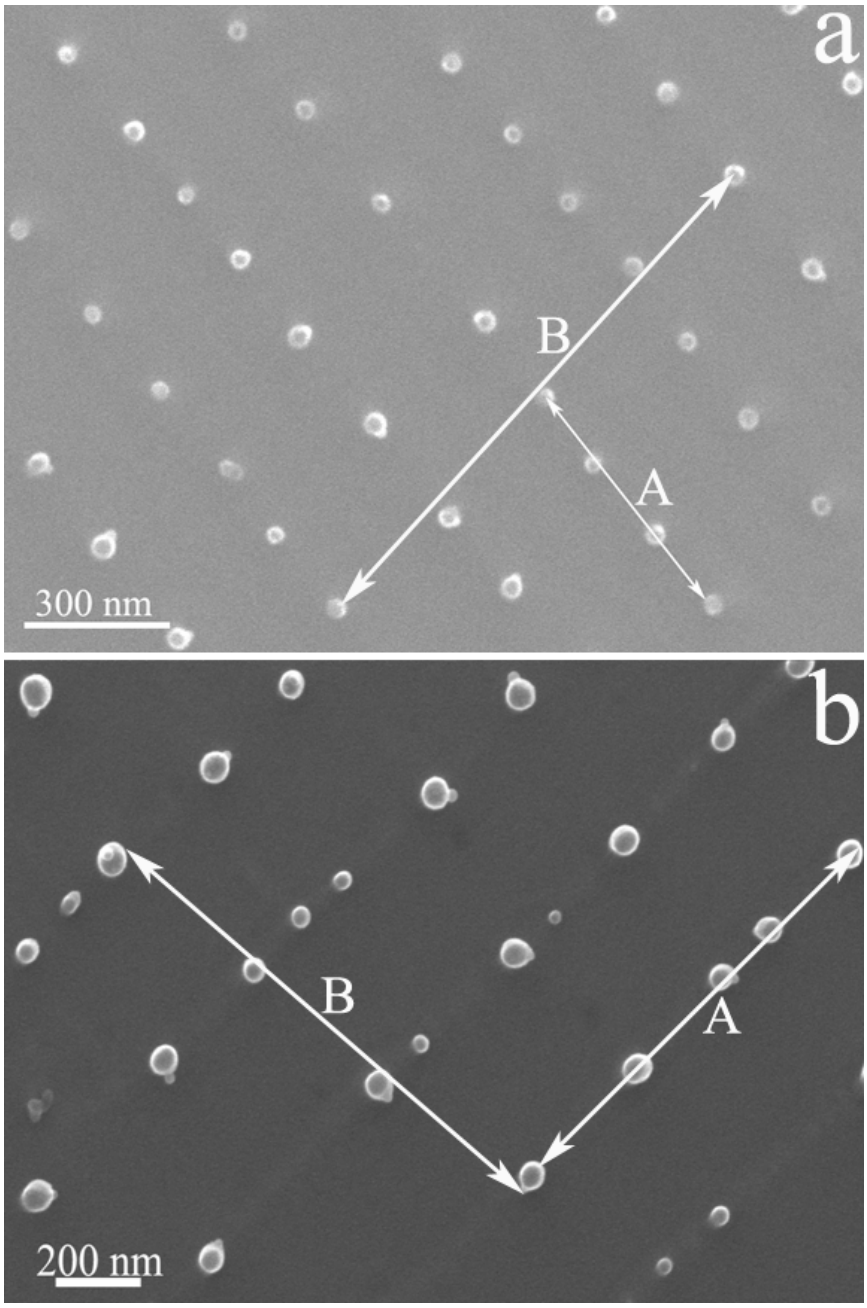

Figure 3.61 (a) SEM image showing the nanoprotrusions formed using Lloyd's mirror. Sample was irradiated by 2000 laser pulses, at an angle of incidence of ~35˚. Arrow A direction is parallel to the orientation of cosine LIPSS, while arrow B is roughly parallel to the 1-D grating formed by interference. Notice the distribution of nanoprotrusions along arrow B is not exactly straight. (b) SEM image showing a more complicated distribution of nanoprotrusions. Sample was irradiated after 2000 pulses, with an incident angle of ~43˚. All nanoprotrusions follow the cosine ripples, which are indicated by arrow A. While in the orthogonal direction, which is indicated by arrow B, the alignment is not so clear.

tends to be interrupted by the other orthogonal grating. That is why the distribution along the interference pattern is not straight.

A more complete coverage of a 2-D nanoprotrusion lattice can be seen in Figure 3.62. The lines spaced according to the ripple equation are straight with almost no alignment defect; however, the lines spaced according to the interference pattern of Lloyd's mirror tend to break and deviations from their straightness can be found in many places.

Figure 3.63, 3.64 and 3.65 are three AFM images taken on the same sample shown in Figure 3.61a. Figure 3.63 shows the coexistence of ripples and protrusions. As shown in Figure 3.63a, the lower right part of the sample is close to the substrate/mirror edge, which means the interference between direct incoming laser beam and the reflected beam is stronger. The highlight of this part of sample is shown in Figure 3.64. FFT in Figure 3.65c further proves that both cosine ripples and interference pattern exist in the surface. Arrow A in Figure 3.65c points to the cosine ripples in the reciprocal space, and arrow B represents interference pattern.

However, nanoprotrusions do not always grow in association with a subjacent ripple structure as remarkably regular as the structure of Figure 3.60. Similar to what we have found for nanoripples produced under Lloyd's mirror configuration, more complex patterns of nanoprotrusions were also detected.

Figure 3.66 shows such irregularity. Figure 3.66a is the top view of the AFM image, and the profile of the trace line in Figure a is shown in Figure b. Figure 3.66c is the FFT of the AFM image, which is similar to what we found in ripple-only samples with multiple orientations, such as Figure 3.42c and Figure 3.43b. As explained in

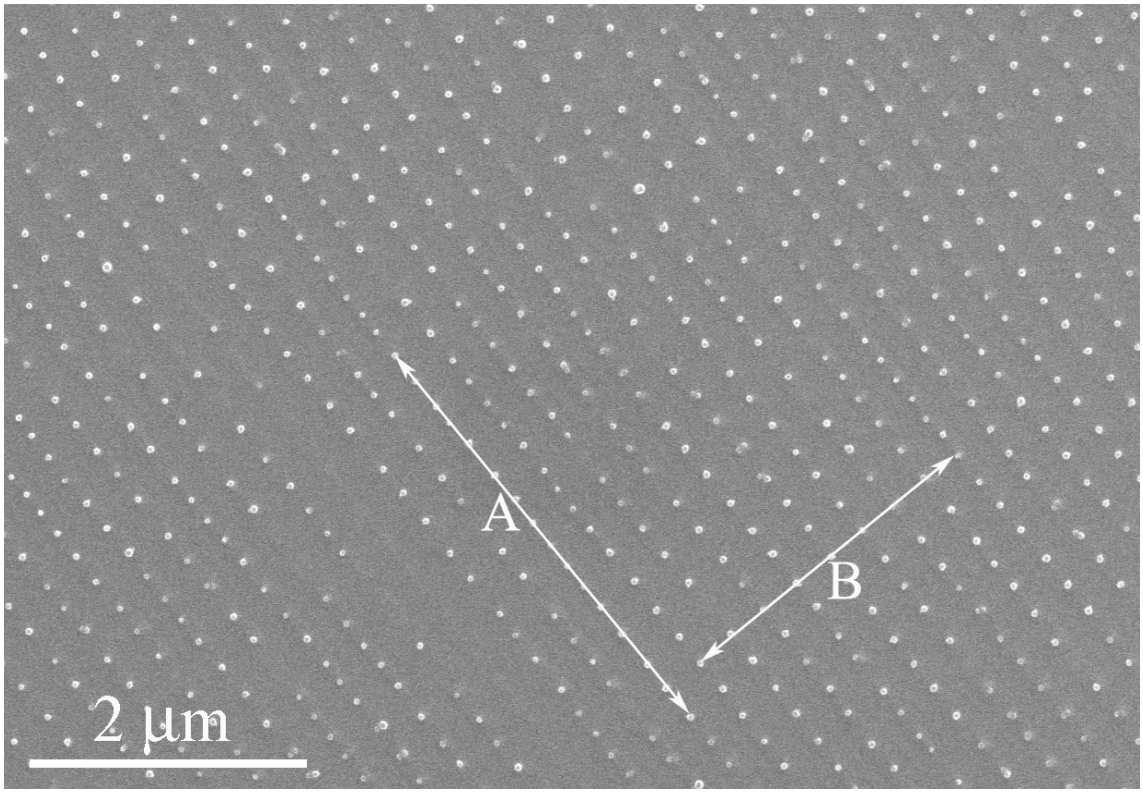

Figure 3.62 Low magnification SEM image of same specimen as in Figure 3.60a showing the extent and regularity of the nanoprotrusion array across a fairly large area. A remarkable alignment can be seen in the array extending from upper left to lower right side of the picture, which is marked by arrow A. Spacing of these lines agrees with the grating equation 3.5. Arrow B is parallel to the interference patter formed by Lloyd's mirror configuration.

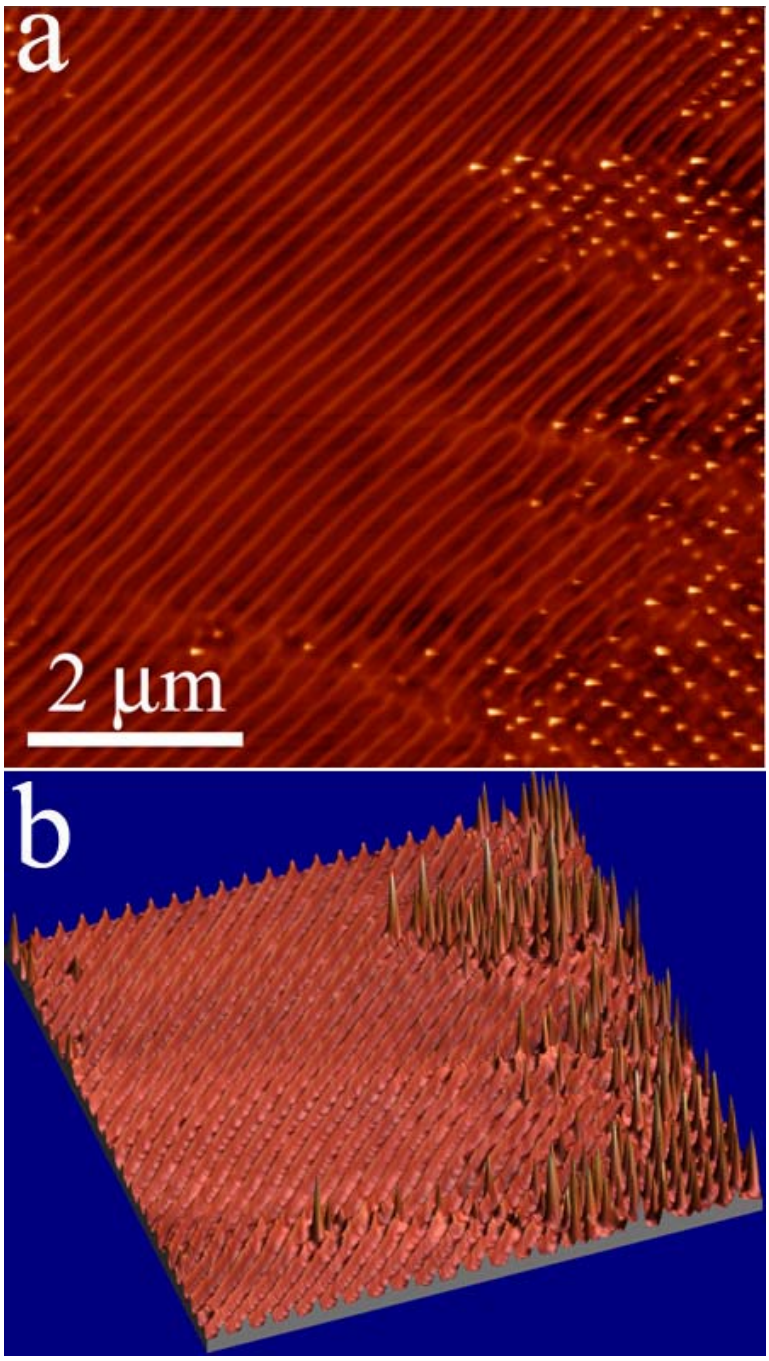

Figure 3.63 AFM images showing coexistence of nanoripples and nanoprotrusions. The lower right part of the sample is sitting close to the edge of mirror/substrate, so the interference is stronger, that is why nanoprotrusions aligned along the interference pattern can be found. Notice the bending of straight cosine ripples in region where nanoprotrusions can be found. (a) Top-view of AFM image. (b) 3-D AFM image.

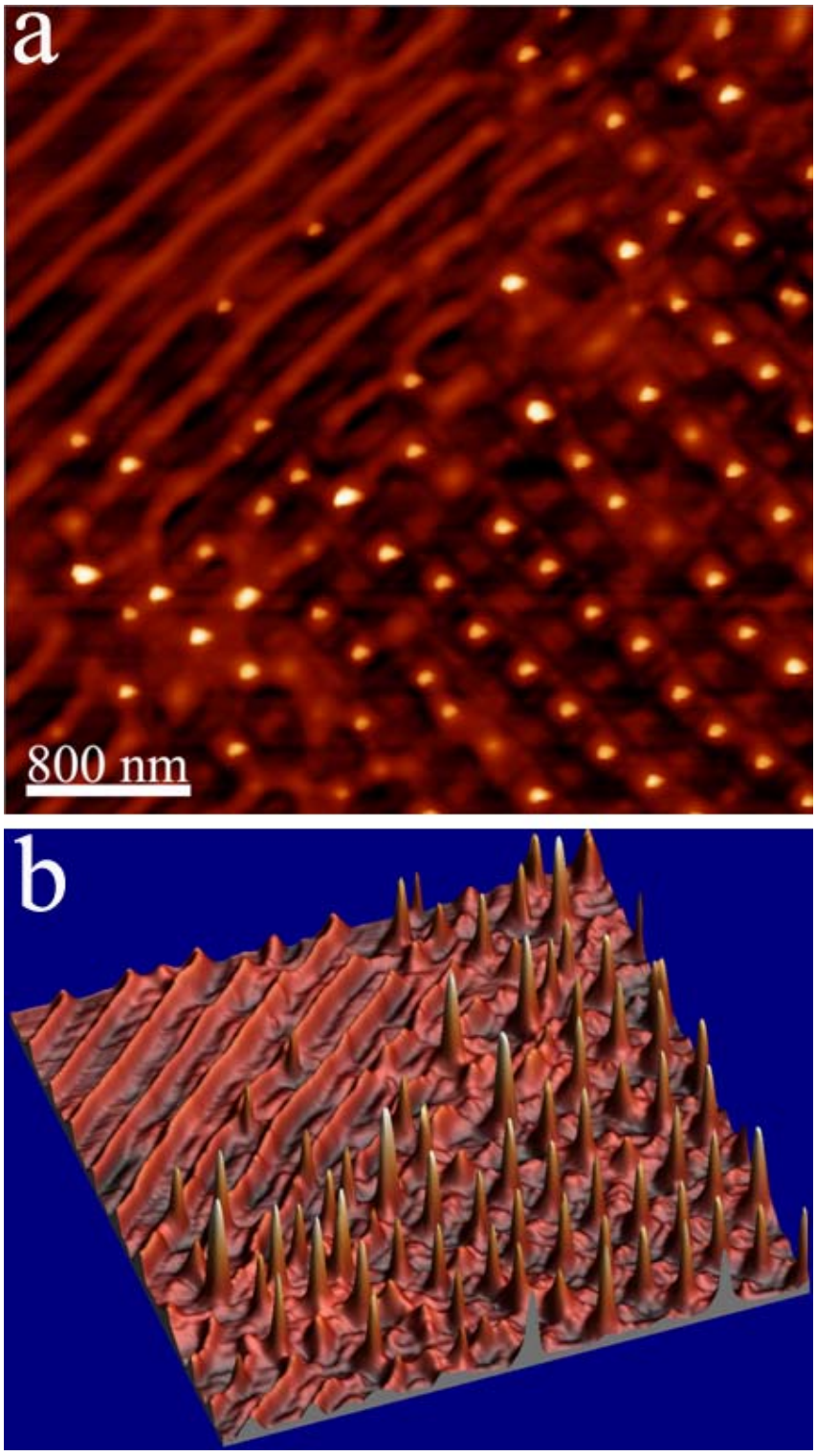

Figure 3.64 (a) Top view of AFM image showing the lower right corner of Figure 3.62. (b) 3-D AFM image showing the surface topography.

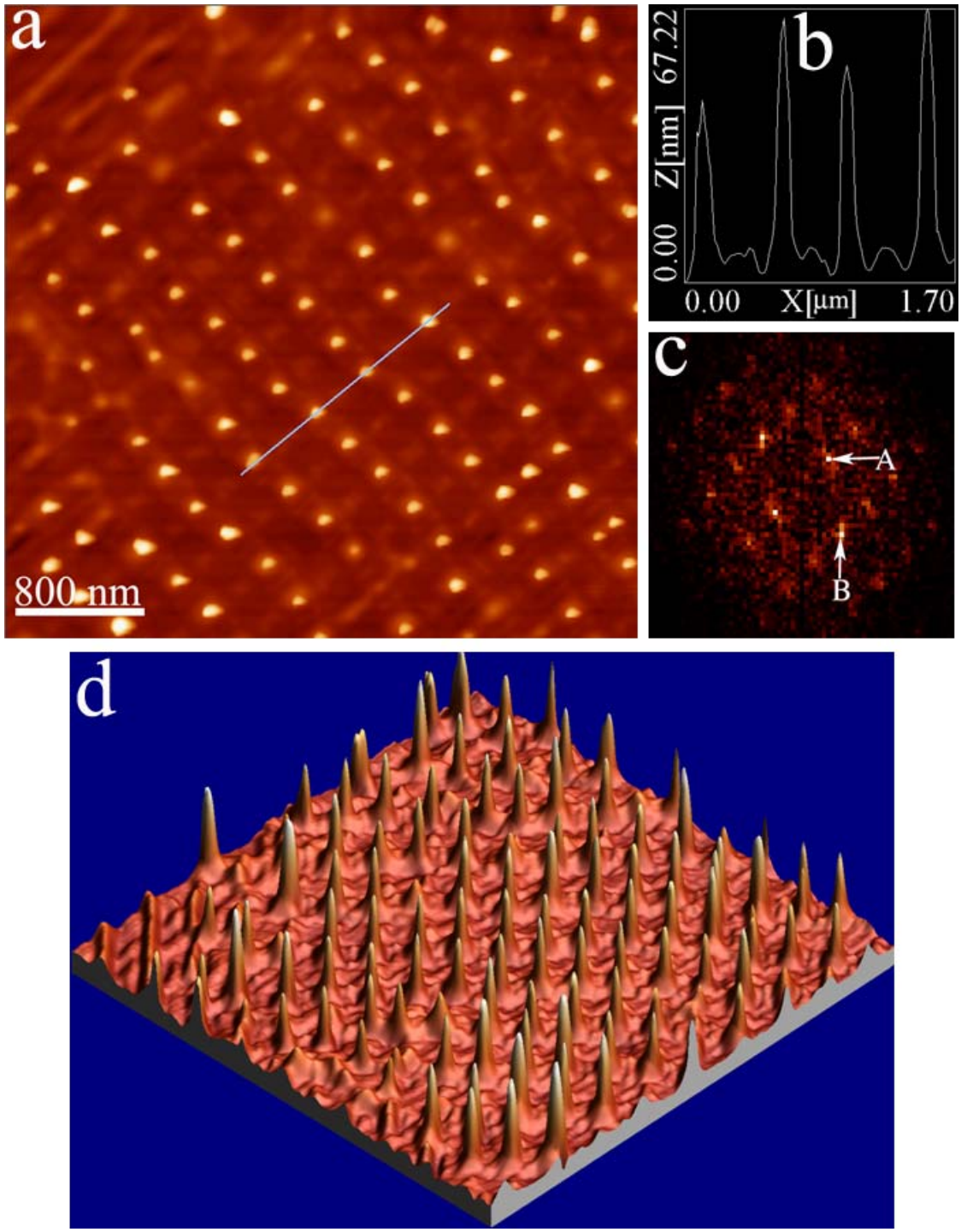

Figure 3.65 (a) 2-D AFM images showing aligned nanoprotrusions prepared under Lloyd's mirror configuration at laser fluence of ~0.7 J/cm^2, 2000 laser pulses, and the incident angle is 35˚. (b) Profile from trace marked on the AFM image. (c) FFT of the AFM image. Point A represents the cosine ripples, and point B represents the interference pattern. (d) 3-D AFM image of the sample.

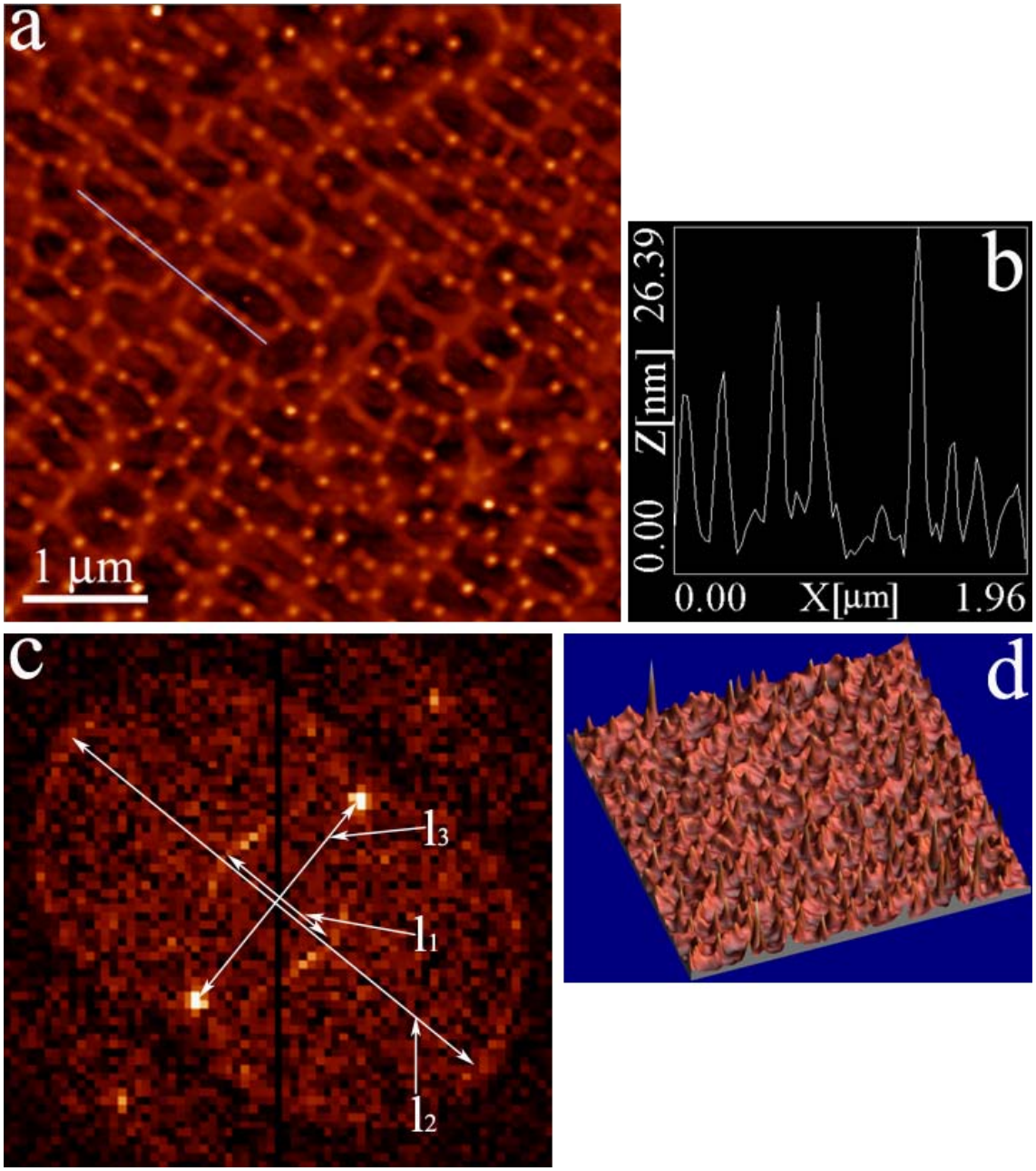

Figure 3.66 AFM images of nanoprotrusions emerging from irregular nanoripple structure. Specimen irradiated at 0.7 J/cm^2, with 1000 pulses. Angle of incidence: 40. (a) 2-D AFM image. (b) Profile taken along line marked in Figure a. (c) FFT with the two circles delineating possible ripple orientations account for apparently chaotic structure. Notice the two bright points at the circles' intersection, showing the prevalent presence of lines in the direction of the profiling, with spacing obeying the ripple equation 3.5. ℓ_1, ℓ_2, and ℓ_3 are marked by the arrows. The values can be used to derive the Λ-values and the value of θ_i.

section 3.3, all these orientations obey the grating equation. The FFT of the image, presented in Figure 3.66c, reveals that this pattern obeys the grating equation. Two circles delineate possible ripple orientations account for apparently chaotic structure. In the FFT we found two bright points at the circles' intersection, showing the prevalent presence of lines in the direction of the profiling, with spacing obeying the ripple equation 3.3 (cosine ripples). ℓ_1, ℓ_2, and ℓ_3 are marked by the arrows. Their values can be used to derive the Λ-values and the value of θ_i.

Another similar "chaotic" distribution of nanoprotrusions can be seen in Figure 3.67, which is also an AFM image. The sample was irradiated by non-polarized laser light with 1000 pulses, and the angle of incidence is 35˚. Compared with Figure 3.66, this image looks more random. However, all the nanoprotrusions are following the nanoripples right beneath them.

SEM study also shows the irregular distribution of nanoprotrusions. Figure 3.68 includes two SEM images, showing the surfaces of two different samples, which have been laser irradiated at an angle of incidence of ~35˚, after 1000 pulses.

Although in a vast majority of our observations the nanoprotrusions were associated with a subjacent organized ripple structure, in some instances no clear ordering was evident. Nonetheless, the apparently disorganized arrays had developed atop of nanoripples, in the same way as did the well ordered nanoprotrusions.

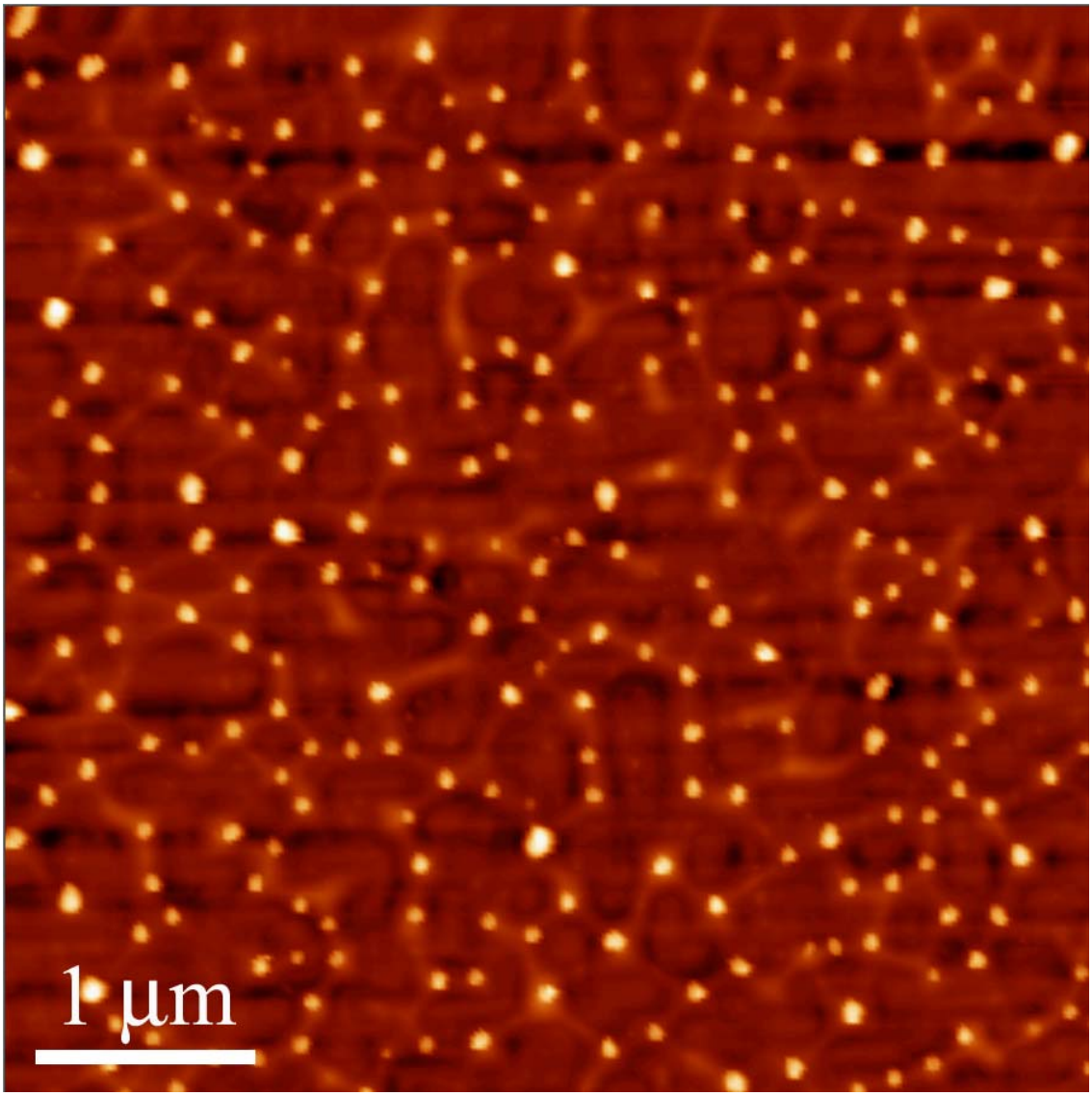

Figure 3.67 2-D AFM of nanoprotrusions emerging from irregular nanoripple structure. Specimen irradiated at 0.7 J/cm^2, with 1000 pulses. Angle of incidence: 35˚. Notice all the nanoprotrusions are sitting right on top of the nanoripples beneath.

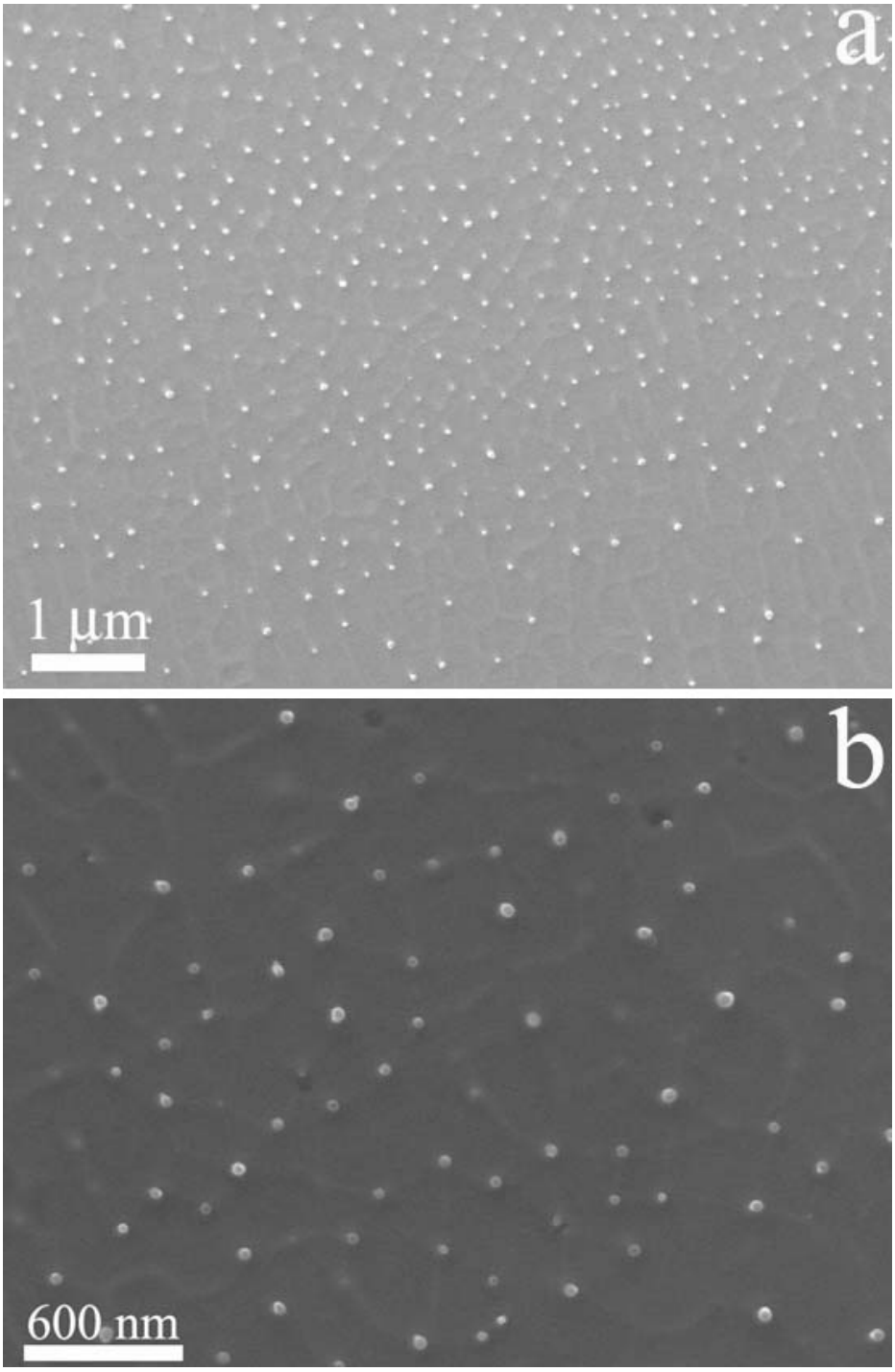

Figure 3.68 SEM images showing irregular distribution of nanoprotrusions, and the relative relationship between nanoripples and nanoprotrusions. (a) Sample has been irradiated by non-polarized laser light under Lloyd's mirror configuration after 1000 pulses; the angle of incidence is ~35˚. (b) Different sample from (a), but was produced under the same experimental conditions.

3.5 Formation of Self-organized Nanoparticles by Single Beam Illumination and Comparison with Nanoprotrusions

3.5.1 Formation and Alignment of Nanoparticles with Non-polarized laser beam

At slightly higher laser fluences than used to produce nanoprotrusions, nanoparticles were produced on the irradiated surface in a vacuum chamber filled with low pressure buffer gas of helium.

First, a thin film is formed as atoms and/or clusters are redeposited during irradiation on the illuminated surface, possibly due to backscattering caused by the gas molecules. Then, the clusters in the film aggregate further into the observed nanoparticles with random distribution. Finally, like any other surface roughness, the nanoparticles interact with the incoming radiation and, provided they can move into or condense on specific sites of the substrate, they could, in addition, order along rows by a mechanism similar to that of nanoripple and nanoprotrusion formation [208].

Prior to laser irradiation in the vacuum chamber, the silicon substrate was immersed in 10% hydrofluoric acid solution to remove the native oxide, as described in section 2. The sample was immediately put into a vacuum chamber and the vacuum system was pumped down to $1x10^{-6}$ Torr to prevent reoxidation of the silicon surface.

Figure 3.69 shows the sample surface after irradiation in 5 Torr He, after 100 pulses. The energy density of the incoming laser beam was ~ 1 J/cm^2. The incoming beam is normal to the sample surface. In this work, all the nanoparticle related work was done by non-polarized light. From Figure 3.69, a thin film with tears and fissures can be seen. Actually, some of the film already clustered into tiny particles. The film shown in the

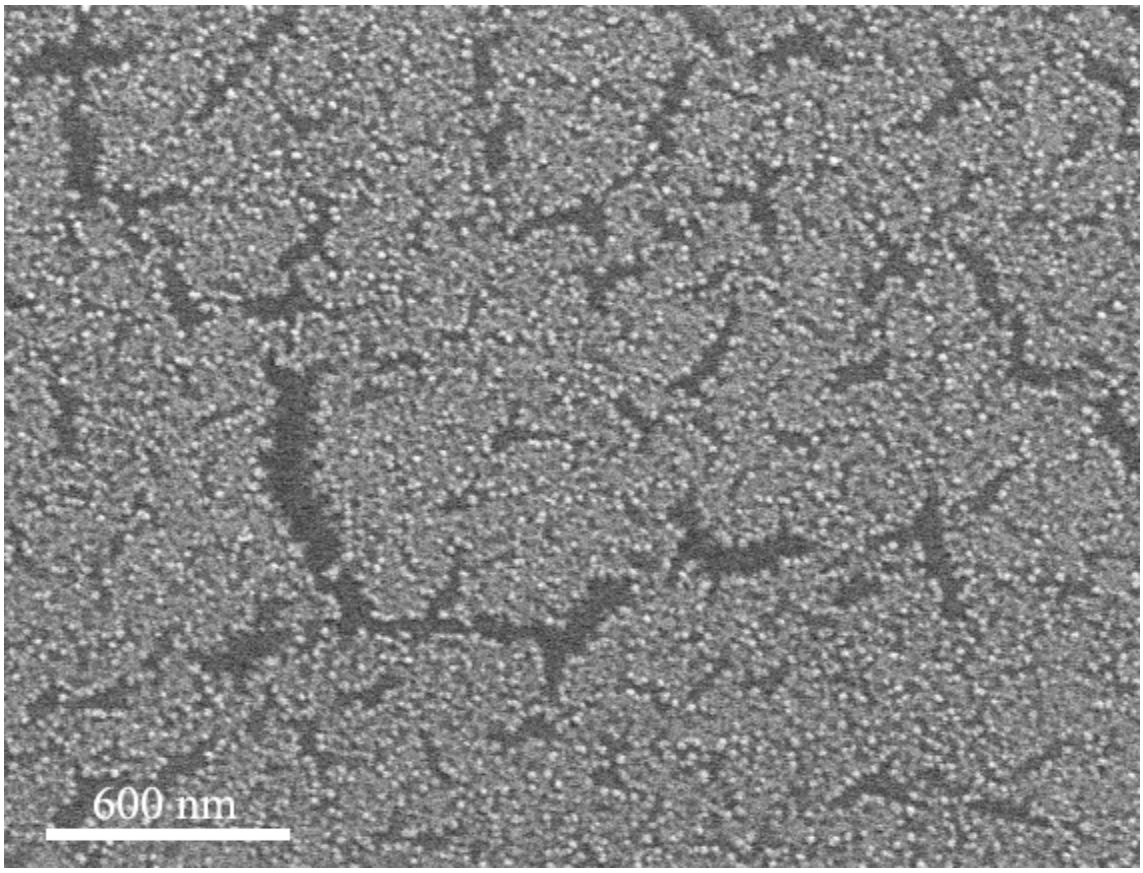

Figure 3.69 SEM image of the silicon film redeposited on the surface. Energy density of incoming laser beam is ~ 1 J/cm^2. Sample was irradiated in a vacuum chamber with a base pressure of 1x10^{-7} Torr, the ambient gas was 5 Torr UHP He. Number of pulses: 100. Non-polarized incoming laser beam was normal to the substrate. Prior to laser irradiation, native oxide layer on the sample surface was removed by 10% HF solution.

image is bright, while the tears and fissures are dark.

After 50 more shots under the same condition, more film has clustered into nanoparticles. Figure 3.70 shows more film has been consumed to form nanoparticles. These two SEM images are strong proof that the formation of nanoparticles is due to the clustering of the thin film.

Additional laser irradiation in helium triggered the self-organization of the nanoparticles into straight line. Figure 3.71 is an SEM image showing that after 200 non-polarized laser pulses at normal incidence, the randomly distributed nanoparticles align along straight lines. Due to normal incidence, the line spacing between aligned nanoparticles is 248 nm.

AFM was also used to characterize the aligned nanoparticles. Figure 3.72 shows both high and low magnification AFM images of the nanoscale-aligned rows of nanoparticles. Figure 3.72d is the profile of the trace line in Figure 3.72b. Arrows “A” represent the profiles of the nanoparticles and arrows “B” represent the profiles of nanoripples. Figure 3.72c is the 3-D AFM image of Figure 3.72b. Both 3-D image and the profile can indicate the relative relation between nanoparticles and nanoripples. It is clear that nanoprotrusions are sitting between nanoripples. And both nano-scale structures have more or less the same height.

Figure 3.73 is the AFM image showing only a small amount of individual nanoparticles. Figure 3.73b is the profile of a trace line connecting the centers of two nanoparticles. From the profile, we can see that the distance between nanoparticles is exactly 248 nm. 3-D AFM image is shown in Figure 3.73c.

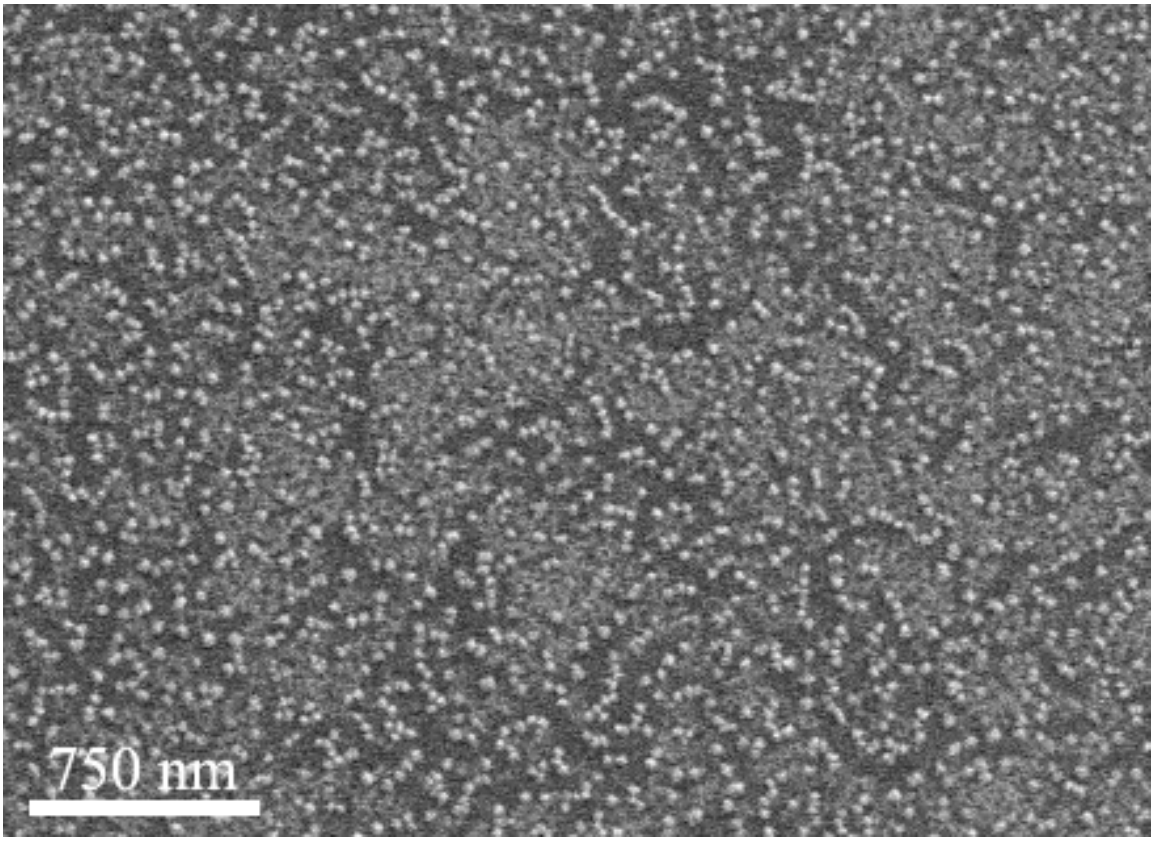

Figure 3.70 SEM image showing the sample irradiated under the same experimental conditions as figure 3.69, but with 50 more laser pulses. The gray region in the image represents thin film, while the dark region is the substrate. Notice that the area covered with thin film has decreased with more number of laser irradiation. In the meantime, the number and dimension of the nanoparticles have increased, which indicates that the formation of nanoparticles is by consuming thin film re-deposited during the laser irradiation.

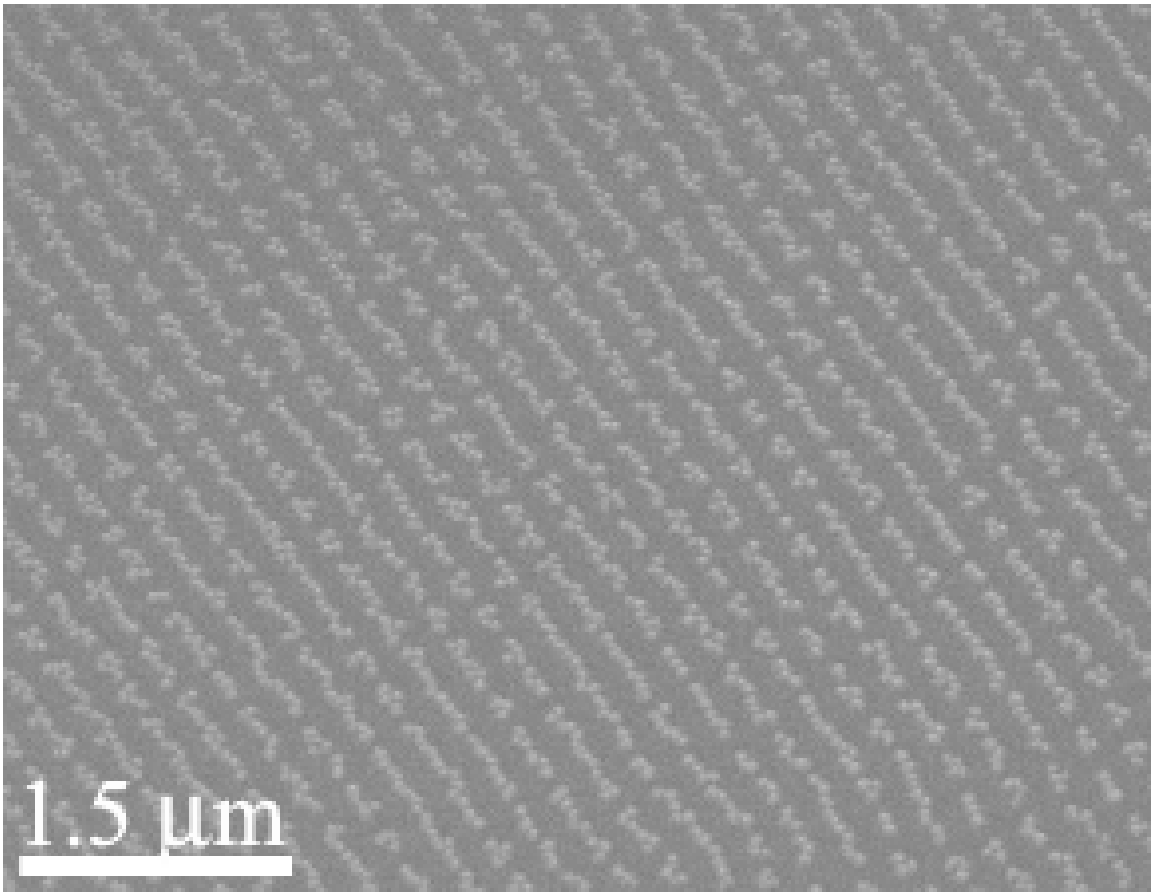

Figure 3.71 SEM images showing after a total of 200 laser pulses, aligned nanoparticles distributed on the surface, exhibiting long range ordering. Sample was irradiated under the same condition as Figure 3.69 and 3.70 but with more number of laser pulses. Notice in this image, all the thin film observed before has been consumed, and the particle size is much bigger.

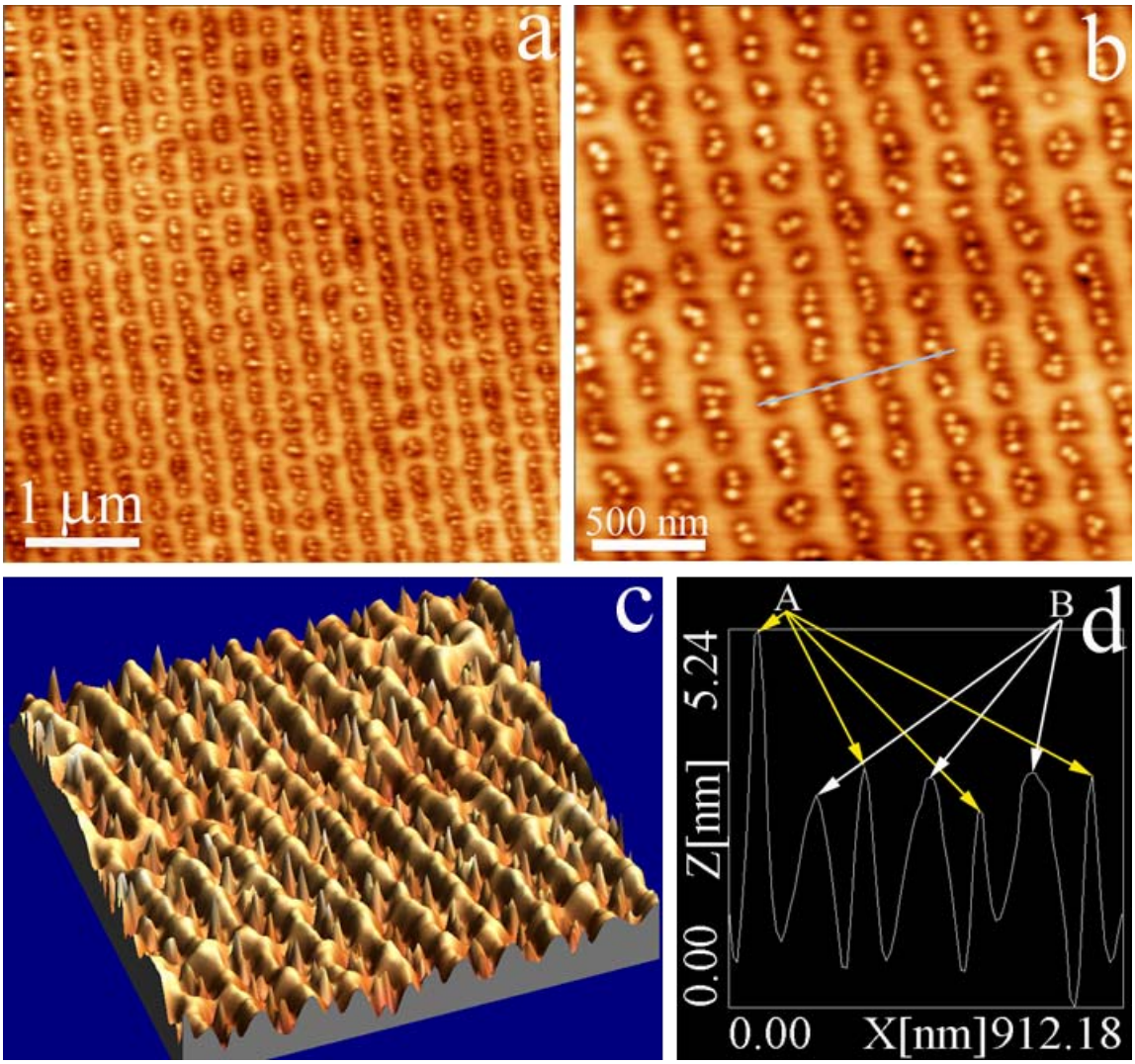

Figure 3.72 AFM study on the self-organized long range nanoparticles. (a) Top view of the sample surface at lower magnification. (b) High resolution 2-D AFM image. (c) 3-D AFM image of Figure b. Notice the nanoparticles are sitting between the nanoripples. (d) Profile of the trace line marked in Figure b. Arrows "A" represent nanoparticles and arrows "B" represent nanoripples. From the profile, we can see that nanoripples and nanoparticles have similar heights.

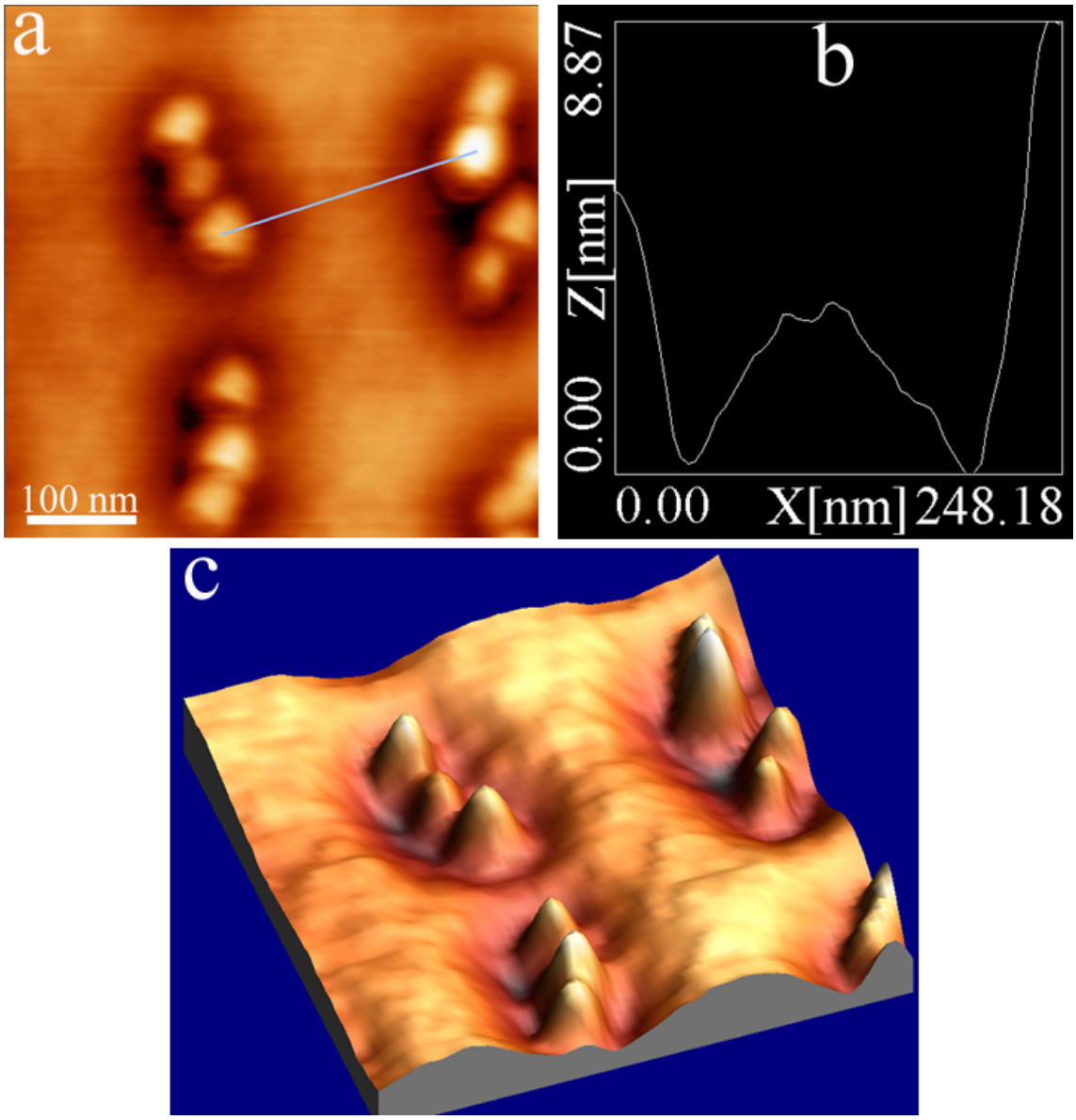

Figure 3.73 AFM image showing only a small region of the long range nanoparticles. (a) 2-D AFM image. Trace line connects two nanoparticles separated by the nanoripple. (b) Profile of the trace line in Figure a. Distance between those two particles is exactly 248 nm, because the incoming beam is normal to the sample surface. (c) 3-D AFM image showing the relative position of nanoparticles and nanoripples.

3.5.2 Comparison between Nanoparticles and Nanoprotrusions

There are several differences between the processing procedures of nanoparticles and those of nanoprotrusions.

Most relevantly, nanoparticles are produced by single beam irradiation, whereas nanoprotrusions were only observed under the double beam irradiation generated with the Lloyd's mirror.

The incident laser fluence to create nanoparticles was on the order of 1 J/cm^2, whereas nanoprotrusions were formed with a beam fluence of 0.7 J/cm^2.

The third difference would be the atmospheres where the treatment is taking place. For nanoprotrusions, we did not observe any difference between processing in vacuum and in air. And the experimental results are not sensitive to native oxide layer either. However, due to the nature of formation of nanoparticles, high base vacuum pressure and oxygen free environment is required.

From a structural point of view, similar to nanoprotrusions, nanoparticles appear in most instances associated with a ripple structure. However, whereas nanoprotrusions grow in the crests of the ripple structure, nanoparticles are detected in the valleys. For example, Figure 3.52 shows the relative position of nanoripples and nanoprotrusions. From that figure, we can see clearly that nanoprotrusions are located on top of the ripples, and the height of the nanoprotrusions is much larger than the nanoripples. Figure 3.72, on the contrary, shows similar heights for both nanoripples and nanoparticles, and the nanoparticles are distributed along the valleys.

Another difference is the stability of the two nanostructures upon thermal treatment. Both samples were annealed at temperatures between 423 and 1073K in vacuum, for 2

hours. Even at the lowest temperature of this range, 423K, nanoparticles performed a Brownian-like motion thus losing their initial alignment, as can be clearly seen from the comparison between SEM images of Figures 3.74a and b. Figure 3.75a, b and c are the AFM images showing the aligned nanoparticles before annealing, after 2 hours' annealing at 250 ˚C, and after annealing at 700 ˚C for 2 hours, respectively. Comparison between those three images indicates that even after annealing at 250 ˚C, the nanoparticles lost their alignment completely. One interesting phenomenon is that the straight nanoripples became zigzag after annealing as well. This is evidence that connects the nanoripples and nanoprotrusions. No changes were observed on the nanoprotrusion structure after annealing in the entire range of temperatures.

It has been previously reported that nanoparticle alignment took place if either a microstructure of cones was present in the substrate or polarized light was employed. In this work we have found that neither one is required to generate an aligned nanoparticle structure. All the samples illustrated by SEM and AFM images in this section were prepared by non-linearly polarized laser light on a smooth silicon surface. The reasons for the differences will be discussed in chapter 4.

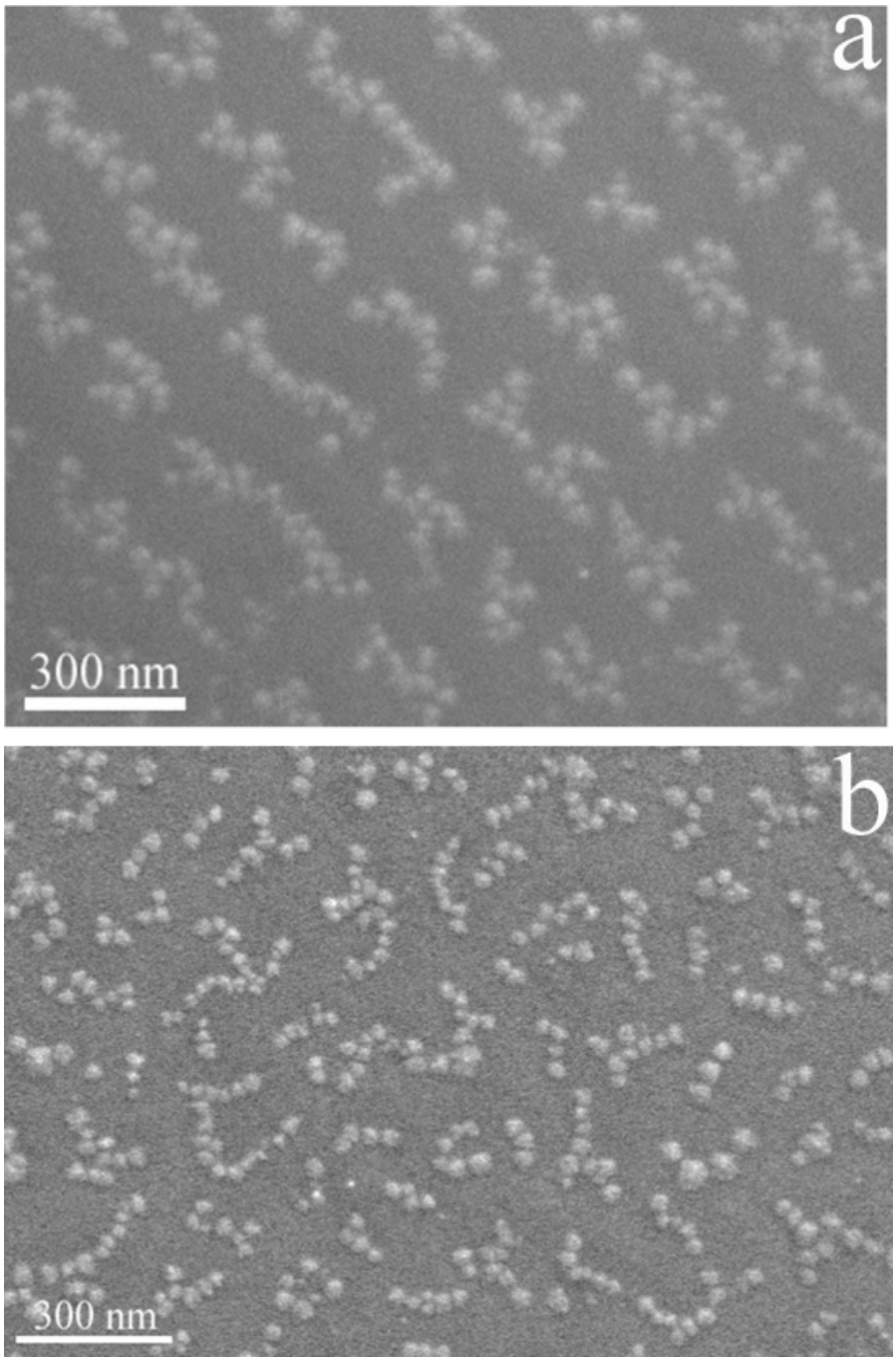

Figure 3.74 SEM images comparing self-organized nanoparticles samples before and after annealing. (a) Long range arrays of aligned nanoparticles after 200 laser pulses. E_d= 1 J/cm^2, 5 Torr UHP He. (b) The alignment no longer exists after annealing treatment in a vacuum chamber at 423 K for 2 hours. Base pressure of the chamber is 1x10^{-7} Torr.

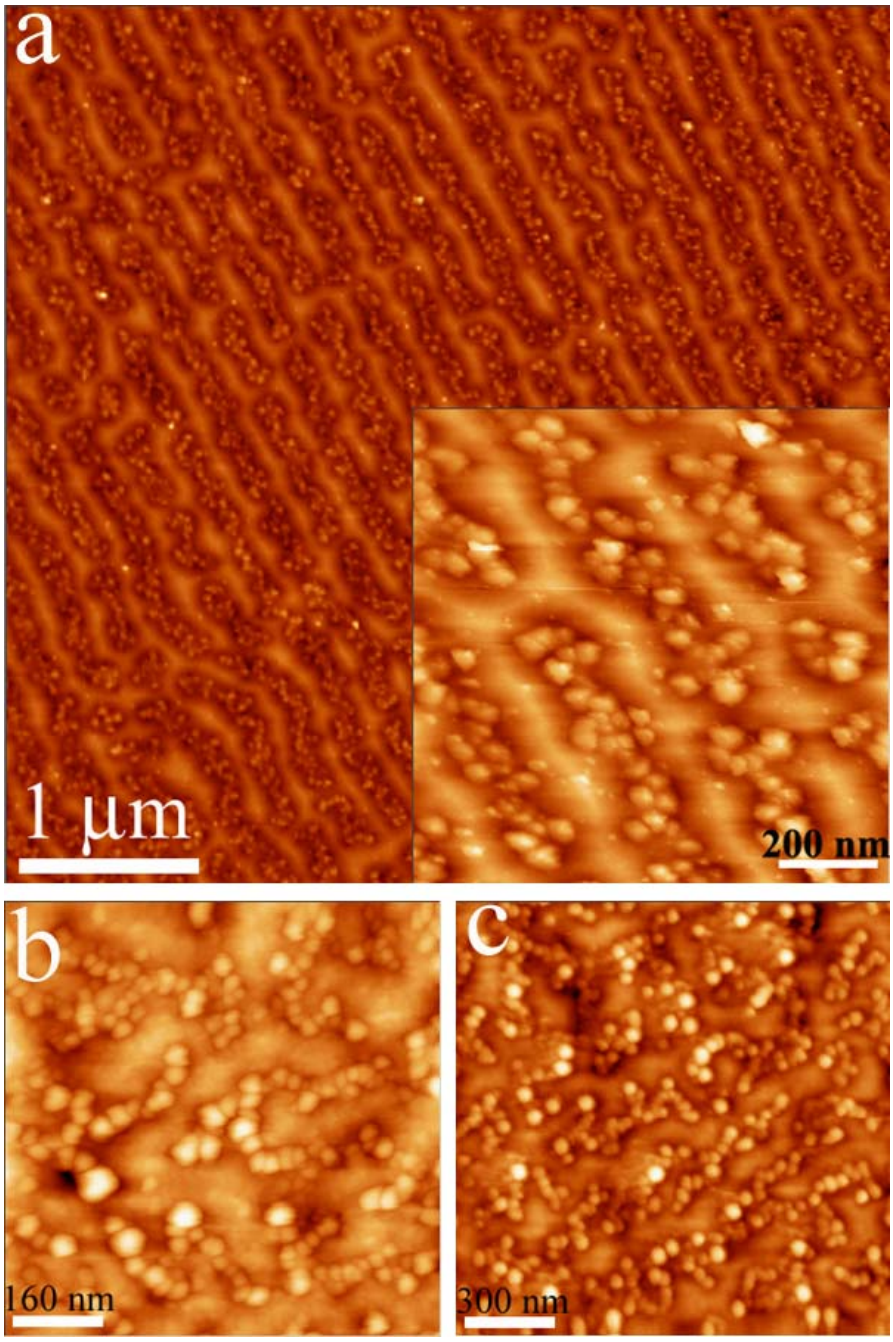

Figure 3.75 Thermal stability study of nanoparticles by AFM. (a) AFM image of Si nanoparticle chains before annealing. Nanoparticles were produced with 200 laser pulses in 5 Torr UHP He (E_d= 1 J/cm^2). Inset in Figure a is the high resolution 2-D AFM image. (b) AFM image showing the sample after annealing in vacuum at 523 K for 2 hours. Even at this low annealing temperature, the alignment of nanoparticles is already lost. (c) AFM image showing the sample after annealing in vacuum at 1023 K for 2 hours.

3.6 Alignment of Au Nanoparticles by Applying the Nanostucture Templates Produced under Lloyd's Mirror Configuration

In section 3.3 and 3.4 nano-LIPSS and nanoprotrusions with long range order have been produced under Lloyd's mirror configuration. Nanoscale silicon lines and protrusions up to 100 nm have been aligned through this treatment. However, due to the formation mechanism of those nanostructures, the only material that can be aligned is the same as the substrate, in our case silicon.

We have been studying on how to align other nanoscale materials other than silicon by applying the templates with nanoripples and nanoprotrusions. In this study, gold particles have been used to test the effectiveness of the method.

3.6.1 Heat treatment on samples with Au film

Au film has been deposited by using an ion beam sputtering machine (Dual Ion Mill 600 from Gatan) operating at 8 KV, 1 mA. The thickness of the film is controlled by the ion beam deposition time. Prior to ion deposition, the base pressure of the vacuum chamber reaches $1x10^{-7}$ Torr. Figure 3.76 is the schematic image of the deposition process. The ion beam shoots the gold target at an angle of incidence of ~30˚. Then a plume forms under irradiation of the continuous ion beam. The silicon substrate, which was prepared using Lloyd's mirror arrangement, was set at a position normal to the plume. The deposition rate of Au film was 30 nm/minute.

Figure 3.77 shows the surface of the silicon substrate after ion beam deposition for 30 seconds. According to the deposition rate of Au film, after 30 seconds deposition, the

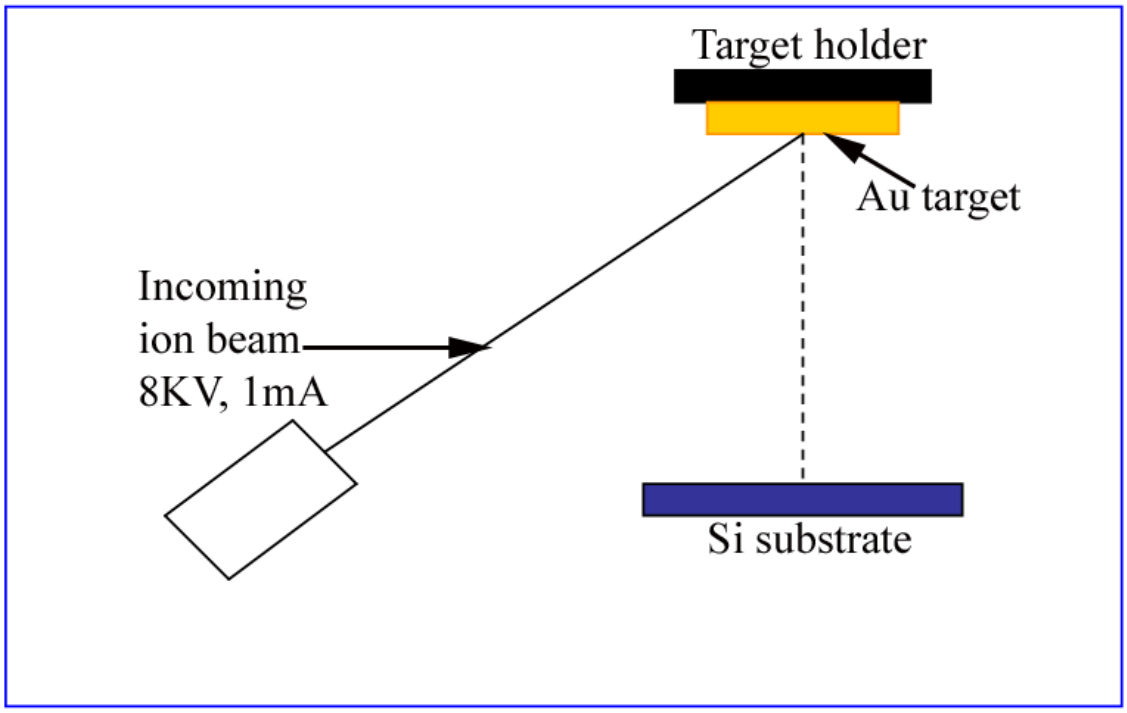

Figure 3.76 Schematic image showing the ion beam deposition of Au film onto the silicon substrate. Base pressure of the vacuum chamber is $1x10^{-7}$ Torr, and the ion beam was generated at 8 KV, and the current has been set to 1 mA. The angle of incidence of the incoming ion beam is ~30˚. The plume reaches the silicon substrate at normal incidence. The thickness of the deposited Au film is controlled by the deposition time. Normally, it takes 60 seconds to deposit 30 nm thick Au film.

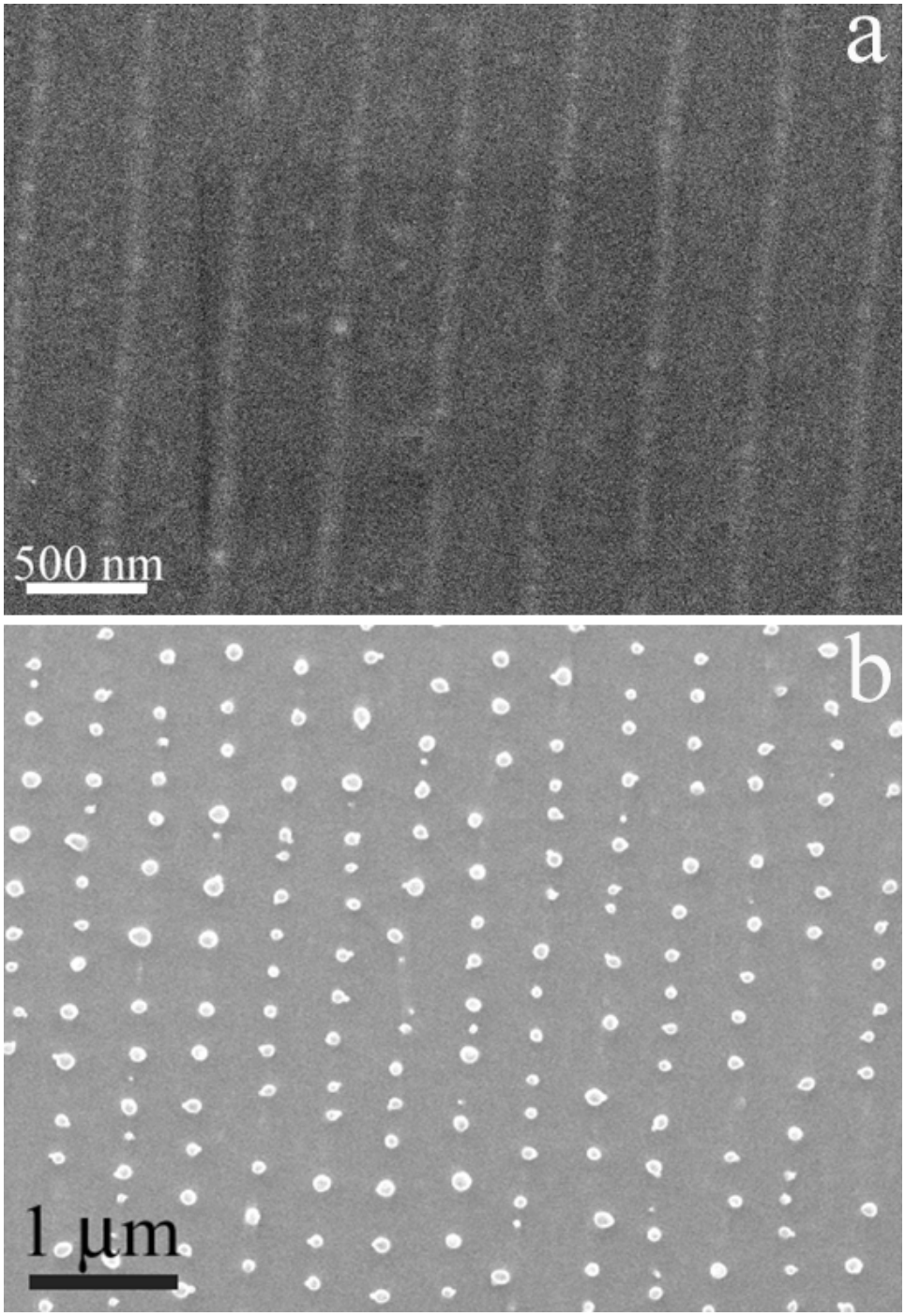

Figure 3.77 SEM image showing the sample with nanoscale structures (nanoriples/ nanoprotrusions) prepared by using Lloyd's mirror configuration. Thin Au film has been deposited by ion beam machine. Configuration is shown in Figure 3.76. The deposition conditions are: Voltage=8 KV, Current=1 mA, and deposition time=30 seconds. Due to the smoothness of the gold film, there is not enough SEM contrast for the film to be detected.

film thickness is 15 nm. However, SEM imaging of the Au film was unsuccessful. This may due to a lack of contrast present in the Au film deposited by ion beam. The film roughness is of a roughness < 1 nm, which is the resolution limit of the microscope we are using (Hitachi 4300), and is beyond the capability of the microscope to image.

In order to increase the roughness of the gold film, we annealed the sample in a furnace at 700 ˚C for 1.5 hours. Figure 3.78a is the SEM image showing the same sample as Figure 3.77 after annealing, and we can see clearly the tiny Au nanoparticles distributed all over the surface. Figure 3.78b is the high resolution SEM image, and from that we can see the diameter of the gold particle formed after film clustering is ~10 nm. The annealing treatment has been proved to be an effective way to increase the clustering of Au thin films, which can increase the contrast of Au specimen under the microscope.

The amount of gold deposition on the surface can be controlled by deposition time and can change the surface morphology dramatically. Figure 3.79 shows the sample annealed under the same heat treatment condition as Figure 3.78, but the ion beam deposition time is 3 minutes instead of 30 seconds. According to the deposition rate, after 3 minutes ion beam deposition, the Au film thickness should be 90 nm. After annealing treatment, the dimension and number of gold particles have drastically increased. Figure 3.79b is the SEM image taken at higher magnifications. Because the atomic weight difference between Si (28) and Au (197) is huge, the difference in SEM contrast is big as well. Due to the large atomic weight of Au, more secondary electrons can be produced by Au specimen, so the gold particle looks much brighter than the silicon specimen. The SEM image in Figure 3.79b also shows that the particle size has increased to ~50-100 nm.

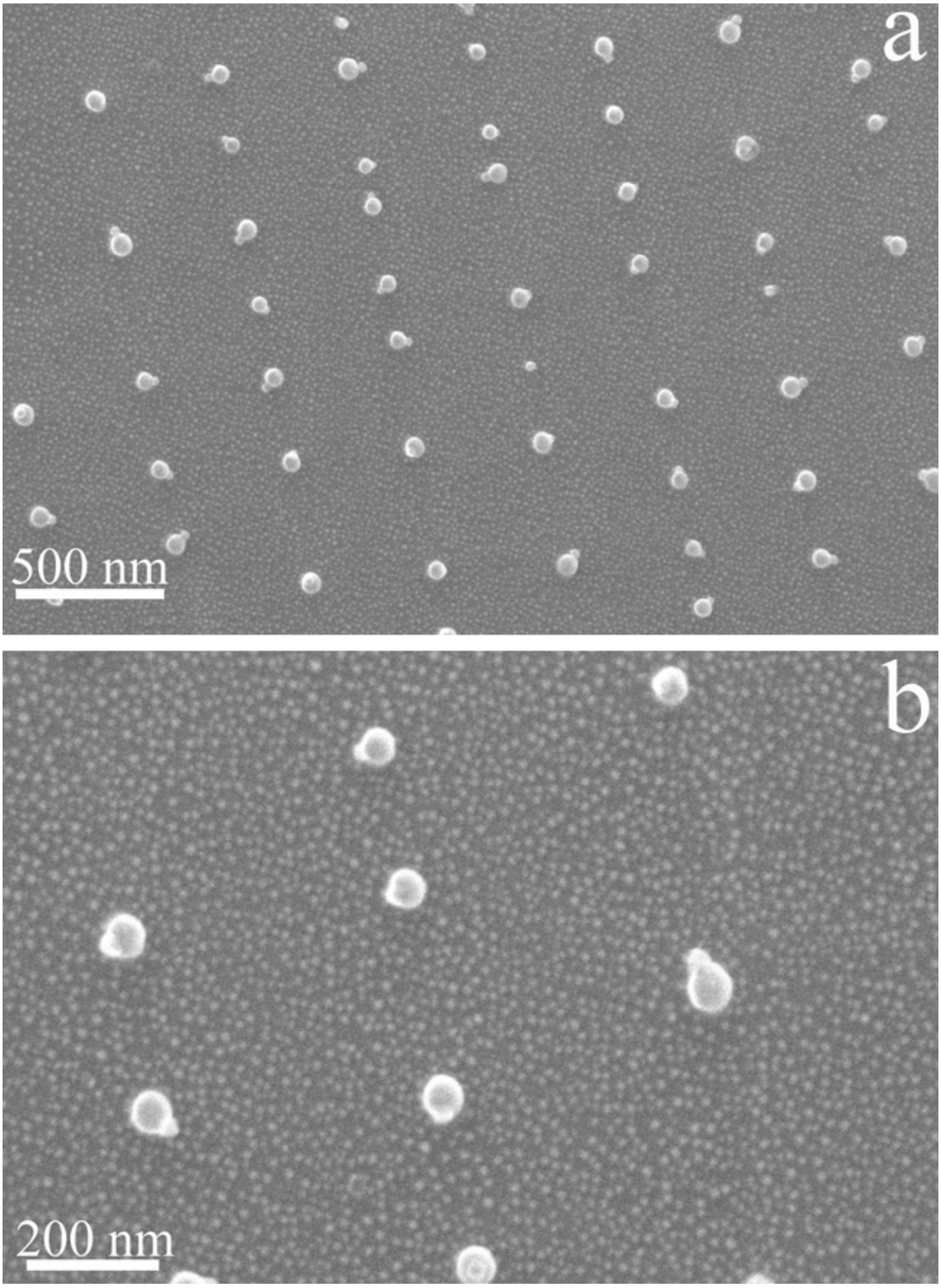

Figure 3.78 SEM images showing the same sample as Figure 3.77, but has been annealed at 700 ˚C for 1.5 hours. Au nanoparticles with diameters ranging from ~5-20 nm can be detected. Au thin film has clustered into nanoparticles during the heat treatment.

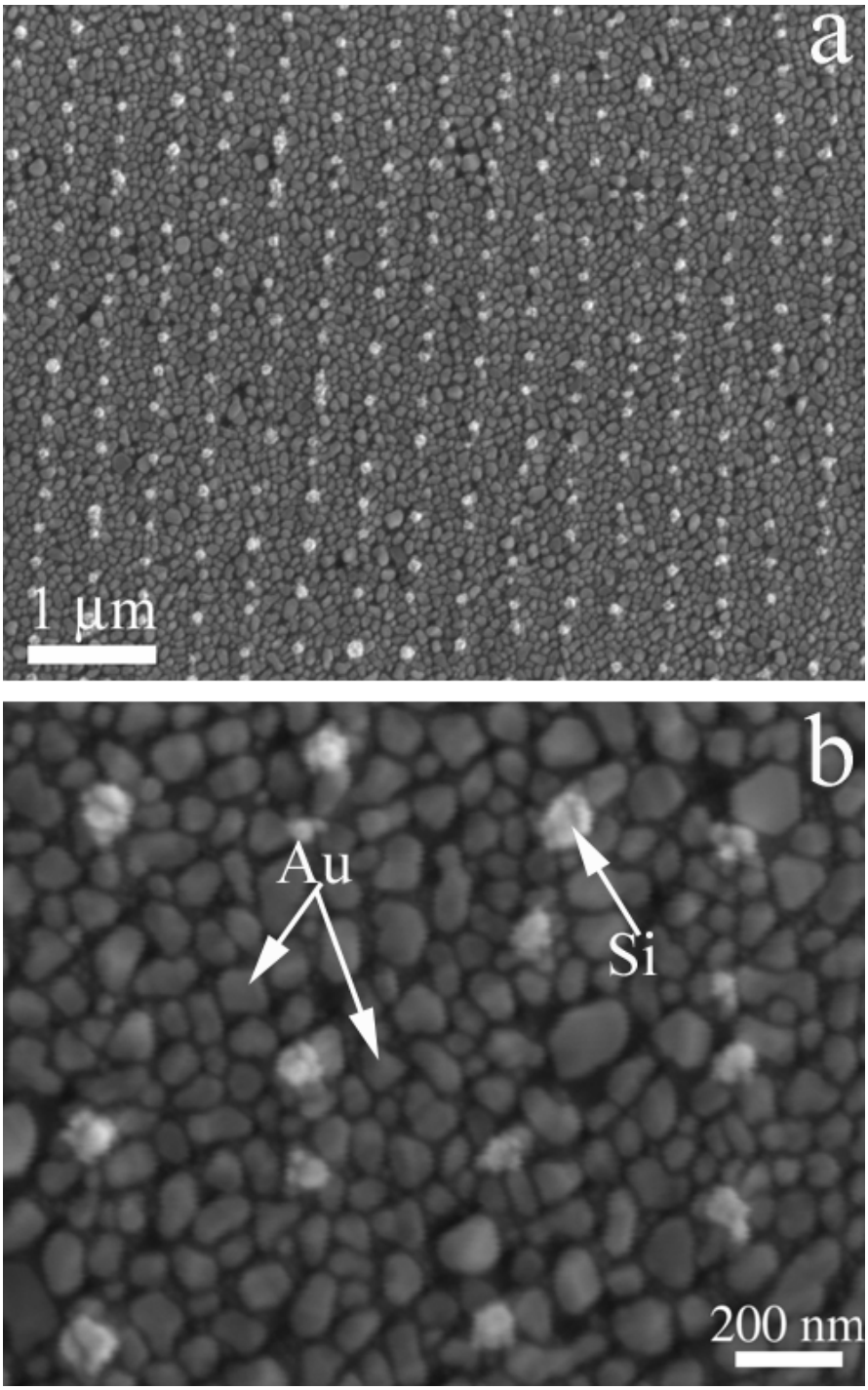

Figure 3.79 SEM images showing samples been annealed under the same conditions as Figure 3.78, but with six times more gold deposition on the surface. (a) SEM image taken at lower magnification showing the number of gold particles has increased. (b) High resolution SEM image showing the gold particle size has increased to 50-100 nm. Arrows in the figure point to silicon protrusions and gold particles respectively.

In all experiments reported below, the deposition time will always be 30 seconds.

The effects of annealing temperature and time have also been studied. First, samples prepared under identical conditions have been annealed at different temperatures for the same amount of time. We have tested all together 12 different temperatures: 400, 450, 500, 550, 600, 650, 700, 750, 800, 850, 900 and 1000 ˚C. And it turned out that the threshold for gold film clustering is ~ 550 ˚C. No clustering has been observed when the annealing temperature is below 550 ˚C. However, the difference between 600 to 900 ˚C is not noticeable. Once the temperature reaches 1000 ˚C, it takes less time for the film to cluster, and after 2 hours, the gold particle size is bigger than samples heat-treated at lower temperatures.

The film clustering process is actually a diffusion process. So it is a function of temperature and time. In order to see how far the gold particle can diffuse at high temperature, we put the sample in a furnace at 800 ˚C for 4 hours and 24 hours, respectively. Figure 3.80 and 3.81 are the SEM images showing the results after 4 hours and 24 hours of heat treatment. There is huge difference between those two samples. After 4 hours annealing, the gold particles tend to move towards the silicon protrusions (Figure 3.80). More gold particles can be found around the protrusions. However, after total of 24 hours' heat treatment, the gold particles have enough time to diffuse into continuous "continents" (Figure 3.81a). Figure 3.81b is the high resolution SEM image showing the large gold particles whose dimension has increased to ~250 nm, while no gold particles are left around the nanoprotrusions. This experiment shows how dramatic the annealing time can affect the diffusion process.

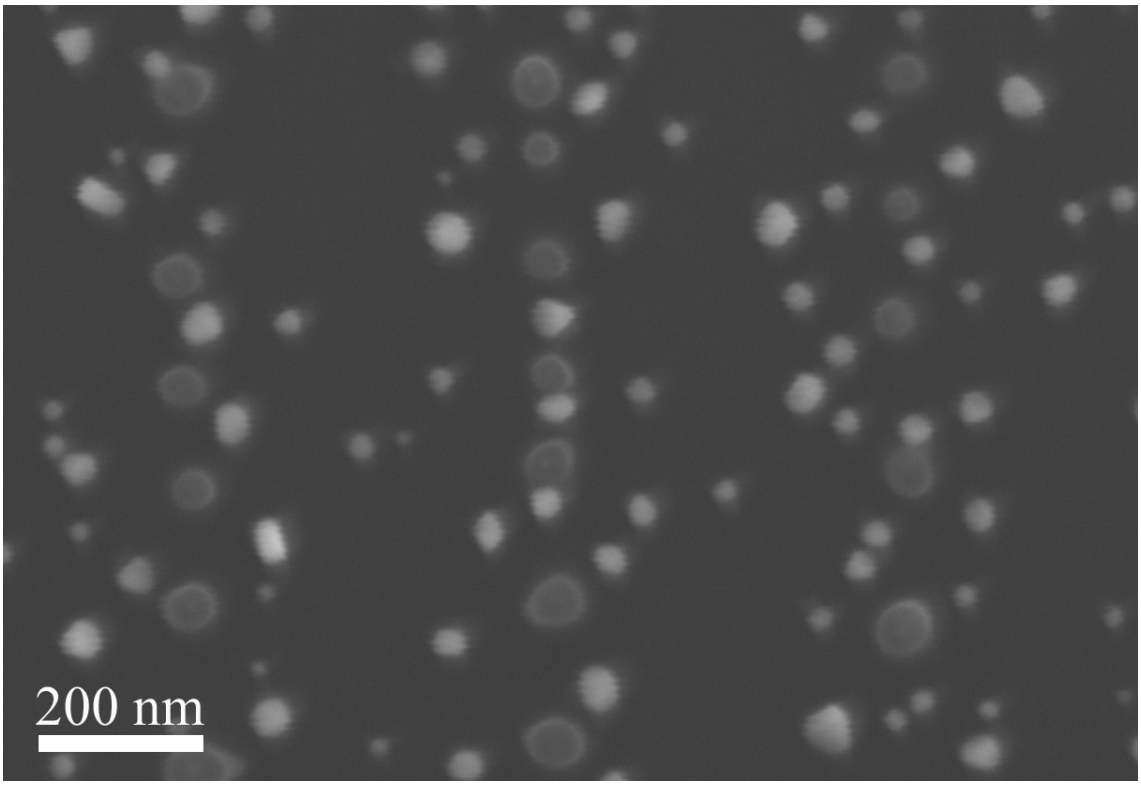

Figure 3.80 SEM image showing the relative position of Au nanoparticles to the nanoprotrusions. It is clear that the gold particles tend to move to the nanoprotrusions. The sample has been annealed for 4 hours at 800 ˚C. Comparing with Figure 3.78b, we can see that the dimension of Au nanoparticles has increased a lot.

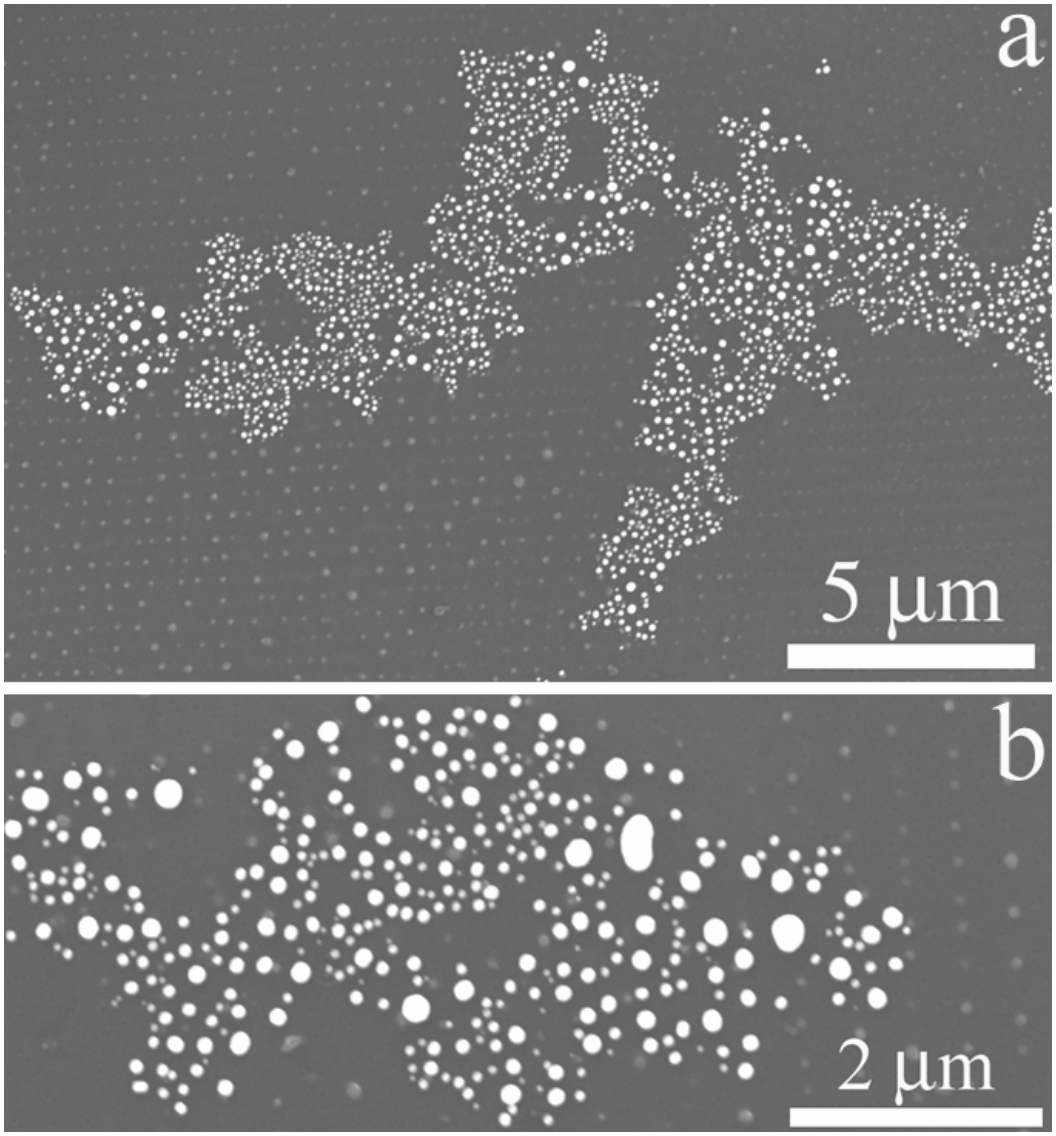

Figure 3.81 SEM images showing the distribution of Au particles after 24 hours annealing at 800 ˚C. (a) Lower magnification SEM image showing that the gold particles moved together forming continuous "continents". (b) High resolution SEM image indicating the diameter of previous ~50 nm gold particles have increased to ~250 nm, and no Au particles are left around the silicon nanoprotrusion.

3.6.2 Alignment of Au Nanoparticles by Depositing Au Film at Low Grazing Angles

In previous section, the gold film was deposited onto the silicon substrate at normal incidence. Upon heat treatment, there is a clear tendency for the gold particles to move towards the silicon nanoprotrusions. However, that is not enough to align gold particles into straight lines.

The height of nanoripples produced by using Lloyd's mirror configuration is ~ 15 to 20 nm, and the diameter of nanoprotrusions formed under the same condition is ~100 nm. If we put the sample surface in such a position that the atomic beam is parallel or at a very small angle to the surface, then the atoms will be blocked by the roughness on the surface and can only be deposited on part of the ripples or protrusions. Figure 3.82 shows the idea of depositing gold film on part of the nanoripples or nanoprotrusions by controlling the grazing angle.

A series of grazing angles have been tested to find out the optimal alignment conditions.

The template used for aligning gold particles was prepared by using Lloyd's mirror with an angle of incidence of ~35˚. The line spacing between cosine ripples in the template was 303 nm and the height of those ripples was 16 nm. Schematic image of the template used and the corresponding grazing angles are shown in Figure 3.83. According to the dimension and line spacing of nanoripples in the template, we can calculate that when the grazing angle is 3˚, the only region that deposition of Au films can take place is on one side of the ripple, as shown by θ_2 in the figure. θ_1 and θ_3 in the figure represent larger and smaller grazing angles respectively. When the grazing angle is

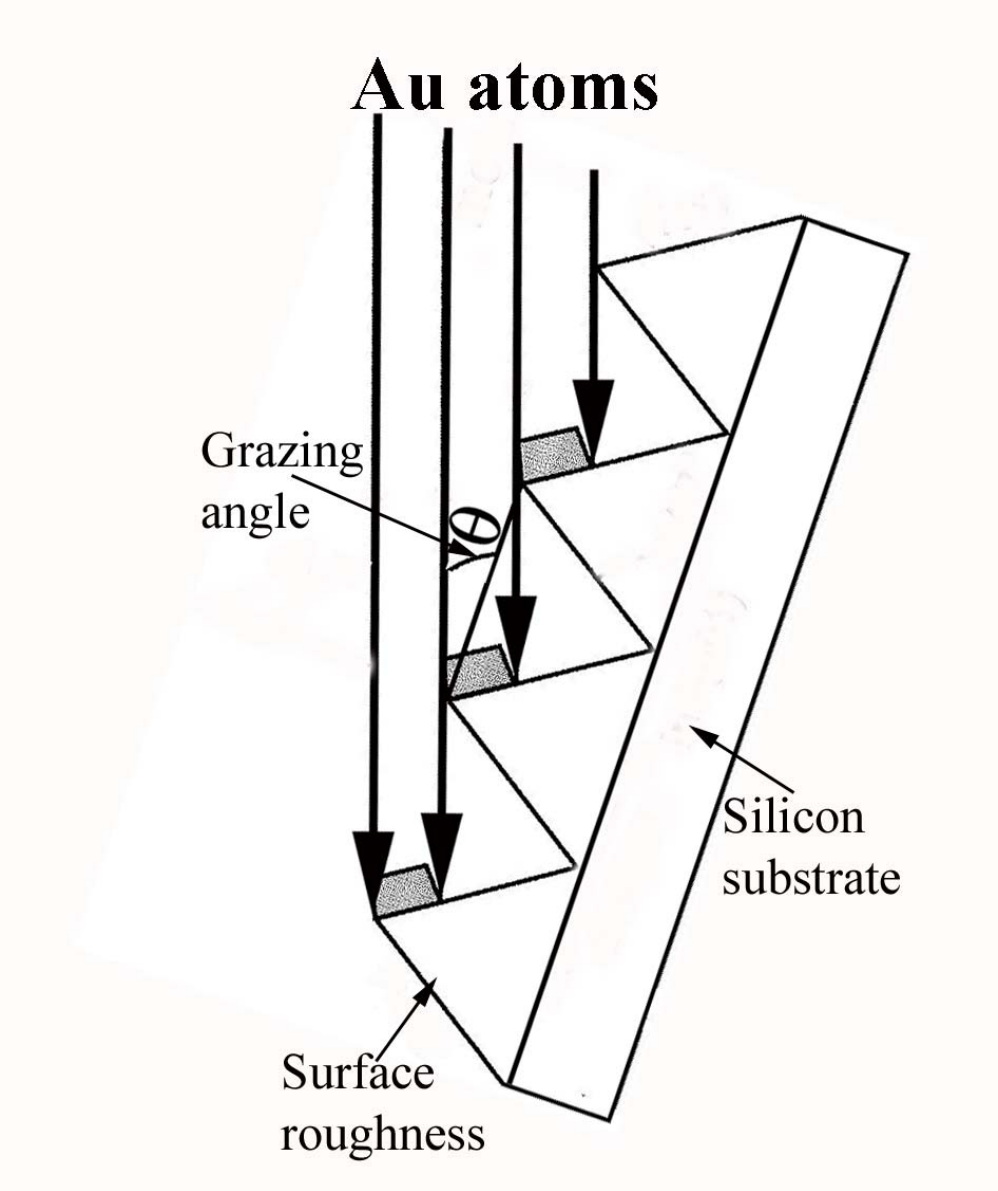

Figure 3.82 Schematic image showing the Au film deposition by ion beam sputter deposition at a very small grazing angle. Due to the surface roughness, gold film can only be deposited on one side of the roughness, thus makes the alignment possible.

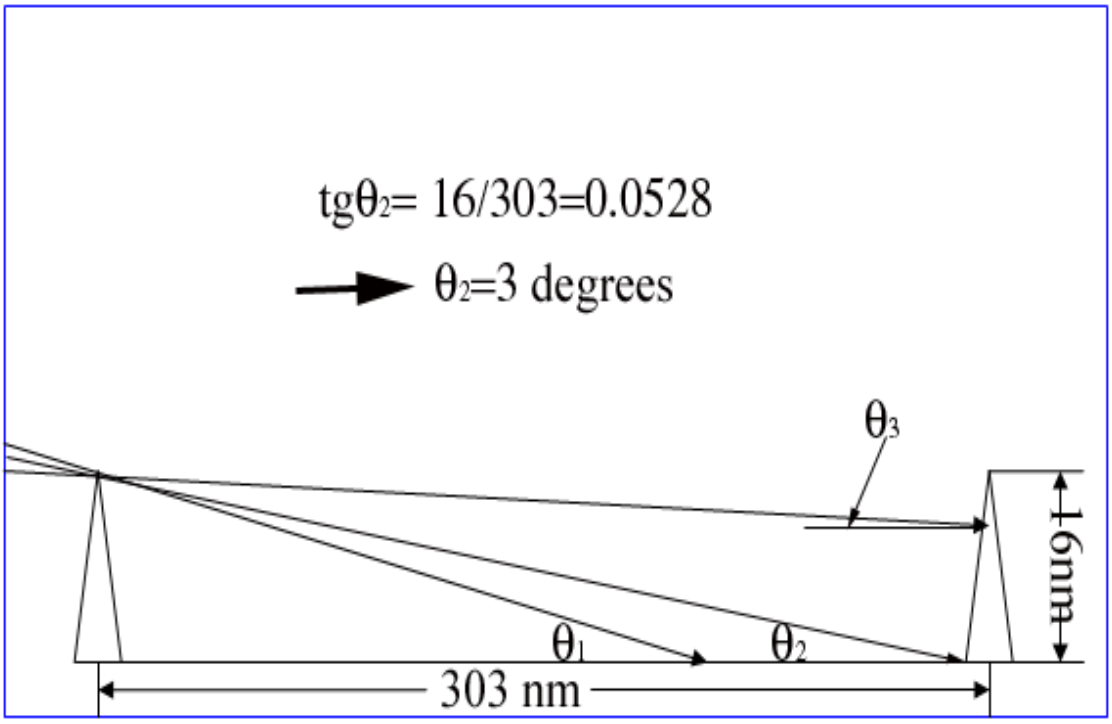

Figure 3.83 Schematic image showing the relationship between grazing angle of the incoming gold ion beam and the region where the beam can cover. The cosine nanoripples in the template is 16-nm-high and 303 nm is the distance between each nanoripples. When the grazing angle is 3˚, the only region that gold deposition can take place is on the left side of the ripple, which is shown in the figure. By increasing or decreasing the grazing angle we can increase or limit the deposition area. When the grazing angle is close to zero, only the top part of the ripples can be covered by the gold films.

close to zero, only the upper part of the ripples will be covered by the deposited gold film, while at larger grazing angle, the region covered by gold increases.

Figure 3.84 is the SEM image showing the distribution of gold nanoparticles after deposition of gold film at a grazing angle of 3˚. The sample has been annealed at 800 ˚C for 3 hours. The deposition of gold film was performed at a base pressure of ~$1x10^{-7}$ Torr. Compared with deposition at normal incidence to the substrate, at small grazing angle, the amount of gold film that can be deposited on the substrate has decreased drastically. The deposition time in this experiment was 5 minutes.

Figure 3.84a shows the alignment of gold strip along the cosine nanoripples, and Figure 3.84b shows that the gold particles are located on silicon nanoprotrusions. We can see that the gold particles on the protrusions are much bigger than that aligned along the nanoripples. The reason is that the dimension of nanoprotrusions is much larger, so the amount of gold deposited on the protrusions is more than that on the ripples. During annealing treatment, the clustering of more gold film leads to the formation of bigger particles.

After increasing the grazing angle, the width of gold strip increase as well. Figure 3.85 shows the surface of a sample that has been deposited with gold film at a grazing of 5˚. We noticed a large increase in the width of the strip made of gold particles.

However, from Figure 3.83, even when the grazing angle is 5˚, the region where gold deposition can take place should be much smaller. The wider distribution of gold particles may due to the diffusion during the heat treatment, but another more important reason is due to the direction of incoming gold ions. In Figure 3.83, we assumed that the incoming Au ions are parallel to each other and normal to the ground. Actually, from

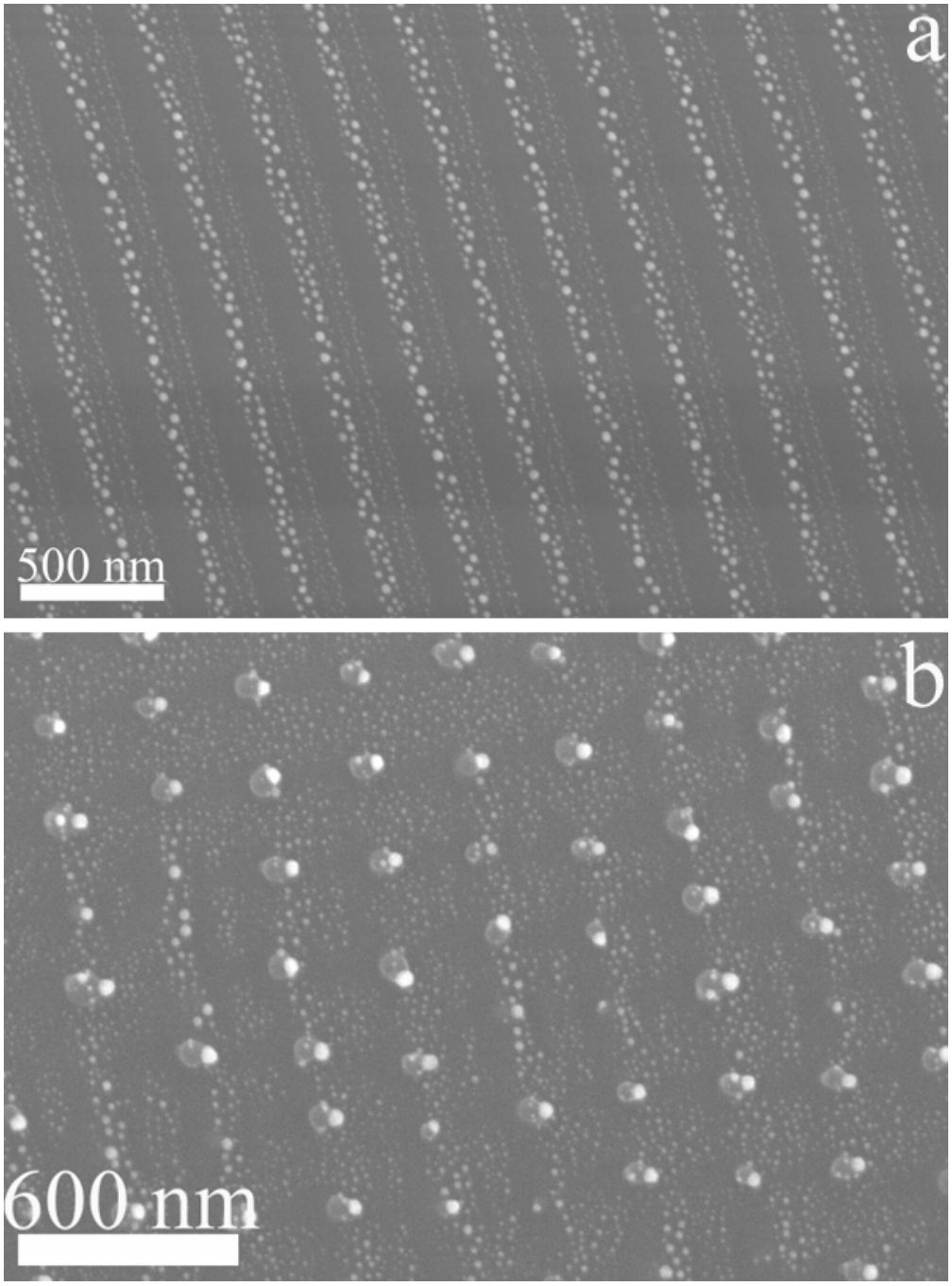

Figure 3.84 SEM image showing the distribution of gold nanoparticles after deposition of gold film at a grazing angle of ~ 3˚ for 5 minutes. The sample has been annealed at 800 ˚C for 3 hours. (a) SEM image shows the alignment of gold strip along the cosine nanoripples. (b) SEM image shows that the gold particles are located on silicon nanoprotrusions. Notice that the gold particles on the protrusions are much bigger than that aligned along the nanoripples, due to the different dimensions of those two nanostructures.

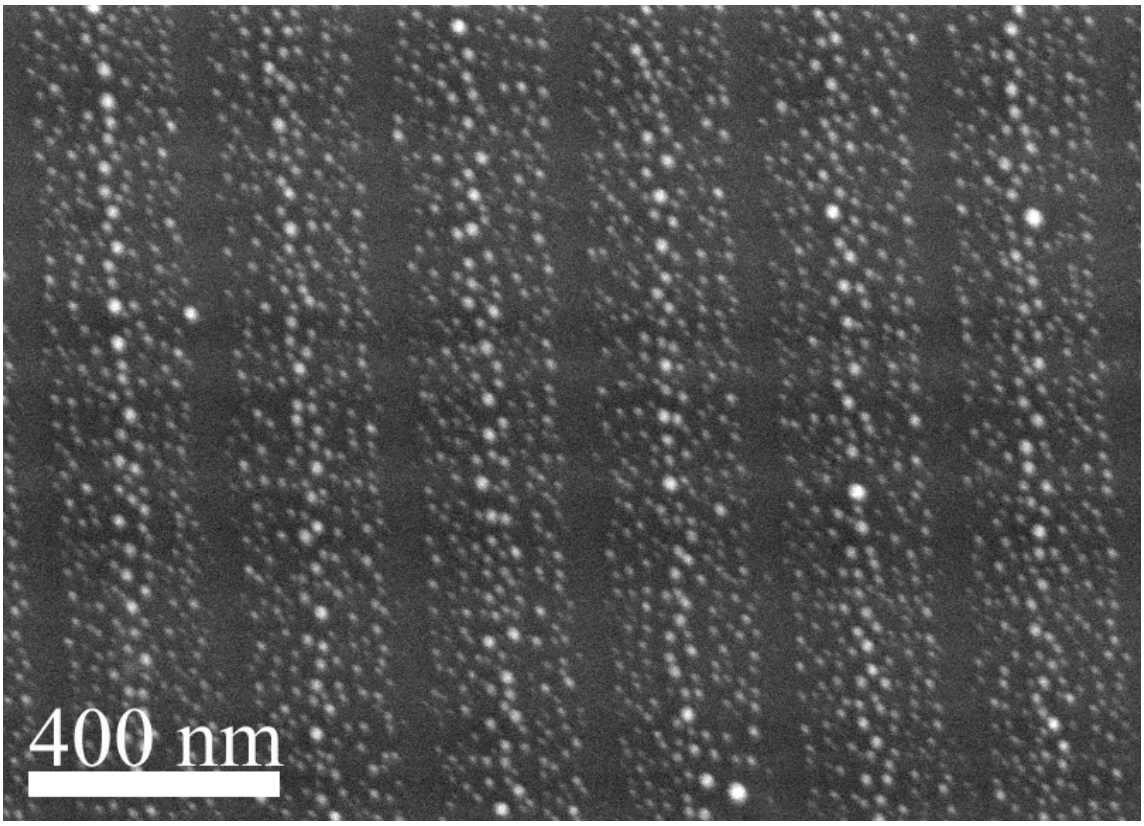

Figure 3.85 SEM image showing the much wider aligned gold stripes after increasing the grazing angle to ~5˚. All the other conditions have been kept the same as Figure 3.84.

what we observed through the deposition chamber window, a plume started to form from the Au target when irradiated by the high energy ion beam, and the plume was composed of atoms forming an opening cone.

In order to restrict the direction of incoming atoms, we put a collimator in the path of the atoms. Figure 3.86 shows the collimator, which is made of two long, narrow pieces of silicon wafers, and is located right on top of the nanostructured template, so that the only ions that can pass through the collimator is normal to the ground. Notice for better visual effect the dimension of the gold plume and the silicon template has been exaggerated.

Figure 3.87 is the SEM image showing much narrower gold strip after using the collimator. Figure 3.87a shows the aligned gold particles covers a wide region of the template. The inset of Figure 3.87a is the high magnification image showing that the gold particles are only located on the nanoripples. Figure 3.87b shows the Au nanoparticles located on the silicon nanoprotrusions. Arrows point to gold particles and silicon protrusions respectively. There is only one gold nanoparticle one each of the nanoprotrusion.

Figure 3.88 are the AFM images of the sample treated under the same conditions as that shown in Figure 3.87. Figure 3.88a is the top view of the sample surface at lower magnification, while Figure 3.88b is the high resolution AFM image showing the nanoripples and the gold particles on top. Due to the weak bonding between gold particles and the nanoripples, some of the gold particles have been moved away from their original location, where is on top of the nanoripples, by the AFM tip during the scanning process. That explains why some gold particles have been found in the region

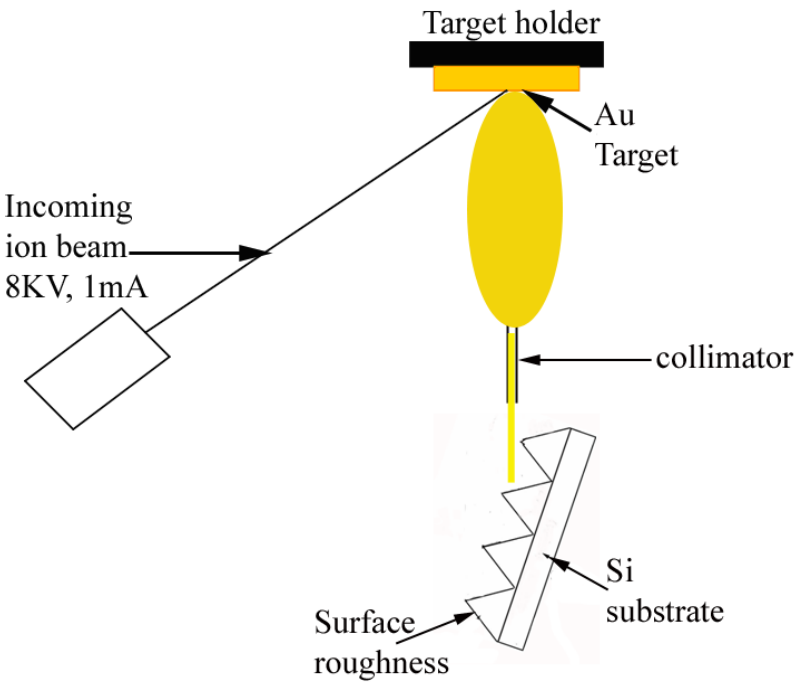

Figure 3.86 Schematic image showing the configuration of collimator, which is made of two long, narrow pieces of silicon wafers, and is located right on top of the nanostructured template, so that the only ions that can pass through the collimator is normal to the ground. Notice for better visual effect the dimension of the gold plume and the silicon template has been exaggerated.

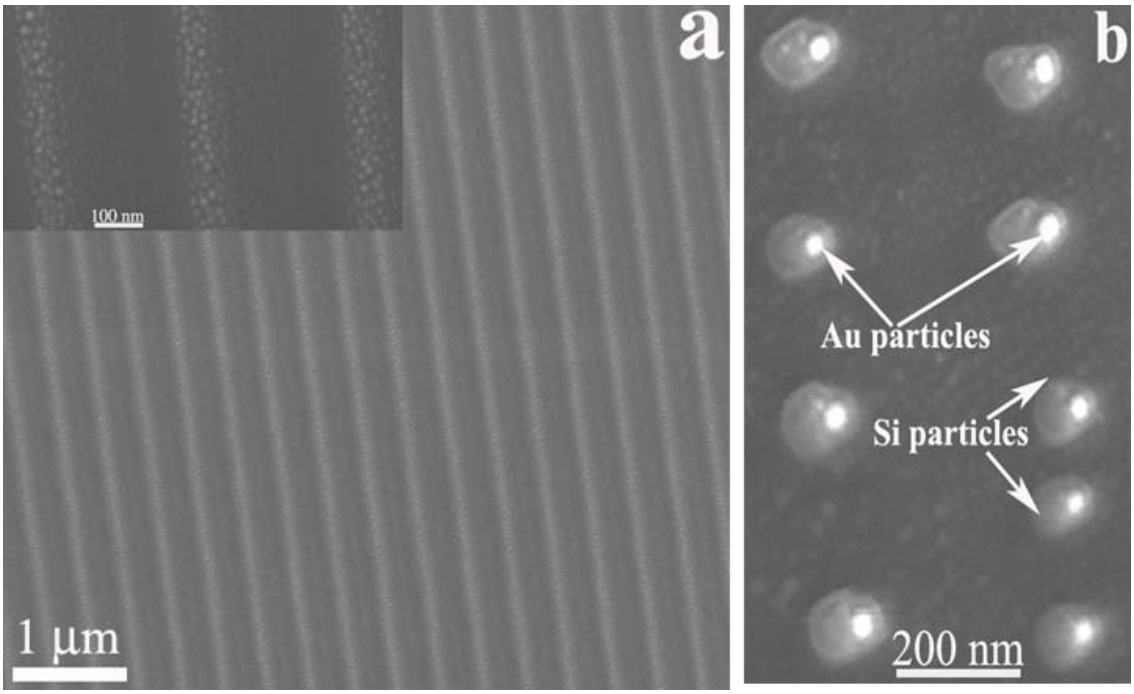

Figure 3.87 SEM images showing much narrower gold strip after using the collimator. Gold film was deposited at a grazing angle of ~3˚ for 5 minutes, and then the sample was annealed at 800 ˚C for 3 hours. (a) SEM image shows the aligned gold particles aligned along nanoripples covering an extended region of the template. The inset of Figure a is the high magnification image showing that the gold particles are only located on the nanoripples due to the application of collimator. (b) SEM image shows the Au nanoparticles located on the silicon nanoprotrusions. Arrows point to gold particles and silicon protrusions respectively. Notice there is only one gold nanoparticle one each of the nanoprotrusion.

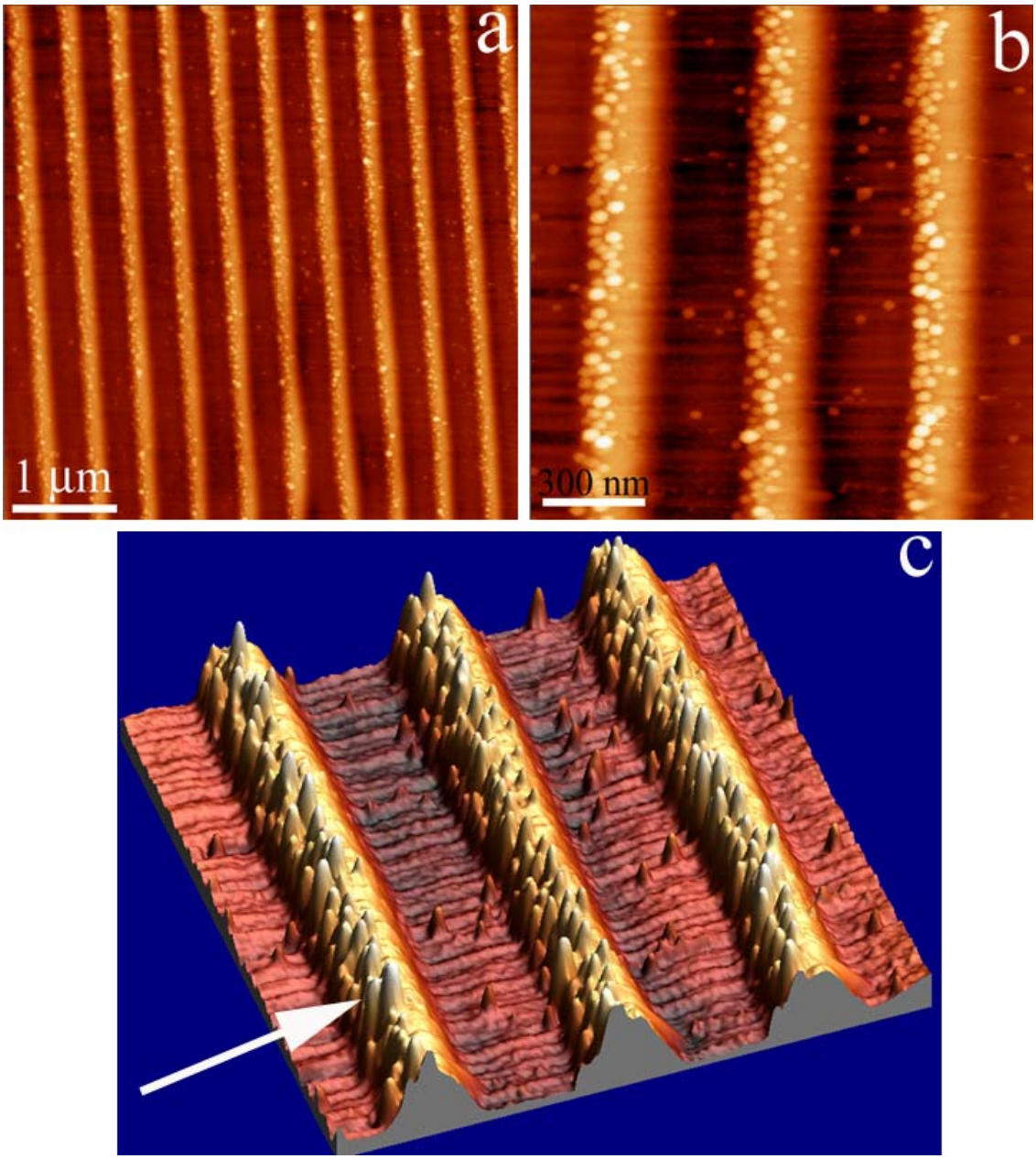

Figure 3.88 AFM images of the sample treated under the same conditions as that shown in Figure 3.87. (a) 2-D AFM image showing the top view of the sample surface at lower magnification. (b) High resolution 2-D AFM image showing the nanoripples and the gold particles on top. Notice the gold nanoparticles observed in the region between the nanoripples are due to the weak bonding between gold particles and the nanoripples, so that they are dragger away from the top of nanoripples by the AFM tip during the scanning process. (c) 3-D image of Figure b. Gold particles are located only on one side of the nanoripples. The incoming ions direction is indicated by the arrow in Figure c.

between the nanoripples. Figure 3.88c is the 3-D image of Figure 3.88b. From this 3-D image, we can see clearly that the gold particles are indeed located only on one side of the nanoripples. The direction of the incoming atoms is indicated by the arrow in Figure c.

We then decreased the grazing angle further to 1.5˚. This time, we obtained even narrower gold strip. Figure 3.89 includes four AFM images showing the surface morphology of silicon template after gold deposition. The deposition time for this sample is still 5 minutes, and sample has been annealed at 800 ˚C for 3 hours. Arrows in the figure indicate where the gold atoms come from. Compared with Figure 3.88, the decrease in grazing angle leads to less gold particle density and smaller particle size.

So far the density of aligned gold particles is so large, that actually they form gold particle lines that can conduct electricity. However, in some cases, less density is expected, so that gold particles can be separated into individual ones.

Figure 3.90 shows much less particle density has been achieved by decreasing the grazing angle. Figure 3.90a is the top view of the sample surface, on which the gold particles are separated from each other, while keep the alignment at the same time. Figure 3.90b is the 3-D AFM image illustrating no gold particles are found in the region between nanoripples/nanoprotrusions.

It seems that so far zero grazing angle works fine for the purpose of aligning gold nanoparticles. Finally, we decrease the deposition time to 2 minutes and keep the grazing angle at 0˚. By doing so, we expected to further decrease the density of gold particles along the nanoripples and form a straight line composed of single particles, instead of a clustering of particles.

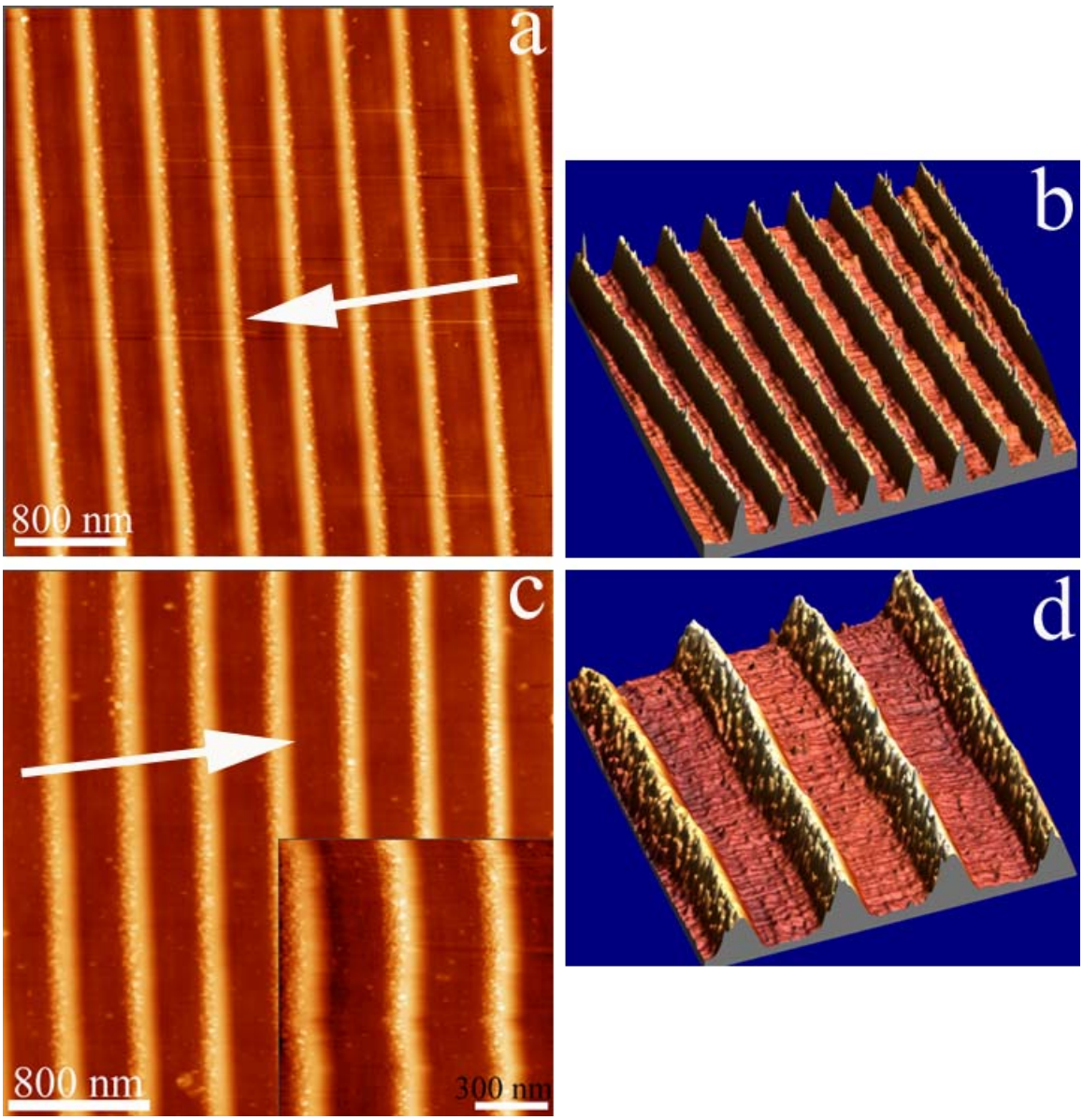

Figure 3.89 AFM images showing the surface morphology of silicon template after gold deposition. The grazing angle is ~1.5 degrees, and deposition time is 5 minutes. After Au thin film deposition, sample has been annealed at 800 ˚C for 3 hours. Arrows in the figure indicate the direction of incoming Au ions. Notice that the less gold particle density and smaller particle size are due to the decrease in grazing angle.

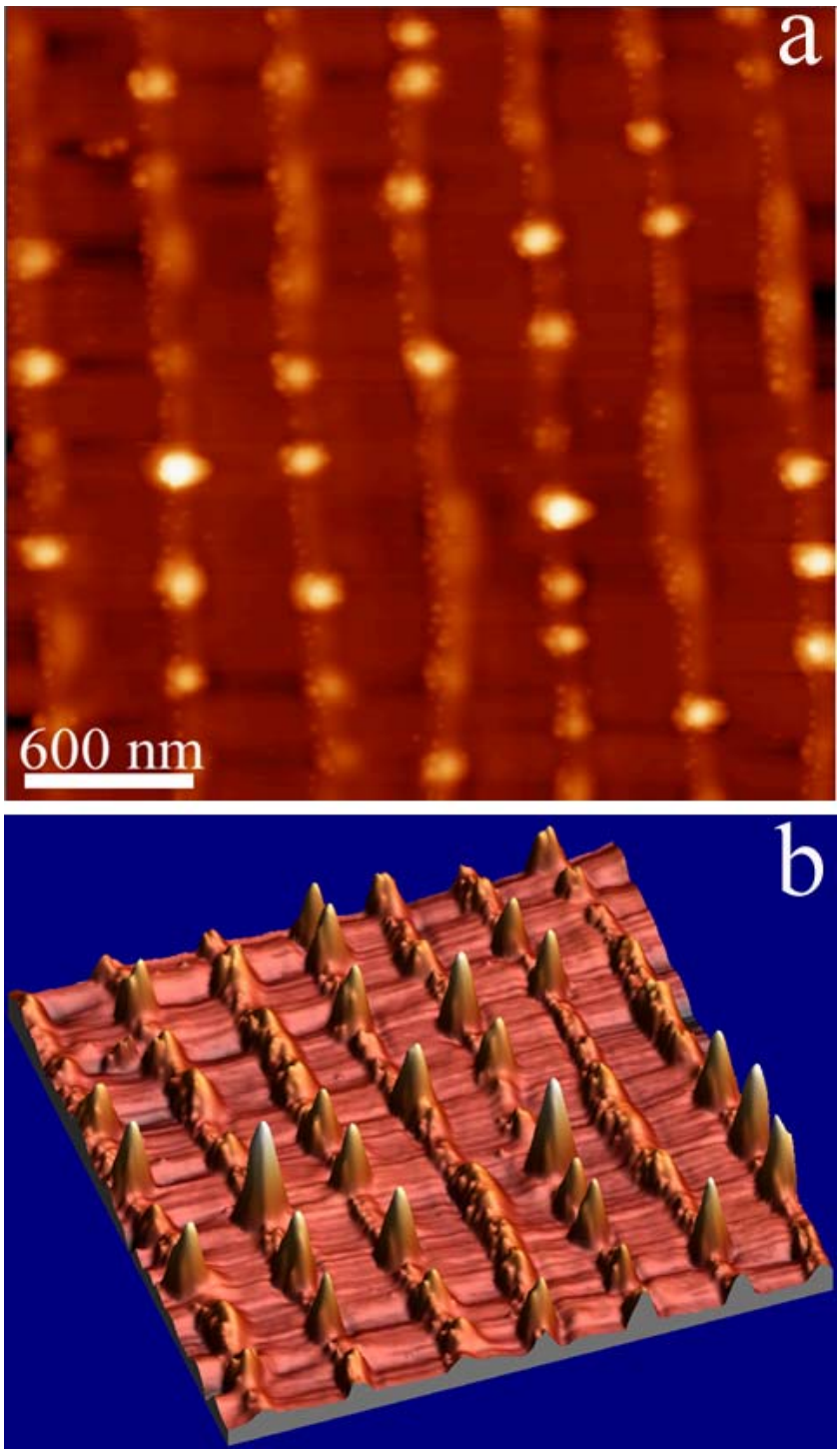

Figure 3.90 AFM images showing much less particle density has been achieved by decreasing the grazing angle to 0˚. (a) Top view of the sample surface, on which the aligned gold particles are separated from each other. (b) 3-D AFM image illustrating no gold particles are found in the region between nanoripples/nanoprotrusions.

Sample shown in Figure 3.91 shows a region in the initial stage of forming nanoprotrusions. So the template here is a combination of initial nanoprotrusion and nanoripples. Because of different dimensions of nanoprotrusions and nanoripples, in Figure 3.91 we found more gold particles on the nanoprotrusions than on the nanoripples. Even on the nanoprotrusions, the gold particles are separated. Since gold is a good catalyst for nanowire growth, and we have a precise control of the location of gold nanoparticles, so we can choose the growth location of nanowires.

Figure 3.92 is another example showing how the individual Au nanoparticles have been aligned into a straight line. The SEM image taken at lower magnification shows that the aligned gold particles are distributed along nanoripples covering an extended region. And the inset on the lower right part is the high resolution SEM image, from which we can see that Au nanoparticles, ~5-10 nm in diameter, are distributed along the nanoripples, and each gold particle is separated from one another.

Based on all the above experiments, the optimal conditions for aligning Au nanoparticles are as follows: deposit the Au film for less than 2 minutes onto the nanostructured template at a grazing angle of ~0˚, and anneal the sample at 800 ˚C for 3 hours so that the deposited gold film can cluster into gold particles. However, if continuous gold stripes/lines that are conductive are required, longer deposition time should be applied. Also, if the goal is to obtain wider distribution of gold particles, then larger grazing angle should be used. Width of gold particle distribution region can vary from ~5 nm (Figure 3.92) to > 300 nm (Figure 3.85) as a function of grazing angles.

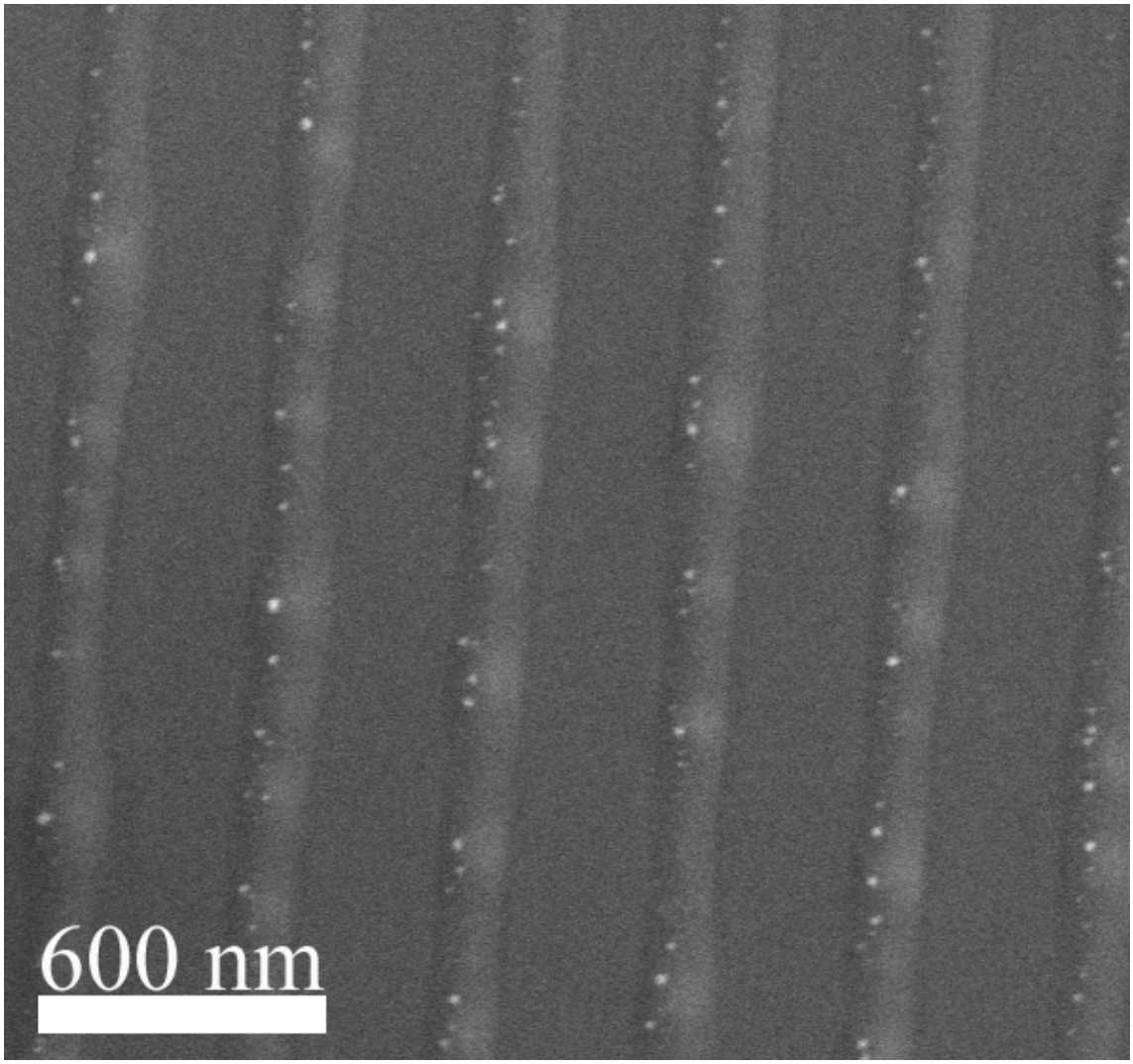

Figure 3.91 SEM image showing the aligned Au nanoparticles along nanoripples/nanoprotrusions on the template. Deposition time is 2 minutes, and the grazing used in the deposition process is 0˚. After that sample has been annealed in a furnace at 800 ˚C for 3 hours. SEM image shows a region in the initial stage of forming nanoprotrusions. Due to different dimensions of nanoprotrusions and nanoripples, there are more gold particles on the nanoprotrusions than on the nanoripples. Notice on the nanoprotrusions, the gold particles are separated.

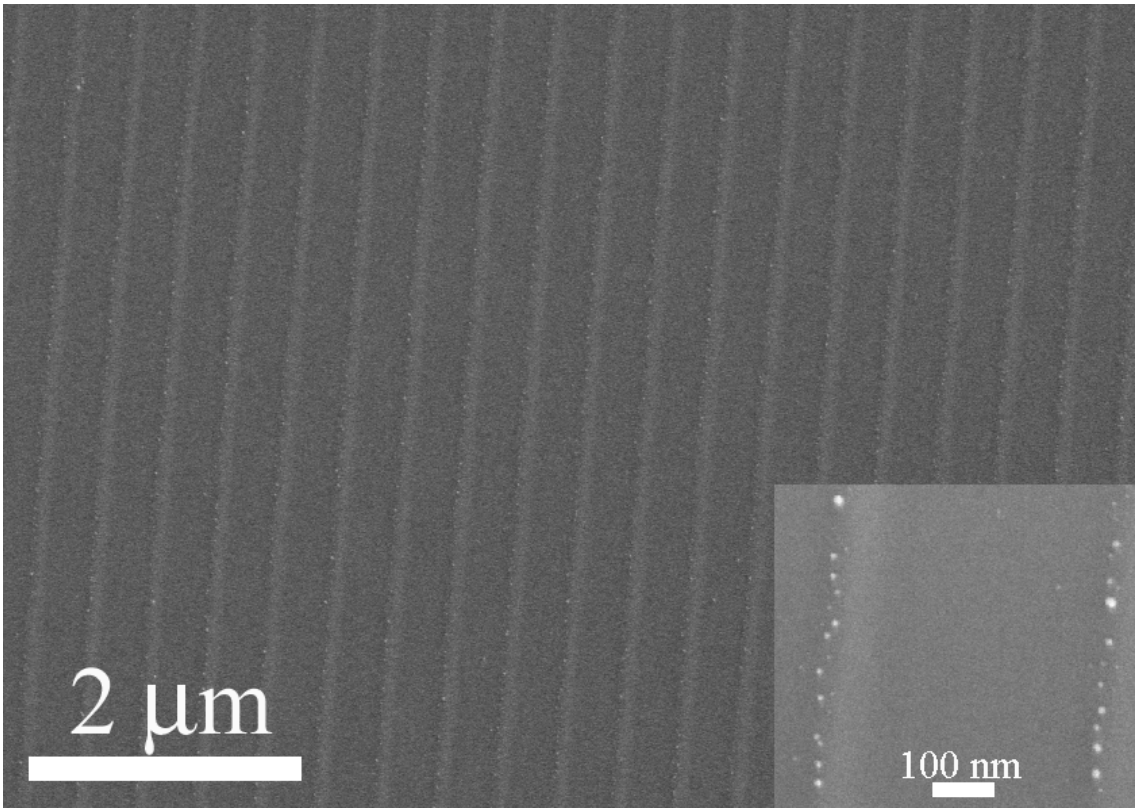

Figure 3.92 SEM image taken at lower magnification shows that the aligned gold particles are distributed along nanoripples covering an extended region. Deposition of Au thin film takes place at zero grazing angle, for only 2 minutes. Then sample was heat treated at 800 ˚C for 3 hours. The inset on the lower right part is the high resolution SEM image, from which we can see that Au nanoparicles 5-10 nm in diameters are distributed along the nanoripples, and each gold particle is separated from one another.

CHAPTER 4

DISCUSSION

4.1 Formation of Nanocolumns

4.1.1 Formation Mechanism of Microstructured Template

Laser-induced surface microstructuring of silicon has been extensively studied [40-45,49,59,210], and has been found to be a function of fluence and of the composition and pressure of the background atmosphere present in the irradiation chamber [43-44]. At a fluence between 2 and 3 J/cm^2 two distinct processes can take place sequentially as a result of cumulative laser irradiation. First, shallow depressions evolve and can reach a depth of a few micrometers and a separation distance of 20 to 30 μm [49]. The second process produces a characteristic microhole/microcone microstructure preceded by a transition stage in the morphology. The third stage—formation of microcones is characterized by a synergistic process involving hole deepening by etching-assisted ablation and cone growth by re-deposition of ablated species on top and to the sides of the laser-melted regions. Since ablation also takes place in these regions, growth can occur only when re-deposition occurs in excess of ablation. The melted microcone tips are preferential sites for deposition, because liquid silicon has a large sticking coefficient [43].

4.1.2 Formation Mechanism of Nanocolumns

A reduction of the laser energy to ≤ 1 J/cm^2 drastically changes the scale of the surface relief, promoting the formation of nanostructures. The growth of nanocolumns can only take place at this low energy density regime and seems to be related to two different growth mechanisms. When a fluence of 0.5 J/cm^2 was used, only the very top of the microcone tip melts. This highly localized melting occurs because the laser fluence decreases away from the center of the tip [54]. The initial protrusion on top of the microcone's tip is most probably related to the melting and subsequent solidification processes. A very small and almost flat depression that is seen around the protrusion is a clear indication that there is liquid transfer from the outer perimeter of the melted pool toward the center, thus creating the initial protrusion. The change in volume during solidification as well as the meniscus angle during solidification may produce changes in the shape of the solidified protrusions [211]. After 2500 pulses the growth rate is strongly accelerated suggesting that another growth mechanism has become active. The transport of material to the tip of the nanocones via the gas phase is clearly demonstrated by the absence of nanocones when the irradiations are conducted in vacuum (Figure 3.7b). A background pressure appears to be required to backscatter silicon atoms or silicon-rich molecules, produced during laser ablation, which will condense at the melted tip of the nanocone. Due to the nanosecond pulse duration, silicon transport to the top could only have taken place in the liquid or gas phase. The liquid could only be removed from the immediate vicinity where melting took place. Clearly the almost negligible changes in the liquid pool surrounding the nanocone indicate that the nanocone does not grow at the expenses of the liquid pool that surrounds it. In fact, in most cases the tall nanocone that

has grown after a large number of pulses is surrounded by smaller nanocolumns that develop from the same melted pool at a later stage. When the laser fluence is increased, say 2.7 J/cm^2, it can melt the silicon surface up to 1 μm, so the liquid pool expands and the growth due to vapor transport involves a large portion of the tip, contributing to microstructural rather than nanocolumn growth.

The second growth mechanism proposed for the fast growth stage of the nanocolumns is the same as that proposed to explain the growth of microcones [31, 56,59,210]. The laser fluence used to grow these nanocolumns is very close to the melting threshold and we could in principle expect that ablation plays a role. However due to the extreme surface roughness, multiple reflection can help to concentrate light in some region, for instance, the bottom of the hole, and strongly increases thermal ablation. After 5000 laser pulses the specimens where the nanocolumns are grown are coated with a thin film of material clearly indicating that significant ablation took place during irradiation at this low fluence.

In summary, the experimental observations suggest that the initial protrusion at the top of the microcones is most likely a result of the solidification process of the laser-melted pool. When the nano-protrusions reach a certain size, deposition of silicon strongly increases their length by continuing irradiation under helium or SF_6, keeping the diameter approximately constant. This last process appears to be similar to that described for microcolumn growth [210].

4.1.3 Field Emission Properties of Nanocolumns

Nanocolumns produced on top of microcolumns are potentially promising materials due to their modest field emission (FE) turn-on field, which is due to a high geometric field enhancement factor. The aspect ratio of nanocolumns is larger than microcolumns, and the corresponding field emission properties of nanocolumns are better than microcolumns.

However, the field emission properties of individual emitters have not been determined due to the size of moveable probe used in the measurement. A 2 mm moveable probe was used for all the measurements in this research. From the SEM images of microcone/microcolumn and nanocolumns, we can see that the distance between the microstructures is ~ 50 μm. So a 2 mm probe covered more than 40 micro-emitters during the measurement and measured an average FE. If a small moveable probe were used, it is possible that better FE properties could be measured.

Carey et al [212] reported their FE measurement on silicon microstructures. The turn-on field they got on microcones is 12 V/μm, which is much smaller than our 55 V/μm. The aspect ratios for both microstructures are very similar, so the only explanation for the discrepancy would be the measurement technique.

4.2 Formation of Nano-LIPSS

The interaction of surface roughness with incoming laser light has been widely reported and analyzed in a series of papers, some of which are referenced in the introduction. Essentially, an interaction with positive feedback is established between the

incoming laser light and the roughness having a wave vector that follows the grating equation. This interaction produces a modulation of the laser light intensity that promotes the formation of a modulated surface topography. Our experiments suggest that the surface modifications start from very smooth undulations, less than 1 nm in height, that do not necessary have the line spacing expected from common LIPSS (Figure 3.18). However, these undulations may evolve towards this spacing and a larger amplitude as the number of pulses is increased. Once the correct spacing is established and as the number of laser pulses increases further and the laser intensity is in the range that favors the formation of LIPSS, the ripples propagate. As the ripples evolve, the diffuse peaks in the FFT of their image change into sharp peaks (Figure 3.16a). The smooth undulations observed during the onset of ripple formation together with the very short duration of the laser pulse suggest that, most probably, they form while a thin melted layer is on the surface and freeze on re-solidification.

4.2.1 Nano-LIPSS formation under Single Beam Illumination

For a single beam of p-polarized laser light, the ripple lines were mostly normal to the surface projection of the electric field vector. In this case, there was a noticeable tendency of the ripple structure to propagate faster in a direction parallel to that projection (Figures 3.19 and 3.20). Rapid lengthening of the ripple lines that initiated at one place tended to form extended structures containing a long stack of very narrow, defect-free lines. If the ripple structure propagated from different centers these elongated structures could have sections that did not match each other. Generally, each stack of

lines may obey the grating equation but can have a different spacing because they may be slightly rotated. As the number of laser pulses increases and these stacks grow sidewise, structures with twisted and rotated lines may result when they come into contact, as is shown in Figure 3.19. These defective structures with bending lines made up of short segments were frequently observed in ripples that obey the sine equation (Eq. 3.1).

In some cases we have measured an increase in the ripples' amplitude from the edge towards the center of the ripple structure (e.g., see profile in Figure 3.23). This result indicates that there was a growth process and that it was arrested at the end of the irradiation. The observed formation of very small depressions (Profile A in Figure 3.24) together with holes surrounded by elevations (Profile B and C in Figure 3.24) and the coalescence of holes into lines as suggested by the well developed structure at the center also indicate a process of ripple maturing. There is evidence that the material removed from the holes has been displaced forming elevations (profiles B and C in Figure 3.24). Careful observation of the ripple structure suggests that the troughs and elevations form by displacement of liquid (see also Figure 3.22). The tenuous surface undulations and holes ahead of the mature ripples is not only a demonstration that ripples grow, but also that the effect of the modulated electromagnetic field generating them extends significantly beyond the ripples (enclosed area in Figure 3.23a).

4.2.1.1 Computer Simulation on Laser Irradiation on the Silicon Surface

A computer calculation of heat evolution during laser irradiation can help to understand these observations. The laser heating and melting of a specimen was

calculated using a finite element code [213]. Consistent with our experimental results, the irradiation fluence was modulated along the x-axis on the specimen surface following a cosine law (see Appendix and legend of Figure 4.1). The model assumed heat conduction in two directions, towards the bulk (z-axis) and along the surface in the x-direction. An average fluence of 0.8 J/cm^2, close to the upper range of temperatures where the nano-LIPSS have been observed, was used to calculate the temperature evolution in the specimen surface along the x-axis. Figure 4.1 shows the results at two locations. At x=0 (upper curve), the fluence was assumed to be 1.2 J/cm^2 while the lower curve represents the temperature evolution at x=λ/2, for a fluence of 0.4 J/cm^2. The difference in temperature between the two curves is significantly less than what would be calculated if no conduction would have taken place along the x-direction. This calculation shows that, within the fluence range used in this work, a surface layer remains melted for a significant part of the pulse duration. Moreover, the liquid silicon at most reaches 100 K above the melting point and the specimen surface is solid when or before the laser pulse ends.

Both, experimental results and computer calculations, indicate that nanoripple formation takes place while the surface of silicon is melted. Thus, the displacement of material from the holes toward the sides must take place while silicon is liquid.

4.2.1.2 Mechanism of LIPSS Formation

A possible mechanism that can drive the liquid is the gradient of surface tension (Marangoni effect). This gradient is due to the existence of a thermal gradient and the fact

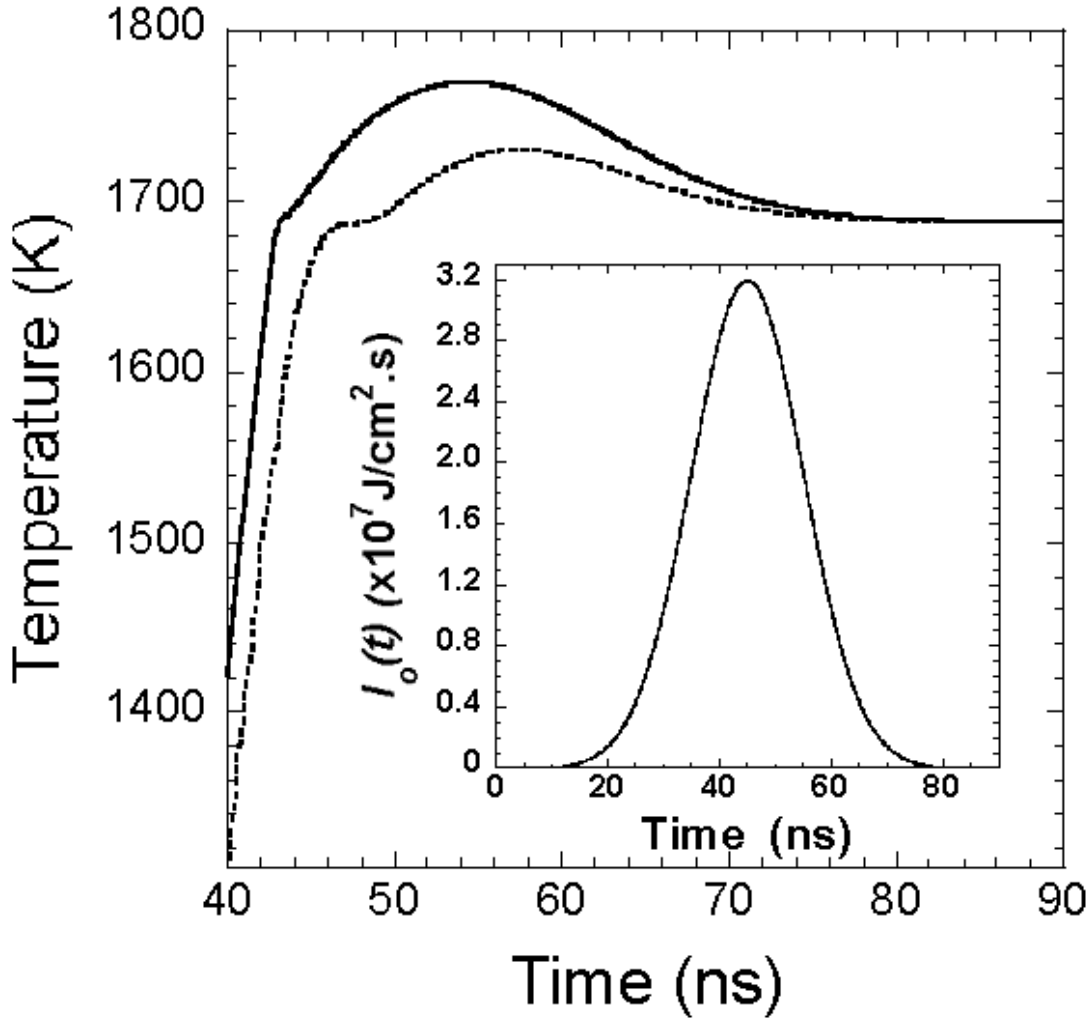

Figure 4.1 Calculated temperature evolution at two locations distant λ/2 during laser irradiation in silicon assuming that the spatial dependence of the fluence (in J/cm^2) is given by $F = 0.8 - 0.4\cos\left(\frac{2\pi}{\lambda}x\right)$. The lower curve is at x=0 (minimum of F) and the upper at x=λ/2 (maximum of F). The insert shows the Gaussian temporal profile of the laser beam used for the calculation. Details of the calculation are given in the Appendix. [217]

that the surface tension of silicon, like that of most elements, decreases as the temperature increases. The liquid displacement cannot be due to ablation because the laser fluence where ripples are formed does not increase the surface temperature much above the melting point.

A first estimate of the likelihood of a mechanism based on the Marangoni flow can be done by neglecting capillary forces. The average velocity of lateral displacement from hotter to colder regions can be written as [214]

$$\overline{v}(x,t) = \frac{h}{2\eta}\frac{d\gamma}{dT}\frac{\partial T}{\partial x} \qquad 4.1$$

The time required for Marangoni fluid convection is $\tau \sim \Lambda/2\overline{V}$ for a ripple spacing of Λ.

The temperature gradient is $\sim 2\Delta T/\Lambda$. Thus,

$$\tau \approx \frac{\eta}{2}\left|\frac{d\gamma}{dT}\right|^{-1}\frac{\Lambda^2}{h\Delta T} \qquad 4.2$$

The surface tension of liquid silicon varies linearly with temperature, with $d\gamma/dT$ = -2.2×10^{-4} $Nm^{-1}K^{-1}$ [215]. The dynamic viscosity η taken as an average within a temperature range of melted silicon is 7.2×10^{-4} kg m^{-1} s^{-1} [215]. The melted layer thickness for the fluence range employed in this work was calculated as ~60 nm. Substituting these values and a ripple spacing of 250 nm into equation 4.2 gives 34 ns for ΔT=50 K. This estimate suggests that liquid convection due to a Marangoni effect is a viable mechanism, since the melt duration is on the same order.

4.3 Formation of Nano-LIPSS Using Lloyd's Mirror Configuration

The induced ripple structures produced using Lloyd's mirror and p-polarized light, had their $\boldsymbol{q}$-vector parallel to the substrate/mirror edge. Under this illumination, the projected electric vector, which was contained in the plane of incidence, was perpendicular to this edge, and hence, normal to the $\boldsymbol{q}$-vector (Figure 3.26). The line spacing is in agreement with the cosine law (equation 3.3) as it should be expected for the $\boldsymbol{q}_3$-vector (Figure 1.23). This result is in contrast with the observations using single beam p-polarized illumination where the $\boldsymbol{q}$-vector of the only observed ripples was parallel to the electric field projection and it followed the sine law. What is even more remarkable is that, with a Lloyd's mirror arrangement, non-linearly-polarized light may induce the formation of single or two mutually orthogonal nano-ripple structures.

For non-linearly-polarized light, it is not possible to establish the relation between the direction of the electric field and the ripple orientation because the latter is not a function of that direction (see equation 1.10 and Figure 1.23). Since the substrate/mirror edge is always normal to the plane of incidence, it should be expected that the $\boldsymbol{q}_1$ and $\boldsymbol{q}_2$ vectors defining the morphology of the ripple structure should always be perpendicular to the substrate/mirror edge, and the $\boldsymbol{q}_3$ vector parallel to it, as observed at all values of θ. Considering that, when using a linearly polarized beam with Lloyd's mirror, only p-polarized light produces LIPSS while s-polarized light does not, it may be concluded that generally only the p-component of the electric field is related to ripple formation. In this scenario, $\boldsymbol{q}_1$ and $\boldsymbol{q}_2$ are parallel to the p-component of the electric field while $\boldsymbol{q}_3$ is perpendicular to it.

A very extensive spatial and temporal coherency is required to produce an interference pattern due to a Lloyd's mirror arrangement, especially if it is generated far from the edge. The reason is that the interference is produced between the incident beam and that reflected in the mirror impinging in the substrate. This explains why we seldom found ripples that are produced by the Lloyd's mirror interference pattern. However, the fact that we were able, at least once, to detect an interference pattern characteristic of the Lloyd's mirror configuration through its imprint in a surface region near the edge with the mirror (Figure 3.30 and Figure 3.51), implies that the UV laser light used in our experiments has a certain degree of temporal and spatial coherency.

When the interference is produced between the incoming beam and the light scattered by each ripple line, the ripples could form if the coherency extended at least over one ripple spacing. The spatial coherency of the laser been used, although limited, is certainly larger than one ripple spacing and thus is capable of generating an extensive ripple structure that even can propagate as the number of laser pulses is increased. The directly incident and the mirror-reflected beams independently produce an interference pattern with their corresponding scattered beams. These two independently generated patterns coincide because their periodicity is only a function of the angle of incidence. Thus, at least one reason why the Lloyd's mirror enhances ripple formation is because the two interference patterns reinforce each other's effects in the substrate.

The FFT of the ripple images provided very useful information in the case of complex structures. It is very difficult to measure a ripple spacing for instance in Figure 3.41 because there are several sets of ripples twisted, rotated, and intersecting each other. The FFT shows that the entire ripple spacings satisfy the grating equation, as represented

in Figure 1.23, and simply indicates that, together with the dominating structure of wave vector $\boldsymbol{q}_3$, there are other ripples present with allowed orientations. The angles of incidence calculated from the FFT are in excellent agreement with the experimental values, and the Λ-values for the spacings also are in very good agreement with those calculated using the measured angle of incidence. The structure presented in Figure 3.42 is even more complex than the previous example but, once more, the FFT reveals that ripple segments with several allowed orientations are present.

In the large number of experiments performed using the Lloyd's mirror set up (Figure 3.51), it was found that at incident angles of 40º and less, the spacings follow equations 3.1 and 3.3 very closely. At angles larger than 40º there was a gradual departure from the dependence given by equation 3.3, observed at lower angles. For angles of incidence of 50º and larger, the data were fitted by the equation

$$\Lambda = \frac{\lambda}{\left(n^2 - \cos^2\theta_i\right)^{1/2}} \qquad 4.3$$

that is obtained when equation 1.14 substitutes for $|\boldsymbol{k}_{//}^{s,a}|$ in equation 1.12, with $\boldsymbol{n}$=1.07. It is well known that plasma oscillations can propagate in the surface of metals and of liquid silicon. These surface electromagnetic waves must satisfy the relation

$$n_{SEW} = \left(\frac{|\varepsilon_1|}{|\varepsilon_1| - 1}\right)^{1/2} \qquad 4.4$$

Fuchs [170] calculated the optical properties of liquid silicon as a function of frequency up to 5 eV, and compared her results with experimental measurements. At a photon energy of 5 eV, the calculated value of $\boldsymbol{\varepsilon}_1$ is -8.71, which gives a value

$\boldsymbol{n}_{SEW}$=1.063, in reasonable agreement with the value used to fit our experimental data. This result indicates that scattered waves resonate with surface electromagnetic waves that are excited by the incident light. These scattered waves are the ones producing the interference pattern that creates the rippled structure at angles of incidence ≥ 50º.

4.4 Formation of Nanoprotrusions Using Lloyd's Mirror Configuration

Nanosecond pulsed laser irradiation can induce surface modifications of materials in the micro- and in the nano-scale. The metric of the modification is a function of melting time and the amount of ablated material, which are a function of the laser fluence and wavelength. Nanostructures form at fluences as low as ~0.45 J/cm^2, and up to ~ 1 J/cm^2. In silicon, we have observed that they always appear after a significant number of laser pulses and in many instances, but not always, they organize during irradiation following a precise pattern. This pattern is dictated by a grating equation that establishes a relationship involving the wavevector of the incident light, the wavevector of the scattered light that propagates on the surface of the specimen, and the wavevector of a Fourier component of the surface roughness (equation 1.10) [29]. As calculated by Akhmanov et al [169], a very significant part of the incident beam energy is transformed into a perturbation propagating on the specimen surface. The ordering process is driven by the modulated intensity field generated by the interference between the surface perturbation and the incident light.

The fluences used in this research promote melting with a modulated thermal field. In sections 4.2 and 4.3, it was inferred that the formation of nanoripples in silicon are

due to liquid transport from the hotter to the colder regions of the surface. Both, the experimental evidence and a theoretical estimation, indicate the feasibility of a thermocapillary process.

The analyses that follow also help to gain some insight into the evolution of the nanoprotrusions produced by using Lloyd's mirror configuration. Let the ripple structure be approximated by a simple system, as depicted in Figure 4.2. The liquid silicon moves along the x-direction driven by the surface tension gradient, towards the temperature minimum, where it encounters fluid moving in the opposite direction, driven by the same forces. Both liquids concurring to this region raise the ripple height in the z-direction.

Using the lubrication approximation reference (quasy-steady state), it can be found that the average velocity in the x-direction, $\bar{v}(x)$ is

$$\bar{v}(x) = \frac{h}{2\gamma}\frac{d\gamma}{dT}\frac{dT}{dx} + \frac{\gamma}{3\eta}h^2\frac{d^3h}{dx^3} \qquad 4.5$$

where η is the dynamic viscosity, γ is the surface tension, $\boldsymbol{h}$ is the thickness of the melted surface layer, and $\boldsymbol{T}$ is the temperature.

The first term describes the motion of liquid due to the gradient of surface tension (Marangoni effect); if $d\gamma/dt < 0$, which is the case for silicon and most liquids, the melt will flow from hotter toward colder regions. The second term is due to the flow induced by capillary forces on curved surfaces (the Laplace effect); this flow opposes the Marangoni build-up of the liquid in the colder regions. In this simplified ripple structure,

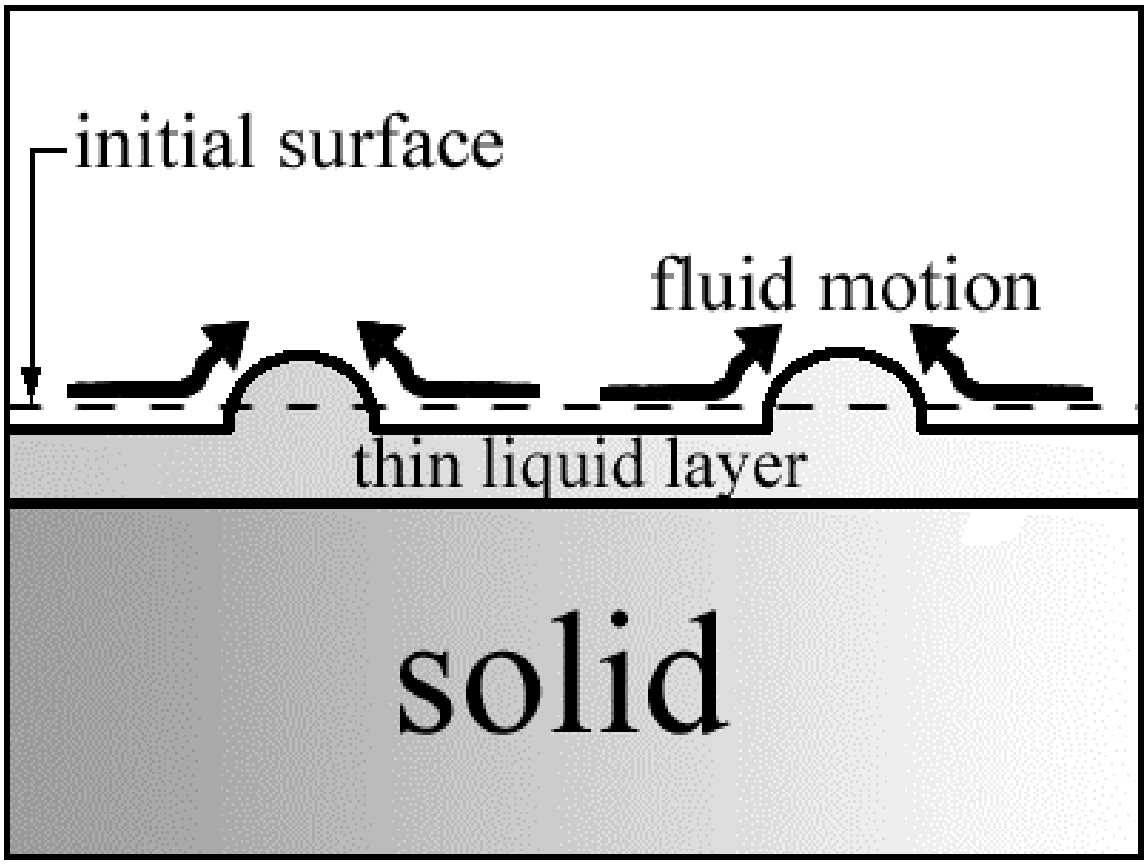

Figure 4.2 Schematic image showing the evolution of the nanoprotrusions. The liquid silicon moves along the x-direction driven by the surface tension gradient, towards the temperature minimum, where it encounters fluid moving in the opposite direction, driven by the same forces. Both liquids concurring to this region raise the ripple height in the z-direction.

the Laplace term only is important where the two flows meet, viz., where the temperature is at a minimum. The strength of the Marangoni term depends on the temperature gradient and on the variation of the surface tension with temperature.

Under equilibrium conditions at the base of the ripple the thermochemical term is counterbalanced by the capillary term due to an increase in curvature as the elevation is formed. As pointed out in Figure 3.54, where a transition from a ripple-only structure to nanoprotrusions is shown, the ripples closer to the nanoprotrusions are taller and thinner than those further away in the all-ripple region. The effect is even clearer in Figure 3.58, where another transition region is shown. In this figure, the ripple line spacing is 400 nm and the ripples more than double their height the closer they are to the protrusion region. Again, the increase in height coincides with a substantial thinning of the ripples.

It can be reasoned that the strength of the thermocapillary term ought to increase for the taller and thinner ripples because the increase in height requires an increase in velocity if the process has to take place during the duration of the pulse. The Marangoni stress also must increase because it has to counterbalance the capillary term increase due to an increase in the curvature at the base of the ripple.

This analysis indicates that the growing ripple front may become unstable as the velocity of the fluid that is pumped to augment the elevation increases, giving rise to nanoprotrusions. Instabilities generated by the thermocapillary stresses have been observed in the spreading of thin liquid films driven by a gradient of surface tension due to a temperature gradient [214,216]. These studies were performed with silicone oil spreading on oxide-covered silicon wafers subjected to a thermal gradient. The formation of finger-like instabilities was related to the Marangoni stress-induced

pumping of liquid from the back to form a bump in the advancing front; this fluid motion can be likened to the liquid displacement that induces ripple formation. Using the lubrication approximation, Cazabat et al. calculated the length h_o near the advancing front where the bump is produced and the capillary forces become comparable to the Marangoni stress. They measured the distance δ between the fingers with the aid of interference microscopy, and determined that the ratio δ/h_o is in the range of 18 to 22 for silicone oils in a wide range of viscosities [214].

In our case, the nanoprotrusions along the ripple line are approximately equally spaced and an average separation, δ, between them can be measured from the AFM images. The value of δ for the experiment illustrated in Figure 3.54 (profile 4) is ~230 nm, and for the experiment of Figure 3.58 (profile B), it is ~430 nm. The height of the ripples contiguous to the line where the nanoprotrusions were generated was taken as the height h_o where the Marangoni stress is comparable to the capillary force, viz., where the velocity of the liquid is close to zero, as per equation 4.5. h_o values of 11nm and of 20 nm were measured for Figure 3.54 and Figure 3.58, respectively, giving a δ/h_o ratio of 21 for these two cases. This result is the same as that derived by Cazabat et al., and it is surprising especially considering that: 1) the viscosity of liquid silicon is ~30 times smaller than the viscosity of silicone oil employed by them, and 2) the Marangoni stress is ~ 5 orders of magnitude higher than those studied there [217].

The extremely high Marangoni stress promotes the very high fluid velocity that is required for the ripple to grow in a few tens of nanoseconds [217]. The increase in pumping speed as the ripple increases its height is owed to a positive feedback with the

incoming radiation. The amplitude of the surface electromagnetic wave excited by the laser beam striking the surface roughness in silicon is [169]

$$E_{s,a} \approx \left(0.032\, nm^{-1} h_o\right) E^i_{//} \qquad 4.6$$

where $\boldsymbol{E_{s,a}}$ is the amplitude of the Stokes and anti-Stokes scattered waves [29], and $\boldsymbol{E^i}_{//}$ is the projection of the electric vector of the incident light on the surface. The amplitude of the electric vector of the scattered light doubles as the ripple doubles in height. The scattered light interferes with the incident light producing an intensity modulation that increases directly proportional to the square of the ripple height. In principle, the maxima and the minima of the light intensity double, and the ripples double in height producing a very large increase in the temperature modulation. This large increase in the temperature gradient increases the thermocapillary stress thus causing a larger fluid velocity and probably the instabilities that become expressed as nanoprotrusions.

In the two cases analyzed above, only one set of ripples were present, both spaced according to the cosine law, equation 3.3. At lower angles of incident laser light, we observed two sets of ripples that intersect each other at right angles. The laser irradiation interacting with these two structures produces a modulated intensity along two mutually orthogonal directions. As already shown in chapters 4.2 and 4.3, a light modulated intensity produces a modulated thermal field where the temperature minima are located at the hills. In this instance, liquid is pulled by the two ensuing orthogonal surface tension gradients, inducing a structure as illustrated in Figure 3.59. It is at the intersections of the two sets of ripples where the nanoprotrusions are produced, as could be expected because at these singular points, liquid is pumped by the action of thermocapillary shear stresses concurring from two directions. The structure seen in

Figure 3.60 is an example of these 2-D nanoprotrusion structures. The spacing between ripple lines in one direction follows equation 3.3, and in the other direction equation 3.2, although the alignment in the latter is less perfect than in the former.

4.5 Alignment of Nanoparticles and Comparison with Nanoprotrusions

As mentioned in section 3, we observed that nanoparticle alignment can be generated by irradiating smooth silicon surface with a non-polarized laser beam. It has been found that the aligned nanoparticles are accompanied by LIPSS, so we may explain the difference in alignment conditions according to this aspect. Experimental results show that only p-polarized laser beam can produce the periodic structures on the surface. In our case, the non-polarized laser beam coming out of the laser cavity may have partial polarization even without using a beam polarizer. That may be the reason that non-polarized light can lead to long-range order of nanoparticles.

The emergence of nanoprotrusions at the elevations of the ripples as an evolutionary step in the development of the nanostructure shown in Figure 3.59 has been observed in a number of regions where broken ripples and nanoprotrusions coexist. At variance with the nanoprotrusions, nanoparticles are located in the valleys of the ripple nanostructure and, according to previous analyses, in the region where, in the absence of the nanoparticles, the temperature is higher during irradiation. In previous studies, SEM studies of a given region, prior to and following a set of laser pulses, revealed that laser–induced nanoparticles move during laser processing but maintain their identity [34,130]. It can be reasoned that although the nanoparticles melt they do not fuse with the

substrate probably due to the adsorbed gases in their surface, or the very thin native oxide covering their surface, and the very short time that they remain melted. The motion of the liquid nanoparticles is also consistent with a thermocapillary process, as supported by studies of the behavior of a liquid particle located on a surface temperature gradient. These studies have established that the particle experiences Marangoni stresses, which force it to move up the gradient, viz., from the cooler to the hotter region [219].

The aligned nanoparticles can loose their ordering by a 2 hr anneal at temperatures as low as 423 K. This observation indicates not only that particles can migrate on the surface but also that the activation energy for migration is fairly low. The diffusion coefficient of nanoparticles can be estimated assuming that the nanoparticles are concentrated along lines separated by a distance Λ and that only two neighboring nanoparticle lines will contribute to an increase in the nanoparticle concentration at a position midway between these two lines. A random walk approximation gives,

$$\sqrt{Dt} \cong \frac{\Lambda}{4} \qquad 4.6$$

assuming Λ=248 nm and t=7200 s, a value of $\boldsymbol{D}$ = 5.3x10^{-15} cm^2/s is obtained. This estimate can be construed as being appropriate at the lowest annealing temperature.

4.6 Alignment of Gold Nanoparticles by Low Grazing Angle Deposition

The alignment of gold nanoparticles/nanostrips has been realized by applying the templates with nano-LIPSS and nanoprotrusions. It should be a universal method to align nanoparticles.

However, in order to form long-range ordered gold particles, heat treatment is required right after the gold thin film deposition. During the heat treatment, Au thin films cluster into nanoscale particles and high temperature can accelerate the diffusion process, which is also required for the alignment.

In the following paragraphs, we will discuss some of the key parameters, such as annealing temperature, annealing time, and grazing angle for deposition.

The annealing process induces a diffusion process in the deposited gold film, so the temperature and annealing time are of vital importance. Figure 3.81 shows that if the sample is annealed at 800˚C for 24 hours, the gold atoms will gather together and form a continuous continent.

The diffusion coefficient increases exponentially with temperature, so by increasing the annealing temperature we can actually decrease the annealing time.

From these analyses, we can limit the diffusion length of gold atoms by controlling the annealing time and temperature. The optimal conditions we found are 800 ˚C and 3 hours.

Another important parameter to consider is the grazing angle at which the incoming atoms reach the sample surface. Theoretically, we can calculate the width of the gold strip by the geometry of the template. However, experimental results show that is not the case. The main reason is due to the shape of the incoming atom beam. Instead of a straight line, the plume coming out of the target is composed of atoms traveling in an opening cone. A collimator sitting on top of the template can make sure that only atoms in the direction can reach the template normal to the surface.

According to the Au-Si phase diagram (Figure 4.3) [220], the eutectic reaction (eq. 4.29) happens at ~360 ˚C.

$$Si + Au \Rightarrow AuSi \qquad 4.7$$

However, our annealing temperature is ~ 800 ˚C. At this temperature, the deposited gold atoms on the surface should form AuSi eutectic alloy with the substrate, and bonding would be so strong that movement of the alloy cannot be observed.

Our experimental results show that gold particles can move freely on the surface. So there should be no formation of AuSi eutectic alloy on the surface. Here, the oxide layer plays an important role. Silicon substrate used in the process didn't undergo oxide layer removal process and more SiO_2 oxide layer forms during the heat treatment. So the deposited gold thin film is actually in contact with the oxide layer instead of the bulk silicon substrate. Hence, the oxide layer acts as a diffusion barrier between the gold film and the silicon substrate, although the annealing temperature is much higher than the eutectic temperature preventing the eutectic reaction from happening. If, the native oxide layer was removed prior to gold film deposition and the annealing process was carried out in a vacuum furnace, we were not able to observe the movement of gold particles on the silicon surface, most likely due to the formation of AuSi eutectic alloy.

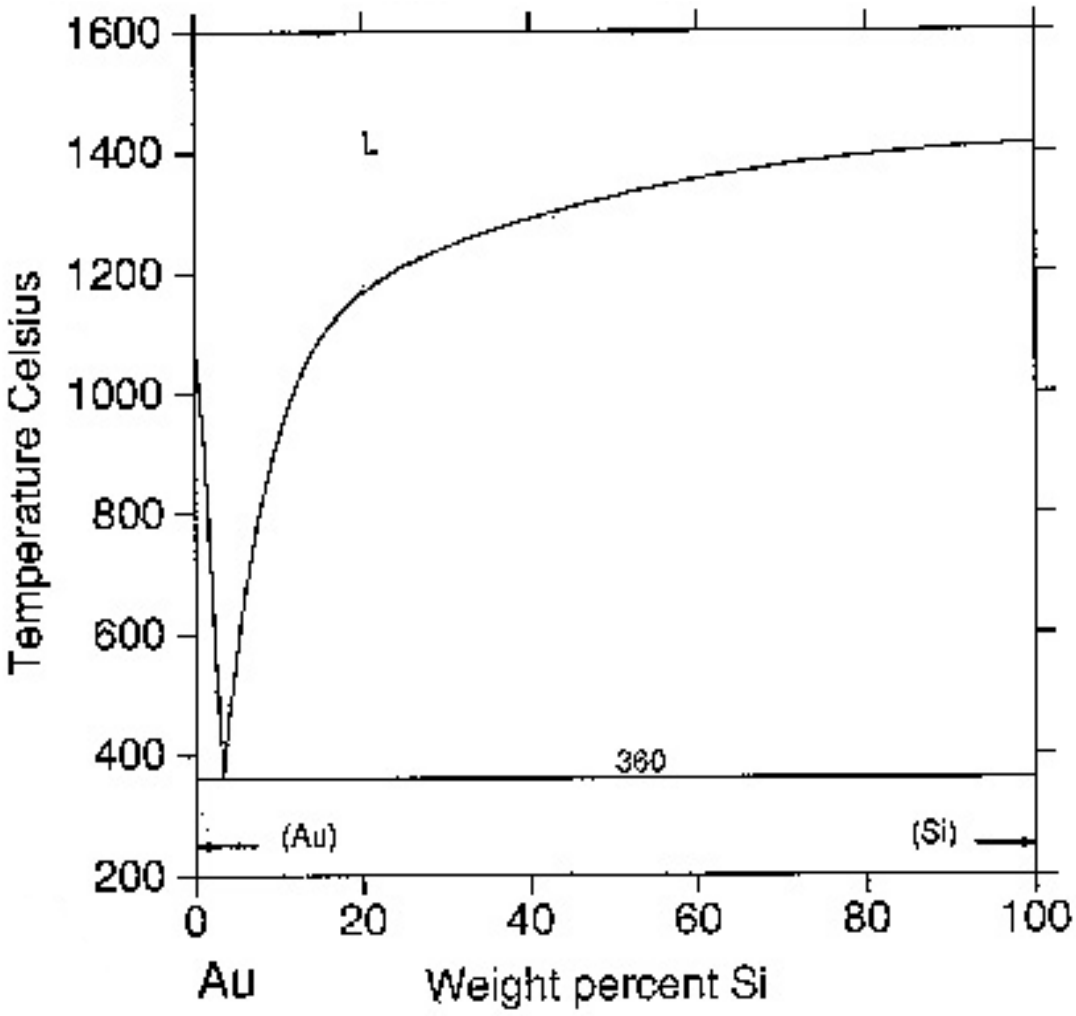

Figure 4.3 Au-Si binary phase diagram. The eutectic temperature in the phase diagram is 360 ˚C, which is much lower than the annealing temperature (~800 ˚C). [220]

Source:

[220] P. Y. Chevnlier, *Thermochimica Acta*, **141,** 217-226 (1989)

CHAPTER 5

SUMMARY, CONCLUSIONS AND FUTURE WORK

5.1 Formation of Nanocolumns on Microstructured Substrate

Laser-generated silicon microcone arrays were used as templates for the growth of nanocolumns using laser irradiation. Laser energy density, ambient atmosphere and number of laser pulses all play important roles in the formation of nanocolumns.

A two-step procedure is required to form the nanocolumns. First, a microcone/microhole structure is formed by irradiating a silicon specimen in SF_6 at a fluence of 2.5 J/cm^2. In the second step the microstructured surface is irradiated at a much lower laser fluence, in an inert ambient at low background pressure.

Due to low-energy irradiation, only the very top of the cone tip was melted.

Irradiation in vacuum cannot generate the nanocolumns, while under SF_6 and He, the nanocolumns grow up to several microns. In vacuum, it is more difficult to trap the ablated material because there is no buffer gas atmosphere.

The aspect ratio of nanocolumns is higher than that of microcolumns, so the threshold of emission field decreases from 55 V/μm to 35 V/μm.

The growth mechanism of the nanocolumns is similar to microcolumns, that is, transportation of silicon-rich molecules in the vapor phase, from the bottom of the holes to the microcone tips. The melted microcone tips are preferential sites for deposition, because liquid silicon has a large sticking coefficient.

5.2 LIPSS Formation under Single Beam Irradiation

1-D gratings were generated on the substrate surface by single beam irradiation using p-polarized laser light.

Experiments described in the thesis consistently showed that the oxide layer stabilizes the ripples, e.g. the ripple's height is larger if this layer has not been removed. For this reason, different experimental conditions have been tested and it turned out that incident angle of laser beam, the ambient atmospheres, the energy density of the laser beam, and polarization of the light can affect the formation of LIPSS.

S-polarized laser light is not able to produce LIPSS in the substrate surface, while only p-polarized light can form the periodic structures. Under this condition the only relationship found between the LIPSS line spacing Λ and the incident angle θ closely follows the sine law: $\Lambda_{1,2} = \lambda/(1 \pm \sin\theta)$.

S*ub*-ripples, whose heights are ~ ¼ of the *mature* ripples have been observed. The line spacing of the *sub*-ripples is identical to that of the *mature* ripples.

Surface roughness analysis shows that the region with Λ_1-spaced ripples is much rougher than the region with Λ_2-spaced ripples. The maximum height increased from 4.47 nm in the former to 10.11 nm in the latter, and the RMS value also increased to 2.33. No clear explanation exists on what factors control the appearance of these two kinds of ripples.

The rippled structure tends to propagate faster in the direction parallel to the polarization vector than in a direction normal to it.

5.3 1-D and 2-D Nanostructures Formed by Using Lloyd's Mirror Configuration

A Lloyd's mirror arrangement, which is possibly the simplest interference system, was installed to produce modulated structures using a two-beam irradiation. Both mirror and substrate are illuminated by the same laser beam. The substrate is thus irradiated with two beams at the same time.

Similar to the single-beam illumination setting, s-polarized light failed to induce ripple formation under Lloyd's mirror configuration. However, p-polarized light is able to form LIPSS under Lloyd's mirror configuration. Similar to single beam illumination system, the only ripples structure is the $\Lambda_{1,2}$-spaced LIPSS.

However, other LIPSS have been observed under the same configuration when using non-polarized light. The most extraordinary structures are two sets of intercepting ripples. The following combinations of intercepting ripples have been observed: 1. Interference pattern that follows equation 3.2 and cosine ripples following equation 3.3; 2. Sine ripples that follow equation 3.1 and cosine ripples that follow equation 3.3.

The angle of incidence, and the line spacings Λ_1, Λ_2, and Λ_3 can be determined from the FFT pattern by measuring the lengths ℓ_1, ℓ_2, and ℓ_3 that have been defined in Figure 1.23.

When the angle of incidence exceeded 40°, the measured spacing departed significantly from the curves plotted using $|\boldsymbol{k}_{//}^{s,a}|=2\pi/\lambda$. Instead, they were seen to change towards and be fitted at θ_i >~45° by another curve that also is described by equation 3.3 but with $|\boldsymbol{k}_{//}^{s,a}|$ given by equation 1.14, for a value of n=1.07.

The Lloyd's mirror set up strongly enhances the formation of ripples and in particular those that are characterized by a $\boldsymbol{q}_3$ wave vector. These ripples, that we never obtained using a single laser beam, are much straighter than those described by either $\boldsymbol{q}_1$ or $\boldsymbol{q}_2$ vectors. At angles of incidence larger than 45^o they extend over the whole irradiated area, that covers several millimeters wide.

5.4 Formation of Nanoprotrusions by Using Lloyd's Mirror Configuration

When two sets of ripples intersect there is a clear tendency to break each other's lines. Each set of ripples forces a modulation on the other. In general, the set that has the longer wavelength tends to dominate, forcing its modulation on the set that has the smaller value of Λ. In some cases, it can be observed that the broken line ends with a droplet-like shape, suggesting the quenching of a retreating liquid line.

A new nanostructure was seen to evolve at the same laser fluences as required for nanoripple formation, but commonly requiring a larger number of pulses. This structure is characterized by steep elevations, 40 to 70 nm in height, and ~ 60 to 100 nm in diameter at their base, organized into lines separated by a precise spacing, and placed on top of a subjacent ripple structure.

The evolution of nanoprotrusions is environment independent.

5.5 Formation of Nanoparticles

At slightly higher laser fluences than used to produce nanoprotrusions, nanoparticles were produced on the irradiated surface in a vacuum chamber filled with

low pressure buffer gas of helium.

First, a thin film is formed as atoms and/or clusters are redeposited during irradiation on the illuminated surface, possibly due to backscattering caused by the gas molecules. Then, the clusters in the film aggregate further into the observed nanoparticles with random distribution. Finally, like any other surface roughness, the nanoparticles interact with the incoming radiation and, provided they can move into or condense on specific sites of the substrate, they could, in addition, order along rows by a mechanism similar to that of nanoripple and nanoprotrusion formation.

Additional laser irradiation in helium can trigger the self-organization of the nanoparticles into straight line.

We have previously reported that nanoparticle alignment took place if either a microstructure of cones was present in the substrate or polarized light was employed. In this work we have found that neither one is required to generate an aligned nanoparticle structure.

5.6 Comparison between Nanoparticles and Nanoprotrusions

Several differences between the processing procedures of nanoparticles and those of nanoprotrusions were found. Most relevantly, nanoparticles are produced by single beam irradiation, whereas nanoprotrusions were only observed under the double beam irradiation generated with the Lloyd's mirror.

The incident laser fluence to create nanoparticles was on the order of 1 J/cm^2, whereas nanoprotrusions were formed with a beam fluence of 0.7 J/cm^2.

The third difference was the atmospheres where the treatment is taking place. For nanoprotrusions, we did not observe any difference between processing in vacuum and in air. And the experimental results are not sensitive to native oxide layer either. However, due to the nature of formation of nanoparticles, high base vacuum pressure and oxygen free environment is required.

From a structural point of view, similar to nanoprotrusions, nanoparticles appear in most instances associated with a ripple structure. However, whereas nanoprotrusions grow in the crests of the ripple structure, nanoparticles are detected in the valleys.

Another difference is the stability of the two nanostructures upon thermal treatment. Both samples were annealed at temperatures between 423 and 1073K in vacuum, for 2 hours. Even at the lowest temperature of this range, 423K, nanoparticles performed a Brownian-like motion thus losing their initial alignment. Nanoprotrusions remained stable in the entire annealing temperature range.

5.7 Alignment of Gold Nanoparticles by using Nanostructured Templates

By using previously produced nanostructured templates with nanoprotrusions and nanoripples, long-range ordered gold nanoparticles were obtained.

Ion beam deposition of gold film onto the nanostructured templates at very small grazing angles is required. Then, heat treatment at high temperature in air is followed to cluster the thin film into nanoparticles.

The width of gold strips can be controlled by using different grazing angles.

Oxide layer between the silicon substrate and gold film acts as a diffusion barrier

and can prevent the formation of low-temperature AuSi eutectic.

5.8 Future Work

The experiments described in chapter 3 motivate the proposed future research projects as follows:

1. To understand the mechanism that controls the different type of LIPSS that appears at the sample surface under given experimental conditions.

2. Develop a more complete computer model to quantitatively evaluate the evolution process of the LIPSS formation using the lubrication approximation.

3. Develop procedures aimed at synthesizing nanoparticles of any native and inducing them to self-organize into periodic, single and crossed linear arrays on a substrate, in a large scale using laser light.

4. Use laser-assisted chemical vapor deposition (LCVD) method together with the Lloyd's mirror arrangement to align nanoparticles on smooth substrate or template with pre-structured long-range ordered nano-LIPSS or nanoprotrusions.

5. Using the oblique deposition method described in section 3 to deposit a given substance at the top of the nanoripples. In that way, the ripple could have different electrical or optical properties than that of the bulk.

BIBLIOGRAPHY

1. W. W. Duley, p. 36 in UV Lasers: Effects and Applications in Materials Science, Cambridge University Press, 1996

2. C. Kittel, p. 307 in Introduction to Solid State Physics, John Wiley & Sons, Inc., New York, 1996

3. C. W. White and P. S. Peercy, p.6, p. 37, p.53 in Laser and Electron Beam Processing of Materials, Academic Press, Inc. 1980

4. G. E. Jellison Jr., D. H. Lowndes, D. N. Mashburn, and R. F. Wood, *Phys. Rev. B* **34**(4), 2408 (1986)

5. D. E. Aspnes and A. A. Studna, *Phys. Rev. B* **27**, 985 (1985)

6. R. F. Wood and G. E. Jellison Jr., "Melting Model of Pulsed Laser Processing", p. 204 in Semiconductors and Semimetals, Vol. 23, "Pulsed Laser Processing of Semiconductors" (R. F. Wood, C. W. White, and R. T. Young, eds.) Academic Press Inc., Orlando, 1984.

7. C. W. White and M. J. Aziz, "Energy Deposition, Heat Flow, and Rapid Solidification during Pulsed-Laser- and Electron-Beam Irradiation of Materials" p. 21 in Surface Alloying by Ion, Electron, and Laser Beams, ASM International, Metals Park, Ohio, 1987

8. E. J. Yoffa, *Appl. Phys. Lett.* **36**, 37 (1980)

9. E. J. Yoffa, *Phys. Rev. B* **21**, 2415 (1980)

10. L. M. Blinov, V. S. Vavilov, and G. N. Galkin, *Sov. Phys. Semicond.* **1**, 1124 (1967)

11. J. F. Ready, in Effects of High Power Laser Radiation, Academic Press, New York, 1971

12. W. R. Sooy, M. Geller, and D. P. Bortfeld, *Appl. Phys. Lett.* **5**, 54 (1964)

13. D. H. Auston, C. M. Surko, T. N. C. Venkatesan, R. E. Slusher, and J. A. Golovchenko, *Appl. Phys. Lett.* **33**, 437 (1978)

14. P. Baeri, S. U. Campisano, G. Foti, and E. Rimini, *Appl. Phys. Lett.* **33**, 137 (1978)

15. J. C. Wang, R. F. Wood, and P. P. Pronko, *Appl. Phys. Lett.* **33**, 455 (1978)

16. J. C. Wang, R. F. Wood, C. W. White, B. R. Appleton, P. P. Pronko, S. R. Wilson, and W. H. Christie, p. 127 in Laser-Solid Interactions and Laser Processing (S. D. Ferris, H. J. Leamy, and J. M. Poate, eds.) AIP Conference Proceedings No. 50, New York, 1979

17. A. E. Bell, *RCA Review* **40**, 295 (1979)

18. C. M. Surko, A. L. Simons, D. H. Auston, J. A. Golovchenko, R. E. Slusher, and T. N. C. Venkatesan, *Appl. Phys. Lett.* **34**, 635 (1979)

19. J. R. Kirkpatrick, G. E. Giles, and R. F. Wood, p. 152 in Heat Transfer and Thermal Control, Vol. 78, AIAA Progress in Astronautics and Aeronautics Series, New York, 1980

20. R. F. Wood and G. E. Giles, *Phys. Rev. B* **23**, 2923 (1981)

21. M. von Allmen, K. Affolter, and M. Wittmer, *Mat. Res. Soc. Symp. Proc.* **1**, 559 (1981)

22. K. G. Svantesson, N. G. Nilsson, and L. Huldt, *Solid State Commun.* **9**, 213 (1971)

23. J. A. van Vechten, p. 429 in Cohesive Properties of Semiconductors Under Laser Irradiation, (L. D. Laude, ed.) Martinus Nighoff, The Hague, 1983

24. H. W. Lo, and A. Compaan, *Phys. Rev. Lett.* **44**, 1604 (1980)

25. H. W. Lo, and A. Compaan, *Appl. Phys. Lett.* **38**, 179 (1981)

26. A. Compaan, M. C. Lee, H. W. Lo, G. J. Trott, and A. Aydinli, *J. Appl. Phys.* **54**, 5950 (1983)

27. S. De Unamuno and E.Fogarassy. A Thermal Description of the Melting of C- and a-Silicon Under Pulsed Excimer Lasers. *Appl. Surf. Sci.* **36**(1-4), 1-11. 1989.

28. R. K. Singh, D. R. Gilbert and J. Viatella. A Novel Method to Predict Laser-Induced, Non-Linear Thermal Effects in Semiconductors. *Materials Science and Engineering B* **40**(1), 89-95. 1996.

29. D. Bauerle, p. 226 in Laser Processing and Chemistry, Springer, 2000.

30. G. B. Shinn, F. Steigerwald, H. Stiegler, R. Sauerbrey, F. K. Tittel, and W. L. Wilson Jr., *J. Vac. Sci. Technol. B* **4**(60), 1273 (1986)

31. Anthony J. Pedraza, Jason D. Fowlkes and Yingfeng Guan, "Generation and manipulation of nanostructures by pulsed-laser processing". SPIE International Proceedings on High Power Laser Ablation 2002, ed. C.R. Phipps, Vol 4760, 164-174 (2002).

32. Anthony J. Pedraza, Jason D. Fowlkes and Yingfeng Guan, "Surface Nanostructuring of Silicon", *Applied Physics A* **77**, 277-284 (2003).

33. A. J. Pedraza, J. d. Fowlkes, D. A. Blom, H. M. Meyer III, *Journal of Materials Science and Engineering* **17**(11) 2815-2822 (2002)

34. J. D. Fowlkes, A. J. Pedraza, D. A. Blom, H. M. Meyer III, *Appl. Phys. Lett.* **80**(20) 3799-3801 (2002)

35. D. Bauerle, p. 571 in Laser Processing and Chemistry, Springer, 2000

36. A. V., A. S. Lomov, G. V. Osipov, M. I. Rabinovich: 'Pattern formation and dynamics of two-dimensional structures in non-equilibrium dissipative media'. In:

Nonlinear Waves 1-Dynamics and Evolution, ed. by A. V. Gaponov-Grekhov, M. I. Rabinovich, J. Engelbrecht (Springer, Berlin, Heidelberg 1989)

37. Haken H.: *Synergetics. An Introduction.* Springer Ser. Syn., Vol. 1, 3rd edn. (Springer, Berlin, Heidelberg 1983)

38. Nicolis G., I. Prigogine: Self-Organization in Non-Equilibrium Systems (Wiley, New York 1977)

39. A. J. Pedraza, in *Lasers in Materials*, edited by R. P. Agarwala, Mater. Sci. forum **301**, 69 (1999).

40. T-H. Her, R. J. Finlay, C. Wu, S. Deliwala, and E. Mazur, *Appl. Phys. Lett.* **73**, 1673 (1998).

41. F. Sanchez, J. L. Morenza, and V. Trtik, *Appl. Phys. Lett.* **75**, 3302 (1999).

42. F. Sanchez, J. L. Morenza, R. Aguiar, J. C. Delgado, and M. Varela, *Appl. Phys. Lett.* **69**, 62 (1996).

43. J. D. Fowlkes, A. J. Pedraza, and D. H. Lowndes, *Appl. Phys. Lett.* **77**, 1629 (2000).

44. A. J. Pedraza, J. D. Fowlkes, and D. H. Lowndes, *Appl. Phys. Lett.* **77**, 3018 (2000).

45. V. V. Voronov, S. I. Dolgaev, S. V. Lavrishchev, A. A. Lyalin, A. V. Simakin, and G. A. Shafeev, Phys. Vib. **7**, 131 (1999).

46. M. Birnbaum, *J. Appl. Phys.* **36**, 3688 (1965).

47. G. N. Maracus, G. L. Harris, C. A. Lo, and R. A. McFarlane, *Appl. Phys. Lett.* **33**, 453 (1978).

48. N. Tsukada, S. Sugata, and Y. Mita, *Appl. Phys. Lett.* **42**, 424 (1983).

49. A. J. Pedraza, S. Jesse, Y. F. Guan, and J. D. Fowlkes, *J. Mater. Res.* **16**(12), 3599 (2001)

50. J. Bloem and L. J. Gilling, Curr. Top. Mater. Sci. **1**, 277 (1978).

51. S. I. Anisimov, V. A. Khokhlov, *Instabilities in Laser-Matter Interaction* (CRC Press, Inc., Boca Raton, FL, 1995).

52. A. B. Brailovsky, S. V. Gaponov, and V. I. Luchin, *Appl. Phys. A* **61**, 81 (1995).

53. E. B. Levchenko and L. Chernyakov, *J. Appl. Mech. Tech. Phys.* **6**, 870 (1983).

54. Stephen Jesse, "A study of the evolution of laser-induced periodic surface microstructures on silicon and electronic transport in composite carbon nanotube networks", PhD Dissertation (2004)

55. F. Sanchez, J. L. Morenza, R. Aguiar, J. C. Delgado, and M. Varela, Appl. Phys. A **66**, 83 (1998).

56. A. J. Pedraza, J. D. Fowlkes, S. Jesse, C. Mao, and D. H. Lowndes, Appl. Sur. Sci. **168**, 251–257 (2000).

57. S. R. Foltyn, Mechanisms of Pulsed-Laser Sputtering, in *Pulsed Laser Deposition of Thin Films*, edited by D.B. Chrisey and G.K. Hubler (Wiley, New York, 1994), pp. 89–113.

58. D. Bauerle, *Laser Processing and Chemistry*, 2nd ed. (Springer, Berlin, Germany, 1996), p. 253.

59. S. Jesse, A. J. Pedraza, J. D. Fowlkes, J. D. Budai, *J. Mater. Res.,* **17**(5), 1002 (2002)

60. R. S. Wagner and W. C. Ellis, Appl. Phys. Lett. 4, 89 (1964)

61. E. I. Givargizov, J. Cryst. Growth 31, 20 (1975)

62. E. I. Givargizov, Growth of Whiskers by the Vapor-Liquid-Solid Mechanism, in Current Topics in Material Science, edited by E. Kaldis (North-Holland, Amsterdam, 1978), Vol. 1, pp. 79-145

63. J. P. Hirth and J. M. Pound, Prod. Mater. Sci. **11**, 107 (1963).

64. L.T. Canham: Appl. Phys. Lett. **57**, 1046 (1990)

65. K. Chen, X. Huang, J. Xu, D. Feng: Appl. Phys. Lett. **61**, 2069 (1992)

66. Y. Kanemitsu: Mater. Res. Soc. Symp. Proc. **358**, 81 (1995)

67. L.N. Dinh, L.L. Chase, M. Ballooch, W.J. Siekhaus, F. Wooten: Phys. Rev. B **54**, 5029 (1996)

68. Y. Kanemitsu, S. Okamoto, M. Otobe, S. Oda: Phys. Rev. B **55**, R7375 (1997)

69. E. Edelberg, S. Bergh, R. Naone, M. Hall, E.S. Aydil: J. Appl. Phys. **81**, 2410 (1997)

70. W. Marine, I. Movtchan, A. Simakine, L. Patrone, R. Dreyfus, M. Sentis, M. Autric, N. Merk: Mater. Res. Soc. Symp. Proc. **397**, 365 (1996)

71. T. Makino, N. Suzuki, Y. Yamada, T. Yoshida, T. Seto, and N. Aya, *Appl. Phys. A* **69**[Suppl], S243 (1999)

72. M.S. Brandt, H.D. Fuchs, M. Stutzmann, J. Weber, M. Cardona: Sol. State Commun. **81**, 302 (1992)

73. S. Nozaki, S. Sato, A. Denda, H. Ono, H. Morisaki: Mater. Res. Soc. Symp. Proc. **358**, 133 (1995)

74. M. Zacharias, P.M. Fauchet: Appl. Phys. Lett. **71**, 380 (1997)

75. M.V. Wolkin, J. Jorne, P.M. Fauchet, G. Allan, C. Delerue: Phys. Rev. Lett. **82**, 197 (1999)

76. B. Delley, E.F. Steigmeier: Phys. Rev. B **47**, 1397 (1993)

77. C. Delerue, G. Allan, M. Lannoo: Phys. Rev. B **48**, 11 024 (1993)

78. Y. Maeda: Phys. Rev. B **51**, 1658 (1995)

79. *Light Emission from Silicon*, eds. S. S. Iyer, R. T. Collins, and L. T. Canham, MRS Symposia Proceedings No. 256, Materials Research Society, 1991

80. G. Ledoux, O. Guillois, D. Porterat, C. Reynaud, F. Huisken, B. Kohn, and V. Paillard, *Phys. Rev. B* **62**(23), 15942 (2000)

81. T. Makimura, Y. Kunii, and K. Murakami, *Jpn. J. Appl. Phys.* **35**, 4780 (1996)

82. S. Botti, R. Coppola, F. Gourbilleau, and R. Risk, *J. Apl. Phys.* **88**(6), 3396 (2000)

83. X. J. Li and Y. H. Zhang, *Phys. Rev. B* **61**(19), 12605 (2000)

84. L. Patrone, D. Nelson, V. I. Safarov, M. Sentis, and W. Marine, *J. Appl. Phys.* **87**(8), 3829 (2000)

85. Y. Yamada, T. Orii, I. Umezu, S. Takeyama, T. Yoshida: Jpn. J. Appl. Phys. **35**, 1361 (1996)

86. T. Yoshida, Y. Yamada, T. Orii: J. Appl. Phys. **83**, 5427 (1998)

87. E. Werwa, A.A. Seraphin, L.A. Chiu, C. Zhou, K.D. Kolenbrander: Appl. Phys. Lett. **64**, 1821(1994)

88. T. Yoshida, S. Takeyama, Y. Yamada, K. Mutoh: Appl. Phys. Lett. **68**, 1772 (1996)

89. Y. Kousaka, K. Okuyama, M. Adachi, T. Mimura: J. Chem. Eng. Japan **19**, 401 (1986)

90. L. C. Chen and E. L. Hall, *Mater. Res. Soc. Symp. Proc.* **285**, 519 (1993)

91. W-. S. Kim, "Pulsed-Laser Deposition of TiN and Si_3N_3 films", MS Thesis (1998)

92. A. Matsunawa, S. Katayama, A. Susuki, and T. Ariyasu, Trans. Jpn. Welding Res. Institute **15**, 233 (1986).

93. Li-Chyong Chen, "Particulates Generated By Pulsed Laser Ablation" p. 167 – 198 in Pulsed Laser Deposition of Thin Films (D. B. Chrisey and G. K. Hubler, eds.) Wiley – Interscience, New York, 1994.

94. D. H. Lowndes, C. M. Rouleau, T. G. Thundat, G. Duscher, E. A. Kenik, and S. J. Pennycook, *J. Mater. Res.* **14**(2), 359 (1999)

95. L. Patrone, D. Nelson, V. I. Safarov, S. Giorgio, M. Sentis, and W. Marine, *Appl. Phys. A* **69**[Suppl], S217 (1999)

96. P. E. Dyer, A. Issa, and P. H. Key, *Appl. Phys. Lett*. **57**, 186 (1990)

97. Y. Nishikawa, K. Tanaka, and Y. Yoshida, *Nippon Kinzoku Kaishi* **55**, 581 (1991)

98. J. A. Greer, and H. J. Van Hook, *Mater. Res. Soc. Symp. Proc*. **191**, 171 (1990)

99. D. H. Lowndes, D. P. Norton, J. W. McCamy, R. Feenstra, J. D. Budai, D. K. Christen, and D. B. Poker, *Mater. Res. Soc. Symp. Proc.* **169**, 431 (1990)

100. A. Cheenne, J. Perriere, F. Kerherve, G. Hauchecorne, e. fogarassy, and C. Fuchs, *Mater. Res. Soc. Symp. Proc.* **191**, 229 (1990)

101. M. H. Wu, R. Mu, A. Ueda, and D. O. Henderson, *Mater. Res. Soc. Symp. Proc.* **638**, F13.2.1 (2001)

102. F. P. Gagliano, and U. C. Paek, *Appl. Opt.* **13**, 274 (1974)

103. D. B. Geohegan, *Mater. Res. Soc. Symp. Proc.* **285**, 27 (1993)

104. H. Dupendant, J. P. Gavigan, D. Givord, A. Lienard, J. P. Rebouillat, and Y. Souche, *Appl. Surf. Sci.* **43**, 369 (1989)

105. K. Murakami, in Laser Ablation of Electronic Materials: Basic mechanisms and Applications (E. Fogarassy and S. Lazare, eds.), North Holland, Amsterdam, p. 125 (1992)

106. D.B. Geohegan, A.A. Puretzky, G. Duscher, and S.J. Pennycook, *Appl. Phys. Lett.* **72**(23), 2987 (1998)

107. L. A. Chiu, A. A. Seraphin, and K. D. Kolenbrander, J. Electron. Mater. **23**, 347 (1994)

108. T. Makimura, T. Mizuta, and K. Murakami, *Appl. Phys. A* **69**[Suppl], S213 (1999)

109. D. B. Geohegan, A. A. Puretzky, G. Duscher, and S. J. Pennycook, *Appl. Phys. Lett.* **73**, 438 (1998)

110. D. B. Geohegan, A. A. Puretzky and D. J. Rader, *Appl. Phys. Lett.* **74**(25), 3788 (1999)

111. D. B. Geohegan, *Appl. Phys. Lett*. **60**, 2732 (1992)

112. D. B. Geohegan and A. A. Puretzky, *Appl. Phys. Lett.* **67**(2), 197 (1995)

113. Alexander A. Puretzky, David B. Geohegan, and C. H. Schittenhelm, Proc. SPIE Int. Soc. Opt. Eng. **4977**, 648 (2003)

114. David B. Geohegan *et al.* Proc. SPIE Int. Soc. Opt. Eng. **4636**, 1 (2002)

115. David B. Geohegan, Alexander A. Puretzky, Xudong Fan, Stephen J. Pennycook, Michael A. Guillorn, Michael L. Simpson, Vladimir I. Merkulov, Derek W. Austin, and David C. Joy, Proc. SPIE Int. Soc. Opt. Eng. **4347**, 1 (2001)

116. David B. Geohegan, Alexander A. Puretzky, Xudong Fan, Michael A. Guillorn, Michael L. Simpson, Vladimir I. Merkulov, and Stephen J. Pennycook, Proc. SPIE Int. Soc. Opt. Eng. **3935**, 2 (2000)

117. T. Makino, N. Suzuki, Y. Yamada, T. Yoshida, T. Seto, and N. Aya, Appl. Phys. A 69 [Suppl], S243 (1999)

118. S. S. Iyer and Y.-H. Xie, Science 260, 40 (1993)

119. A. G. Nassiopoulos, S. Grigoropoulos, and D. Papadimitriou, Appl. Phys. Lett. 69(15), 2267 (1996)

120. B. H. Choi, S. W. Hwang, I. G. Kim, H. C. Shin, Y. Kim, and E. K. Kim, Appl. Phys. Lett. 73(21), 3129 (1998)

121. A. J. Pedraza, J. D. Fowlkes, Y. F. Guan, Appl. Phys. A **77**, 277 (2003)

122. J. D. Fowlkes and A. J. Pedraza, Mat. Res. Soc. Symp. Proc. **737**, F5.7.1 (2003)

123. Y. Yamada, T. Orii, I. Umezu, and T. Yoshida, Jpn. J. Appl. Phys., Part 1 **35**, 1361 (1996)

124. T. Yoshida, S. Takeyama, Y. Yamada, and K. Mutoh, Appl. Phys. Lett. **68**, 1772 (1996)

125. T. Makimura, Y. Kunii, and K. Murakami, Jpn. J. Appl. Phys., Part 1 **35**, 4780 (1996)

126. T. Makimura, T. Sakuramoto, and K. Murakami, Jpn. J. Appl. Phys., Part 2 **35**, L735 (1996)

127. T. Makimura, Y. Kunii, N. Ono, and K. Murakami, Jpn. J. Appl. Phys., Part 2 **35**, L1703 (1996)

128. D. H. Lowndes, C. M. Rouleau, T. Thundat, G. Duscher, E. A. Kenik, and S. J. Pennycook, J. Mater. Res. **14**, 359 (1999)

129. J. D. Fowlkes, A. J. Pedraza, D. A. Blom, and H. M. Meyer III, Appl. Phys. Lett. **80**(20), 3799 (2002)

130. A. J. Pedraza, J. D. Fowlkes, D. A. Blom and H. M. Meyer III, J. Mater. Res., **17**(11), 2815 (2002)

131. C. Wu, C. H. Crouch, L. Zhao, J. E. Carey, R. Younkin, J. A. Levinson, E. Mazur, R. M. Farrell, P. Gothoskar, and A. Karger, Appl. Phys. Lett. **78**, 1850 (2001)

132. J. F. Young, J. E. Sipe, and H. M. van Driel, Phys. Rev. **B30**, 2001 (1984)

133. M. J. Birnbaum, Appl. Phys. 36, 3688 (1965)

134. V. P. Aksenov and B. G. Zhurkin, Dokl. Akad. Nauk SSSR 265, 1365 (1982)

135. A. M. Bonch-Bruevich, M. K. Kochengina, M. N. Libenson, s. d. Pudkov, and V. V. Trubaev, Izv. Akad. Nauk SSSR, Ser. Fiz. 46, 1186 (1982)

136. A. M. Prokhorov, V. A. Sychugov, A. V. Tishchenko, and A. A. Khakimov, Pis'ma Zh. Tekh. Fiz. 8, 961, 1409 (1982) [Sov. Tech. Phys. Lett. 8, 415, 605 (1982)]

137. P.M. Fauchet, and E. Siegman, Surface ripples on silicon and gallium arsenide under picosecond laser illumination, Appl. Phys. Lett. 40, 824-826 (1982)

138. N. R. Isenor, Appl. Phys. Lett. 31, 148 (1977)

139. S.R.J. Brueck and D.J. Ehrlich, Stimulated surface-plasma-wave scattering and growth of a periodic structure in laser-photodeposited metal films, Phys. Rev. Lett. 48, 1678-1681 (1982)

140. Fritz Kellmann, Laser-driven corrugation instability of liquid metal surfaces, Phys. Rev. Lett. 51,2097-2099 (1983)

141. Jeff F. Young, J.S, Preston, H.M. van Driel, and J.E. Sipe, Laser-induced periodic structures. II. Experiments on Ge, Si, Al and brass, Phys. Rev. B 27, 1155-1172 (1982)

142. J. F. Figueira and S. J. Thomas, Generation of Surface Microstructure in Metals and Semiconductors by Short Pulse CO2 Lasers, in Proceedings of the International Conference on Surface Studies with Lasers, F. R. Aussenegg, A. Leitner, M. E. Lippitsch, eds, Springer-Verlag, Berlin, 212-215, (1983)

143. A. K. Jain, V. N. Kulkarni, D. K. Sood, and J. C. Uppal, J. Appl. Phys. 52, 4882 (1981)

144. V. N. Anisimov, V. Yu. Baranov, L. A. Bol'shov, A. M. Dykhne, D. D. Malyuta, V. D. Pis'mennyi, A. Yu. Sbrant, and M. A. Stepanva, Poverkhnost', No. 7, 138 (1983)

145. Zhou Guosheng, P.M. Fauchet, and E. Siegman, Growth of spontaneous periodic surface structures on solids during laser illumination, Phys. Rev. B 26, 5366-5381 (1982)

146. V. P. Aksenov and B. G. Zhurkin, Preprint No. 56, 194, FIAN, Moscow (1982).

147. D.J. Ehrlich, S.R.J. Brueck and J.Y. Tsao, Time-resolved measurements of stimulated surface polariton wave scattering and grating formation in pulsed-laser annealed germanium, Appl. Phys. Lett. 41, 630-632 (1982)

148. Noriaki Tsukuda, Sumio Sugata, and Yoh Mita, New Experimental Evidence of Surface Ripples on GalliumArsenide Surface in Laser Annealing, Appl. Phys. Lett. 42, 424-426 (1983)

149. G. G. Gromov and V. B. Ufimtsev, Dokl. Akad. Nauk SSSR 272, 1405 (1983), Pis'ma Zh. Tekh. Fiz. 9, 580 (1983) [Sov. Tech. Phys. Lett. 9, 249 (1983)]

150. J. F. Young, J. S. Preston, H. M. van Oriel, and J. E. Sipe, Phys. Rev. B 27, 1141, 1155 (1983)

151. M. Oron and G. Sorensen, Appl. Phys. Lett. 35, 782 (1979)

152. P. V. Bazakutsa, A. M. Prokhorov, V. A. Sychugov, and A. V. Tishchenko, Pis'ma Zh. Tekh. Fiz. 9, 705 (1983) [Sov. Tech. Phys. Lett. 9, 303 (1983)]

153. V. V. Bazhenov, A. M. Bonch-Bruevich, M. N. Libenson, V. S. Makin, s. D. Pudkov, and V. V. Trubaev, Pis'ma Zh. Tekh. Fiz. 9, 932 (1983) [Sov. Tech. Phys. Lett. 9, 402 (1983)]

154. P.A. Temple and M.J. Soileau, Polarization Charge Model for Laser-Induced Ripple Pattern in Dielectric Materials, IEEE Journal of Quantum Electronics QE-17, 2067-2072 (1981)

155. F. Keilmann and Y.H. Bai, Perodic surface structures frozen into CO2 laser-melted quartz, Appl. Phys. A 29, 9-18 (1982)

156. P.E. Dyer, R.J. Farley, R. Giedl and D.M. Karnakis, Excimer laser ablation of polymers and glasses for grating fabrication, Applied Surface Science 96-98, 537-549 (1996)

157. M. Siegrist, G. Kaech, and F. K. Kneubuhl, Appl. Phys. 2, 45 (1973)

158. D. C. Emmony, R. P. Howson, and L. J. Willis, Appl. Phys. Lett. 23, 598 (1973)

159. C. T. Walters, Appl. Phys. Lett. 25, 696 (1974)

160. L. J. Willis and D. C. Emmony, Opt. Laser Technol. 7, 222 (1975)

161. N. R. Isenor, Appl. Phys. Lett. 31, 148 (1977)

162. V. I. Konov, A. M. Prokhorov, V. A. Sychugov, A. V. Tishchenko, and V. N. Tokarev, Zh. Tekh. Fiz. 53, 2283 (1983) [Sov. Phys. Tech. Phys. 28, 1404 (1983)]

163. Matthias Bolle and Sylvain Lazare, Characterization of submicrometer periodic structures produced on polymer surfaces with low-fluence ultraviolet laser radiation, J. Appl. Phys. 73, 3516-3524 (1993).

164. P.E. Dyer and R.J. Farley, Dynamic of laser-induced periodic surface structures in excimer laser ablation of polymers, J. Appl. Phys. 74, 1442-1444 (1993)

165. M. Csete and Zs. Bor, Laser-induced periodic surface structure formation on polyethylene terephthalate, Applied Surface Science 133, 5-16 (1998)

166. G. A. Rozgonyi, H. J. Leamy, T. T. sheng, and G. K. Celler, in Laser-Solid Interactions and Laser Processing—1978 (Materials Research Society, Boston), Proceedings of the Symposium on Laser-Solid Interactions and Laser Processing, edited by S. D. Ferris, H. J. Leamy, and J. M. Poate (AIP, New York, 1979), p. 457.

167. V. P. Aksenov and B. G. Zhurkin, Dokl. Akad. Nauk SSSR 265, 1365 (1982) [Sov. Phys. Dokl. 27, 630 (1982)].

168. D. Bauerle, p. 571 in Laser Processing and Chemistry, Springer, 2000.

169. S. A. Akhmanov, V. I. Emel'yanov, N.I. Koroteev, and V. N. Seminogov, Sov. Phys. Usp. **28**, 1084 A. (1986)

170. Monika S K Fuchs, J. Phys.: Condens. Matter **12,** 4341 (2000)

171. V. I. Emel'yanov and V. N. Seminogov, Zh. Eksp. Teor. Fiz. 86, 1026 (1984) [Sov. Phys. JETP 59, 598 (1984)]

172. V. I. Emel'yanov and V. N. Seminogov, Kvant. Elektron. 11, 871 (1984) [Sov. J. Quantum Electron. 11, 591 (1984)]

173. G. A. Golubenko, A. A. Samokhin, and V. A. Sychugov, ibid., 1850 [Sov. J. Quantum electron. 11, 1239 (1984)]

174. M. I. Tribel'skii and S. M. Gol'dberg, Pis'ma Zh. Tekh. Fiz. 8, 1227 (1982) [Sov. Tech. Phys. Lett. 8, 526 (1982)]

175. V. I. Emel'yanov, E. M. Zemskov, and V. N. Seminogov, Kvant. Electron. 10, 2389 (1983) [Sov. J. Quantum electron. 10, 1556 (1983)]

176. V. I. emel'yanov, e. M. Zemskov, and V. N. Seminogov, ibid. 11, 2283 (1984) [sov. J. Quantum Electron. 11, 1484 (1984)]

177. M. J. Soileau, IEEE J. QE-20, 464 (1984)

178. H. J. Leamy, G. A. Rozgonyi, T. T. Sheng, and G. K. Celler, Appl. Phys. Lett. 32, 535 (1978)

179. J. A. Van Vechten, Solid State Commun. 39, 1285 (1981)

180. R. W. Rendell and K. L. Ngai, Bull. Am. Phys. Soc. 27, 235 (1982)

181. J. F. Young, J. E. Sipe, J. S. Preston, H. M. vanDriel, Appl. Phys. Lett. 41(3), 261 (1982)

182. R. M. Walser, M. F. Becher, J. G. Ambrose, and D. Y. Sheng, in Laser and Electron-Beam Solid Interactions and Materials Processing, edited by J. F. Gibbons, W. Hess, and T. Sigmon (Elsevier, New York, 1981), p. 177.

183. G. N. Maracas, G. L. Harris, C. A. Lee, and R. A. Mcfarlane, Appl. Phys. Lett. 33, 453 (1978)

184. D. Haneman and R. J. Nemanich, Solid State Commun. 43, 203 (1982)

185. L. J. Willis and D. C. Emmony, Opt. Laser Technol. 7, 222 (1975)

186. J. F. Young, J. E. Sipe, and H. M. van Driel. Optics Lett. 8, 431 (1983)

187. J. C. Koo and R. E. Slusher, Appl. Phys. Lett. 28, 614 (1976)

188. S. R. J. Brueck and D. J. Ehrlich, Phys. Rev. Lett. 48, 1678 (1982)

189. A. M. Bonch-Bruevich, M. N. Libenson, and V. s. Makin, Pis'ma Zh. Tekh. Fiz. **10**, 3 (1984) [Sov. Tech. Phys. Lett. **10**, 1 (1984)].

190. H. H. Solak, D. He, W. Li, S. Singh-Gasson, F. Cerrina, B. H. Sohn, X. M. Yang, and P. Nealey, Appl. Phys. Lett. 75(15), 2328 (1999)

191. H. H. Solak, D. He, W. Li, and F. Cerrina, J. Vac. Sci. Technol. B 17(6), 3052 (1999)

192. J Jorritsma, M A M Gijs J M Kerkhof and J G H Stienen. General technique for fabricating large arrays of nanowires. Nanotechnology 7, 263-265. 1996.

193. D.E.Prober, M. D. Feuer and N. Giordano. Fabrication of 300A metal lines with substrate-step techniques. Appl.Phys.Lett. 37[1], 94-96. 1980.

194. E.Olson, G. C. Spalding A. M. Goldman and M.J.Rooks. New method for fabricating ultra-narrow metallic wires. Appl.Phys.Lett. 65[21], 2740-2742. 1994.

195. J.Jorritsma, M. A. M. Gijs C. Schonenberger and J. G. H. Stienen. Fabrication of large arrays of metallic nanowires on V-grooved substrates. Appl.Phys.Lett. 67[10], 1489-1491. 1995.

196. http://ksks.essortment.com/historyoflaser_rsny.htm

197. David J. Elliott, p. 48 in Ultraviolet Laser Technology and Applications, Academic Press, Inc., San Diego, 1995

198. W. W. Duley, p. 36 in UV Lasers: Effects and Applications in Materials Science, Cambridge University Press, 1996

199. C. Kittel, p. 307 in Introduction to Solid State Physics, John Wiley & Sons, Inc., New York, 1996

200. C. W. White and P. S. Peercy, p.6, p. 37, p.53 in Laser and Electron Beam Processing of Materials, Academic Press, Inc. 1980

201. D. E. Aspnes and A. A. Studna, *Phys. Rev. B* **27**, 985 (1985)

202. T.C.Wong, C. P. Li R. Q. Zhang and S. T. Lee. Gold nanowires from silicon nanowire templates. *Appl.Phys.Lett.* **84**[3], 407-409 (2004)

203. http://personal.cityu.edu.hk/~appkchu/AP4120/2v.pdf

204. L. R. Baylor, V. I. Merkulov, E. D. Ellis, D. H. Lowndes, *J. Appl. Phys.* **91**, 4602 (2002)

205. R. H. Fowler and L. Nordheim, *Proc. R. Soc. London*, Ser. A **119**, 683 (1928)

206. http://www.newport.com/file_store/PDFs/tempPDFs/UV_Laser_Line_Polarizing_e3555.pdf

207. Max Born and Emil Wolf, Principles of Optics, Cambridge University Press, 7th Edition (1999), p. 291

208. Y. F. Guan, A. J. Pedraza, J. D. Fowlkes and D. C. Joy, to be published in *J. Vac. Sci. Technol. B* Vol. **22**, No. 6 (2004)

209. T. J. Chuang, *J. Chem. Phys.* **74**, 1453 (1981)

210. A. J. Pedraza, J. Fowlkes, D. H. Lowndes, *Appl. Phys. Lett.* **74**, 2322 (1999)

211. T. Surek and B. Chalmers, *J. Cryst. Growth*, **29**, Issue 1, 1 (1975)

212. J. E. Carey, L. Zhao, C. Crouch, C. Wu, and E. Mazur, Lasers and Electro-Optics, 2001. CLEO '01. Technical Digest. 555-556 Summaries of papers presented at the Conference on Meeting Date: 05/06/2001 -05/11/2001, Publication Date: 2001 Location: Baltimore, MD , USA

213. FlexPDE Software, 2000 PDE Solutions Inc.

214. A. M. Cazabat, F. Heslot, S. M. Troian and P. Carles, *Nature* **346**, 824 (1990)

215. T. Abe, Editor, in Properties of Crystalline Silicon (R. Hull, Editor, London: INSPEC, The Institution of Electrical Engineers, 1999), Ch. 1.1

216. P. Carles, S. M. Troian, A. M. Cazabat and F. Heslot, *J. Phys.: Condens. Matter* **2**, SA477 (1990)

217. A. J. Pedraza, Y. F. Guan, J. D. Fowlkes and D. A. Smith, to be published in *J. Vac. Sci. Technol. B* Vol. **22**, No. 6 (2004)

218. Jason Fowlkes, "Laser-induced nanostructures in silicon", PhD Dissertation (2002)

219. Alexander A. Nepomnyashchy, Manual G. Velarde, and Pierre Colinet, Interfacial Phenomena and Convection, Chapman & Hall/CRC, Boca Raton, Ch.2, p. 19 (2002)

220. P. Y. Chevnlier, *Thermochimica Acta*, **141,** 217-226 (1989)

APPENDIX

Two-dimensional computer simulation of laser melting

Heat evolution due to laser heating was calculated using computer software (Flex-PDE) to solve the differential equation for heat diffusion

$$\rho c \frac{\partial T}{\partial x} = \nabla(k\Delta T) + Q_m \frac{dz_i}{dt} + P(x,z,t) \qquad \text{A-1}$$

where the two source terms account for melting/freezing and for laser heating, $\boldsymbol{Q_m}$ is the heat of melting, $\boldsymbol{dz_i/dt}$ is the rate of displacement of the solid/liquid interface located at $\boldsymbol{z_i}$, and ***P(x,y,t)***, the laser heating contribution, is given by

$$P(x,z,t) = \alpha(1-R)I_o(x,t)e^{-\alpha z} \qquad \text{A-2}$$

R is the reflectivity, α is the absorption coefficient, and z is the axis normal to the surface pointing inward to the material. The profile of laser energy per unit time, per unit area, can be approximated by a Gaussian curve of the form:

$$I_o(x,t) = A(x)\exp\left[-\frac{2(t-\delta)^2}{\sigma^2}\right] \qquad \text{A-3}$$

where ***A(x)*** is assumed to vary periodically across the surface, in the x- direction, according to

$$A(x) = \frac{2F}{\sigma\sqrt{\pi}}\left(1-\alpha\cos\frac{2\pi x}{\lambda}\right) \qquad \text{A–4}$$

F is the fluence. Heat radiation at the surface is neglected.

From the formulas we can see that the accuracy of the simulation depends on the thermal and optical properties of the silicon. In order to increase the accuracy of our computer program, two sets of thermal and optical data from different groups have been tested. Also, our computer simulation results through FlexPDE have been compared with the results from those two groups respectively.

Table A-1 lists all the thermal and optical parameters from Unamuno et al [27].

Table A-1 Thermal and optical parameters from Unamuno et al. [27]

Parameter	Symbols in FlexPDE	Material	Value and references
Density ρ (g/cm^3)	rho	c-Si	2.32
		l-Si	2.52
Melt latent (J/cm^3)	Qm	c-Si	4535.95
Melting Temperature(K)	Tm		1685
Thermal conductivity (w/cm.K)	lambda	c-Si: T<1200K	$1523.7*T^{-1.226}$
			$9*T^{-0.502}$
		T≥1200K	$0.5+2.93x10^{-4}(T-T_M)$
		l-Si	
Specific heat (J/g.K)	cp	c-Si	$0.695*\exp(2.375x10^{-4}T)$
		l-Si	1.0465
Reflectivity	Ref		0.66
Absorption (cm^{-1})	Absor		$1.7x10^6$
Width of the domain (cm)	w		$0.1x10^{-4}$
Height of the domain (cm)	h		$50x10^{-4}$
Energy density (J/cm^2)	E		3
Pulse width (s)	D		$25x10^{-9}$
Pulse delay (s)	Dela		$45x10^{-9}$
Maximum pulse amplitude (W/cm^2)	A		E/D*(2/PI)^0.5=$1.197x10^8$
Incident laser power (W/cm^2)	I0		$A*\exp[\frac{-2*(t-Dela)^2}{D^2}]$
Heat source	P		Absor*(1-Ref)*I0*exp(-Absor*y)

FlexPDE descriptions for Unamuno's data are:

```
DEFINITIONS
  Qm= 4536                  { latent heat }
  Tm= 1687                    { Melting temperature }
  T0= 1                    { Melting interval +- T0 }
  Tinit
  sinit

  lammain=4.0559-0.014648*temp+2.541e-5*temp^2-2.4507e-8*temp^3+1.3684e-
11*temp^4-4.361e-15*temp^5+7.351e-19*temp^6-5.0801e-23*temp^7
  lamadd=arctan((temp-1687)/1)*0.284111/PI+0.1421
  lambda =lammain+lamadd= 4.0559-0.014648*temp+2.541e-5*temp^2-2.4507e-
8*temp^3+1.3684e-11*temp^4-4.361e-15*temp^5+7.351e-19*temp^6-5.0801e-
23*temp^7+ arctan((temp-1687)/1)*0.284111/PI+0.1421 {Thermal conductivity w/cm.k}
  rho= 2.42 + ARCTAN((temp-1687)/1)*0.2/PI                { Density g/cm3 }
  cp = 0.78572-2.51e-4*temp+5.93e-7*temp^2-2.83e-10*temp^3+4.1e-14*temp^4
{ Heat capacity J/g.k}
  E= 1.0 {Energy density J/cm^2}
  D=25e-9 {Pulse width s}
  Dela=45e-9 {pulse Delay s}
  A= E/D*(2/PI)^0.5 {max pulse amplitude, W/cm^2}
  I0= A*exp(-2*(t-Dela)^2/D^2)  {incident laser power, W/cm^2}
  Absor=arctan((1687-temp)/1)*190000/PI+1655000 {Absorption coefficient cm-1}
  Ref=0.6691-3.1255e-5*temp+8.5224e-8*temp^2-5.71e-11*temp^3+1.222e-
14*temp^4+1.31e-18*temp^5-8.4e-22*temp^6+8.51e-26*temp^7 {Reflectivity}
  P=Absor*(1-Ref)*I0*exp(-Absor*y)  {Heat generation function- another source of heat}
  w = .1e-4 { width of the domain, cm}
  h =  5e-4 {height of the domain.cm}
```

The following lists thermal properties data from Singh's paper [28]:

Solid thermal conductivity: 0.337 $W.cm^{-1}.K^{-1}$
Liquid thermal conductivity: 0.7 $W.cm^{-1}.K^{-1}$
Solid specific heat capacity: 2.167 $J.cm^{-3}.K^{-1}$ = 0.9341 $J.g^{-1}K^{-1}$
Liquid specific heat capacity: 2.4 $J.cm^{-3}.K^{-1}$ = 0.9524 $J.g^{-1}K^{-1}$
Melting temperature: 1685 K
Latent heat of fusion: 4206 $J.cm^{-3}$
Reflectivity of solid: 0.59
Reflectivity of liquid: 0.73
Solid thermal diffusivity: 0.156 $cm^2.s^{-1}$

FlexPDE descriptions for Singh's data are:

```
DEFINITIONS
 Qm= 4206          { latent heat J/cm^3}
 Tm= 1685            { Melting temperature K}
 T0= 1                 { Melting interval +- T0 }
 Tinit
 sinit

 lambda = ArcTAN(temp-1685)*0.363/PI+0.5185{w/cm.k}
 rho= 2.42 + ARCTAN((temp-1687)/1)*0.2/PI              { Density g/cm^3 }
 cp = ArcTAN(temp-1685)*0.0183/PI+0.94325     { heat capacity J/g.k}
 E= 1.0 {Energy density J/cm^2}
 D=25e-9 {Pulse width s}
 Dela=45e-9 {pulse Delay s}
 A= E/D*(2/PI)^0.5 {max pulse amplitude, W/cm^2}
 I0= A*exp(-2*(t-Dela)^2/D^2)  {incident laser power, W/cm^2}
 Absor=arctan((1687-temp)/1)*190000/PI+1655000 {Absorption coefficient cm-1}
 Ref=Arctan(temp-1685)*0.14/PI+0.66 {Reflectivity}
 P=Absor*(1-Ref)*I0*exp(-Absor*y)  {Heat generation function- another source of heat}
 w = .1e-4 { width of the domain, cm}
 h =  5e-4 {height of the domain.cm}
```

Figure A-1 to Figure A-3 compare the thermal and optical properties of silicon from two different sources.

Table A-2 to table A-4 list the computer simulation results by using Singh and Unanmuno's data respectively. From the comparison, we can see that our computer simulation is very close to the experimental results.

Figure A-4 to Figure A-23 show the simulation results of surface temperature as functions of time and distance. Both Singh and Unanmuno's thermal and optical parameters for silicon have been applied.

The FlexPDE code for this simulation is attached at the end of the appendix.

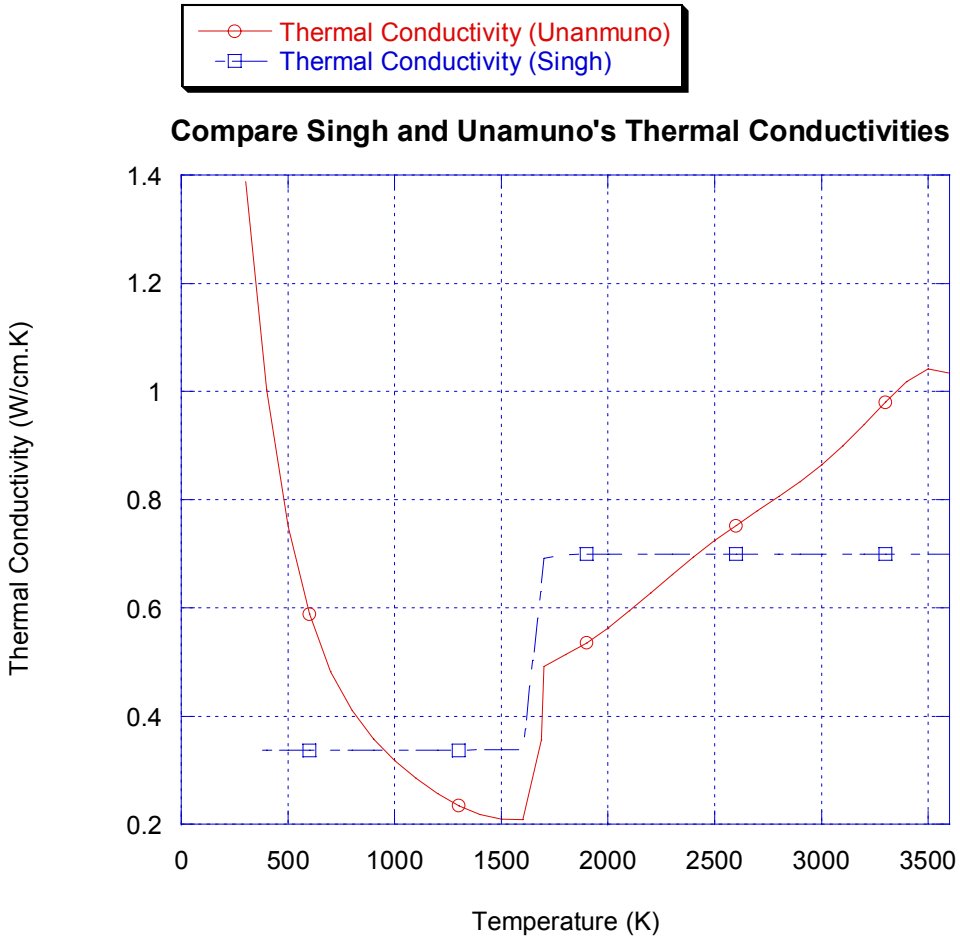

Figure A-1 Compare the thermal conductivities of silicon as a function of temperature from Unanmuno et al and Singh et al's data.

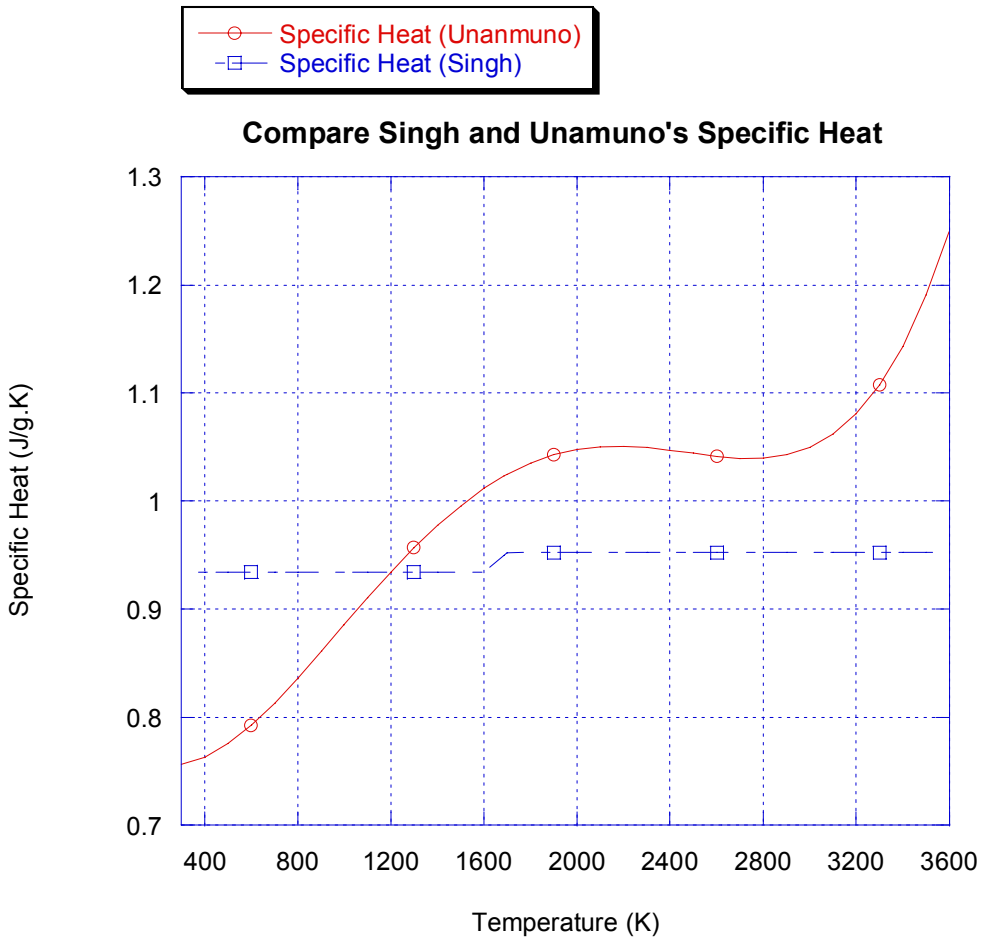

Figure A-2 Specific heat as a function of temperature from Unanmuno and Singh's reports.

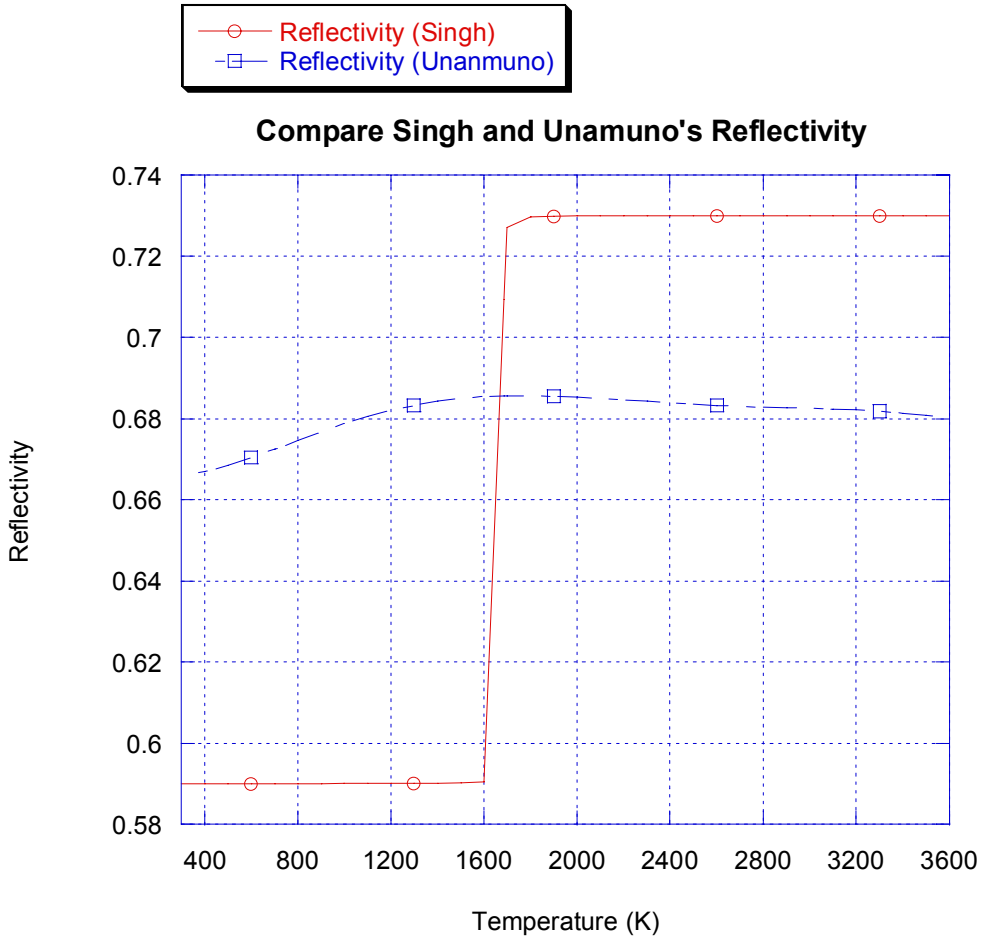

Figure A-3 Reflectivity as a function of temperature from Unanmuno and Singh's reports.

Table A-2 Compare the Melting Threshold using both Singh and Unamuno's data

	Unamuno's	Singh's	FlexPDE (using Unamuno's data)	FlexPDE (using Singh's data)
Melting Threshold (248nm,25ns)(J/cm^2)	0.75	~ 0.5	0.69	0.57

Table A-3 FlexPDE Simulation Results using Unamuno's data

Energy Density (J/cm^2)	Melting time (ns)	Melting Depth (nm)		Maximum Surface Temperature (K)
		FlexPDE	Unamuno's	
1	52 (40-92)	200	200	1820
1.5	120 (40-160)	400	400	2200
2	227 (33-260)	600	600	2600
2.5	390 (30-420)	750	750	3000
3	622 (28-650)	950	930	3400

Table A-4 FlexPDE Simulation Results using Singh's data

Energy Density (J/cm^2)	Melting time (ns)	Melting Depth (nm)		Maximum Surface Temperature (K)
		FlexPDE	Singh's	
1	50 (39-89)	200	200	1760
1.5	(35-125)	300	300	2000
2	(30-180)	500	500	2320
2.5	(28-260)	700	700	2720
3	(28-360)	900	N/A	3150

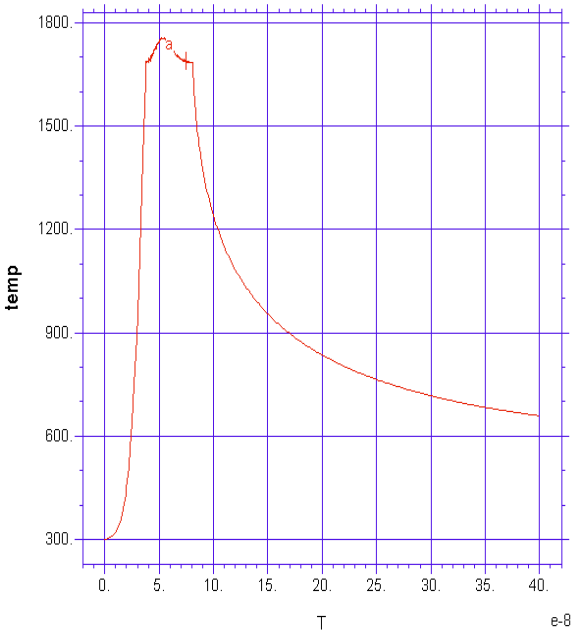

Figure A-4 Temperature vs. Time (Ed=1 J/cm2) (Using Singh's data)

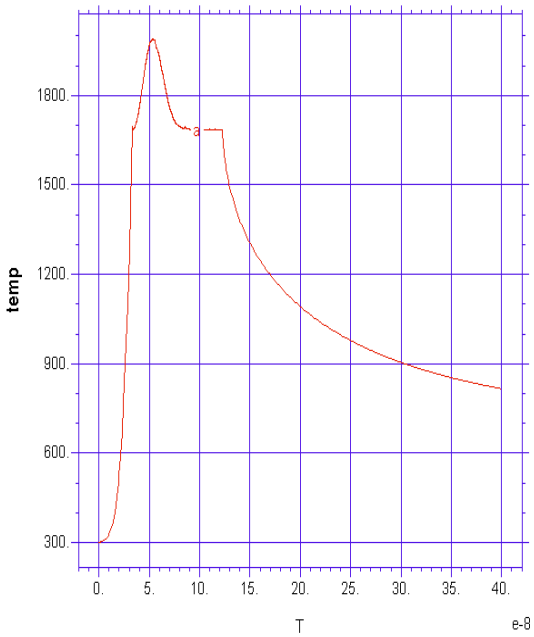

Figure A-5 Temperature vs. Time (Ed=1.5 J/cm^2) (Using Singh's data)

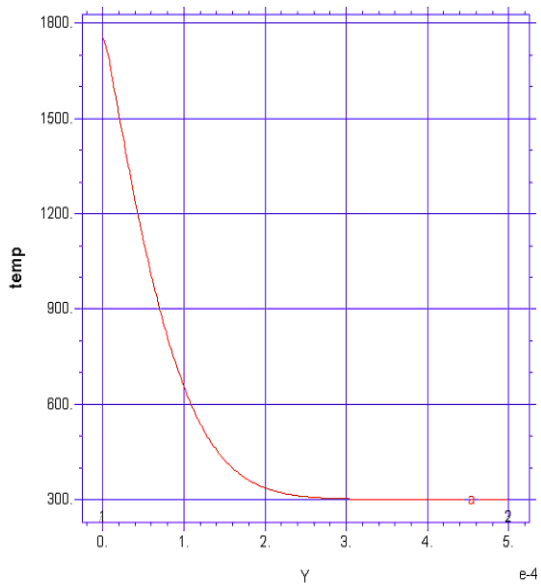

Figure A-6 Temperature vs. Distance at 54ns. (E$_d$=1 J/cm^2). (Using Singh's data)

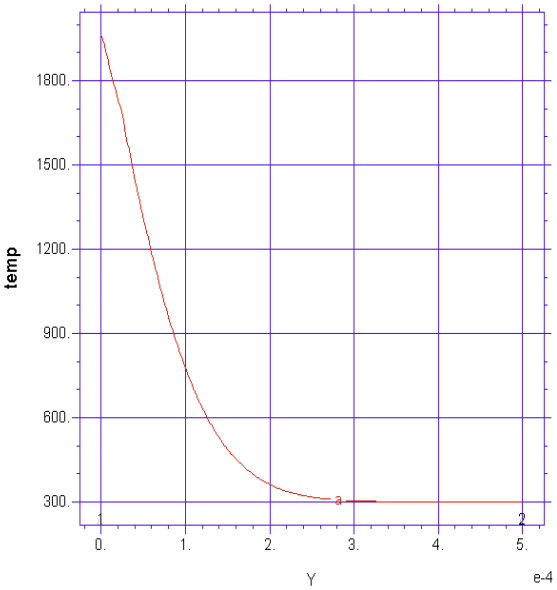

Figure A-7 Temperature vs. distance at 54 ns. (E$_d$=1.5 J/cm^2). (Singh's data)

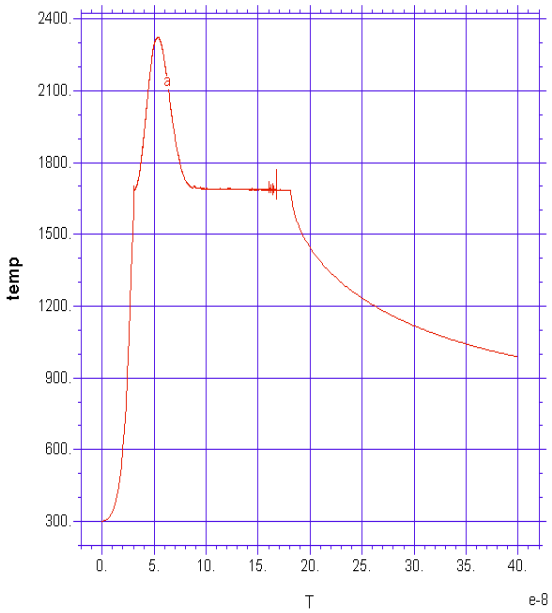

Figure A-8 Temperature vs. time. (E_d=2 J/cm^2). (Using Singh's data)

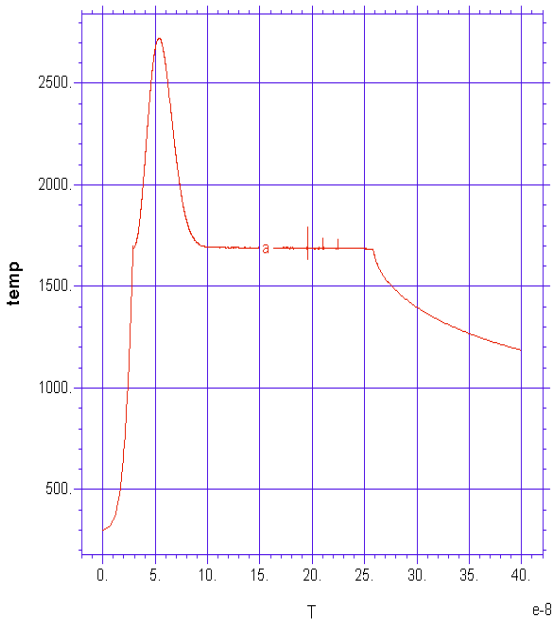

Figure A-9 Temperature vs. time. (E_d=2.5 J/cm^2). (Singh's data)

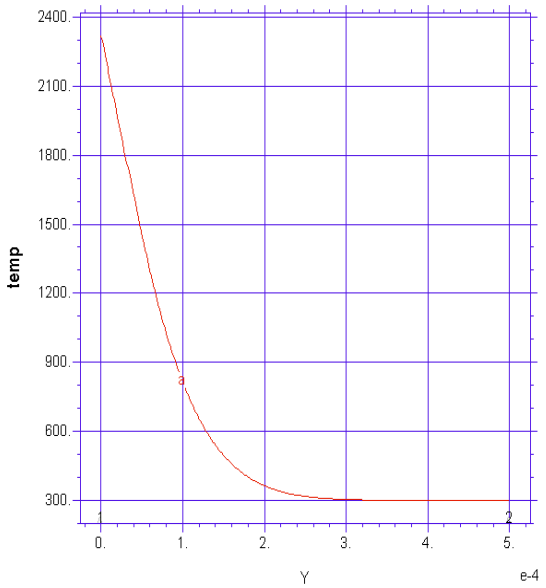

Figure A-10 Temperature vs. Distance at 55ns. (E_d=2 J/cm^2). (Using Singh's data)

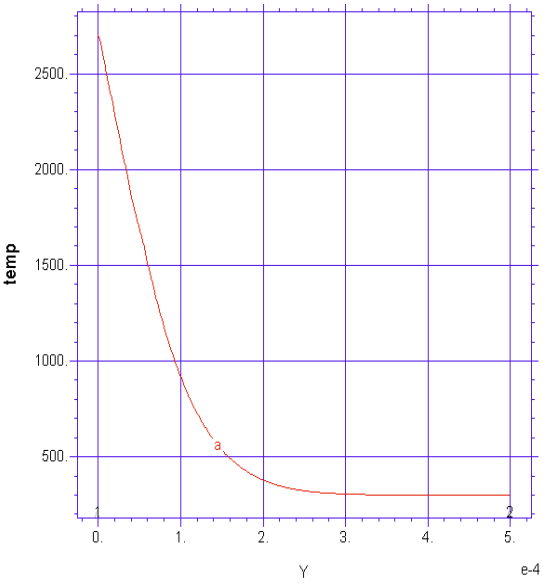

Figure A-11 Temperature vs. distance at 55 ns. (E_d=2.5 J/cm^2). (Singh's data)

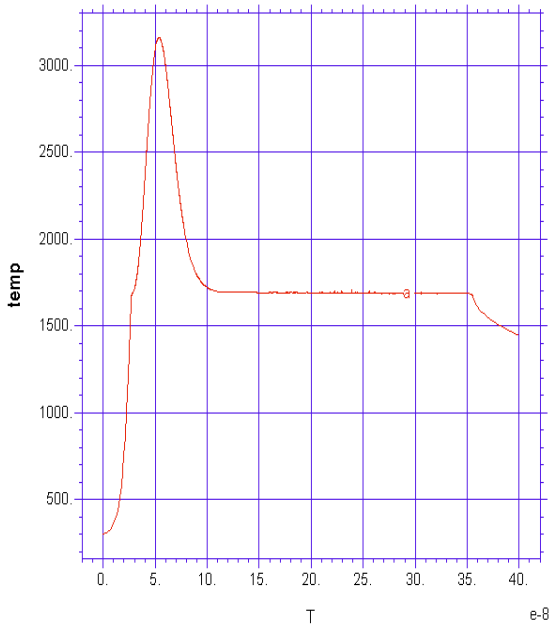

Figure A-12 Temperature vs. time. (E_d=3 J/cm^2). (Using Singh's data)

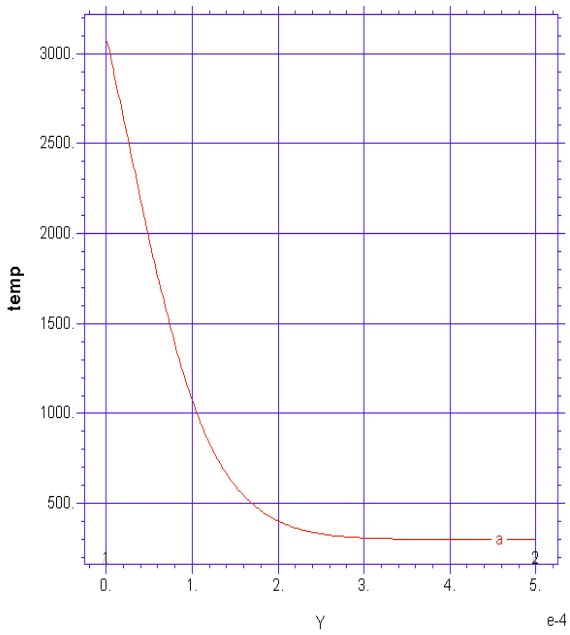

Figure A-13 Temperature vs. distance at 58 ns (E_d=3 J/cm^2). (Singh's data)

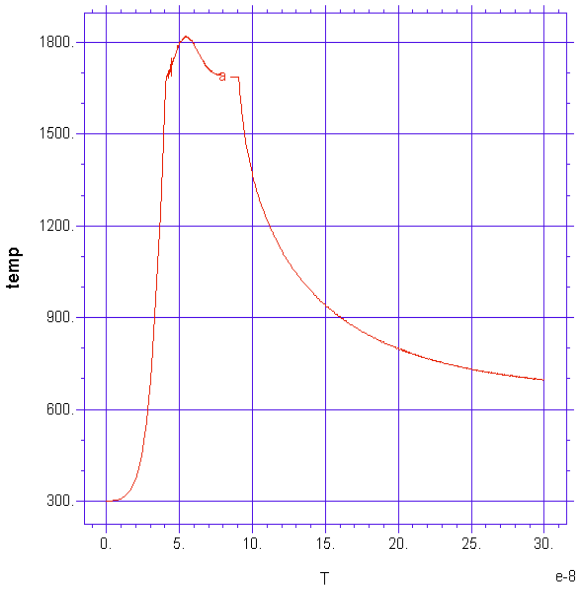

Figure A-14 Temperature vs. time. (E_d=1 J/cm^2). (Using Unamuno's data)

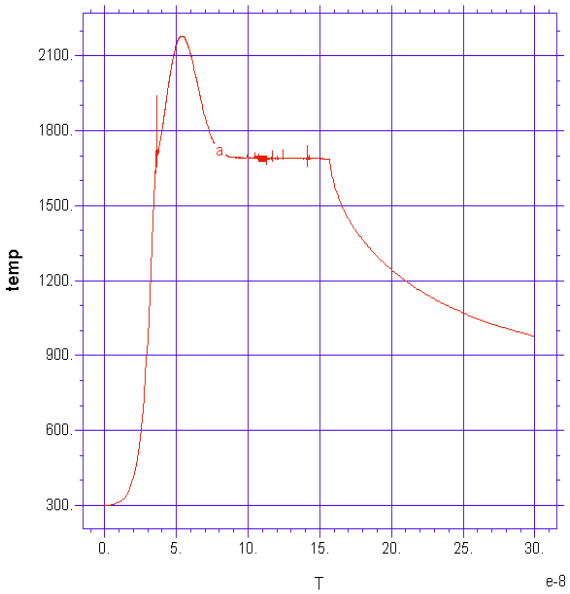

Figure A-15 Temperature vs. time. (E_d=1.5 J/cm^2). (Unamuno's data)

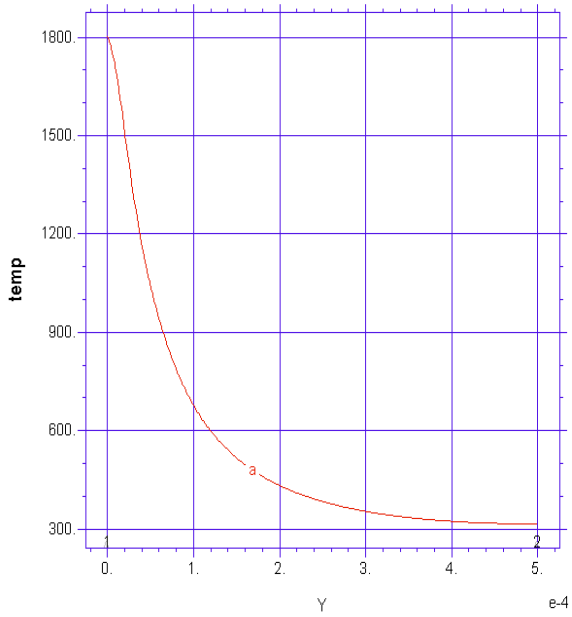

Figure A-16 Temperature vs. Distance at 59ns. (E_d=1 J/cm^2). (Using Unamuno's data)

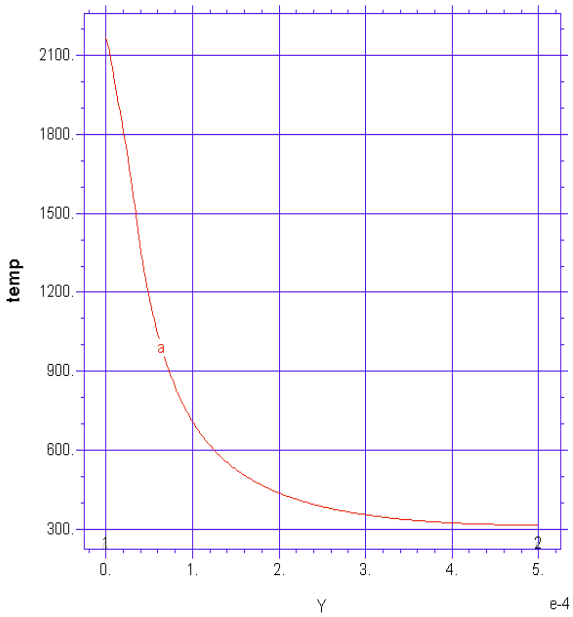

Figure A-17 Temperature vs. distance at 56 ns. (E_d=1.5 J/cm^2). (Unamuno's data)

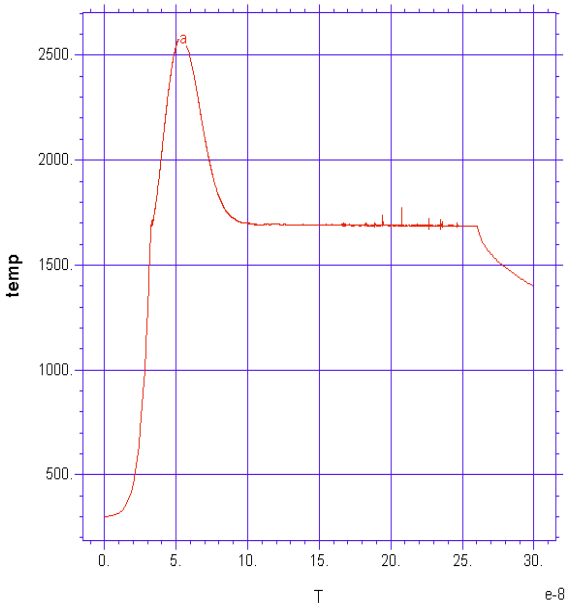

Figure A-18 Temperature vs. time. (E_d=2 J/cm^2). (Using Unamuno's data)

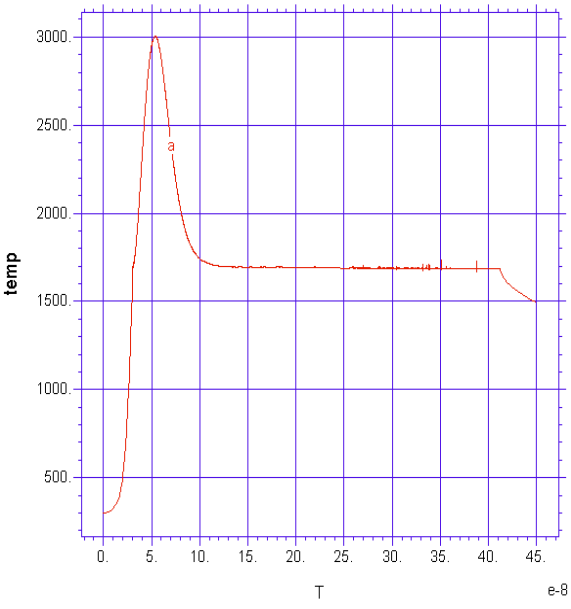

Figure A-19 Temperature vs. time. (E_d=2.5 J/cm^2). (Unamuno's data)

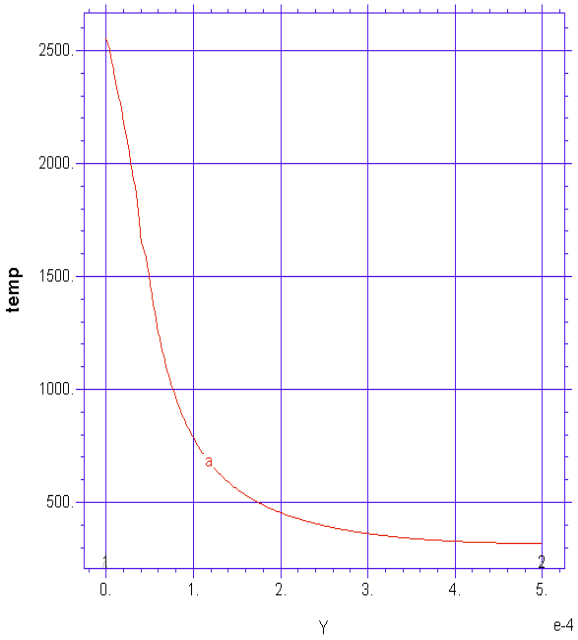

Figure A-20 Temperature vs. Distance at 57ns. (E_d=2 J/cm^2). (Using Unamuno's data)

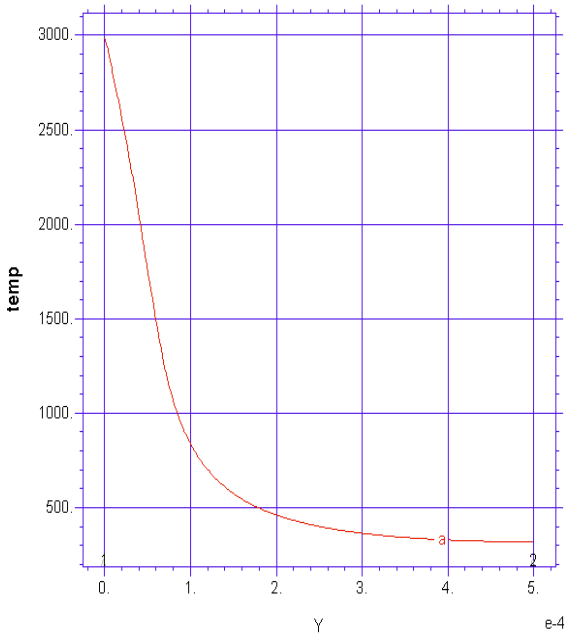

Figure A-21 Temperature vs. distance at 56 ns. (E_d=2.5 J/cm^2). (Unamuno's data)

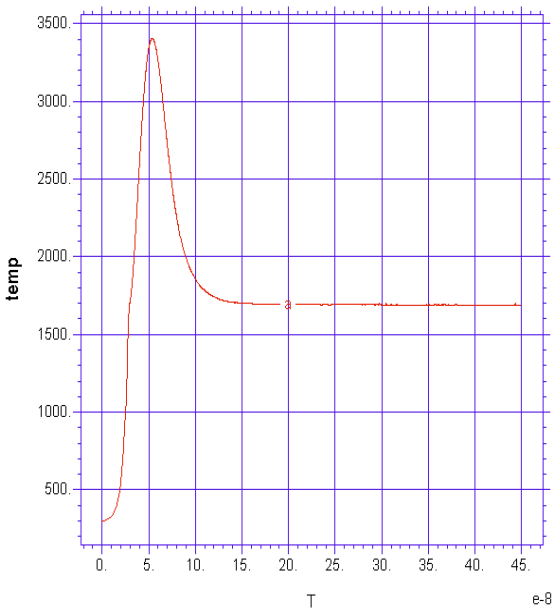

Figure A-22 Temperature vs. time. (E_d=3 J/cm^2). (Using Unamuno's data)

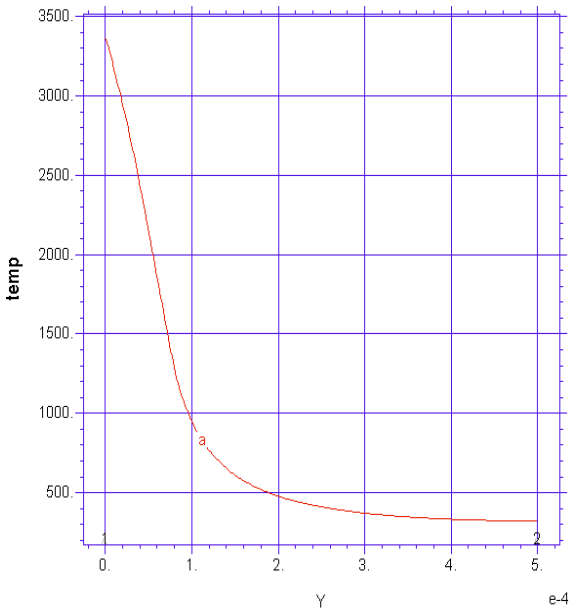

Figure A-23 Temperature vs. distance at 57 ns (E_d=3 J/cm^2). (Unamuno's data)

Supplementary:
The FlexPDE program script:

```
{
  This problem shows the application of FlexPDE to the laser melting of silicon.
}


TITLE
   'Laser Melting'
COORDINATES
    cartesian('x','y')

SELECT
! errlim = 1E-4
!  cubic
  smoothinit
  gridlimit = 3
regrid=off

VARIABLES
  temp(range=3000)
  solid(range=1)

DEFINITIONS

  Qm= 4536                  { latent heat }
  Tm= 1687                    { Melting temperature }
  T0= 1                     { Melting interval +- T0 }

  Tinit
  sinit

  lammain=4.0559-0.014648*temp+2.541e-5*temp^2-2.4507e-8*temp^3+1.3684e-
11*temp^4-4.361e-15*temp^5+7.351e-19*temp^6-5.0801e-23*temp^7
  lamadd=arctan((temp-1687)/1)*0.284111/PI+0.1421
  lambda =lammain+lamadd {w/cm.k}
  rho= 2.42 + ARCTAN((temp-1687)/1)*0.2/PI                { Density g/cm3 }
  cp = 0.78572-2.51e-4*temp+5.93e-7*temp^2-2.83e-10*temp^3+4.1e-14*temp^4
{ heat capacity J/g.k}
  E= 3{Energy density J/cm2}
  D=25e-9 {Pulse width s}
  Dela=45e-9 {pulse Delay s}
  A= E/D*(2/PI)^0.5 {max pulse amplitude, W/cm^2}
```

```
 I0= A*exp(-2*(t-Dela)^2/D^2)  {incident laser power, W/cm^2}
 Absor=arctan((1687-temp)/1)*190000/PI+1655000 {Absorption coefficient cm-1}
 Ref=0.6691-3.1255e-5*temp+8.5224e-8*temp^2-5.71e-11*temp^3+1.222e-
14*temp^4+1.31e-18*temp^5-8.4e-22*temp^6+8.51e-26*temp^7 {Reflectivity}
 P=Absor*(1-Ref)*I0*exp(-Absor*y)  {Heat generation function- another source of heat}
 w = .1e-4 { width of the domain, cm}
 h =  5e-4 {height of the domain.cm}

INITIAL VALUES
  temp=Tinit
  solid =  0.5*erfc((tinit-Tm)/T0)

EQUATIONS
  rho*cp*dt(temp) - div(lambda*grad(temp))  = P  +  Qm*1e9*(0.5*erfc((temp-Tm)/T0)
- solid)
  dt(solid) - 1e-6*div(grad(solid)) =  1e9*(0.5*erfc((temp-Tm)/T0) - solid)

BOUNDARIES

 region 1
   Tinit=300
    sinit=1
   start(0,0)
   natural(temp)=0 line to (w,0)
   natural(temp)=0 line to (w,h)
   natural(temp)=0 line to (0,h)
   natural(temp)=0 line to finish
 feature
    start(0,h/250)  line to (w,h/250)


TIME  0 by 1e-9 to 450e-9

MONITORS
  for cycle=1
 { elevation(temp) from(w/2,0) to (w/2,h) {range=(300,4000)}
  elevation(solid) from(w/2,0) to (w/2,h) }
{contour(temp)}
{contour(solid)}
{contour(rho)}
{contour(cp)}
{contour(Qm)}
{contour(P)}

PLOTS
```

```
  for t= 0 by 10e-9 to 40e-9 by 1e-9 to endtime
  { for t=50e-9 by 1e-9 to 60e-9}
   elevation(solid) from(w/2,0) to (w/2,h/1)
   elevation(temp) from(w/2,0) to (w/2,h/1) {range=(300,4000)}
{   contour(temp)painted range=(300,4000)  }


HISTORIES
   history(solid)   at (w/2,0)
   history(temp)   at (w/2,0)
  { history(temp) at (w/2,h) }

END  34804
```

VITA

Yingfeng Guan was born in Changsha, China on October 8, 1973. He graduated from the High School attached to Hunan Normal University in 1992 and entered the Department of Materials Science and Engineering at Central South University (CSU), China. In 1996, he completed his undergraduate study and received his Bachelor of Science degree in Materials Science. In 1999, he completed his Masters of Science degree at the same school. The thesis was entitled, "Calculation and Evaluation of Al_2O_3-Ln_2O_3 (Ln=Nd, Ce, Yb, Pr, Sm, Eu, Dy) Pseudo-Binary Phase Diagrams with CALPHAD Technique". In 2000, he came to the University of Tennessee, Knoxville and enrolled in the doctoral program in the Department of Materials Science and Engineering. After receiving his Doctor of Philosophy degree in December 2004, he will work for Prof. Anthony J. Pedraza as a postdoctoral research assistant at The University of Tennessee, Knoxville.